

Talapatra, Sandeep K. (2012) *Mechanistic investigation of small molecule inhibitors of kinesin-5 and kinesin-6 family members in cancer drug development*. PhD thesis.

<http://theses.gla.ac.uk/3770/>

Copyright and moral rights for this thesis are retained by the author

A copy can be downloaded for personal non-commercial research or study, without prior permission or charge

This thesis cannot be reproduced or quoted extensively from without first obtaining permission in writing from the Author

The content must not be changed in any way or sold commercially in any format or medium without the formal permission of the Author

When referring to this work, full bibliographic details including the author, title, awarding institution and date of the thesis must be given

Mechanistic investigation of small molecule inhibitors of kinesin-5 and kinesin-6 family members in cancer drug development

Sandeep Kumar Talapatra

Submitted to the University of Glasgow
in fulfillment of the requirements for the Degree of
Doctor of Philosophy

September, 2012

The Beatson Institute for Cancer Research

Garscube Estate, Switchback Road
Glasgow, G61 1BD
Scotland, UK

Abstract

The kinesins form a superfamily of molecular motors that use energy from ATP turnover to generate force. They carry out a diverse set of cellular functions by transducing this force to transport cargos along microtubule (MTs) tracks. Kinesins are distributed among 14 families with different structural organisations all sharing a conserved motor domain that is comprised of a catalytic site for ATP hydrolysis and a MT binding site. Kinesins perform different functions with numerous key roles in mitosis.

The kinesin-5 family member, Eg5, has been shown to play a key role in cross-linking and separating anti-parallel MTs. Inhibition of Eg5 leads to the formation of characteristic monoastral spindles, cell cycle arrest and may also lead to apoptotic cell death. This has led to Eg5 being identified as a potential target for drug development in cancer chemotherapy. To understand the mode of interaction between the protein and the potent drug candidate ispinesib, an extensive study using biochemical and biophysical techniques together with crystallography is presented in this thesis.

Sustained chemotherapy imposes selection pressure on cancer cells, and can generate resistant mutants against chemotherapeutic agents. We have employed crystallographic, biochemical and biophysical approaches to understand the underlying molecular mechanism of resistance to Eg5 inhibition. These approaches establish that the point mutations in the inhibitor-binding pocket decrease the potency of SB743921, a potent Eg5 inhibitor binding at a site near loop L5, by more than 1000-fold. By determining crystal structures of the mutant Eg5 motor domains in the presence and absence of SB743921 and combining the results with calorimetric and molecular dynamics studies, we show that the development of resistance is due to changes in the global flexibility of the protein.

In a second approach to address drug resistance towards allosteric inhibitors binding at the loop L5 site, we have also characterised inhibitor binding to a novel and distinct allosteric pocket in Eg5. This is the first experimental characterisation of protein-ligand interactions in this new site. These studies also revealed an unexpected second site. Extensive biophysical characterisation was used to determine the importance of each site to the observed biochemical activity.

Finally, I have investigated kinesin-6 members as new targets for therapeutic intervention. Among kinesins involved in the mitotic phase, the members of kinesin-6 family are of particular interest as potential drug targets because of their important roles during the anaphase to telophase transition until completion of cell division by cytokinesis. This family consists of three members in humans; MKLP-1, MKLP-2 and MPP1 with a unique structural feature of a long insertion of around 100 amino acids in the loop L6 region. This unique feature makes them interesting not only as a drug target but also to understand their role in protein function. The motor domain of the kinesin-6 family members, MKLP-2 and MPP1 were cloned, expressed and purified and crystallisation trials were carried out. Moderately potent inhibitors were identified by biochemical screening of freely available compound collections. Selectivity analysis was also carried out against other kinesin members to provide specificity data about the inhibitor.

In collaboration with Christophe Labiere from Dr. Catherine Guillou's laboratory at the CNRS, Gif-sur Yvette, France, a SAR investigation of the MKLP-2 inhibitor paprotrain was carried out using 135 analogues. This required extensive biochemical screening against MKLP-2 to identify more potent analogues of paprotrain.

The first objective of this research is to investigate the mechanism by which existing Eg5 inhibitors block catalytic activity and the mechanism through which Eg5 develops resistance to these inhibitors. A second objective was to lay foundations for structural and biochemical characterisation of kinesin-6 family members. The results of this thesis provide a detailed understanding of Eg5 inhibition by ispinesib and describe an unexpected resistance mechanism towards allosteric Eg5 inhibitors dependent on unfavourable entropic effects in the mutant. The experimental characterisation of a new allosteric inhibitor binding site presented here, together with the crystal structure of an inhibitor binding at this site, provides a foundation for structure based design approaches. The work also provides an extensive study on MPP1 and MKLP-2 cloning, protein expression and purification together with screening and characterisation of their inhibitors.

Contents

Abstract.....	2
Contents.....	4
List of Figures.....	8
List of Tables.....	10
List of manuscripts.....	11
Preface.....	13
Acknowledgement.....	14
Author's Declaration	15
Definitions / Abbreviations	16
1 Introduction	21
1.1 Kinesin, a perspective.....	22
1.1.1 <i>Structure and organisation of kinesins</i>	23
1.1.2 <i>Mechanism of Kinesin motility</i>	29
1.2 Function of Kinesins.....	30
1.2.1 <i>Mitotic Kinesins</i>	31
1.2.2 <i>Kinesin-5 family</i>	32
1.2.2.1 Human Eg5.....	33
1.2.2.1.1 Structure and organisation.....	33
1.2.2.1.2 Functions and interactions	36
1.2.2.1.3 Clinical relevance of Eg5.....	38
1.2.2.1.4 Progress in Eg5 drug development.....	45
1.2.3 <i>Kinesin-6 family</i>	46
1.2.3.1 MPP1.....	47
1.2.3.1.1 Structure and organisation.....	48
1.2.3.1.2 Physiological function and interactions.....	49
1.2.3.1.3 Clinical relevance of MPP1	50
1.2.3.2 MKLP-2.....	54
1.2.3.2.1 Structure and organisation.....	54
1.2.3.2.2 Physiological functions and interactions.....	56
1.2.3.2.3 MKLP-2 as a potential anti-cancer drug target.....	59
1.3 Kinesins as potential drug targets for cancer chemotherapy	62
2 Material and methods.....	64
2.1 Materials.....	64
2.2 Human kinesin, Eg5.....	66
2.2.1 <i>Sub-cloning into E. coli expression vectors</i>	66

2.2.1.1	Cloning of ispinesib resistant mutants of Eg5	66
2.2.1.2	Cloning of wild-type and Eg5 mutants with a double hexa histidine tag for Ni-NTA immobilisation	66
2.2.2	<i>Protein expression and purification</i>	67
2.2.2.1	Wild-type and mutants of Eg5.....	67
2.2.2.2	Eg5 with double hexa-histidine tag.....	68
2.2.2.3	Determination of protein concentration and mass spectrometry fingerprint analyses.....	68
2.2.2.4	Polymerisation of tubulin into MTs.....	69
2.2.3	<i>Steady state ATPase assay</i>	69
2.2.3.1	Measurement of kinetic parameters	69
2.2.3.2	Measurement of inhibition of Eg5 ^{WT} and mutants	69
2.2.4	<i>Isothermal titration calorimetry (ITC)</i>	70
2.2.4.1	Study of wild-type Eg5 with ispinesib	70
2.2.4.2	Study of wild-type and mutant Eg5 with SB743921, BI8, ispinesib and monastrol.....	71
2.2.5	<i>Surface plasmon resonance</i>	71
2.2.5.1	Study of two site binding of BI8 to Eg5	72
2.2.6	<i>Crystallisation of Eg5-ADP mutants and Eg5-ADP- inhibitor complexes</i>	72
2.2.6.1	Crystallisation of the “ispinesib mutants”: Eg5 ^{D130V} , Eg5 ^{A133D} and Eg5 ^{DM}	72
2.2.6.2	Crystallisation of Eg5 ^{WT} -ispinesib, Eg5 ^{WT} -SB743921 and Eg5 ^{A133D} -SB743921 complexes.....	72
2.2.6.3	Crystallisation of Eg5 ^{WT} - BI8.....	73
2.2.7	<i>Data collection, processing, structure determination, refinement and model quality</i> 73	
2.2.7.1	Eg5 in complex with ispinesib.....	73
2.2.7.2	Eg5 mutants.....	74
2.2.7.3	Eg5 ^{WT} and Eg5 ^{A133D} in complex with SB743921.....	78
2.2.7.4	Structure of Eg5-BI8 quaternary structure	78
2.3	<i>MPP1</i>	79
2.3.1	<i>Human MPP1</i>	79
2.3.1.1	Sub-cloning into <i>E. coli</i> expression vectors	79
2.3.1.2	Expression and purification of protein.....	79
2.3.1.3	<i>In vitro</i> screening for inhibitors of the human mitotic kinesin MPP1.....	80
2.3.1.3.1	Steady state ATPase measurements and determination of IC ₅₀ values	80
2.3.1.3.2	Determination of the type of inhibition of physodic acid for MPP1 in the absence and presence of MTs.....	81
2.3.1.3.3	Cytophos assay.....	81
2.3.1.4	Crystallisation trials.....	82
2.3.2	<i>MPP1 orthologues in other species</i>	83
2.3.2.1	Sub-cloning into <i>E. coli</i> expression vectors	83
2.3.2.2	Study of MPP1 inhibitor using steady state ATPase assay	83
2.3.2.3	Crystallisation trials.....	83
2.4	<i>Human MKLP-2</i>	84
2.4.1	<i>Sub-cloning into E. coli expression vectors</i>	84
2.4.1.1	Cloning of MKLP-2 ⁵⁶⁻⁵⁰⁵ , ΔL6 and point mutants of MKLP-2	84
2.4.2	<i>Expression and purification of protein of MKLP-2 constructs</i>	84

2.4.3	<i>Kinetics and inhibition measurement of MKLP-2 using steady state ATPase assay</i>	85
2.4.4	<i>Crystallisation trials</i>	85
3	Results	86
3.1	Analysis of ispinesib as a potent inhibitor of Eg5	86
3.1.1	<i>Biochemical and biophysical studies of ispinesib binding to Eg5</i>	86
3.1.2	<i>Structural analysis of Eg5-ispinesib complex</i>	87
3.1.2.1	Twining and pseudotranslational symmetry	89
3.1.3	<i>Comparison of ispinesib binding to Eg5 and comparison with other allosteric inhibitors</i>	90
3.2	Understanding the mechanism of resistance of Eg5 towards small molecule inhibitors	95
3.2.1	<i>Kinetic analysis of Eg5</i>	95
3.2.2	<i>Calorimetric analysis of SB743921 binding to Eg5^{WT} and mutants</i>	99
3.2.3	<i>Evaluation of Eg5^{D130V}, Eg5^{A133D} and Eg5^{DM} structures and comparison to Eg5^{WT}</i>	100
3.2.4	<i>Structural determination and comparison of Eg5^{WT}-SB743921 and Eg5^{A133D}-SB743921 complexes</i>	105
3.3	Studies on a novel allosteric inhibitor-binding pocket of Eg5	108
3.3.1	<i>Kinetic studies of BI8</i>	108
3.3.2	<i>The crystal structure of Eg5-BI8 and comparison with the structure of Eg5-ispinesib</i>	109
3.3.2.1	The novel Eg5 inhibitor-binding pocket for BI8 binding	109
3.3.2.2	Analysis of the second inhibitor-binding site for BI8 and comparison with phase II clinical candidate ispinesib binding	111
3.3.3	<i>Isothermal titration calorimetry</i>	115
3.3.4	<i>SPR analysis of BI8 binding to Eg5</i>	122
3.3.4.1	Study of two site binding of BI8 to Eg5	122
3.4	MPP1	125
3.4.1	<i>Human MPP1</i>	125
3.4.1.1	Physodic acid discovered as an inhibitor of human mitotic kinesin MPP1	125
3.4.1.1.1	MPP1 expression and purification	125
3.4.1.1.2	Steady state ATPase measurements and determination of IC ₅₀ values	126
3.4.2	<i>Identification of compound inhibiting MPP1</i>	130
3.4.2.1.1	Cytophos assay	130
3.4.3	<i>Initial SAR study of inhibitor analogues of Norlobaric acid</i>	137
3.4.3.1.1	Determination of the type of inhibition of physodic acid for MPP1 in the absence and presence of MTs	143
3.4.3.2	Crystallisation trials	144
3.4.4	<i>MPP1 orthologues from M. musculus, R. norvegicus and X. laevis</i>	145
3.4.4.1	Protein expression of different MPP1 motor domain orthologues	145
3.4.4.2	Study of Physodic acid using steady state ATPase assay	147

3.4.4.3	Crystallisation trials.....	151
3.5	Human MKLP-2	152
3.5.1	<i>Expression and purification of protein.....</i>	152
3.5.2	<i>Characterisation of putative inhibitor-binding site</i>	154
3.5.3	<i>SAR study of MKLP-2 inhibitors using steady state ATPase assays</i>	156
3.5.4	<i>Crystallisation trials.....</i>	170
4	Discussion and future perspectives	171
4.1	Understanding the mechanism of Eg5 targeting drugs and future directions	171
4.1.1	<i>A better understanding of ispinesib binding and affinity towards the Eg5 motor domain</i>	171
4.1.2	<i>The underlying mechanism of resistance of Eg5 towards small molecule inhibitors</i> <i>172</i>	
4.1.3	<i>Dissection of the novel allosteric site of Eg5 and its significance in drug discovery of Eg5 targeting drugs.....</i>	177
4.1.4	<i>Future perspectives of drugs targeting Eg5.....</i>	179
4.2	Development of MPP1 as a new drug target.....	180
4.2.1	<i>Analysing the inhibitor of MPP1</i>	180
4.2.2	<i>Orthologues of human MPP1 for drug discovery.....</i>	182
4.3	Advances and progress in drug discovery of MKLP-2	182
4.3.1	<i>Identification of unique structural elements in MKLP-2 involved in inhibitor-binding</i>	182
4.3.2	<i>Progress of paprotrain based drug design of MKLP-2 inhibitors.....</i>	183
4.4	Conclusion	184
5	Bibliography	185

List of Figures

Figure 1-1: Structural representation of motor proteins.	22
Figure 1-2: Phylogenetic tree of kinesins.	23
Figure 1-3: Classification of kinesins based on the position of the motor domain.	24
Figure 1-4: Overall structure and important binding sites of kinesins.	26
Figure 1-5: Key structural features driving conformational changes during the ATPase cycle of conventional kinesin.	28
Figure 1-6: Different models depicting conventional kinesin motility.	30
Figure 1-7: Phylogenetic tree representing members of the kinesin-5 family.	33
Figure 1-8: Eg5 structural organisation and homotetramerisation.	33
Figure 1-9: Crystal structure of the motor domain of Eg5 and the loop L5.	35
Figure 1-10: Prediction of quaternary structure of the Eg5 stalk domain.	36
Figure 1-11: Eg5 function in the formation of the bipolar spindle.	37
Figure 1-12: Role of kinesin-5 (Eg5) in neuronal migration.	38
Figure 1-13: Over-expression of Eg5 in pancreatic cancer.	39
Figure 1-14: Phenotypic screen to identify inhibitors of bipolar spindle formation.	40
Figure 1-15: Figure showing the conformational changes of the inhibitor-binding region.	41
Figure 1-16: Conformational changes in the switch II cluster on inhibitor binding.	42
Figure 1-17: Stereo plot of monastrol and STLC bound in the allosteric pocket.	43
Figure 1-18: Schematic representation of the contacts between monastrol (a) and STLC (b) and residues of the Eg5 inhibitor-binding pocket.	43
Figure 1-19: Chemical structures of Eg5 inhibitors.	44
Figure 1-20: Phylogenetic tree representing the kinesin-6 family.	46
Figure 1-21: Bar diagram of <i>H. sapiens</i> kinesin-6 family members and sequence alignment of the loop L6 region.	47
Figure 1-22: Identification of the phospho epitope of MPP1.	48
Figure 1-23: Structural prediction into various domains of MPP1.	49
Figure 1-24: Interactions of MPP1.	50
Figure 1-25: Interaction and function of MPP1.	51
Figure 1-26: Co-localisation and interaction of MPP1 and PRC1.	51
Figure 1-27: Over-expression and siRNA treatment of MPP1.	52
Figure 1-28: Localisation of MKLP-2 during cell division.	54
Figure 1-29: Structural prediction of MKLP-2.	56
Figure 1-30: Interactions of MKLP-2.	57
Figure 1-31: Expression profile of MKLP-2 in pancreatic adenocarcinoma cells (PDAC).	60
Figure 1-32: Inhibition of MKLP-2 by paprotrain.	61
Figure 2-1: Protein purification of Eg5 ^{D130V}	68
Figure 3-1: Characterisation of Eg5 inhibition by ispinesib.	87
Figure 3-2: Overall structure of the ADP-Eg5-ispinesib ternary complex (chain B).	89
Figure 3-3: Interactions of ispinesib with the Eg5 inhibitor-binding region and comparison with other inhibitors of Eg5.	94
Figure 3-4: Kinetic data for wild-type and mutant Eg5 (Basal ATPase).	97
Figure 3-5: Kinetic data for wild-type and mutant Eg5 (MT-stimulated ATPase).	98
Figure 3-6: ITC analyses of SB743921 binding to wild-type and mutant Eg5.	100
Figure 3-7: Loop L5 region of Eg5 ^{WT} in comparison with Eg5 mutants.	103

Figure 3-8: Crystal structures of wild-type and mutant Eg5 in complex with SB743921.	107
Figure 3-9: Biochemical and phenotype characterisation of the Eg5-BI8 complex.	109
Figure 3-10: Characterisation of the novel inhibitor-binding pocket in Eg5.	111
Figure 3-11: Characterisation of the second allosteric binding pocket.	113
Figure 3-12: Comparison of Eg5-BI8 and Eg5-ispinesib complexes.	114
Figure 3-13: ITC analyses of ligand binding to Eg5.	121
Figure 3-14: Binding studies of BI8, ispinesib and monastrol to double histidine tagged Eg5 immobilised on NTA surface.	123
Figure 3-15: Bar diagram of full length MPP1 and two expressed MPP1 motor domains.	126
Figure 3-16: Characterisation of the basal and MT-stimulated ATPase activity of MPP1.	127
Figure 3-17: Schematic representation of inhibitor screening against MPP1 activity.	137
Figure 3-18: Structure of depsides and depsidones.	138
Figure 3-19: Inhibition of MPP-1 ₅₄₋₄₉₁ ATPase activity by depsidones.	139
Figure 3-20: Type of inhibition of MPP-1 ₅₄₋₄₉₁ ATPase activity measured with Physodic acid.	144
Figure 3-21: Sequence alignment of MPP1 motor domains from different species.	146
Figure 3-22: Protein expression of MPP1 orthologues.	146
Figure 3-23: Characterisation and inhibition of the basal and MT-stimulated ATPase activity of MPP1 orthologues from three different species.	148
Figure 3-24: Sequence alignment and SDS-PAGE of purified MKLP-2 motor domain. ..	153
Figure 3-25: Characterisation of the basal and MT-stimulated ATPase activity of MKLP-2.	155
Figure 3-26: Structure of paprotrain with the different regions of modification for SAR study.	157
Figure 4-1: Structural changes that occur around the A133D mutation due to thermodynamic fluctuation on inhibitor-binding.	175
Figure 4-2: The far-reaching effects of the A133D mutation propagated throughout the SB743921- Eg5 ^{A133D} complex during MD simulations that predicts the rigidification of the structure when compared with the Eg5 ^{WT} complex.	176
Figure 4-3: BI8 binding and mechanism of inhibition.	178
Figure 4-4: Chemical structures of compounds tested for MPP1 inhibition.	181

List of Tables

Table 1-1: Tabular representation of molecular motors during mitosis.....	32
Table 2-1: Data collection and refinement statistics for the Eg5–ispinesib complex.	74
Table 2-2: Table representing data collection and refinement statistics of Eg5 mutant and complexes with SB743921.	76
Table 2-3: Table representing the different regions of wild-type and mutant Eg5 as seen in the solved structure together with the Ramachandram plot.	77
Table 2-4: Data collection and refinement statistics of Eg5 in complex with BI8.....	78
Table 3-1: Inhibition of the Eg5 ATPase activity by ispinesib.	87
Table 3-2: Thermodynamic data for binding of ispinesib to Eg5-ADP.	87
Table 3-3: r.m.s. deviations in Å calculated for wild-type and mutant Eg5 structures.	104
Table 3-4: Basal and MT-stimulated steady state ATPase activity of MPP1 proteins	129
Table 3-5: Inhibition profiling of 13 compounds against MPP1 activity using Cytophos assay.....	131
Table 3-6: SAR study of depsidones and depsides from lichen as potential inhibitors of human MPP1.	140
Table 3-7: Specificity of Physodic acid tested on the inhibition of the basal and MT-stimulated ATPase activities of a variety of human kinesins involved in mitosis or intracellular transport.	142
Table 3-8: Kinetic parameters for MPP1 from three different species and inhibition of their basal and MT-stimulated ATPase activity by Physodic acid.....	150
Table 3-9: Summary of kinetic parameters for wild-type and mutants of MKLP-2.....	156
Table 3-10: Inhibition of basal and MT-stimulated ATPase activities by paprotrian analogues.	158

List of manuscripts

Accepted manuscripts

The structure of the ternary Eg5-ADP-ispinesib complex. Sandeep K. Talapatra, Alexander Schuettelkopf, Frank Kozielski. *Acta Cryst* **D68**, 1311-1319

Co-author publications

Indolobenzazepin-7-ones and 6-, 8-, and 9-membered ring derivatives as tubulin polymerization inhibitors: synthesis and structure--activity relationship studies. Aurelien Putey, Florence Popowycz, Quoc-Tuan Do, Philippe Bernard, Sandeep K. Talapatra, Frank Kozielski, Carlos M. Galmarini, and Benoit Joseph. *J. Med. Chem.* 2009, **52**, 5916–5925.

Submitted manuscripts

First author publications

Structural Insights Into a Novel Inhibitor Binding Pocket in Kinesin Spindle Protein. Venkat Ulaganathan and Sandeep K. Talapatra (joint first author), Kristal Kaan, Oliver Rath, Katarzyna Tkocz, David Hackney and Frank Kozielski. *Submitted to JACS Journal*.

The mitotic kinesin Eg5 overcomes inhibition to the phase I/II clinical candidate SB743921 by an allosteric resistance mechanism. Sandeep K. Talapatra, Nahoum Anthony, Simon MacKay, Frank Kozielski. *Submitted to PLOS Biology Journal*.

Manuscripts in preparation

First author manuscripts

The specificity of two kinesin inhibitors, SB743921 and paprotrain, is determined by their unique subfamily-specific structural features. Marta Klejnot, Sandeep K. Talapatra and Frank Kozielski. *Manuscript in preparation*.

Depsidones from lichens as natural product inhibitors of M-Phase Phosphoprotein 1, a human kinesin involved in cytokinesis. Sandeep K. Talapatra, Oliver Rath, Sophie Tomasi, Eddie Clayton, Dimitrios A. Skoufias and Frank Kozielski. *Manuscript in preparation*.

Co-author manuscripts

New Arylindole Inhibitors of Kinesin MKLP-2. 2. Synthesis, Biological Evaluation and Structure-Activity Relationships. Christophe Labrière, Sandeep K. Talapatra, Sylviane Thoret, Cécile Bougeret Frank Kozielski, Catherine Guillou. *Manuscript in preparation*.

Development of Optimized S-Trityl L-Cysteine Based Inhibitors of Kinesin Spindle Protein with potent *in Vivo* Antitumor Activity in Lung Cancer Xenograft Models. James A. D. Good, Fang Wang, Oliver Rath, Hung Yi Kristal Kaan, Sandeep K. Talapatra, Dawid Podgórski, Simon P. MacKay and Frank Kozielski. *Submitted J. Med. Chem* .

Preface

This thesis is dedicated to my father Samir Chandra Talapatra who passed away untimely on 29th June 2012 suffering from liver cancer. His blessing, inspiration and motivation have been the key force behind pursuing this PhD.

Acknowledgement

First and above all, I would like to thank my father, Late Mr. Samir Chandra Talapatra and my mother, Mrs. Soma Talapatra for by their continuous hard work and belief in my capabilities that I am able to present this thesis.

I am obliged and gratified to my supervisor Dr. Andrew Pannifer, for his guidance, understanding and contribution in presenting this thesis. I would also like to express my gratefulness to my previous supervisor, Prof. Frank Kozielski, for his support and guidance throughout my research project. I am also grateful to my advisor, Prof. David Gillespie, for his support and advice. I would also like to thank the past and present members of the R09 group, Alexander Schüttelkopf, James Good, Marta Klejnot, Oliver Rath, Venkat Ulaganathan and Fang Wang for their help and suggestions during my PhD work.

I am also grateful to Dr. Christopher H. Gray for all his guidance, advice and support during the most demanding times of my PhD. Special mention to all the collaborators Prof. Simon Mackay and Dr. Nahoum Anthony (University of Strathclyde), Prof. David Hackney (Carnegie Mellon University), Prof. Benoit Joseph (University Claude Bernard Lyon).

I thank Prof. Alan Cooper, Margaret Nutley and Dr. Sharon Kelly (all from University of Glasgow) for their input towards my project.

Not the least, the completion of my PhD projects has been possible with the love, continual encouragement and support of my wife, Mrs Moon Sarma Talapatra.

The Beatson Proteomics Facility, Molecular Technology Services and Central Services at the Beatson Institute have been tremendously helpful in providing the their services. I would also like to acknowledgement the European Synchrotron Radiation Facility (ESRF), Diamond Light Source (DLS) for providing us with beamtime and assistance for X-ray crystallography.

Last but not least, I am grateful to the Cancer Research UK (CRUK) for funding my PhD and research.

Author's Declaration

I declare that I am the sole author of this thesis and the work presented here is entirely my own, except where acknowledged to others. This thesis does not include work that has been submitted for consideration for another degree in this or any other university. This is a true copy of the thesis, including any required final revisions, as accepted by my examiners.

Definitions / Abbreviations

Å	Ångström
aa	amino acid
A ₆₀₀	Absorbance at 600 nm
ADP	Adenosine diphosphate
AMP-PNP	Adenylyl-imidodiphosphate
ATP	Adenosine triphosphate
AU	Asymmetric unit
Cdk1	Cyclin dependent kinase 1
cDNA	Complementary deoxyribonucleic acid
CENP-E	Centromere-associated protein E
CIPD	Chronic Inflammatory Demyelinating Polyneuropathy
cm	Centimetre
CPC	Chromosomal Passenger Complex protein
cryo-EM	Cryo-electron microscopy
Da	Dalton
DM	Double mutant
ΔH	Enthalpy change
ΔS	Entropy change
DMSO	Dimethyl sulfoxide
DTT	Dithiothreitol
EC ₅₀	Half maximal effective concentration
EDTA	Ethylenediaminetetraacetic acid

Na-EGTA	Ethylene glycol tetraacetic acid
ESRF	European Synchrotron Radiation Facility
HCC	<u>Hepatocellular carcinoma</u>
HEPES	4-(2-hydroxyethyl)-1-piperazineethanesulfonic acid
HPV	Human papillomavirus
hr	hour
HT	High-throughput
IC ₅₀	half maximal inhibitory concentration
IPTG	Isopropyl β-D-1-thiogalactopyranoside
ITC	Isothermal titration calorimetry
KAP	kinesin accessory protein
K ₂ HPO ₄	Dipotassium phosphate
K _a	acid dissociation constant
kcal/mol	kilocalorie per mole
KCl	potassium chloride
K _d	dissociation constant
kDa	Kilodalton
KHC	Kinesin Heavy Chain
KIF	Kinesin Family Member
K _i ^{app}	apparent inhibition constant
KLC	Kinesin Light Chain
MCAK	Mitotic centromere-associated kinesin
MD	motor domain

MDR	multiple drug resistant
MES	2-(<i>N</i> -morpholino)ethanesulfonic acid
mg	milligrams
Mg ²⁺ ADP	Magnesium (II) Adenosine-5'-triphosphate
Mg ²⁺ ATP	Magnesium (II) Adenosine diphosphate
MgCl ₂	Magnesium chloride
MIA	Maximum inhibition attained
mins	minutes
MKLP-1	Mitotic kinesin like protein 1
MKLP-2	Mitotic kinesin like protein 2
ml	millilitre
mm	millimetre
mM	milli molar
MPP1	M-phase phosphoprotein 1
mRNA	messenger Ribonucleic acid
MT	microtubules
<i>N</i>	Stoichiometry
NaCl	Sodium chloride
Ncd	Non-claret disjunctional
NCI	National Cancer Institute
NEB	New England Biolabs
Ni ²⁺ NTA	Ni(II)-nitrilotriacetic acid
nm	Nanometre

Nm	Nanomolar
NMR	Nuclear magnetic resonance
NTA	Nitriloacetic acid
PAGE	Polyacrylamide gel electrophoresis
PCR	Polymerase chain reaction
PEG	Polyethylene glycol
PGP	P-glycoprotein
PIPES	Piperazine-N,N'-bis(2-ethanesulfonic acid)
PMSF	Phenylmethane sulfonylfluoride
PtK	Protein tyrosine kinase
rmsd	Root-mean-square deviation
RT	Room temperature
SAR	Structure-activity relationship
SAXS	Small-angle X-ray scattering
SDS	Sodium dodecyl sulfate
sec	seconds
siRNA	Small interfering ribonucleic acid
SPR	surface plasmon resonance
STLC	S-trityl-L-cysteine
TB	Terrific broth
TPX2	Targeting Protein for Xklp2
Tris	Tris(hydroxymethyl)aminomethane
uv	Ultra violet

Xklp2 *Xenopus* plus-end-directed kinesin-like protein 2

1 Introduction

Cell cycle progression is fundamentally dependent on the highly organised movement of genetic material to the poles of the mitotic spindle and into daughter cells. Spindle formation, chromosome separation and chromosome motility all require a force-generating sub-cellular machinery to drive proteins and chromosomes in a spatially and temporally controlled manner to segregate chromatids correctly.

Three major families of cytoskeletal molecular motors have been identified which are able to generate force in cells, in each case converting the chemical energy of ATP into mechanical force (Figure 1-1). The first of these families to be identified was myosin in 1939.¹ Myosin slides over actin filaments and is, for example, the major force generator in muscle tissue. Subsequently, dynein was discovered in 1963² and was shown to be important in transporting vesicles and positioning the Golgi complex. In contrast to myosin, dynein moves along microtubule (MT) tracks. Then in 1985^{3,4}, the first member of the kinesin family (named conventional kinesin; kinesin-1) was discovered. Like dynein, kinesins move along MT tracks and the family is now known to consist of more than 650 proteins, with important functions in a range of cellular processes including mitosis, meiosis and axonal transport.⁵ Members of the kinesin family have now been shown to play critical roles in the formation of the mitotic spindle, MT sliding during metaphase and in the depolymerisation of MTs during different stages of mitosis. Their important biological roles in the cell cycle⁶ and the mechanism by which the kinesins convert chemical energy into force has raised a number of questions about the structure of these proteins, and the key features of the proteins required to create and transmit this force. Clinical interest in certain kinesins is also high with anti-proliferative inhibitors currently in Phase II clinical trials.⁷⁻¹⁰ The work presented in this thesis focuses on investigating the molecular mechanism of allosteric inhibition of the kinesin-5 family member Eg5 by a number of different series of compounds in order to understand the key interactions and the implications for kinesins as a therapeutic target. In addition, progress in the expression, purification and crystallisation of two members of the kinesin-6 family, MPP1 and MKLP-2, is described together with initial progress towards developing inhibitors of these proteins.

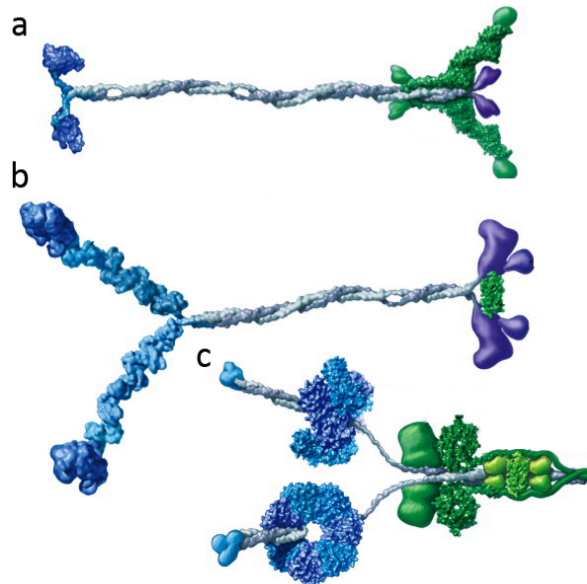


Figure 1-1: Structural representation of motor proteins.

Domain organisation of a) conventional kinesin, b) myosin V, and c) cytoplasmic dynein. The motor domains are represented in shades of blue, followed by the stalk domain in grey and the tail domains in purple. The light chains bound to or bound close to the tail domain, are represented in green. The figure depicts the overall similarity in the structure of all three superfamilies of proteins, which may have diversified from a common ancestor. Adapted from Kolomeisky et al., 2007.¹¹

1.1 Kinesin, a perspective

The kinesins (KIF) were first identified in the mid-1980s in squid and mammalian brain, using *in vitro* motility assays.^{4,12-14,15} The kinesin superfamily consists of at least 650 distinct motor proteins. The first major members of the kinesin superfamily were initially identified based on observations made using electron microscopy on mouse brain.^{1,3} Recent analysis has identified many different families with the total number of families identified to be fourteen.^{16,4,12,3} In mammals, 45 KIF genes that are related to kinesins have been identified to belong to these families, but there could be many more KIF proteins as multiple isoforms are generated by alternative mRNA splicing (Figure 1-2).¹⁷

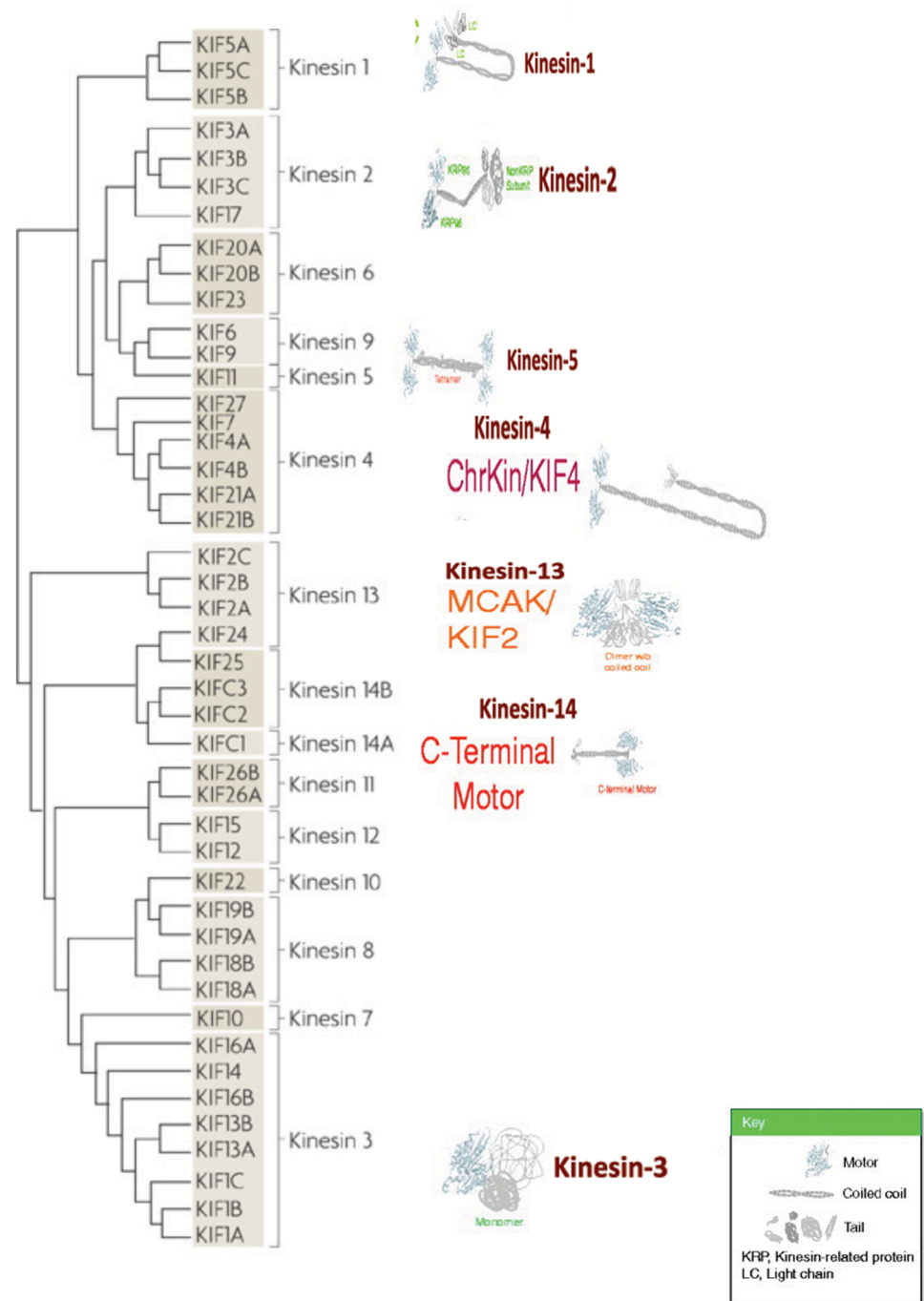


Figure 1-2: Phylogenetic tree of kinesins.

Current phylogenetic tree based on sequence homology analysis categorises kinesins into 14 distinct families, with each member of a family sharing sequence homology, domain organisation, motility characteristics and similar functions (Red: chromosome and spindle organisation; green: vesicular and organelle transport). The individual families are represented in brown. Adapted from Hirokawa *et al.*, 2009 and Dagenbach *et al.*, 2004.^{16,18}

1.1.1 Structure and organisation of kinesins

Typically, kinesins consist of three main domains; (1) the motor domain (MD), responsible for ATP hydrolysis and MT-binding. It also supports force generation with the aid of the small neck linker region that follows the motor domain, (2) the tail domain which binds

diverse cargos or adaptor proteins and (3) the stalk or coiled coil domain which links the motor and tail domains and mediates oligomerisation of a number of different kinesins.^{19,20}

Based on the arrangement of these three domains, the kinesins are divided into three categories: N-terminal, Internal or C-terminal. N-type kinesins (e.g. conventional kinesin, kinesin-1) have the MD situated at the N-terminus and move towards the plus-end of MTs (the dynamically growing end) with the exception of KIF14 where the motor domain is located internally but have consensus N-type motor sequence as other N-terminal kinesins.^{21,22} C-type kinesins (e.g. kinesin-14 family members) have their MD at the C-terminus and travel to the MT minus end. M-type kinesins have the MD situated in the middle of the amino acid sequence and diffuse one-dimensionally along MTs in the proto-filament promoting depolymerisation of the terminal MT dimer (Figure 1-3).²³

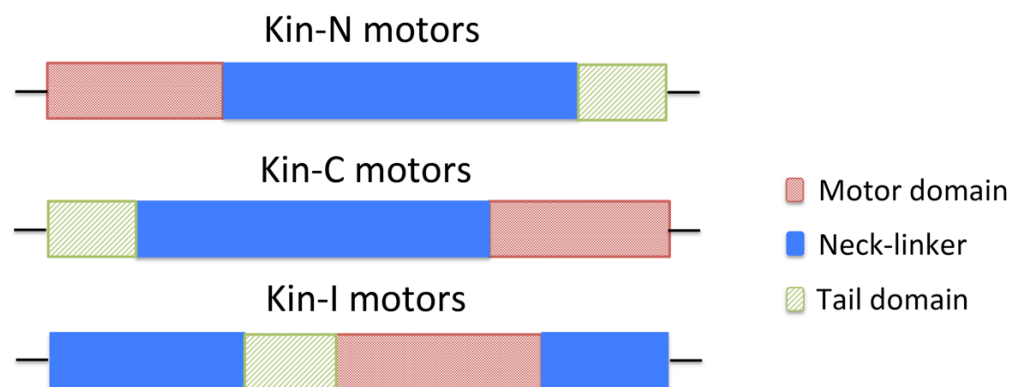


Figure 1-3: Classification of kinesins based on the position of the motor domain.

Bar diagram representing, Kin-N (N-terminal motor domain), Kin-C (C-terminal motor domain) and Kin-I (internal motor domain). Taxonomy of the kinesin superfamily illustrated here by amino acid sequence conservation. The red colour indicates the approximate position of the catalytic core; the blue colour indicates the position of the coiled coil region and the green colour represents the tail domain with all domains corresponding to the sequences alignment of different kinesins. The orphan kinesin motors also have their catalytic cores positioned at the N-terminus of the polypeptide chain. Adapted from Vale *et al*, 1997.¹²

The 105 crystal structures of kinesins deposited in the PDB show the conserved nature of the motor domain irrespective of the position of the motor domain.²⁴⁻²⁶ The overall structure of the motor domain of conventional kinesin demonstrates an eight-stranded β -sheet, surrounded by three major α -helices on each side (Figure 1-4a). The force generating function of kinesins uses chemical energy from ATP hydrolysis. For this the motor domain contains the catalytic site for ATP binding. There is considerable structural detail in the PDB revealing the interactions between kinesins and ADP.^{27,28} This active site,

includes a highly conserved loop, the P-loop (GxxxxGKS/T) or Walker motif, which is conserved in kinesins, G proteins and myosins and interacts with the α - and β -phosphates of ADP. The ADP binding to this exposed surface cleft is co-ordinated with a magnesium ion.²⁹ The P-loop motif also shares similarity with a diverse set of proteins such as adenylate kinase, transducin, Ras and RecA though there is no other structural or sequence similarity (Figure 1-4b).^{30,31} Interactions with the γ -phosphate are also mediated by conserved residues. In human conventional kinesin, amino acids 201–203 contain the universally conserved Ser-Ser-Arg motif, which is similar to that of myosin.³² For example in the structures of human Eg5 and mouse Kif1a both in complex with AMPPNP (a slowly hydrolysable form of ATP) there is an interaction between γ -phosphate of AMPPNP with Ser223 of Eg5 and Ser215 of Kif1a.³³ In the structure of Dictyostelium myosin with Mg^{2+} ADP–AlF₄ (a Mg^{2+} -ADP-Pi analogue) bound, Ser243 of this motif performs a similar function. This provides evidence about the conserved nature of ATP binding sites where interactions with ATP and ADP form the basis of the whole cycle of motility in these proteins. Another highly conserved motif in kinesins, switch I (SSRSH) (Figure 1-4c) act as a γ -phosphate sensor and translates local changes to larger conformational changes in the third conserved motif, switch II (DLAGSE) cluster (Figure 1-4d) that is responsible for motility.²⁴

In kinesins, loop L11, helix 4, loop L12 and helix 5 (L11- α 4-L12 and α 5) form the MT-binding site that consists of primarily positive charged residues that communicate via electrostatic interactions with negative charged residues of MTs. Experimental evidence illustrates that loops L7 and L8 are also involved in MT-binding. The nucleotide hydrolysis cycle as mentioned above is responsible for conformational changes that affect binding of kinesin to MTs.³³⁻³⁵

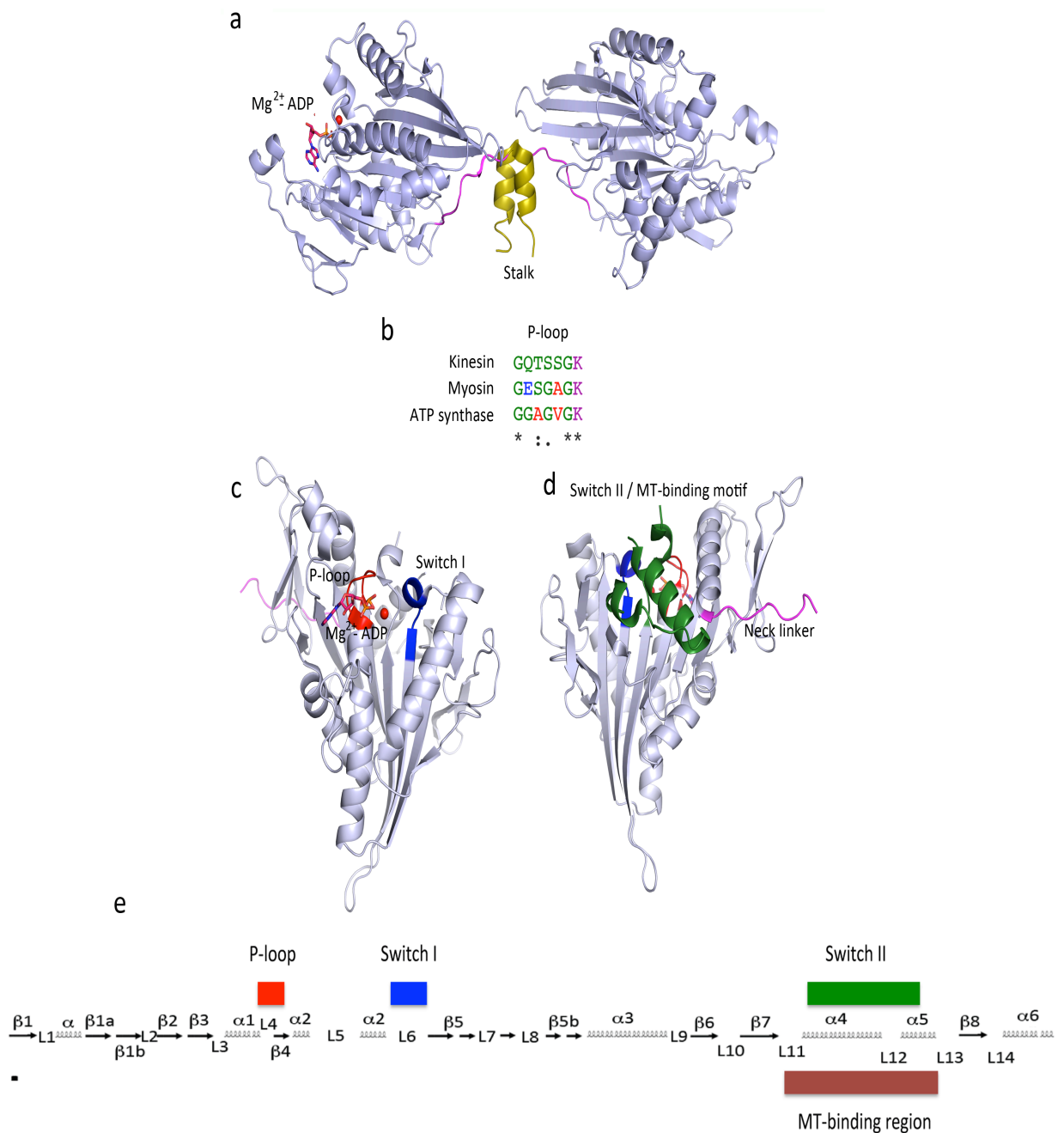


Figure 1-4: Overall structure and important binding sites of kinesins.

a) The dimeric structure of *Drosophila* conventional kinesin reveals the conserved core structure of kinesins with eight β -strands surrounded by six major α -helices represented in gray, the neck linker (magenta) and the portion of the stalk domain that promotes dimerisation (yellow).³⁶ It also shows Mg^{2+} -ADP bound to the P-loop. b) P-loop motif is conserved in kinesins as in various other ATPase proteins like closely related, myosin and also divergent ATPase protein, ATP synthase. c) Overall structure of the kinesin motor domain where the Mg^{2+} -ADP is bound to the P-loop (red) and the switch I (blue) which undergoes conformational changes during the ATPase hydrolysis cycle and d) the switch II cluster (green) and neck linker (magenta) which on response to changes in switch I undergoes larger conformational changes to either bind to or release from MTs. e) Major secondary structural elements of kinesin motor domain showing the P-loop, Switch I, Switch II and MT-binding region. Adapted from Kull *et al*, 1996.²⁴

Linking the motor domain to the stalk domain is a short polypeptide of ~15 residues. This region is termed the neck linker and is a vital component in transmitting force from the motor domain. The motor classification is also related to the conserved nature of the neck linker sequence. The characteristic motif L*E/DLKGN preceding the first strand of the catalytic core is present in C-types kinesins (Kin-C). Similarly, the N-type kinesin (Kin-N) motor domain contains the consensus sequence K/R*I*N***V/IN at the beginning of the neck linker region. N-type kinesins contain some highly conserved hydrophobic residues in the neck linker C-terminal to this conserved sequence.^{12,22}

The movement in and around the neck linker is controlled by the ATPase cycle of the kinesin motor (Figure 1-5a) as seen in myosin (Figure 1-5b). When kinesin is not bound to MTs, the neck linker fluctuates between a “docked” state and an “undocked” state.²⁸ On binding to MTs, the neck linker is in an “undocked” state. ADP is released from the kinesin prompting ATP binding. This does not change this state but when ATP is hydrolysed and inorganic phosphate is released, the neck linker shifts downwards toward the C-terminal of helix α_4 , adopting a “docked” state, where the movement of helix α_4 creates the necessary space to accommodate the neck linker. This is brought about by movement of switch I (Figure 1-5c) that initiate the switch II (α_4 - L12 - α_5) conformational changes which in turn allows the neck linker to move down to the “docked” position (Figure 1-5d). Thus, this conformational change in the neck linker is believed to be crucial in producing force for the movement of the motor along MTs and also for giving the motor directionality.³³

In contrast to this model of ATP hydrolysis and neck linker movement, studies on conventional kinesin-ADP and AMPPNP crystal structures reveal that in the absence of MTs, the neck linker can adopt both docked and undocked states.^{37,38} The common belief is that the movement between two states is related to the nucleotide activation, which only occurs on MTs binding linking the nucleotide hydrolysis to the motility of kinesins along MT tracks.

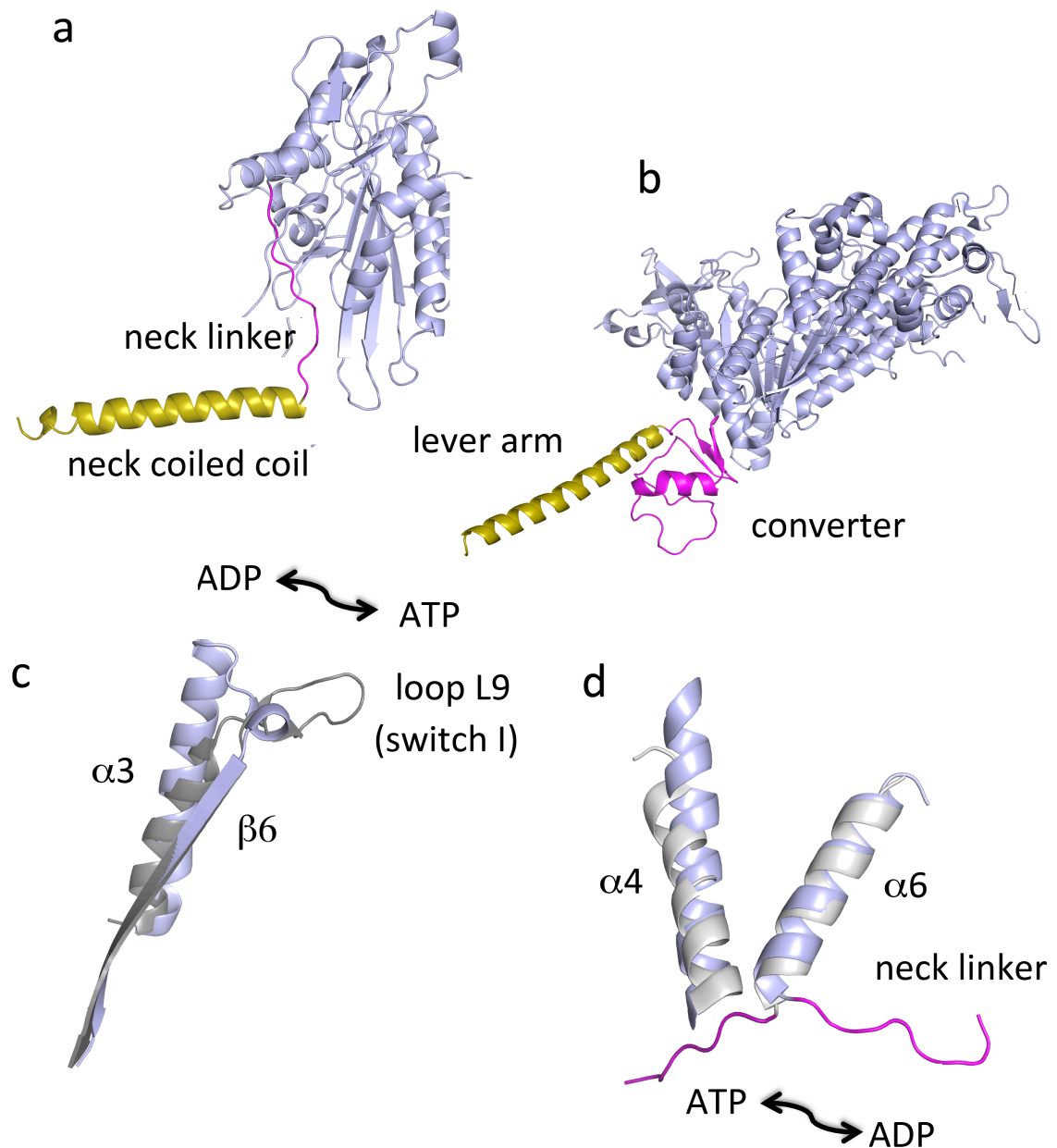


Figure 1-5: Key structural features driving conformational changes during the ATPase cycle of conventional kinesin.

The catalytic domains of a) conventional kinesin (PDB code 1BG2) and b) myosin (PDB code 2YCU) are grey with the force generating region (neck linker in kinesin and converter in myosin) coloured in magenta and the amplifier regions (neck coiled coil in kinesin and lever arm in myosin) in yellow. This represents the functionally similar regions of conventional kinesins and myosin. The conformational change from the ATP (blue) to the ADP (gray) state for c) switch I and d) switch II and neck linker region. Adapted from Sablin *et al*, 2001.³⁹

Homodimerisation is necessary for the function⁴⁰ of certain kinesins, which is mediated by the stalk domain that follows the neck linker region. The stalk domain can also induce oligomerisation into higher oligomers as is observed in kinesin-5 to form homotetramers. The stalk domain has a number of further functions beyond homo-oligomerisation and has also been shown to regulate the activity of the motor domain.^{38,41} In addition, in

some kinesins, e.g. kinesin-2 (Kif3A/Kif3B), the stalk domain mediates interactions with either a different kinesin or with non-motor proteins.⁴² The structure of the entire stalk domain of conventional kinesin is hypothesised to form an interrupted coiled coil structure where the presence of heptad repeats in its sequence facilitates formation of the coiled coil.⁴³ The flexible regions called hinges in the stalk domain may help in facilitating interaction between the motor domain and the tail domain, which has been shown to be important in regulating activity of the motor domain.⁴⁴

The stalk domain of conventional kinesin links the MD to the tail domain, which plays both an important regulatory role and a functional role in binding cargos or adapter proteins. Studies have shown that conventional kinesin folds into a closed conformation on interaction between the motor and the tail domain, inhibiting motor domain activity and processivity.⁴⁵ This restricts the unwanted use of ATP when kinesin is not performing its functions. The other significant role of the tail domain is to selectively binding cargo/adapter proteins. The tail domains of different kinesins show very low, or no, sequence similarity, which may explain the cargo specificity of different kinesin subfamilies, allowing each one to bind different cargos. There is a wide range of different possible cargos including vesicles, proteins and organelles. Some kinesin tail domains bind MTs, in an ATP-independent manner. In conjunction with MT-binding by the motor domain, this may induce the formation of large protofilament sheets, suggesting a tail-induced MT bundling property.^{46,47}

1.1.2 Mechanism of Kinesin motility

Conventional kinesins depend upon their processive movement along MT tracks to perform their different roles in cellular transport. Kinesin motility forms an integral part in kinesin function. For example, conventional kinesin takes around hundred steps before dissociating from the MT, where each 8 nm step uses the chemical energy from one single molecule of ATP producing a force of 6-8 pN.^{48,49} On the contrary, Ncd (kinesin-14), a MT minus end directed non-processive kinesin, dissociates from the MT track after each step. It works as an organised collection of multiple motors in a cluster that alternatively bind to the MT to generate motility.

Several alternative models have been proposed for conventional kinesin motility along MTs. Each one relies on the oligomeric nature of conventional kinesin and they are summarised in Figure 1-6.

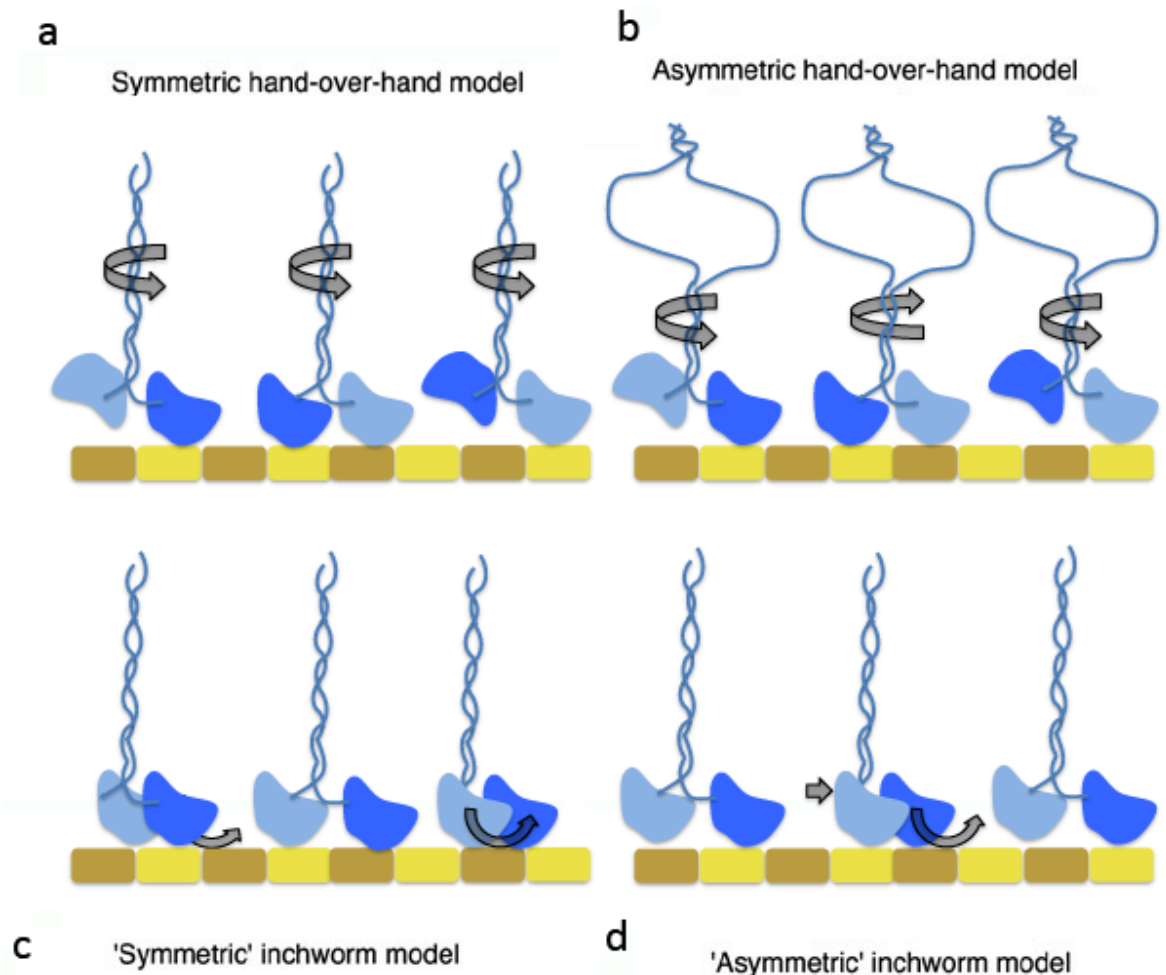


Figure 1-6: Different models depicting conventional kinesin motility.

a) In the symmetric hand-over-hand model, the lagging head passes the leading head on the same side (red arrows in front of the coiled coil neck). b) In an asymmetric hand-over-hand model, torsion force around a flexible hinge domain above the neck (red arrow) causes movement of the lagging head from the other side of the leading head as shown by the green arrow behind the neck. c) In a symmetric inchworm model, both heads hydrolyses ATP in the lagging head thereby pushing the leading head forward. d) In the asymmetric inchworm model, only the leading head hydrolyses ATP while the lagging head is pulled up passively. The term 'asymmetric' refers to ATP hydrolysis occurring in one head. Figure adapted from Manfred *et al*, 2000 and 2003.²⁰

1.2 Function of Kinesins

Kinesins have multiple roles and can be divided into the mitotic kinesins, which form the focus of this thesis, and kinesins involved in intracellular transport. The roles played by these cytoplasmic transport kinesins are beyond the scope of this thesis but are briefly outlined here. Kinesins have been implicated in normal functioning of neurons by transporting vesicles, protein complexes and membranous organelles. Synaptic transmission in dendrites requires kinesins to transport mRNP (messenger ribonucleoprotein).⁵⁰ Kinesins transport vesicles, such as endosomes and lysosomes, and

organelles, such as the endoplasmic reticulum and Golgi apparatus to their respective destinations in the cell via movement along MTs.⁵¹ Kinesins also transport components of the cilia in intraflagellar transport.^{52,53,54,55}

1.2.1 Mitotic Kinesins

At least 16 human kinesins are involved in various steps of mitosis. Kinesins are involved in spindle assembly, maintenance, chromosome segregation, mitotic checkpoint control and cytokinesis (Table 1-1).⁵⁶ Initial experiments on immunodepletion of kinesins in *Xenopus* eggs provided the first evidence on the function of kinesins in the various stages of mitosis.⁵⁷ Sequence similarity analysis reveals high sequence similarity between KLP61F and human Eg5 and a study on *Drosophila* kinesin-5 member, KLP61F, identified its role in cross-linking MTs.⁵⁸ Another study of the yeast kinesin genes provided additional evidence on the involvement of six kinesin genes in mitosis and cytokinesis.⁵⁹ A summary of kinesins involved in mitosis is shown in Table 1-1. Among different roles of kinesins mentioned above, Eg5 (kinesin-5) is responsible for the separation of centrosomes and formation of the bipolar spindle.⁵⁶ CENP-E (kinesin-7) is responsible to establish bipolar connections for monopolar chromosomes and align them at the spindle equator;⁶⁰ MCAK (kinesin-13) is responsible for chromosome alignment during prometaphase transition,⁶¹ Kif14 (kinesin-3) is required for chromosome congression and alignment³⁸ and also for cytokinesis,²¹ Kif18A controls chromosome movement to regulate mitotic chromosome positioning⁶² & Kif18B (kinesin-8) controls MT dynamics during metaphase alignment of bipolar spindle.^{63,64} Other kinesins such as members of the kinesin-6 family, MKLP-1, MKLP-2 and MPP1 are involved in cytokinesis.^{38,65-67} Most of the mitotic kinesins work exclusively during cell division but there is also evidence that some have a limited role in other functions. For example, MKLP-1 is involved in dendritic targeting in neuronal cells.⁶⁸

Table 1-1: Tabular representation of molecular motors during mitosis.

Mitotic kinesins are involved in various stages facilitating spindle assembly, chromosome alignment and cytokinesis. Table adapted from Good *et al*, 2011.¹⁵

Stages of cell cycle	Kinesins involved	References
Interphase	----	----
Prophase / Prometaphase	Eg5, KifC1, Kif2A, Kif15	Le Guellec <i>et al</i> , 1991 ⁵⁷ Oguchi <i>et al</i> , 2011 ⁶⁹
Metaphase	MCAK, CENP-E, Kif14, Kif18A, Kif18B, Kid	Ems-McClung <i>et al</i> , 2010 ⁷⁰ Gruneberg <i>et al</i> , 2006 ²¹ Huang <i>et al</i> , 2009 ⁷¹ Lee <i>et al</i> , 2010 ⁷²
Anaphase	Kif4A, Kif4B	Kurasawa <i>et al</i> , 2004 ⁷³
Telophase/ Cytokinesis	MKLP-1, MKLP-2, MPP1, Kif4A, Kif4B, Kif14	Li <i>et al</i> , 2010 ⁶⁵ Fontijn <i>et al</i> , 2001 ⁶⁶ Abaza <i>et al</i> , 2003 ⁶⁷

1.2.2 Kinesin-5 family

During a study on *Aspergillus nidulans*, a gene was found to play a central role in nuclear division.⁷⁴ It was observed that the temperature-sensitive mutant of this gene caused mitotic arrest. The gene was named 'bim' (blocked in mitosis). A few years later, a homologue of bim was discovered during a differential screening of *Xenopus* egg cDNA for identifying genes necessary for nuclear division and cell proliferation.⁵⁷ This gene was later classified as a member of the kinesin-5 family along with the human homologue called Eg5/KSP/KIF11 (Figure 1-7).

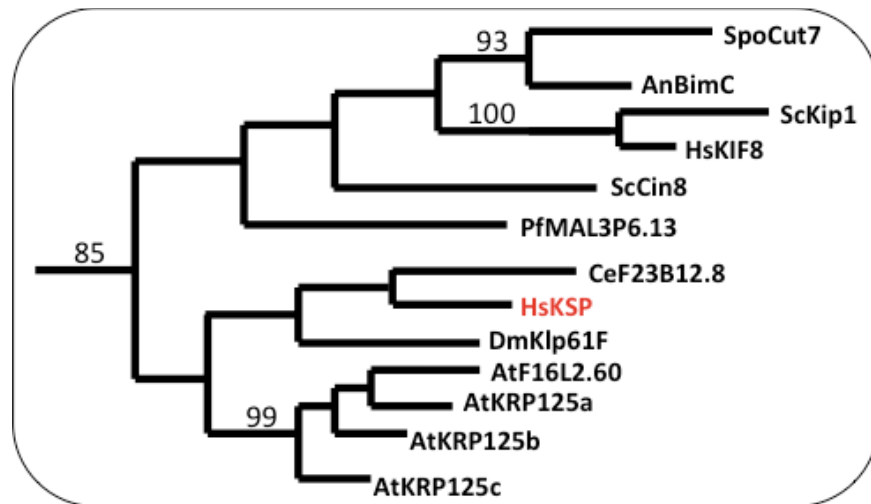


Figure 1-7: Phylogenetic tree representing members of the kinesin-5 family.

The tree of kinesin-5 family members was built from a kinesin motor domain sequence alignment using the heuristic search method of PAUP v4.0b10.¹⁸

1.2.2.1 Human Eg5

1.2.2.1.1 Structure and organisation

Human Eg5 consists of the conserved motor domain of ~350 residues at the N-terminus, an interrupted α -helical coiled coil stalk domain of around 460 residues, and a putative globular C-terminal tail domain of ~220 residues (Figure 1-8a).

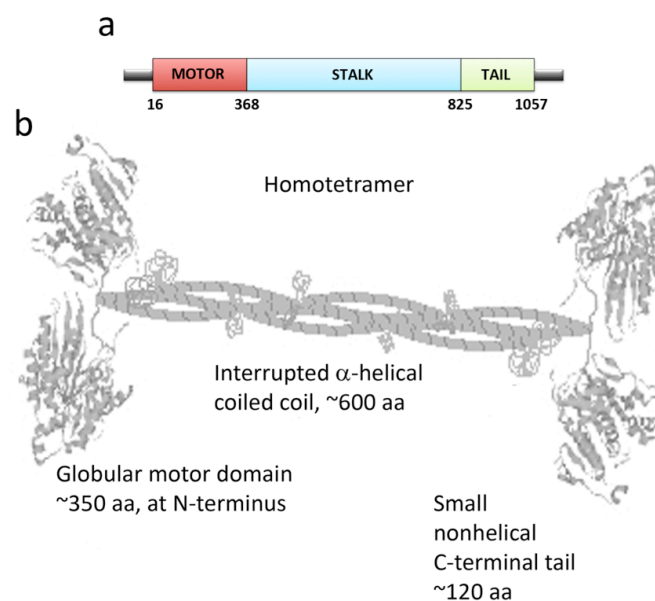


Figure 1-8: Eg5 structural organisation and homotetramerisation.

a) Domain organisation of full length Eg5. b) Homotetrameric model of Eg5 showing its quaternary structure. Figure adapted from http://www.cellbio.duke.edu/kinesin/BE5a_BimC.html.

Eg5 functions as a homotetramer (Figure 1-8b), in contrast to many other kinesins.^{75,76} Many kinesins function as dimers but some function as monomers or in alternative oligomeric states.⁷⁷ Studies on electron micrographs of rotary-shadowed Eg5 have generated evidence on this physiological behaviour of Eg5.⁷⁸ The tetramer is formed by two anti-parallel dimers of Eg5 assembling into a “dumbbell-shaped bipolar kinesin” with two motor domains at each end, which allows it to bind MTs at both its ends of the oligomer.

The structure of the Eg5 motor domain in complex with $Mg^{2+}ADP$ ²⁸ provides insights into the catalytic domain of the protein (Figure 1-9a). The core of the motor domain consists of an eight-stranded β -sheet, skirted by six major α -helices on each side²⁴ typical of the conserved motor domain of the conventional kinesins. A crystal structure of Eg5 bound to AMPPNP (a slowly-hydrolysable ATP analogue) reveals a docked neck linker similar to that of kinesin-1.²⁷ A number studies have tried to understand the different stages of the ATPase cycle in kinesins.⁷⁹ In particular Ryo *et al*, 2004 compared the crystal structures of various nucleotide bound states of Kif1a revealing the mechanism of interaction between kinesin and MTs necessary for kinesin motility.^{33,80} However, Kif1a is a monomeric kinesin and the mechanism of oligomeric kinesins may be different. The structure of different states in the ATPase cycle of dimeric or other higher oligomeric kinesin may give a better understanding of this.

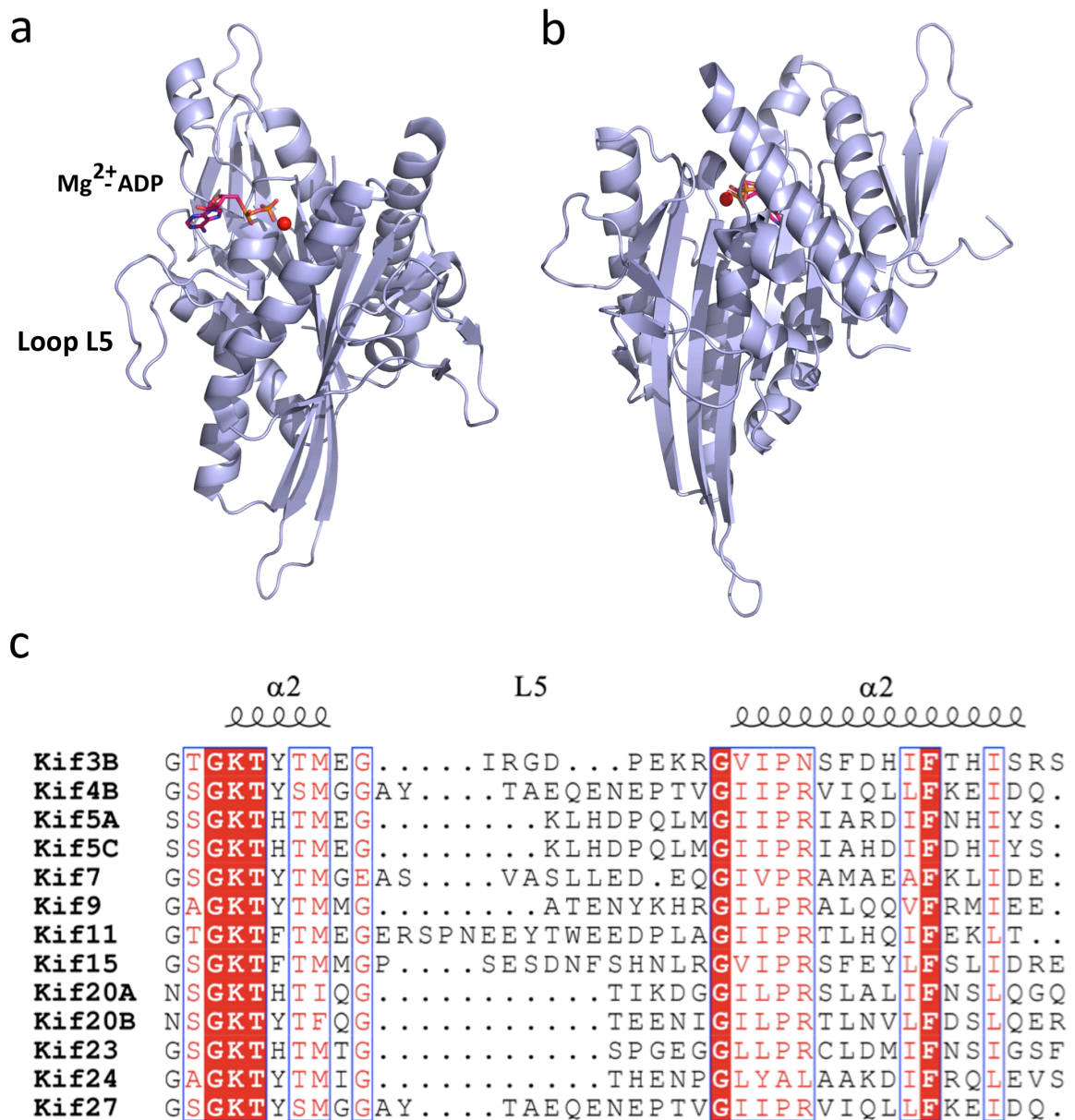


Figure 1-9: Crystal structure of the motor domain of Eg5 and the loop L5.

Overall structure of Eg5 motor domain containing eight β -strands flanked by six major α -helices. a) Front view and b) back view of the motor domain. c) Sequence alignment of $\alpha 2$ -L5 regions of 12 kinesins that can be expressed and purified under *in vitro* conditions and loop L5 in Eg5/Kif11 marked in red.

A unique feature of the motor domain of Eg5 is the length of loop L5, which is a loop that interrupts helix $\alpha 2$ and consists of ~18 residues (Glu116 to Ile133) and is the longest among all kinesins (Figure 1-9b). Kinetic studies have confirmed the role of loop L5 in regulating the ATPase cycle of Eg5 and MT-binding.^{81,82} During the ATPase cycle, loop L5 moves between an 'open' conformation, when ADP is bound, and a 'closed' conformation in the ATP bound state which is relayed to the neck linker region of the protein for further conformational changes and affects force generation and movement of Eg5 along the MT track. Further experimental evidence links loop L5 with the initial acceleration of ADP

release during the MT-binding along with loop L5 mediating the slow isomerisation of Eg5 dimer heads by preventing them from binding the MTs until ADP is released.⁸³

Structural information on the stalk and the tail domain of Eg5 is limited. Evidence from kinesin-1 and other kinesins shows that the stalk domain facilitates dimerisation.⁸⁴ The PAIRCOIL2 program⁸⁵ predicts a disrupted coiled coil region of Eg5 from residues 400 – 850 (Figure 1-10). The stalk domain has regions with high and low probability scores of forming a coiled coil but without high resolution structural data the exact structure is still obscure.

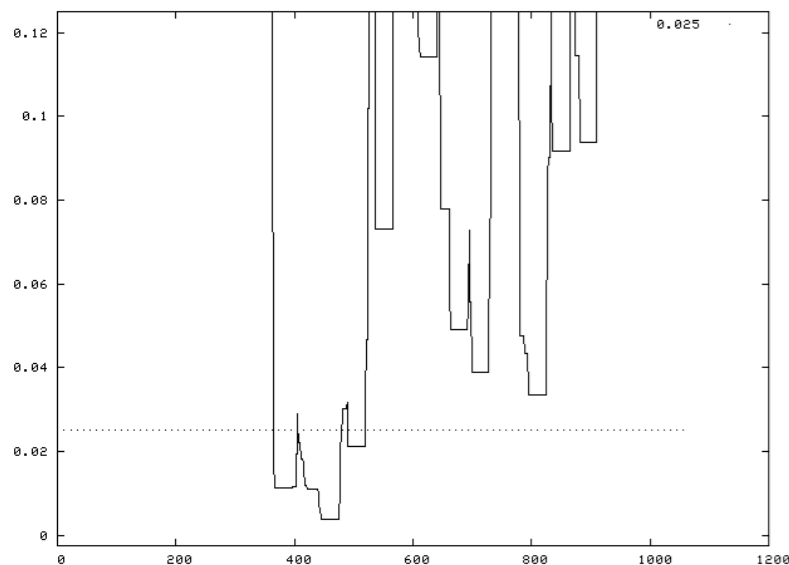


Figure 1-10: Prediction of quaternary structure of the Eg5 stalk domain.

Output from the PAIRCOIL program of p-value versus residue number shows that the stalk domain of Eg5 spans from around residue 400 to 850 and residues 400-500 have a high probability of coiled coil formation with a p-value <0.02 whereas the rest of the stalk domain has a lower probability.⁸⁵

1.2.2.1.2 Functions and interactions

The main function of Eg5 is to separate the duplicated centrosomes bound to the mitotic spindle by cross-linking anti-parallel MTs and sliding them apart to form the bipolar spindle (Figure 1-11 a-b).^{56,86,87} This has been investigated using various studies for the last two decades.^{75,88} An initial study on human Eg5 revealed that the inhibition of Eg5 by antibodies caused HeLa cells to arrest in mitosis with a characteristic formation of monoastral spindles with an array of MTs emanating from a pair of non-separated centrosomes, which eventually led to apoptotic cell death (Figure 1-11c).⁸⁹ Another study

using siRNA to knockdown Eg5 in PtK cells also resulted in the monoastral spindle phenotype and mitotic arrest.⁹⁰

The C-terminal tail domain of Eg5 has multiple roles. Phosphorylation of Thr927 of the tail domain by protein kinase p34cdc2/cyclin-dependent kinase 1 (Cdk1) helps to regulate the association of Eg5 with MTs during early prophase and it is essential for Eg5 activity. A single point mutation of Thr927 in the tail domain is able to inhibit the interaction between Eg5 and the spindle apparatus.⁵⁶ Among other roles, the tail domain has been shown to interact with p150 (Glued), a subunit of the dynactin complex that mediates the association of Eg5 with MTs and/or the spindle apparatus.^{91,92} Other experimental evidence suggests that the tail domain of Eg5 might also bind to MTs allowing more efficient separation of spindle MTs.⁹³ Whether this role is played alone or in interaction with the other proteins is still unknown.⁹⁴

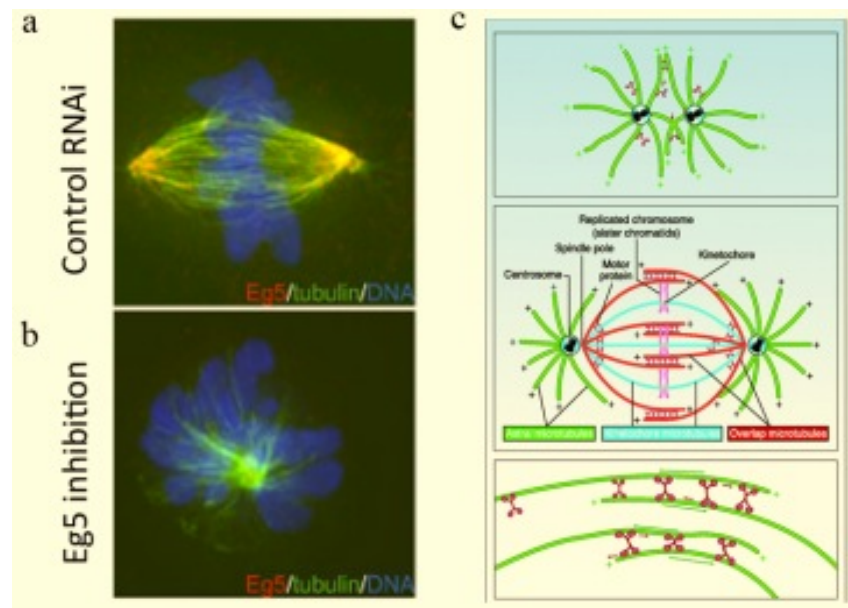


Figure 1-11: Eg5 function in the formation of the bipolar spindle.

a) Normal cell in a control setup showing chromosomes (blue) aligned at the metaphase plate of a bipolar spindle (yellow). b) Monoastral spindle caused due to treatment with the Eg5 inhibitor monastrol or siRNA to inhibit Eg5. c) Eg5 homotetramer cross-linking MTs and separating them while moving towards the MT plus-end. Figure taken from Stout *et al*, 2006.^{89,90}

There is also evidence that Eg5 has some function in addition to mitosis. Eg5 plays a role in developing neurons, where it was shown to express in dividing neuroblasts. Eg5 expression in postmitotic neurons has been shown using immunofluorescence microscopy with an antibody against Eg5. It is generally localised in the cell body along

the length and distal region of axon or dendrites. As in mitosis, Eg5 in neurons is involved in regulating MT organisation and behaviour, which can help in neuronal migration, axon regeneration and axonal growth although the exact mechanism is still unclear (Figure 1-12).⁹⁵⁻⁹⁷

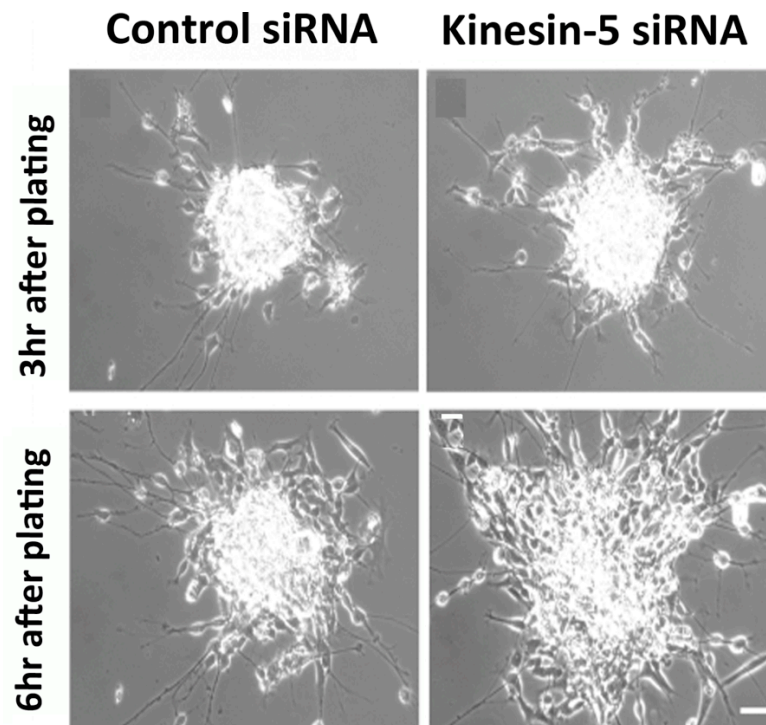


Figure 1-12: Role of kinesin-5 (Eg5) in neuronal migration.

Cultured neuron cells after 3 hr and 6 hr of siRNA treatment. Cells treated with control siRNA shows diminished migration whereas cells treated with siRNA against Eg5 shows accelerated migration depicting the role of Eg5 in controlling neuronal cell migration. Figure taken from Falnikar *et al*, 2011.⁹⁶

1.2.2.1.3 Clinical relevance of Eg5

The important role of Eg5 in cell division raises the possibility of Eg5 being a potential therapeutic target and correlations between aberrant Eg5 expression and certain cancers have been observed.⁹⁸⁻¹⁰¹ Eg5 over-expression has been implicated in tumourigenesis in blast crisis chronic myeloid leukaemia in transgenic mice.^{102,103} It has also been shown to be involved in the anti-proliferative action of all-*trans*-retinoic acid in pancreatic cancer cells.^{104,105} In addition, Eg5 promotes pancreatic cancer cell proliferation, colonisation and tumour malignancy based on the up-regulation of both mRNA and protein levels (Figure 1-13).¹⁰⁰ More recently, in non-muscle invasive urinary bladder cancer, Eg5 over-expression is seen as a potential prognostic clinicopathological factor, which can be

related to tumour recurrence and progression.¹⁰⁶ These findings suggest that Eg5 may play a role in the pathogenesis of multiple cancers with an essential role during mitosis. Eg5 as a drug candidate for cancer chemotherapy can be used for targeting slow-down and regression of tumour growth with higher mitotic index.

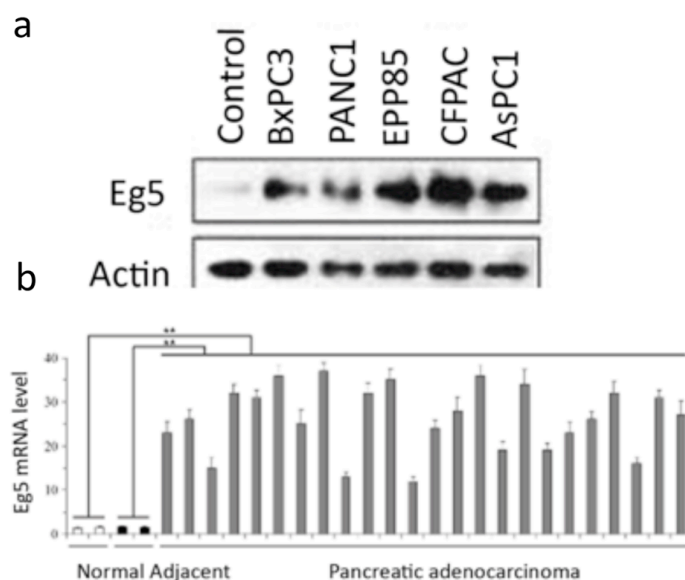


Figure 1-13: Over-expression of Eg5 in pancreatic cancer.

a) Western blot analysis of Eg5 protein in different cancer cell lines and compared to normal cell (control) reveals its over-expression. b) Analysis of Eg5 mRNA in normal cells and pancreatic adenocarcinoma cell lines shows a correlation between mRNA and protein levels. Adapted from Liu *et al*, 2010.¹⁰⁰

Mayer *et al*¹⁰⁷ were the first to discover an inhibitor of Eg5 while conducting a phenotypic screen for small molecules that inhibit the formation of bipolar spindle (Figure 1-14). They identified 5 hits out of more than 16000 compounds that specifically affected proliferating cells undergoing mitosis but did not affect tubulin polymerisation or MTs. One of these 5 compounds, named monastrol, was proposed to inhibit Eg5 function because of the characteristic monoastrol spindle phenotype in dividing cells. Monastrol exhibits relatively weak potency in biochemical assays ($IC_{50} = 14 \mu M$) but is a widely accepted Eg5 inhibitor used for further studies.¹⁰⁸

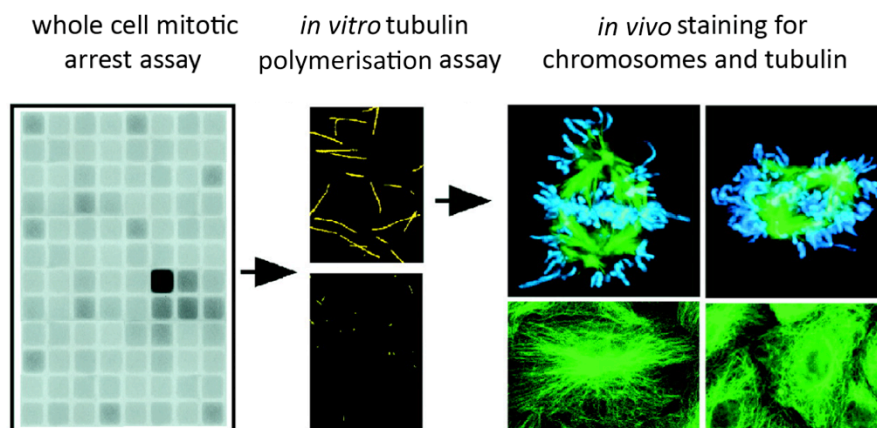


Figure 1-14: Phenotypic screen to identify inhibitors of bipolar spindle formation.

Screening of more than 16000 compounds identified five inhibitors that specifically block bipolar spindle formation with characteristic monoastal spindles and mitotic defects. One of the inhibitors was later found to inhibit Eg5. Figure taken from Mayer *et al*, 1999.¹⁰⁷

A later study on small molecule libraries from NCI (National Cancer Institute) using *in vitro* assays led to the discovery of S-trityl-L-cysteine (STLC), which is more potent than monastrol with an IC_{50} of ~ 200 nM.¹⁰⁹ STLC and monastrol inhibit basal and MT-stimulated Eg5 ATPase activity by preventing ADP release and MT gliding in motility assays.¹¹⁰ Tumour cell lines treated with STLC undergo mitotic arrest through the activation of the spindle assembly checkpoint by the phosphorylation of BubR1.¹¹¹ The resulting prolonged mitotic arrest led to the activation of caspase pathways for eventual apoptosis.¹¹²

Crystal structures of the ternary complex of Eg5 and Mg^{2+} ADP with S-monastrol¹¹³ and STLC¹¹⁴ provide a greater insight into the inhibitor-binding pocket. The inhibitor-binding pocket of Eg5 is an allosteric site about 12 Å away from the nucleotide pocket. Comparison with the apo Eg5-ADP structure reveals the conformational changes that occur upon inhibitor binding. First, to accommodate the inhibitor, Arg119 (on helix $\alpha 2$) and Tyr211 (on helix $\alpha 3$) move outwards, while Trp127 of loop L5 swings downwards, by about 7 Å, from a solvent exposed region to form an aromatic C-H- π -interaction with the inhibitor (STLC). These conformational changes by the so-called gatekeeper residues close the entrance of the induced-fit inhibitor-binding pocket (Figure 1-15).

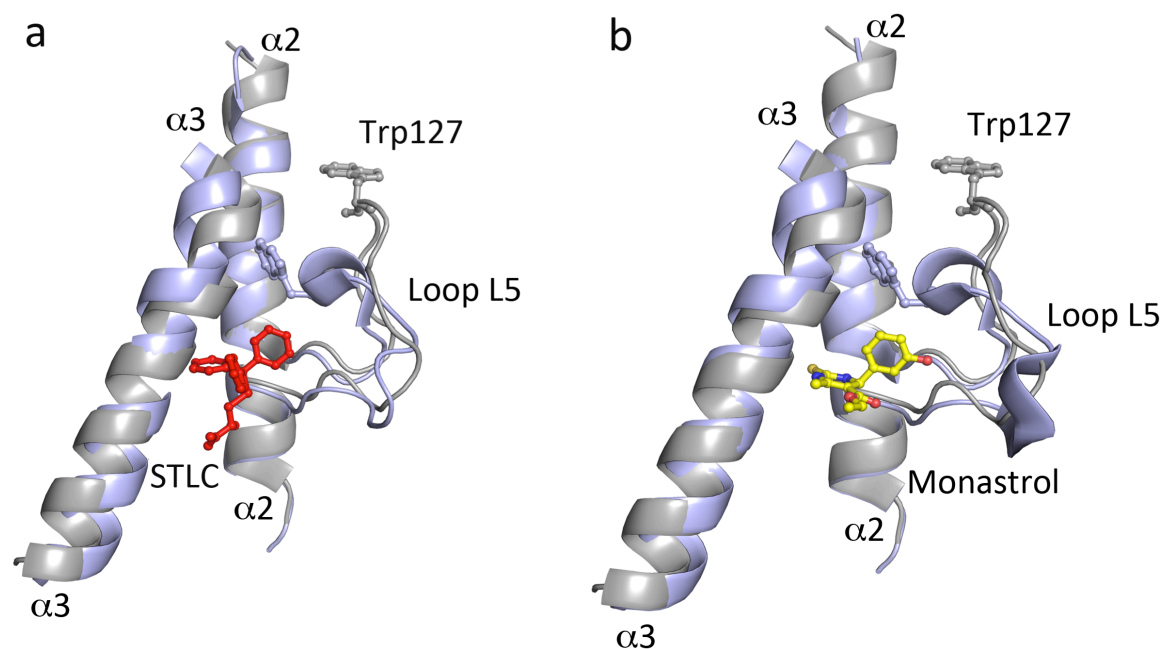


Figure 1-15: Figure showing the conformational changes of the inhibitor-binding region.

The conformational changes in the loop L5 region on binding of a) STL (native/apo = grey, inhibitor bound = blue and inhibitor=red) b) Monastrol (native/apo = grey, inhibitor bound = blue and monastrol = yellow) that take place upon inhibitor-binding where loop L5 swings downwards to close the pocket. Adapted from Yan *et al*, 2004¹¹³ and Kaan *et al*, 2010.¹¹⁴

Second, the switch I cluster sways outward towards the solvent by around 6 Å in the inhibitor bound structures. Changes in the inhibitor-binding pocket are translated to shifts in helix $\alpha 4$, $\alpha 5$ (switch II cluster) and the neck linker, where the helix $\alpha 4$ shifts upwards creating space for the neck linker to adopt a docked conformation parallel to the helix $\alpha 6$ (Figure 1-16). Maliga *et al*. used spectroscopic probes dissecting the structural changes caused by monastrol binding and observed structural changes consistent with those seen in the crystal structure.^{114,115}

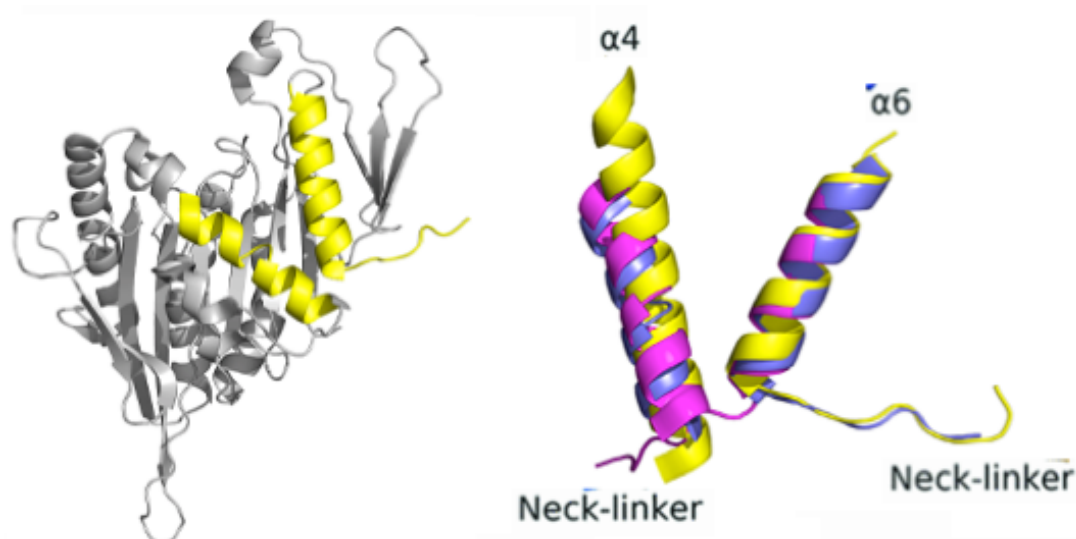


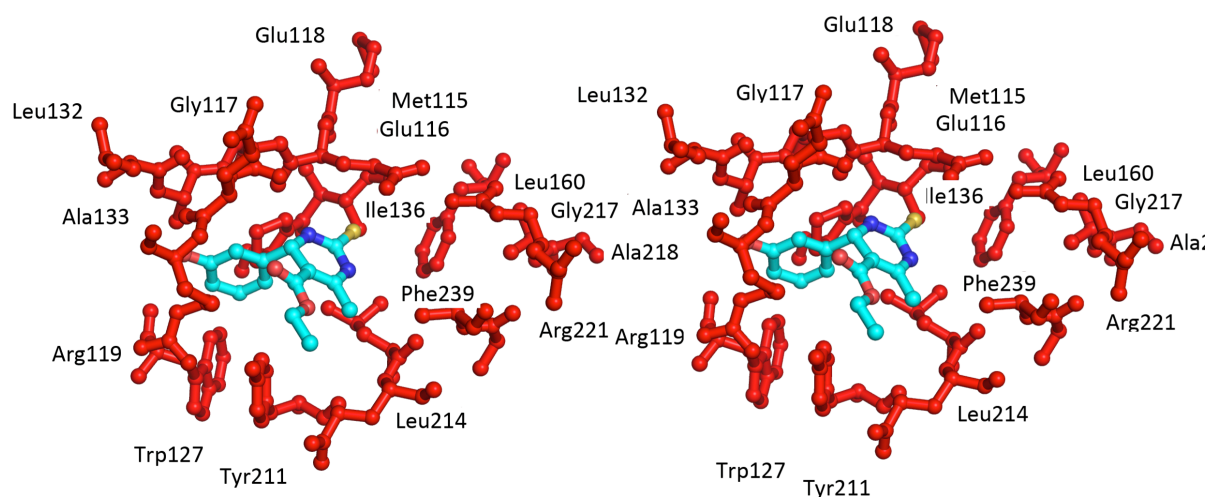
Figure 1-16: Conformational changes in the switch II cluster on inhibitor binding.

The switch II cluster consisting of helix $\alpha 4$ along with helix $\alpha 6$ and the neck linker region undergoes conformational changes from native to intermediate to final inhibitor bound state. Helix $\alpha 4$ rotates to open up space for the neck linker to adopt a docked conformation, parallel to helix $\alpha 6$. The native state is represented in yellow, the intermediate state in blue and the final docked state in magenta. Adapted from Kaan *et al*, 2010.¹¹⁴

Interaction studies of Eg5 and the inhibitors reveal the key residues important for inhibitor binding (Figure 1-18). This provides evidence towards the development of inhibitor analogues with higher potency. In the monastrol bound structure of Eg5, the 3-hydroxy group on the phenyl ring forms hydrogen bonds with Glu118 and Arg119. The phenyl ring forms a C—H— π interaction with Pro137 and π — π interactions with Trp127 and Tyr211 and the carbonyl oxygen of the ester forms a long-range polar interaction with Arg119 (Figure 1-17- A).

In the STLC-bound structure of Eg5, the three phenyl rings in STLC display several hydrophobic interactions with the alkyl moieties of the Glu215, Glu116 and Arg119 side chains. The first phenyl group of STLC forms an edge—face interaction with the phenyl ring of Trp127 and a C—H— π interaction with the pyrrolidine ring of Pro137, a stacked π — π interaction is formed between the second phenyl group and Tyr211 and a C—H— π interaction forms between the third phenyl group and the side-chain of Leu214 (Figure 1-17 - B). The hydrophilic part of STLC containing the cysteine moiety has several polar interactions: the amine group hydrogen-bonds with the main-chain carbonyl oxygen of Gly117 and a carboxyl oxygen of Glu116, while an oxygen atom of the STLC carboxyl group forms a salt bridge with the guanidinium group of Arg221. This contrasts with monastrol where polar interactions are much more limited.

a



b

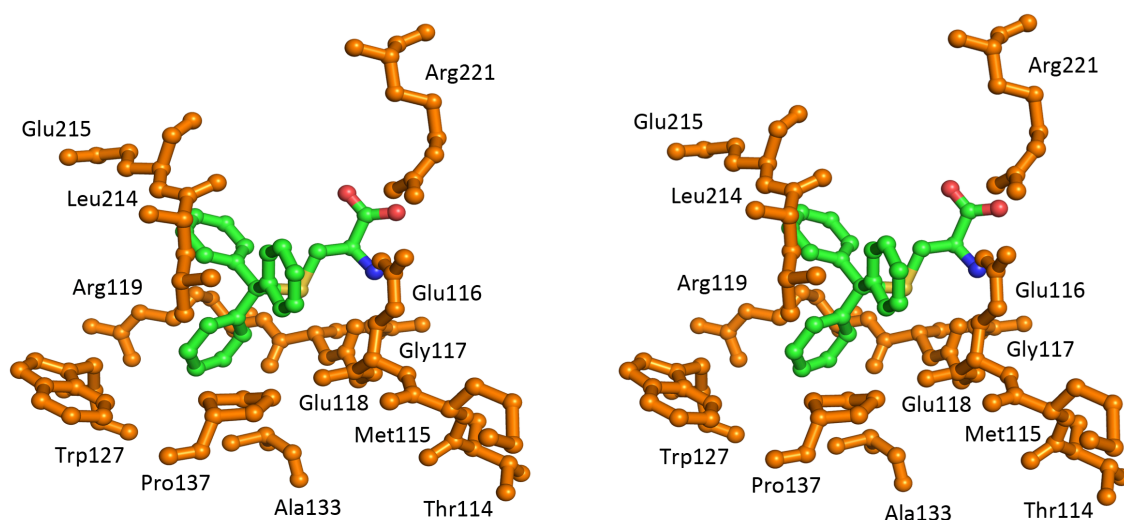


Figure 1-17: Stereo plot of monastrol and STLc bound in the allosteric pocket.

a) Monastrol and b) STLc interactions in the inhibitor-binding pocket showing the interacting residues, which determine the potency of the inhibitors.^{113,114}

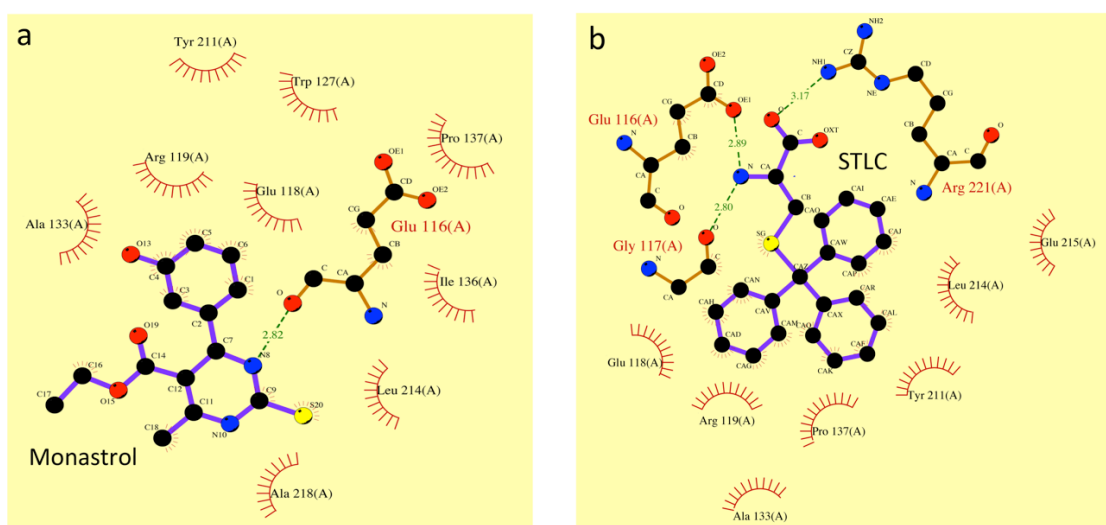


Figure 1-18: Schematic representation of the contacts between monastrol (a) and STLc (b) and residues of the Eg5 inhibitor-binding pocket.

Using the LIGPLOT¹¹⁶ programme the interactions between the inhibitors and Eg5 residues from the inhibitor-binding pocket are depicted. Hydrophobic contacts (up to a distance of 3.9 Å) and hydrogen bonds are depicted with red and green dashed lines, respectively. The ethyl group of (S)-monastrol points toward the solvent with major hydrophobic interactions around the inhibitor-binding pocket. In the STLC structure the hydrophilic parts of the inhibitor within the cysteine moiety have several hydrogen bond interactions with Gly117, Glu116 and Arg221. The buried trityl group forms multiple hydrophobic interactions.

Other known inhibitors of Eg5 like ispinesib¹¹⁷, tetrahydroisoquinolines¹¹⁸, C2-hydroxymethyl dihydropyrrole¹¹⁹ and pyrrolotriazine-4-one based inhibitors¹²⁰ bind to the same site as monastrol and STLC but demonstrate greater potency (Figure 1-19).

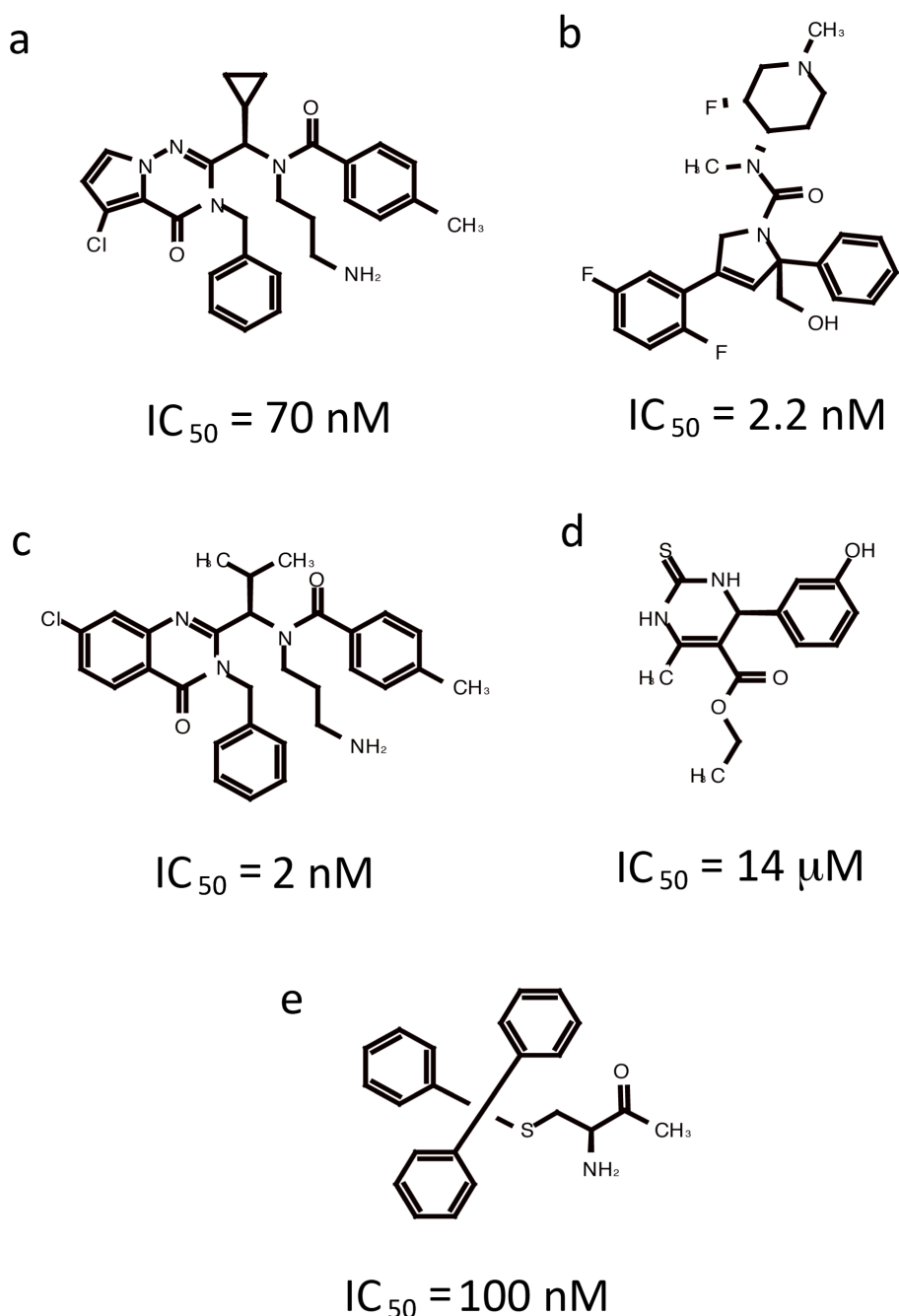


Figure 1-19: Chemical structures of Eg5 inhibitors.

Allosteric loop L5, Eg5 inhibitors pyrrolotriazine-4-one based inhibitor (a), MK-0731 (b), ispinesib (c), (S)-monastrol (d), and (R)-STLC (e) with their respective IC₅₀ measured under MT-stimulation.

1.2.2.1.4 Progress in Eg5 drug development

Currently, several Eg5 allosteric inhibitors are in Phase I and II clinical trials. Ispinesib, developed by Cytokinetics and GlaxoSmithKline, was the first to enter into human trials.^{121,122} Other compounds like MK-0731¹¹⁹ by Merck and ARRY-520 are also highly potent against tumour cell proliferation with IC₅₀ in the low nanomolar range. The Phase I study of ispinesib and other drugs have showed that these drugs have tolerable side-effects such as fatigue, nausea and neutropenia and Phase II studies are ongoing. Some of these compounds are presented in Figure 1-19.^{7,123-125} However, resistance is a key challenge in cancer chemotherapy and evidence of resistance to first generation molecules such as ispinesib is emerging in tumour cell lines in the form of Eg5 mutants.^{126,127} To identify these mutants, HTC116 cells have been cultured in presence of ispinesib. Two point mutants namely D130V and A133D of Eg5 were identified. These mutants reduced the potency of the inhibitor by about 100 – 200 fold. These two mutations are located close to the inhibitor-binding region (loop L5) and contribute towards the hydrophobic interactions with different inhibitors binding this pocket. Studies to understand the mechanism of resistance have provided very limited information.¹²⁶

In order to overcome resistance generated by mutations at the loop L5 allosteric site, identification of inhibitors binding at alternative sites has attracted attention. New benzimidazole inhibitors have been identified which bind to a different allosteric site between helix $\alpha 4$ and $\alpha 6$ without being competitive with ATP.¹²⁸ These new inhibitors of Eg5 provide an avenue towards novel site binding that can be used as an alternative chemotherapy addressing either drug resistance against Eg5 inhibitors binding to loop L5 or in combined chemotherapy.

In addition to these allosteric inhibitors, a series of ATP competitive Eg5 inhibitors have also been identified.¹²⁹⁻¹³¹ However their specificity towards Eg5 is questionable due to the conserved nature of the ATP binding pocket of the kinesin superfamily.¹⁵

Phase II trials of ispinesib and its more potent analogue SB743921 on patients suffering from Hodgkin and non-Hodgkin Lymphoma have revealed promising results. The future directions towards these drugs would be to test them as a single agent or in combinational therapy in Phase III, in the hope of achieving synergistic effects and identification of tumours, which can be treated with such drugs.⁸

1.2.3 Kinesin-6 family

The kinesin-6 family members (Figure 1-20) are unique among the kinesin superfamily because of a particularly long insertion of 100 aa (8 kD–10 kD) into loop L6 of the motor domain (Figure 1-21b). The three members belonging to this family are mitotic kinesin-like protein 1 (MKLP-1, KIF23, KNSL5, CHO1), mitotic kinesin-like protein 2 (MKLP-2, KIF20A, RAB6KIFL, rabkinesin-6) and M phase phosphoprotein 1 (MPP1, KIF20B, KRMP1, M-phase phosphoprotein 1, MPHOSPH1) (Figure 1-21a, Figure 1-20). They are all N-terminal motors and move towards the plus-end of MTs (Figure 1-20).^{67,132,133} Kinesin-6 members are involved in the metaphase-to-anaphase transition leading to the physical division of the cell into two daughter cells via cytokinesis.

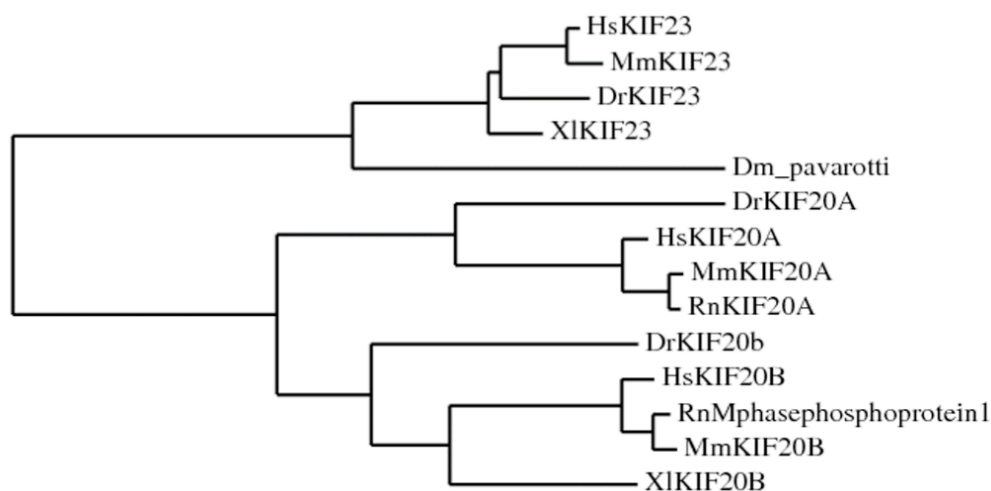


Figure 1-20: Phylogenetic tree representing the kinesin-6 family.

The phylogenetic tree of the kinesin-6 family shown above was built from a kinesin motor domain sequence alignment using web-based Phylogeny.fr.^{134,135}

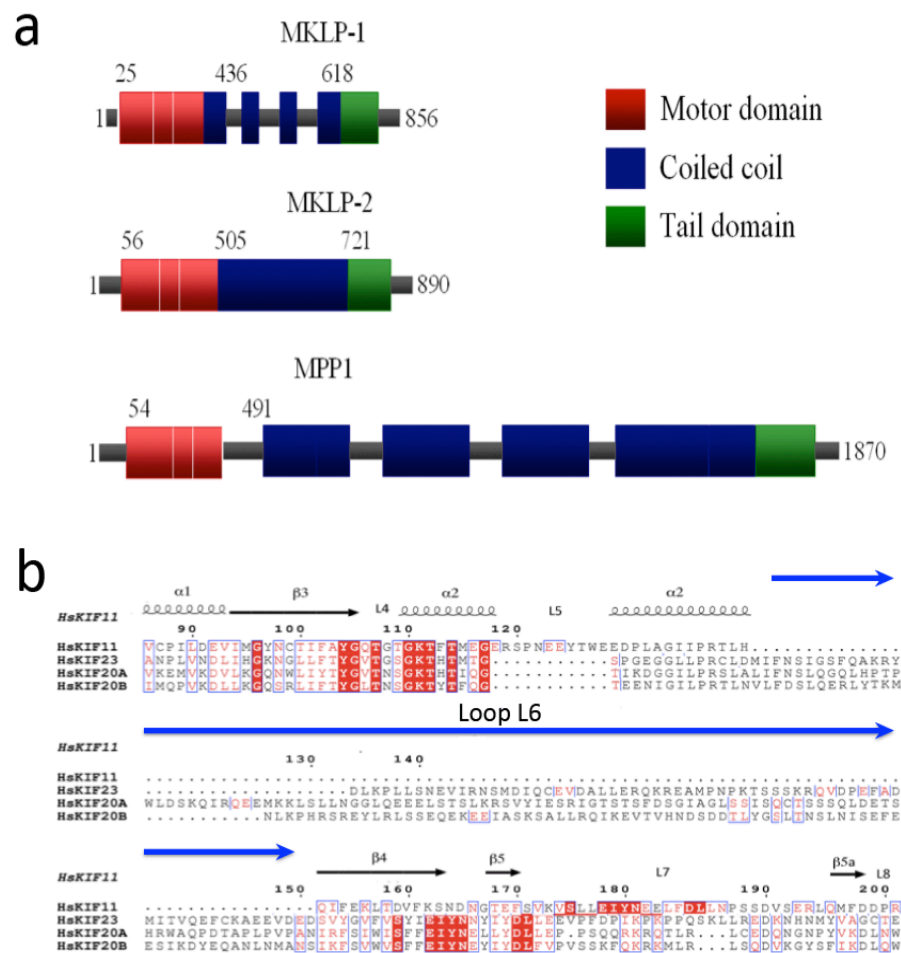


Figure 1-21: Bar diagram of *H. sapiens* kinesin-6 family members and sequence alignment of the loop L6 region.

a) The figure depicts the domain structure of full-length kinesin-6 members. MKLP-1 and MKLP-2 are of similar length where MPP1 is almost double the size. The difference in length is caused due to the longer discontinuous stalk domain of MPP1. b) Sequence alignment of the motor domain of Eg5 with kinesin-6 members showing the location of the long loop L6 insertion (blue arrow) following the helix $\alpha 2$.

1.2.3.1 MPP1

MPP1 is proposed to be a potential new target for cancer chemotherapy. The initial identification of MPP1 and its link to mitosis was made using the MPM2 antibody, which specifically recognises a phosphorylated threonine residue, in the M-phase cells (Figure 1-22). Subsequent investigations identified the full-length MPP1 and its role in cytokinesis.^{67,136}

The MPM2 monoclonal antibody binds to a phospho amino acid-containing epitope of about 10 residues present on more than 40 proteins of M-phase eukaryotic cells. During cDNA analysis of one such protein, MPP1 was identified with a distinct 'FTPLQ' peptide

sequence near its C-terminus that provided the first evidence that the protein is exclusively phosphorylated during mitosis.^{136,137}

```

1556.....IEDGSVVLDSCEVSTENDQSTRFPKPELEIQFTPLOPNKMAVKHPGCTTPVTVKIPKARKRKSNEEED
          LVKCEENKKNATPRTNLKFPISDDRNSSVKKEQKVAIRPSSKKTYSLSQASIGVNLATKKKEGTLQKF
          GDFLQHSPSILQSKAKKIETMSSSKLSNVEASKENVSQPKRAKRKLYTSEISSPIDISGQVILMDQKM
          KESDHQIIKRRLRTKTAK .....1780

```

Figure 1-22: Identification of the phospho epitope of MPP1.

MPP1 was identified in cells at G2/M transition using antibodies binding specific phosphorylated epitopes (amino acids highlighted in yellow and red).

1.2.3.1.1 Structure and organisation

MPP1 is a large protein of about 1900 residues being approximately double the size of both MKLP-1 (850 aa) and MKLP-2 (890 aa) (Figure 1-21a). In addition to the conserved motor domain, MPP1 and the other kinesin-6 members contain an extension of around 50 residues at the N-terminus preceding the motor domain. These are predicted to be structurally disordered based on secondary structure prediction servers such as Phyre (ver. 2.0) and Jpred3.¹³⁸⁻¹⁴⁰

Much of the motor domain of MPP1 (residues 54 to 480) can be modelled using widely available homology modelling software such as the Swissmodel server¹⁴⁰ using the Eg5 native structure as a template (PDB code: 1II6²⁸). The key structural difference, the long insertion of loop L6, can only be modelled with low confidence leading to a low confidence for the model as a whole (Z-value = -4.508). Predictions in this loop are limited to secondary structure modelling. Secondary structure predictions also suggest that the loop (Figure 1-23) is dominated by disordered regions.^{139,140} Very little is known about the 10-15 residues long neck linker of MPP1 following the motor domain and is thought to be involved in controlling MT-binding and motility.

The α -helical coiled coil stalk of MPP1 is connected to the motor domain via the neck linker region. The coiled coil of MPP1 is predicted to span the region from residue 500 to residue 1520⁶⁷ (Figure 1-23) and is extraordinarily long compared to most other kinesins. It is also substantially longer than the coiled coil regions of its closely related family members MKLP-1 and MKLP-2.⁸⁵ The stalk domain is likely to be involved in dimerisation of MPP1, which is a physiological requirement for proper functioning of MPP1.¹⁴¹

The C-terminal tail domain of MPP1 has a unique sequence and spans around 200 residues. Unlike in other kinesin-6 members, there is no leucine zipper present in the sequence of MPP1.

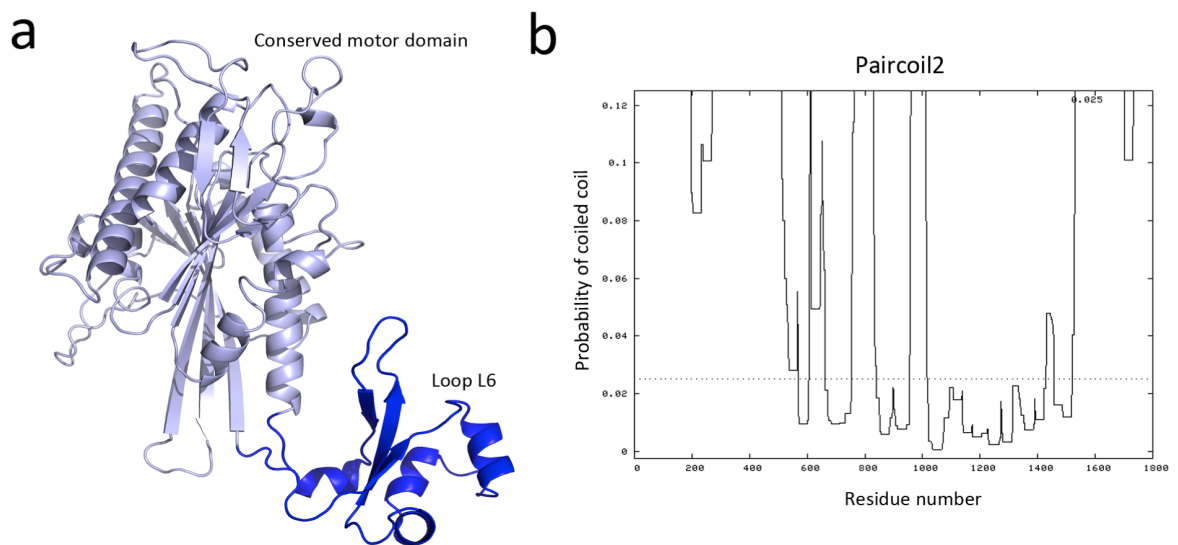


Figure 1-23: Structural prediction into various domains of MPP1.

a) Structural modelling of the MPP1 motor domain (shown in pale blue) predicts structural similarity with other kinesins. The long loop L6 insertion is mostly disordered with few broken α -helices as shown in blue. In addition, the confidence score for the region is around -5.46 suggesting poor structural prediction in the region. The modelling analysis suggests a poor modelling of the MPP1 structure emphasising the need for a crystal structure. b) The coiled coil prediction using PAIRCOIL2 where the x-axis represents the amino acid residue number versus P-value (probability of being coiled coil) on the y-axis. The graph shows that residues 500 – 1600 form the discontinuous stalk domain of MPP1 that is longest among the kinesin-6 members.^{85,140}

1.2.3.1.2 Physiological function and interactions

To identify the function of MPP1, fluorescence microscopy, FACS and siRNA studies were performed showing MPP1 expression is increased during G2/M phase, with an interspersed behaviour in the cell during interphase. MPP1 is found to be concentrated at the midbody during the metaphase-to-anaphase transition, until the completion of cell division by cytokinesis.⁶⁷

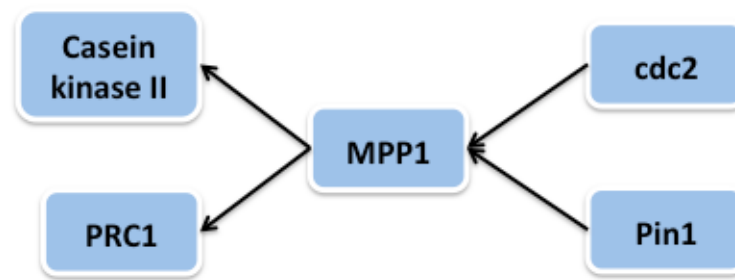


Figure 1-24: Interactions of MPP1.

Using the EMBL data mining software, STRING 8, MPP1 interactions with other proteins in published research were identified. Proteins that may be controlled, or may regulate, MPP1 are shown here.¹⁴¹⁻¹⁴⁴

Figure 1-24 depicts MPP1 interactions with other proteins based on previous published research.¹⁴¹⁻¹⁴⁴ The interactions shown above were based on different observations. In 2001 a protein named KRMP1 was identified with an N-terminal kinesin motor domain and a sequence similar to kinesin-6 family members. The protein was phosphorylated both at the head and tail domain for its proper localisation and function during mitosis. Thr1604 in the tail domain was identified by alanine scanning mutagenesis to be the candidate for phosphorylation by cdc2 kinase. This chemical alteration induces Pin1 to bind to MPP1 via the Pin1 WW domain. This is in agreement with other kinesins phosphorylated by cdc2 kinase, as the motifs are similar, e.g. Eg5 (Figure 1-25). Thus, Pin1 can bind to MPP1 only when it is activated by phosphorylation. On the other hand, casein kinase II is thought to phosphorylate the head domain of MPP1 but the exact importance of such a phosphorylation is yet to be understood.^{67,141} Among other known studies, over-expression of MPP1 in COS-7 cells led to mitotic arrest at G2-M phase but co-expression of Pin1 reversed the process suggesting the role of Pin1 in regulation of MPP1.¹⁴¹

1.2.3.1.3 Clinical relevance of MPP1

Studies on MPP1 over-expression in a set of bladder cancer cell lines exhibited evidence of MPP1 and PRC1 interaction during late anaphase to early telophase but the interaction was more pronounced in cells about to undergo cytokinesis suggesting the importance of this interaction during cytokinesis (Figure 1-26). To support this, exogenous PRC1 was transfected into cells and analysed by immuno-precipitation where it was seen to coprecipitate with endogenous MPP1.¹⁴⁵

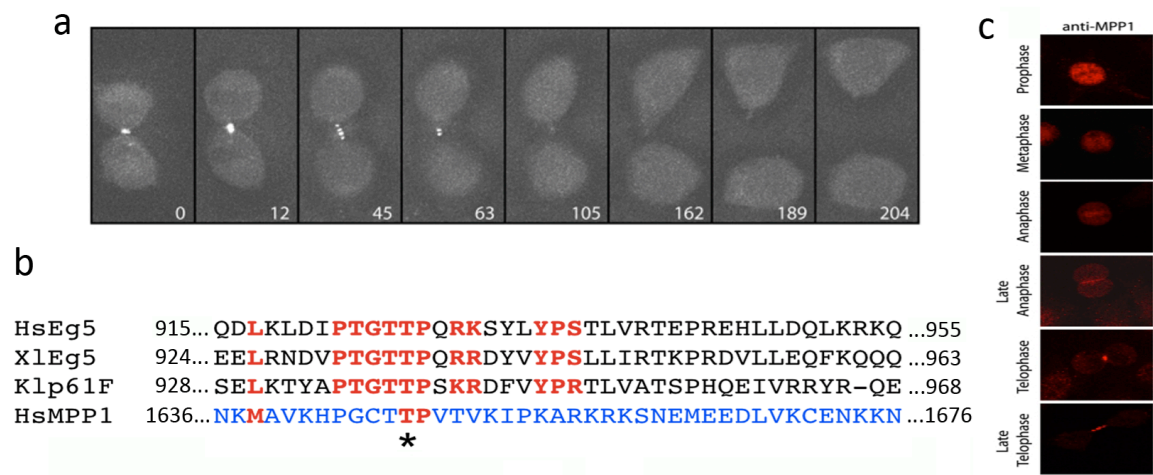


Figure 1-25: Interaction and function of MPP1.

a) Localisation of exogenous GFP-MPP1 during cytokinesis depicting the role of MPP1 in cytokinesis. As seen MPP1 is concentrated at the mid-body during late mitosis until the cell physically divides into two daughter cells. b) The relationship between different proteins based on the sequence similarity, which displays C-terminal phosphorylation sites, which is important for the regulation of these proteins. “*” represent the site for phosphorylation. c) MPP1 localises to mitotic structures in HeLa cells stained with the anti-MPP1 antibody. MPP1 is more interspersed during prophase and metaphase stage but becomes concentrated at the midbody region during the transition into anaphase. The highest concentration of MPP1 at the midbody is seen during telophase suggesting it role during cytokinesis. Adapted from Abaza *et al*, 2003 and Kamimoto *et al*, 2001.^{67,141}

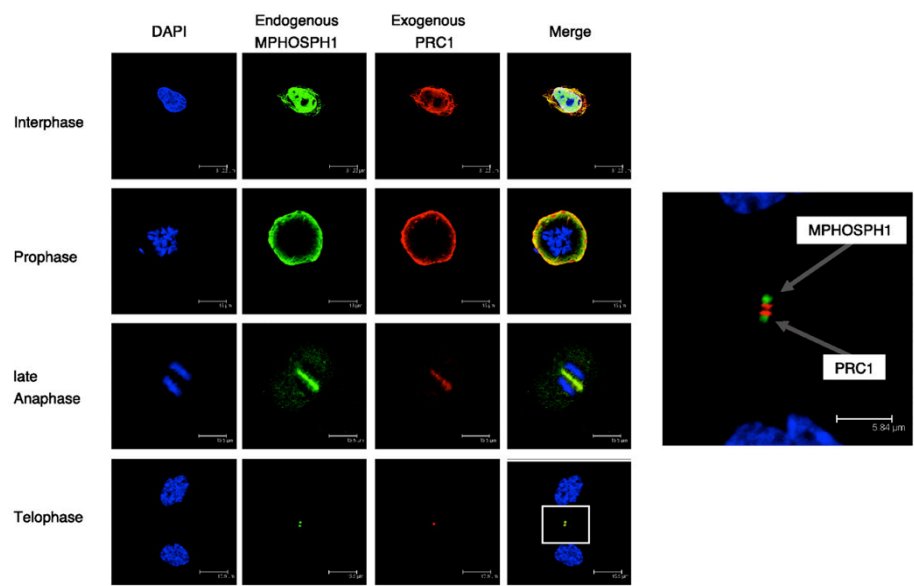


Figure 1-26: Co-localisation and interaction of MPP1 and PRC1.

In UM-UC-3 cells, endogenous MPP1 (green) co-localises with exogeneous PRC1 (red). The panel of images on the left shows the localisation of MPP1 and PRC1 during various stages of the cell cycle. The figure on the right shows the localisation of MPP1 and PRC1 at the midbody during telophase. Adapted from Kanehira *et al*, 2007.¹⁴⁵

Bladder cancer has high incidence, poor prognosis and low survival rate.¹⁴⁶ In order to provide a marker for identifying the disease Kanehira *et al*, identified the genes that are upregulated both at mRNA and protein levels in a subset of bladder cancer cell lines like

J82 and UM-UC-3. They identified that MPP1 is up regulated at both levels (Figure 1-27). MPP1 up-regulation also coincided with PRC1 over-expression suggesting PRC1 and MPP1 interaction during cytokinesis. MPP1 or PRC1 inhibition resulted in decreased cell viability with cytokinetic defects. With an exclusive role in mitosis and cancer cells with higher mitotic index in cancer cells, MPP1 has been proposed as a potential target for cancer treatment with a particular focus on bladder cancer.¹⁴⁵

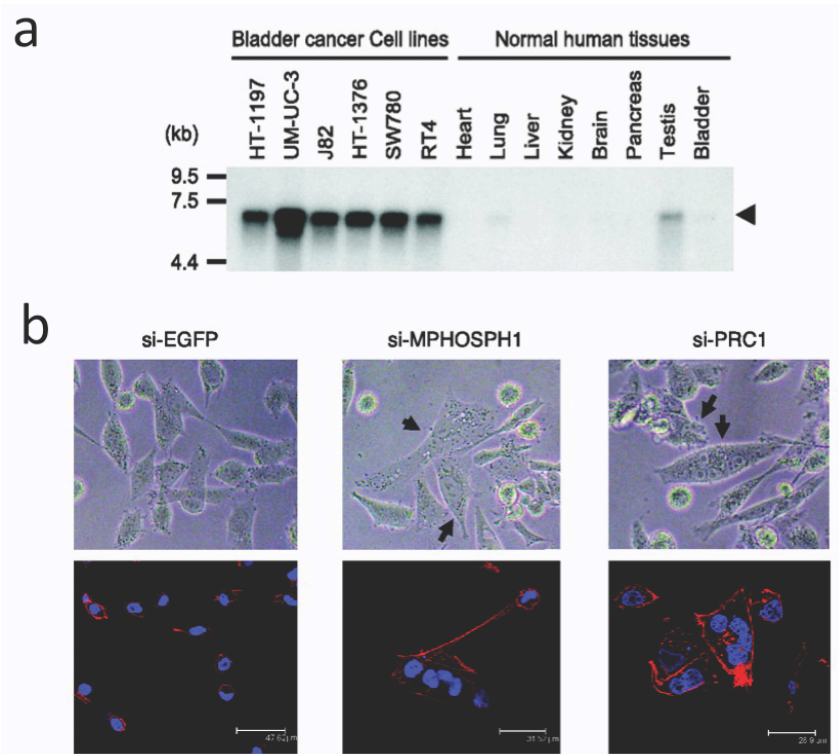


Figure 1-27: Over-expression and siRNA treatment of MPP1.

a) Northern blot showing over-expression of MPP1 in bladder cancer cell lines in comparison to normal cell lines. b) siRNA against MPP1 in cells where it is over-expressed leads to cytokinesis defects with bi- and multi nucleated cells which eventually die by apoptosis. Adapted from Kanehira *et al*, 2007.¹⁴⁵

In addition to its role in cytokinesis, one study has shown that MPP1 plays a role in polyneuropathy in patients suffering from CIDP (Chronic Inflammatory Demyelinating Polyneuropathy). Immunoprecipitation and immunohistochemistry on tissue samples from these patients identified a strong presence of MPP1.¹⁴⁷

The importance of MPP1 has been identified during the late stages of mitosis and cytokinesis, but structural information of MPP1 is still elusive. Thus, structural analysis of MPP1 will not only provide information about the core motor domain structure but, importantly, insights into loop L6 region which would be particularly interesting given its extreme length and unknown function. The low degree of predicted order in the L6 loop

may create challenges in crystallising the motor domain and structural investigations could also include solution-based methods such as small angle X-ray scattering (SAXS) or electron cryo-microscopy in combination with 3D image reconstruction to provide additional structural insights. Structures of the other domains of MPP1 will also help to decipher the relation between the structure and function but to date no structural evidence is available for any of the domains of MPP1.

1.2.3.2 MKLP-2

MKLP-2 shares structural similarity with the other kinesin-6 family members, MKLP-1 and MPP1. MKLP-2 is concentrated in the cells undergoing mitosis and is mostly interspersed during the interphase stage of mitosis. The role of MKLP-2 has been observed in the transport of different proteins from kinetochores to the central spindle during the metaphase-to-anaphase transition and it plays an important role during cytokinesis^{66,132,148} (Figure 1-28). siRNA studies of MKLP-2 have shown that depletion of the protein leads to cytokinetic defects with formation of binucleated or multinucleated cells.^{38,149} MKLP-2 function in higher eukaryotes is distinct from MKLP-1 whereas in lower organisms (Xenopus, *C. elegans*, *Drosophila*) the MKLP-1 homologue CHO1/Pavarotti/Zen4 performs the functions of both proteins.^{65,150}

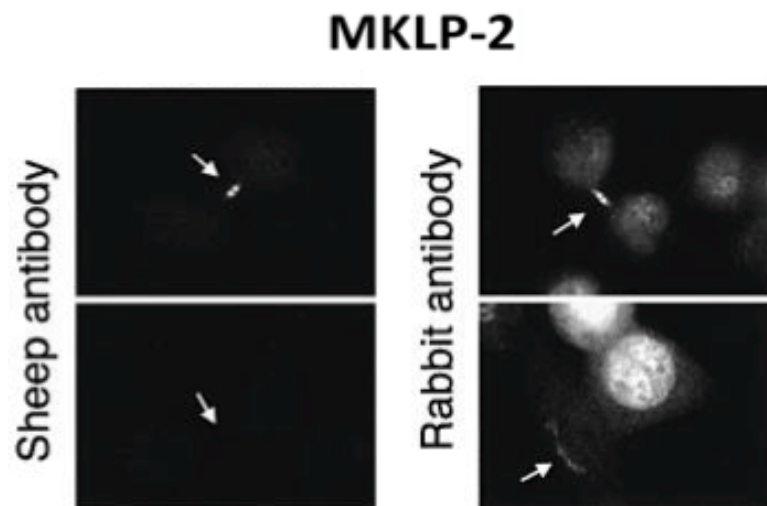


Figure 1-28: Localisation of MKLP-2 during cell division.

Antibodies against MKLP-2 (red) display that MKLP-2 is concentrated during anaphase until completion of cytokinesis. Adapted from Hill *et al*, 2000.¹³²

1.2.3.2.1 Structure and organisation

MKLP-2 has (Figure 1-21) very limited structural information available. Like conventional kinesin, it is predicted to contain three distinct domains: the conserved motor, followed by the central stalk domain connected to the motor domain via a neck linker and a C-terminal tail domain following the stalk domain.

There are many crystal structures of the motor domain of at least 7 different mitotic kinesins available⁶ but to date there is no structural information available for MKLP-2 or

for any other kinesin-6 member. As previously mentioned for MPP1 a key feature of interest in the kinesin-6 family is the long L6 loop. The biological significance of this loop is yet to be understood. Molecular modeling using Swissmodel¹⁴⁰ reveals that the motor domain has similar structural features as other conventional kinesins. The only difference is the long loop L6 that is predicted to comprise of β -strands connected by loops and show a higher degree of structural order than MPP1 (Figure 1-29).

Similar to MPP1, MKLP-2 also has around 50 residues at the N-terminus preceding the motor domain and is predicted to be disordered based on secondary structure prediction programs.¹³⁸⁻¹⁴⁰

The motor domain of MKLP-2 is connected to the coiled coil region via 10 to 15 residues of the neck linker region. The function and physiological role of the neck-linker region of MKLP-2 is still unknown. The coiled coil region as predicted by PAIRCOIL⁸⁵ ranges from residue 550 to 750. The C-terminal 150 residues are predicted to form the tail domain. By analogy with other kinesins, it is thought that the coiled coil plays an integral part in oligomerisation (dimerisation) whereas the tail is involved in binding and carrying cargo proteins along MTs. Interestingly, among other interactions, the C-terminal coiled coil domain of *Drosophila* orthologue of MKLP-2, subito, can also bind to MTs independent of the motor domain.¹⁵¹ The secondary structure prediction of the tail domain using PSIPRED also shows that the tail domain might be a part of the coiled coil region.¹⁵² Interestingly, a leucine zipper was also identified in the MKLP-2 tail domain between residues 660 to 720. Its role is not well demonstrated but may assist in dimerisation of MKLP-2.¹⁵³

An atomic resolution structure of MKLP-2 or other structural information would provide a firmer understanding of the loop L6 region along with confirming that the rest of the catalytic domain is conserved as in other kinesins. It is still unknown whether the loop L6 plays any role in kinesin function but more structural information may provide clues and also assist in the design of experiments to probe its function.

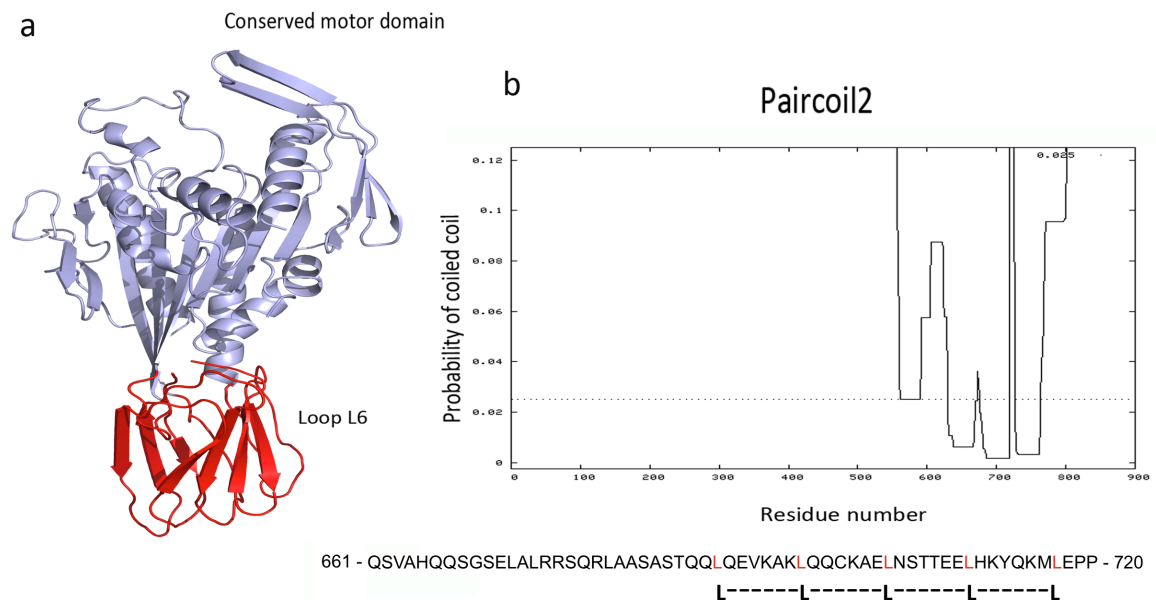


Figure 1-29: Structural prediction of MKLP-2.

Structural modelling of the MKLP-2 motor domain using the Eg5 structure, 1II6²⁸, as a template predicts a high degree of structural similarity with other kinesins represented in blue. The long loop L6 insertion (red) is predicted to contain β -sheets. However the confidence of the model is low with a Z-score of -4.312 due to the difficulty of modelling loop L6. b) The coiled coil prediction using PAIRCOIL2 shows that residues 550 – 800 forms an interrupted coiled coil stalk domain. c) Leucine zipper of MKLP-2 stalk domain that may assist in oligomerisation.^{140,152-154}

1.2.3.2.2 Physiological functions and interactions

MKLP-2 was first identified to be involved in intracellular transport mainly through interaction with the Golgi complex.¹⁵⁵ Later investigations using immunofluorescence microscopy showed that MKLP-2 was detected in mitotic, but not in interphase cells.

Detailed experiments by Hill *et al*¹³², using rabbit and sheep antibodies against MKLP-2 provides evidence of the involvement of the protein during mitosis especially from the beginning of the anaphase-to-metaphase transition until the completion of cell division by cytokinesis, until the cell divides into two daughter cells. During metaphase, MKLP-2 is thought to be cytosolic, but as the spindle starts to elongate, the protein localises in the spindle, parallel to its axis with short linear structures of the MTs.

Intense MKLP-2 staining was noted at the midbody region of dividing HeLa cells. This provides evidence that MKLP-2 levels reach its peak during mitosis and rapidly diminish thereafter.¹³²

Human MKLP-2 might have two MT-binding domains as observed for subito, a *Drosophila* orthologue of MKLP-2.¹⁵¹ MT binding is necessary for localisation of MKLP-2 to the

midbody region. MKLP-2 also has MT-bundling activity which is regulated by Plk1. MKLP-2 phosphorylation decreases the MT-bundling capacity of MKLP-2.¹⁴⁹ Thus interaction of MKLP-2 with MTs plays an important role in the proper function of MKLP-2.

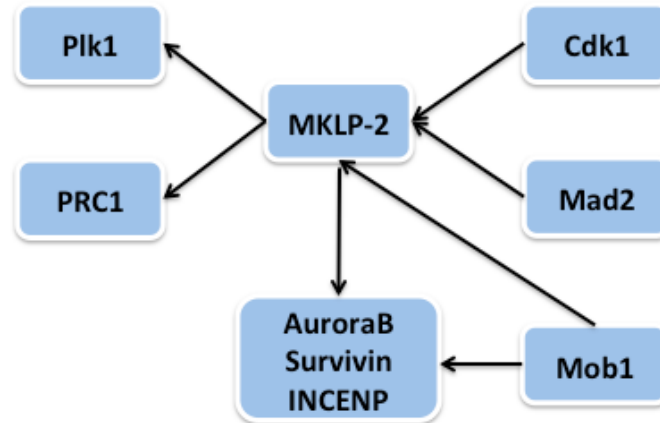


Figure 1-30: Interactions of MKLP-2.

Using the EMBL data mining software, STRING 8, MKLP-2 interactions with other proteins in published research were identified. Proteins that may be controlled, or may regulate, MKLP-2 are shown here.^{142,148,149,156,157}

Figure 1-30 summarises the interactions of MKLP-2 with other proteins during the different phases of mitosis.^{65,142,148,149,157-161} Immunohistochemistry studies have shown that MKLP-2 is localised at the central spindle from metaphase to late anaphase.¹⁴⁸ To maintain an association with the central spindle during the latter stages of cell cycle, CPC (chromosome passenger complex) protein Plk1 first phosphorylates Ser528 of MKLP-2 and then binds to this phosphorylated protein. Neef *et al*, used siRNA and immunoprecipitation on HeLa cells to provide evidence of the direct interaction of Plk1 with MKLP-2. PRC1, a protein essential for the formation of midzone during late mitosis and completion of cell cycle by cytokinesis interacts with MKLP-2, for timely recruitment of Plk1 to the central spindle.^{21,65} Interfering with either of these three proteins hinders their overall function leading to mitotic defects. Other interactions like that of Kif4¹⁶², a chromokinesin important for cytokinesis and PRC1 and its relation to MKLP-2 and Plk1 is still unknown but understanding the relationship between these proteins will help to understand their role during cytokinesis.^{65,149}

Another CPC protein, Aurora B kinase is associated with MTs during chromosome movement and segregation.¹⁶³ Inhibition of Aurora B function by RNA interference or microinjection of antibodies impairs the alignment of chromosomes at the spindle

equator.¹⁶⁴ Aurora B has variety of functions during various stages of mitosis and is associated with a number of different kinesins. Relocation of Aurora B along with INCENP and survivin from the centromere to the central spindle during anaphase is mediated by MKLP-2.¹⁴⁸ The exact interacting region of MKLP-2 with Aurora B is still unknown but a mutant of MKLP-2 lacking the motor domain demonstrates concentration of the CPC complex at the centrosomes and not the central spindle.¹⁶⁵ In addition, Aurora B phosphorylates MKLP-1 at two distinct sites at the N-terminus and C-terminus of the protein but its role in regulating MKLP-2 is still unclear. Therefore, the role of MKLP-2 is vital at the later stages of cell cycle but the whole process still remains indistinct.¹⁵⁶

There is also evidence that MKLP-2 and the CPC complex depend on each other for their association with midzone MTs. Studies have shown that interfering with any of the proteins of the CPC-MKLP-2 complex hinders their localisation to the central spindle.^{148,166} Phosphorylation of INCENP by Cdk1-cyclin B inhibits INCENP binding to Aurora B impairing the proper localisation of the CPC-MKLP-2 complex to central spindle.¹⁵⁷ On the other hand, Cdc14A dephosphorylates INCENP enabling its interaction with Aurora B. Thus, Cdk1 and Cdc14A exert an indirect control on MKLP-2. Alternatively, a study by Gruneberg *et al*, 2004 have shown that localisation of Cdc14A to the central spindle is MKLP-2 dependent.¹⁴⁸

To help in successful completion of the bipolar spindle attachment, Mad2 forms an inactive complex with Cdc20 to capture cells in metaphase. Therefore deregulation of Mad2 induces failure in cytokinesis.¹⁶⁷ In this connection, Mad2 in HeLa cell lines has been observed to be closely associated with MKLP-2 for its function. Mad2 helps to correctly localise MKLP-2 to the central spindle after metaphase. This is brought about by Mad2 keeping MKLP-2 in a folded inactive state inhibiting the latter from binding to MTs until the completion of metaphase. The interactions of Mad2 to MKLP-2 is mediated by the C-terminal amino acids ranging from 871-880 of the former with residue number 871 of the latter.¹⁶⁵ It has also been reported that MKLP-2 recruitment to the central spindle during early anaphase is also dependent on Mob1, a protein that acts as kinase-activating subunit during various stages of mitosis.¹⁶⁸

Another role of MKLP-2 has been associated with virus duplication and cytokinesis of virus infected host cells. In HPV infection the integration of the viral DNA with the host DNA is followed by ubiquitin-mediated degradation of p53 by papillomavirus E6

protein.¹⁶⁹ This leads to the activation of papillomavirus E2 that is responsible for regulating viral replication, transcription and is responsible for partitioning viral episomes into host daughter cell during cell division. Yeast hybrid screens and spectroscopy provides evidence of the association of E2 protein with MKLP-2 specifically with interactions mediated by the C-terminal residues of MKLP-2 during the host cell division. Though this interaction has been studied, the exact role of MKLP-2 during this process of viral hijack of the host life cycle is yet to be determined. It has been proposed that MKLP-2 binds E2 and transports E2 to segregate viral episomes.¹⁷⁰

1.2.3.2.3 MKLP-2 as a potential anti-cancer drug target

Aberrant MKLP-2 expression has been linked to a number of aggressive tumour types. Pancreatic ductal adenocarcinoma (PDAC) is an aggressive cancer with a very low survival rate.¹⁷¹ The principal approach to treat patients affected with PDAC is either by surgery or chemotherapy, including 5-fluorouracil or gemcitabine, with or without radiation. New avenues of treatment, particularly with fewer side effects would not only provide an alternative but also enhance the quality of life of the patients and there is some evidence that MKLP-2 is a potential target for PDAC. Using genome-wide cDNA microarrays of approximately 27,000 genes, MKLP-2 was identified as one among several others to be over-expressed in PDACs.¹⁷² Interestingly, a recent study by Imai and others¹⁷³ have revealed that MKLP-2 is a tumour-associated antigen, which may form the basis of anti-cancer therapy in pancreatic cancer. The expression of MKLP-2 in pancreatic cancer cells is about 100-fold higher than in normal cells. RNA interference and immunofluorescence studies have confirmed such over-expression in cancer cells (Figure 1-31).¹⁷³ Higher levels of MKLP-2 were also observed in western blot and immuno-histochemical analyses.

In addition, quantitative proteomics study provides information about the role of MKLP-2 in gastric cancer cells.¹⁷⁴ Mouse models and gene expression profiling of human gastric cancer-specific genes have shown up-regulation of MKLP-2 along with several other genes.^{175,176}

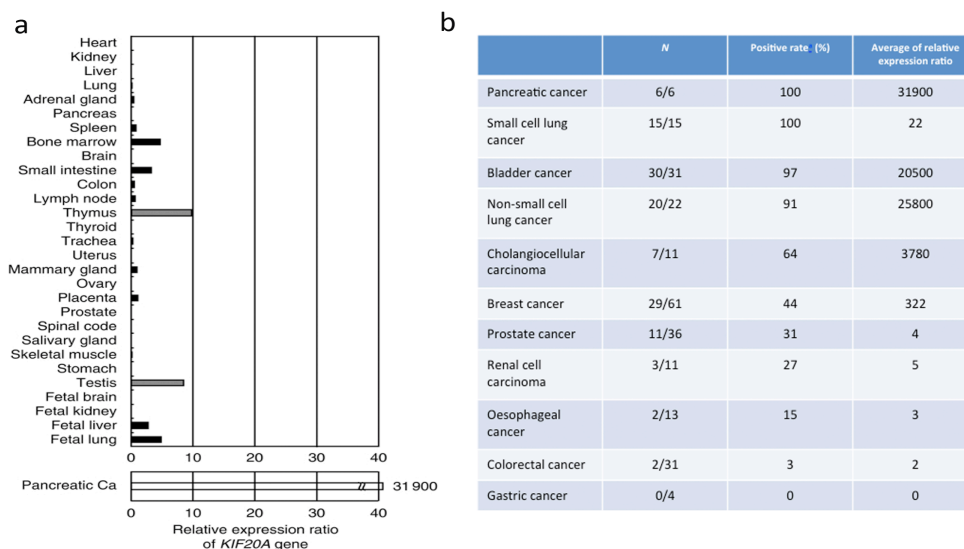


Figure 1-31: Expression profile of MKLP-2 in pancreatic adenocarcinoma cells (PDAC).

a) Relative expression levels of MKLP-2 in normal cells compared to PDAC cells indicated the over-expression of MKLP-2 by 30,000-fold. b) Tabular representation showing higher expression levels of MKLP-2 in pancreatic cancer. Adapted from Imai *et al*, 2011.¹⁷³

Another disease, HCC (hepatocellular carcinoma) is a common fatal malignant tumour that is characterised by a high incidence of recurrence, development of resistance to chemotherapy, and low sensitivity to radiation therapy. In HCC, MKLP-2 mRNA transcription and protein expression have been shown to be up-regulated during hepatocarcinogenesis in both human and mouse and high levels are linked to chromosome instability.¹⁷⁷

Based on all the above studies, MKLP-2 is considered to be a potential new target for cancer chemotherapy. In response to these findings, paprotrain (PAssenger PROtein TRANsport INhibitor) has been identified as the first inhibitor of MKLP-2¹⁶⁶. The inhibitor is thought to bind to an allosteric site in the motor domain as it does not compete with either ATP or MTs.¹⁶⁶ *In vitro* and cell-based studies have confirmed the low micromolar affinity of the inhibitor to MKLP-2. Further studies would be to determine drug-like properties and develop more potent analogues of this inhibitor (Figure 1-32).

Contrary to what has been presented in different research publications, it can be predicted that MKLP-2 can emerge a potential target with its important role in mitosis. Cancer cells with higher mitotic index can be potentially inhibited from dividing by targeting proteins involved in mitosis therefore making MKLP-2 an interesting target for future cancer chemotherapy.

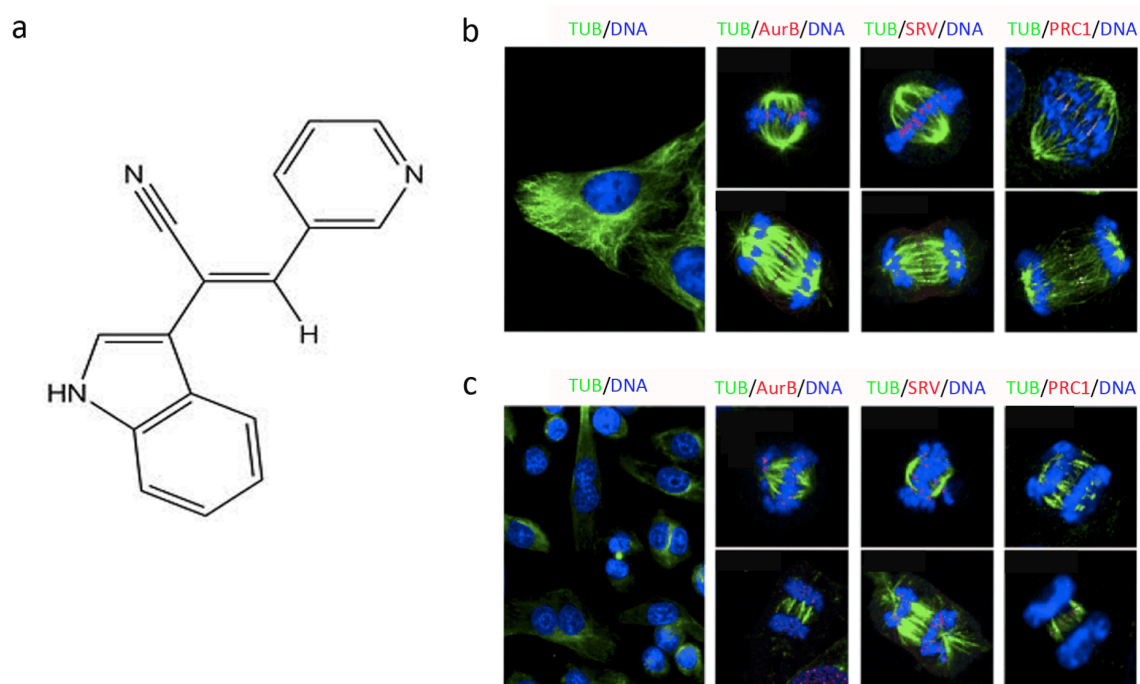


Figure 1-32: Inhibition of MKLP-2 by paprotrain.

a) Chemical structure of paprotrain, the first inhibitor of MKLP-2 with low micromolar IC_{50} . b) Immunostaining of untreated control cells. c) Cells treated with paprotrain induce binucleated cells and inhibit the relocation of the CPC from the inner centromeres to the central spindle during anaphase. MTs (TUB) are represented in green, Aurora B (AurB), survivin (SRV), and PRC1 in red and DNA in blue. Adapted from Tcherniuk *et al*, 2010.¹⁶⁶

1.3 Kinesins as potential drug targets for cancer chemotherapy

Although strong evidence is emerging for kinesins representing valid or at least potential cancer targets, a number of existing marketed drugs such as the vinca alkaloids and taxol are already available which interfere with MT dynamics.^{178,179} The question therefore arises as to whether kinesin-targeting therapies offer the prospect of an advantage over these compounds. Particular problems with these existing drugs are considerable side-effects, including peripheral neuropathy, and drug-resistant tumours.^{178,180} The indications are that Eg5-targeting compounds do indeed have advantages, particularly at the level of side-effects.^{111,124,179} This is probably due to the more restricted expression profile of Eg5, which contrasts, with the ubiquitous expression of tubulin. Currently, neutropenia (abnormally low number of neutrophils) is the major side effect of existing Eg5 inhibitors. Combined with the continuing progress of Eg5 inhibitors in Phase II clinical trials where their efficacy is showing promising results, the interest in kinesin-targeting therapies continues to grow. Important challenges remain such as finding tumour types and subtypes that respond to Eg5 targeting drugs and also subsequently addressing resistance to Eg5 inhibitors that has been observed in cell culture. A large part of the work presented in this thesis aims to further our understanding of the molecular mechanism of kinesin inhibition by clinically interesting compounds. This knowledge will be useful in understanding the causes of resistance and also provide a detailed understanding of new inhibitor pockets, which may assist in slowing the onset of resistance.

The clinical significance of MPP1 is less well understood but there have been studies to show that it plays a certain role in different types of cancer.^{145,181} To date one patent has been deposited for MPP1 inhibitors but has not been pursued.¹⁸² Therefore, to contribute towards developments in this area, an inhibitor of MPP1 has been identified and presented in this thesis. This could be a useful tool compound to further validate MPP1 as a clinically relevant target.

MKLP-2 has only recently gained importance as an anti-cancer target. This has led to the discovery of the first specific inhibitor causing cell cycle arrest and apoptotic cell death. The work presented in this thesis on MKLP-2 is towards improving the potency of the drug candidate.¹⁶⁶ It forms a basis for future MKLP-2 drug design and in validating MKLP-2

as a cancer chemotherapeutic target. Also, the work lays the foundations for structural studies to understand the role of loop L6.

2 Material and methods

2.1 Materials

Codon-optimised cDNAs were purchased from GenScript. pET28a (non cleavable C-terminal his-tag) vector was obtained from previous lab members. The pSUMO (with a N-terminal SUMO fusion tag, Ulp1 cleavage site and his-tag) vector was obtained from Dr. Kristal Kaan (previous lab member). pProExHT (precision protease-cleavable N-terminal his-tagged) expression vector was bought from Invitrogen. All restriction enzymes were obtained from New England Biolabs, Inc. DNA ligation kit were bought from Qiagen. Primers for sub-cloning, TB medium, IPTG (isopropyl β -D-thiogalactoside), TBS-T, Tris-HCl, NaCl, $MgCl_2$, imidazole, Urea, Methanol, DTT, P20, β -mercaptoethanol, Guanidine hydrochloride and PIPES were bought from Sigma. The accessories for the QiaCube™ robot (NTA columns and the HotStar HiFidelity PCR kit) were obtained from Qiagen. 1 ml His-Trap FF, 1 ml HiTrapQ FF, 1 ml HiTrapQ FF, Superose 12 10/300 GL and Superose S75 columns were purchased from GE Healthcare. BL21(DE3)pLysS, BL21(DE3), Rosetta-gami(DE3)pLysS, Origami2(DE3)pLysS cells, Bug Buster™ and Benzonase™ Nuclease were bought from Novagen. Amicon Ultra filtrations units for the concentration of proteins were obtained from Millipore. SDS-PAGE gels, running and NuPAGE transfer buffers were obtained from Invitrogen. BL21-CodonPlus (DE3)-RIPL and ArcticExpress cells were purchased from Agilent Technologies. The Cytophos assay kit was obtained from Cytoskeleton. Lyophilised tubulin (Tebu-Bio, Cat. No. - 027T240-B) was used for all experiments involving MTs. Ispinesib and SB743921 were bought from Selleck Chemicals. BI8 and paprotrain were obtained from Sai Advantium. Crystallisation screens: Index, PEG Ion, Natrix and Crystal Screen HT were obtained from Hampton Research whereas JCSG+ and PACT were obtained from Qiagen. 96 well crystallisation plates were obtained from Greiner Bio-one and 24 well linbro VDX plates from Hampton Research.

All cloned expression constructs were verified by DNA sequencing. All purification steps were performed using an ÄKTA purifier at 4°C (GE Healthcare) and purified proteins were analysed by SDS-PAGE after each step of purification. Finally, the purified proteins were analysed by mass spec fingerprint analysis.

The buffers used are as follows:

Buffer A: 50 mM PIPES, pH 6.8, 2 mM MgCl_2 , 200 mM NaCl and 10 mM imidazole

Buffer B: 50 mM PIPES, pH 6.8, 2 mM MgCl_2 , 200 mM NaCl and 500 mM imidazole

Buffer C: 50 mM PIPES pH 6.8 and 200 mM NaCl

Buffer D: 50 mM PIPES, pH 6.8, 50 mM KCl, 1 mM DTT and 1 mM MgCl_2

Buffer E: 50 mM PIPES, pH 6.8, 2 mM MgCl_2

Buffer F: 20 mM PIPES, pH 6.8, 300 mM NaCl, and 2 mM β -mercaptoethanol

Buffer G: 50 mM Tris, pH 7.0, 200 mM NaCl, 1 mM MgCl_2 , 0.5 mM EDTA and 0.05% P20

Buffer H: 10 mM HEPES, pH 8.3, 150 mM NaCl, 350 mM EDTA, 0.005% P20

Buffer I: 50 mM PIPES, pH 6.8, 1 mM MgCl_2 and 1 mM

Buffer J: 50mM PIPES, pH 6.8, 1 mM MgCl_2 , 1 mM Mg^{2+} ATP and 250 mM NaCl

Buffer K: 20 mM PIPES, pH 7.3, 250 mM NaCl, 1 mM PMSF, 1 mM Na-EGTA, 1 mM MgCl_2 , 2 mg/ml lysozyme, 10 mg/ml DNase and 20 mM imidazole

Buffer L: 20 mM PIPES, pH 7.3, 250 mM NaCl, 1 mM Na-EGTA, 2 mM MgCl_2 , 10 mM imidazole

Buffer M: 20 mM PIPES, pH 7.3, 250 mM NaCl, 1 mM Na-EGTA, 2 mM MgCl_2 , 1 M imidazole

Buffer N: 20 mM PIPES, pH 7.3, 1 mM Na-EGTA, 1 mM MgCl_2

Buffer O: 20 mM PIPES, pH 7.3, 1 mM Na-EGTA, 1 mM MgCl_2 , 1 M NaCl

Buffer P: 20 mM PIPES, pH 7.3, 1 mM Na-EGTA, 1 mM MgCl_2 and 200 mM NaCl

2.2 Human kinesin, Eg5

2.2.1 Sub-cloning into *E. coli* expression vectors

The motor domain of human Eg5 (residues 1-368) was obtained from the initial cloning into the modified pProEx expression vector using *NcoI* and *XhoI* restriction sites, yielding a PreScission protease-cleavable N-terminal hexa his- tagged protein.¹¹⁴

2.2.1.1 Cloning of ispinesib resistant mutants of Eg5

Single Eg5 mutants for D130V (named Eg5^{D130V}), A133D (named Eg5^{A133D}) and an expression clone carrying both mutations (Eg5^{DM}) were introduced using the following forward and reverse primers according to the recommendations of the QuickChange kit: Eg5^{D130V} (Forward: 5'-G TAT ACC TGG GAA GAG GTT CCC TTG GCT GGT ATA AT-3'; Reverse: 5'-AT TAT ACC AGC CAA GGG AAC CTC TTC CCA GGT ATA C-3'), Eg5^{A133D} (Forward: 5'-GG GAA GAG GAT CCC TTG GCT GGT ATA ATT CCA CGT ACC C-3'; Reverse: 5'-G GGT ACG TGG AAT TAT ACC ATC CAA GGG ATC CTC TTC CC-3'); Eg5^{DM} (Forward: 5'-GAG TAT ACC TGG GAA GAG GTT CCC TTG GAT GGT ATA ATT CCA CG-3'; Reverse: 5'-CG TGG AAT TAT ACC ATC CAA GGG AAC CTC TTC CCA GGT ATA CTC-3'). Each mutant was confirmed by DNA sequencing and subsequently expressed and purified as described for Eg5^{WT}.

2.2.1.2 Cloning of wild-type and Eg5 mutants with a double hexa histidine tag for Ni-NTA immobilisation

A modified expression vector to generate N-terminal histidine tagged protein was created. DNA coding for a double histidine tag separated by a ten amino acid linker was cloned into the pET28a. The forward and reverse inserts with both blunt and sticky ends created by restriction digests of *NcoI* and *XhoI* are (Forward: 5'-C ATG CAT CAC CAT CAC CAT CA C GGA GCG ACA GCT GGC TCA GGG ACC GCC ACG CAT CAC CAT CAC CAT CAC ACC ATG GAG CAG CGG CCT GCT CGA GTG AG- 3'; Reverse: 5'-TC GAC TCA CTC GAG CAG GCC GCT GCT CCA TGG TAT GAT GAT GGT GGT GGT GCG TGG CGG TCC CTG AGC CAG CTG TCG CTC CGT GGT GAT GAT GGT GAT G- 3'). The blunt ends of the inserts and the original pET28a vector were cleaved using restriction enzymes *NcoI* and *XhoI* at 37°C for 2 hr. Running on a 1.2% agarose gel separated the restricted plasmid and insert. Subsequently, the double histidine tag insert was ligated to create a modified double histidine tag pET28a vector using the DNA ligation kit. The inserts for Eg5 wild-type and the mutants

were then subsequently cloned into the newly created modified pET28a vector using the created cloning site between *NcoI* and *XhoI* sites.

2.2.2 Protein expression and purification

The plasmids were transformed into BL21-CodonPlus-RIL Competent *E. coli* and grown in 6 L of Terrific Broth (TB) at 37°C, supplemented with 100 mg/L ampicillin, to an A_{600} of 0.6 and induced overnight with 0.5 mM IPTG at 20°C. Harvested cells were resuspended in buffer A supplemented with 1 mM PMSF, 1 mM Mg-ATP, and 2 mg/ml lysozyme and subjected to one cycle of freeze-thaw before 1 mM DNaseI and 10 mM MgCl₂ were added. Sonication was then carried out using the Vibra-Cell VCX 750 sonicator (Sonics & Materials, Inc.) with a 13 mm probe, at 90 % amplitude and 8 x 8 secs ON and OFF pulses and centrifuged (1h, 4°C, 31400 g).

2.2.2.1 Wild-type and mutants of Eg5

Supernatant from centrifuged lysate were pooled and loaded onto a 5 ml Ni-NTA HisTrap FF column that has been equilibrated in buffer A. The proteins were eluted on a gradient of buffer B after washing the bound protein with a mixture of 4% and 96% of buffer B and A respectively. Fractions with protein of interest as seen by the UV trace were pooled and the buffer was exchanged using Desalting 26/10 column for buffer C. 1 mg of PreScission protease, 1 mM Mg²⁺ATP, and 2 mM MgCl₂ were added to the protein and incubated overnight at 4°C. To remove uncleaved protein and protease a second Ni-NTA affinity chromatography was performed. The cleaved protein that came as a flow-through was then subjected to size exclusion chromatography on a Superdex 200 16/60 column equilibrated in gel filtration buffer D. Fractions containing the protein of interest from the UV trace were pooled and concentrated on an Amicon Ultra filtration device with size exclusion limit of 30 kDa, to a final concentration of approximately 10 mg/ml, frozen in liquid nitrogen, and stored at -80°C.

Eg5 wild-type and mutants were purified following the above protocol apart for Eg5^{DM} where buffer D contained 150 mM KCl instead of 50 mM. All the steps of purification were checked by SDS-PAGE for the protein by running 10 ul of the fractions obtained.

Eg5 wild-type and mutant protein after the final gel filtration chromatography were obtained at approximately 95% purity. One representative SDS-PAGE for Eg5^{D130V} is shown is Figure 2-1.

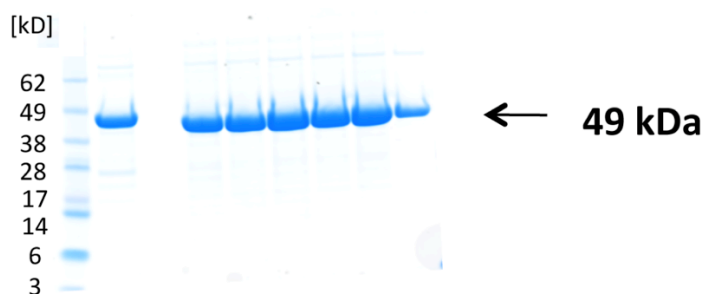


Figure 2-1: Protein purification of Eg5^{D130V}.

The figure shows an example of the protein obtained from purification of Eg5^{D130V}.

2.2.2.2 Eg5 with double hexa-histidine tag

Supernatant were pooled from the centrifuged bacterial cell cultures and loaded onto a 5 ml Ni-NTA HisTrap FF column that has been equilibrated in buffer A. The proteins were eluted on a gradient of buffer B after washing the bound protein with a mixture of 4% and 96% of buffer B and A respectively. Fractions of protein were pooled and diluted with buffer E. Ion exchange chromatography was then performed to separate recombinant protein from other contaminants that were not separated during the affinity purification. The protein from ion exchange was then subjected to size exclusion chromatography on a Superdex 200 16/60 column equilibrated in gel filtration buffer D. Fractions containing the protein of interest were pooled and concentrated on an Amicon Ultra filtration device, with a size exclusion limit of 30 kDa, to a final concentration of approximately 1 mg/ml, frozen in liquid nitrogen, and stored at -80°C.

2.2.2.3 Determination of protein concentration and mass spectrometry fingerprint analyses

Protein concentrations were determined using two independent methods. The Bradford reagent was used as an initial estimation of the protein concentration according to the supplier's instructions. For ATPase assays, ITC measurements and SPR assays the concentration of native and denatured proteins (6.7 M GuHCl with 20 mM sodium phosphate to pH 7.0) were measured at 280 nm using a molar extinction coefficient of 23150 M⁻¹cm⁻¹ (Eg5 wild-type and mutants: 20650 M⁻¹cm⁻¹ and ADP: 2500 M⁻¹cm⁻¹).

The presence of the mutants was confirmed by mass spectrometry peptide fingerprint analysis with coverage of 78%, 88% and 70% for D130V, A133D and DM, respectively. In all cases the peptide carrying the mutation was identified.

2.2.2.4 Polymerisation of tubulin into MTs

Lyophilised tubulin was solubilised in 100 μ l of G-PEM buffer (1 mM GTP, 80 mM PIPES, 1 mM Na-EGTA, 1 mM $MgCl_2$, pH 7.0) to a final concentration of 10 mg/ml. To polymerise and stabilise MTs, 1 μ l of taxol (10 mM stock in DMSO) was added to 100 μ l of tubulin and incubated overnight at 37°C.

2.2.3 Steady state ATPase assay

Steady state basal and MT-stimulated ATPase rates were measured using the pyruvate kinase/lactate dehydrogenase-linked assay.¹⁸³ For each measurement a concentration series of either ATP or MTs or inhibitor was used. The amounts of Eg5 were optimised at 80-100 nM for basal and 5 nM for MT-stimulated activity assays. The mixture of ATPase buffer along with inhibitor/MTs/ATP in increasing concentration was added to each well. The enzyme was added just before the start of each experiment. The reaction mixtures were measured for 30 min in a TEECAN Sunrise™ at 340 nm.

The raw data was processed using the equation in 2.2.3.1 and the data plotted using either Michaelis-Menten equation for enzyme kinetics. Data were plotted and analysed using Kaleidagraph 4.0 (Synergy Software).

2.2.3.1 Measurement of kinetic parameters

The kinetic parameters k_{cat} , $K_{m, ATP}$, $K_{m, MTs}$ were initially calculated and optimised for wild-type and mutants, based on the rates computed from the following equation.

$$OD/min (s^{-1}) = (2 \cdot \Delta A/min) / (\epsilon_{NADH} \cdot 60 \cdot C_{enzyme})$$

where, ϵ_{NADH} corresponds to the molar extinction coefficient of NADH (6220 $\Delta A/mol/cm$), $\Delta A/min$ is the absorbance decrease at 340 nm per min, and C_{enzyme} is the molar concentration of kinesin used in the assay. The factor 2 is a correcting factor taking into account the length of the optical path in the 96-well plate, normalised to a path of 1 cm.

2.2.3.2 Measurement of inhibition of Eg5^{WT} and mutants

The IC_{50} values for the inhibition of the basal and MT-stimulated ATPase activities of Eg5 were measured for ispinesib and SB743921 between concentrations of 0 and 1 μ M for Eg5^{WT} and between 0 and 120 μ M for the Eg5 mutants. STLC was measured from 0 μ M to

12 μM for Eg5^{WT} and from 0 μM to 150 μM for the Eg5 mutants. The Mg^{2+}ATP concentration was fixed at 1 mM for all measurements. For the inhibition of the MT-stimulated ATPase activity, the MT concentration was fixed at 2 μM .

2.2.4 Isothermal titration calorimetry (ITC)

ITC was performed as previously described by Sheth et al, 2009¹²⁶ with certain modifications. Purified Eg5 was subjected to gel filtration chromatography in buffer F to remove excess ATP and then dialysed overnight against buffer A supplemented with 0.5 mM ADP and 5 mM MgCl_2 . The protein was diluted to a final concentration of 20 μM with dialysis buffer. Its concentration was then verified by absorption measurements at 280 nm using an extinction coefficient as mentioned previously. Two independent methods were used for concentration determination, the first was by using Eg5 denatured in 6.7 M guanidine hydrochloride with 20 mM phosphate at pH 7.0, second was by measuring the concentration of the folded protein in solution directly obtained after dialysis. Finally 1% DMSO was added to the protein solution. The inhibitor was prepared in 100% DMSO and then diluted in dialysis buffer to a final concentration of 250 μM or 500 μM of ispinesib with 1% DMSO. All solutions were centrifuged for 5-10 min at room temperature prior to loading of the samples into either a Microcal VP-ITC or an iTC₂₀₀ titration calorimeter.

The heat of dilution was estimated by titrating into protein-free buffer subtracted prior to data analysis. The thermodynamic parameters N (stoichiometry), K_a (association constant), and ΔH (enthalpy change) were obtained through fitting of the experimental data using the single-site binding model of the Origin software package (version 7.0), whereas the free energy of binding (ΔG) and entropy change (ΔS) were then calculated from the fitted values. For each experiment, at least two independent titrations were performed, which were analysed independently. The resulting thermodynamic values were then averaged. Data fitting was done with either one site binding or two site sequential binding model as described previously by Freyer et al, 2008.¹⁸⁴

2.2.4.1 Study of wild-type Eg5 with ispinesib

ITC experiments were performed with a Microcal VP-ITC titration calorimeter (Microcal Inc., North Hampton, MA). All titrations were carried out at 25°C with a stirring speed of around 350 rpm. In total 26 injections were performed per titration with the first

injection of 5 μ l followed by 25 injections of 10 μ l for 20 s with a gap of 240 s between them.

2.2.4.2 Study of wild-type and mutant Eg5 with SB743921, BI8, ispinesib and monastrol

ITC experiments were performed with an iTC₂₀₀ (GE Healthcare). All titrations were carried out at 25°C with a stirring speed of around 1000 rpm. In total 20 injections were performed per titration with the first injection of 0.5 μ L followed by 19 injections of 2 μ l for 4 sec with a gap of 240 s between them.

2.2.5 Surface plasmon resonance

All experiments were performed using a Biacore T200 (Biacore) with running buffer G supplemented with fresh 1% DMSO before each run. The experiments were carried out at 25°C. Experiments for each protein-inhibitor set were performed at least in duplicate. Double His-tagged Eg5 (200 nM) was immobilised on the surface of NTA sensor chip charged with Ni²⁺ to approximately 2,000 RU. The sensor surface was regenerated between each experiment with a 60s and 120s injection of 1M imidazole and stripping buffer H respectively.

For analyte preparation, each of the compounds analysed were prepared in DMSO (50 mM). A concentration series for each inhibitor was prepared ensuring a consistent final DMSO concentration of 1%. To correct for the minor DMSO volume effect, a DMSO calibration series was prepared and measured using 0.5% and 1.8% of DMSO in running buffer. Protein immobilisation on the chip was carried out at a flow rate of 5 μ l/min whereas for the experiments a flow rate of 30 μ l/min was used.

The steady state analyses of molecular interactions were calculated after subtraction of backgrounds (inhibitor-binding to a control flow cell) using BIAcore T200 Evaluation software and Kaleidagraph 4.0. The binding constant K_D was evaluated according to the appropriate binding model. For two site binding, two sequential first-order binding model¹⁸⁵ was used whereas for one site binding the pseudo-first-order kinetic model¹⁸⁶ was applied assuming one molecule of the ligand (Eg5) binds to one molecule of the analyte (BI8 - Benzimidazole number 8).

2.2.5.1 Study of two site binding of BI8 to Eg5

To investigate two site binding and analyse the affinity for both sites, BI8 was measured for a range from 0 to 528 μ M. BI8 was injected first to determine the binding affinity of two sites followed by single ispinesib injection at 10 μ M to competitively displace BI8 from the site around loop L5. BI8 was then injected for the second time using the same concentration range to determine the K_D only for the second novel site.

2.2.6 Crystallisation of Eg5-ADP mutants and Eg5-ADP-inhibitor complexes

2.2.6.1 Crystallisation of the “ispinesib mutants”: Eg5^{D130V}, Eg5^{A133D} and Eg5^{DM}

Crystals for the three Eg5 mutants (the “ispinesib mutants”) appeared after 3 days in hanging drops containing a mixture of 1 μ l of protein and 1 μ l of reservoir solution. Eg5^{D130V} crystals were obtained in 14% w/v PEG (polyethylene glycol)-3350, 0.2 M sodium nitrate and 0.1 M MES (pH 5.6). Eg5^{A133D} crystals appeared in a reservoir solution containing 16% w/v PEG-3350, 0.2 M sodium nitrate and 0.1 M MES (pH 5.6). The crystals of these two single mutants only appeared after micro or macro seeding using Eg5^{WT} crystals grown under similar conditions. Eg5^{DM} crystals grew in completely different solution containing 0.02 M Calcium chloride dehydrate, 0.02 M Cadmium chloride hydrate, 0.02 M Cobalt(II) chloride hexahydrate and 20% w/v PEG-3350. For data collection crystals were immersed in a solution containing 1.2 times the concentration of components in well condition supplemented with 15% glycerol as cryoprotectant then subsequently flash frozen in liquid nitrogen.

2.2.6.2 Crystallisation of Eg5^{WT}-ispinesib, Eg5^{WT}-SB743921 and Eg5^{A133D}-SB743921 complexes

Eg5^{WT} or Eg5^{A133D} were incubated with 1 mM of ispinesib or SB743921 (diluted into protein from a 50 mM stock in DMSO) for 2 hr at 4°C. Before setting up crystal trays, the sample was centrifuged at 14000 g for 5 min at 4°C to pellet undissolved inhibitor. Small crystals for all three complexes (Eg5^{WT}-ispinesib, Eg5^{WT}-SB743921 and Eg5^{A133D}-SB743921) appeared after two to three days in hanging drops by mixing 1 μ l of protein-inhibitor complex (11 mg/ml) with 1 μ l of reservoir solution. For Eg5^{WT}-ispinesib crystals, the reservoir solution contains 0.1 M Tris, pH 8.5, 0.02 M MgCl₂ and 20% (w/v) PEG 8000. For

Eg5^{WT}-SB743921 and Eg5^{A133D}-SB743921 the reservoir solution contains 0.02 M calcium chloride dehydrate, 0.02 M Cadmium chloride hydrate, 0.02 M Cobalt(II) chloride hexahydrate and 20% w/v PEG-3350. All crystals were grown in 24 well Linbro plates by vapour diffusion at 4°C in hanging drops.

To obtain good diffraction quality single crystals, streak seeding were performed into drops containing 1:1 ratio of protein-inhibitor complex to well solution. Single crystals appeared overnight and were allowed to grow for several days before immersing in cryoprotectant solution containing 1.2 times the concentration of components in well condition supplemented with 15% glycerol as cryoprotectant then subsequently flash frozen in liquid nitrogen.

2.2.6.3 Crystallisation of Eg5^{WT}- BI8

In collaboration with Dr. Venkat Ulaganathan, Eg5 (10 mg/mL) was mixed well with 2 µL BI8 (50 mM) and the mixture was incubated at 4°C for 2 hr. The mixture was then centrifuged at 13000 g for 5 min to remove any undissolved inhibitor. Diffraction quality single crystals of the complex were obtained in sitting drop by vapour diffusion using 1 µL of protein complex and 1 µL of the reservoir solution (0.1 M HEPES buffer, pH 7.5, 20 % (w/v) PEG-3350 and 0.1 M magnesium chloride) in VDX plates at 19° C. The crystal was cryoprotected using 0.12 M HEPES buffer at pH 7.5, 22 % (w/v) PEG 3350, 0.12 M magnesium chloride and 15 % (v/v) PEG-400 and flash frozen in liquid nitrogen for diffraction measurements.

2.2.7 Data collection, processing, structure determination, refinement and model quality

2.2.7.1 Eg5 in complex with ispinesib

Diffraction data were collected at 100 K on beamline I02 of Diamond Light Source (Oxfordshire). Data were processed and scaled to 2.6 Å using XDS/XSCALE¹⁸⁷, truncated and processed with the CCP4 suite of programs.¹⁸⁸ The Matthews Coefficient¹⁸⁹ was used to determine the number of molecules in the asymmetric unit and the solvent content. Then structure of the Eg5-ispinesib complex was solved in space group $P2_1$ by molecular replacement with MOLREP using the Eg5 tetramer of PDB entry 2GM1 as the search model.¹²⁰ Improvement of this structure then proceeded using iterative cycles of model building with Coot¹⁹⁰ and reciprocal space refinement using PHENIX or REFMAC5.¹⁹¹

Simulated annealing refinement was performed using PHENIX¹⁹², resulting in a final model with an R_{free} of 25.4% and overall reasonable geometry. Coordinates and dictionaries for ispinesib were obtained from the Dundee PRODRG server¹⁹³. Data and refinement statistics are given in Table 2-1.

Table 2-1: Data collection and refinement statistics for the Eg5–ispinesib complex.

Values in parentheses pertain to the highest-resolution shell. Ramachandran plot statistics were obtained with MolProbity¹⁹⁴.

Statistics	Eg5-ispinesib
Unit cell dimensions	$a = 64.7 \text{ \AA}$, $b = 112.6 \text{ \AA}$, $c = 106.9 \text{ \AA}$, $\alpha = 90.0^\circ$, $\beta = 90.0^\circ$, $\gamma = 90.0^\circ$
Space group	$P2_1$
Molecules per asymmetric unit	4
Resolution range (\AA)	30.0–2.6
Total reflections	134457
Unique reflections	45511
Completeness (%)	95.7 (91.0)
Multiplicity	3.0 (2.7)
R_{sym} (%)	6.9 (62.2)
$I/\sigma(I)$	13.3 (2.0)
$R_{\text{work}} / R_{\text{free}}$ (%)	20.4 / 25.3
Wilson B (\AA^2)	59.9
Average B (\AA^2):	
- Overall	57.7
- Protein	58.2
- Solvent	48.1
- ADP	33.8
- ispinesib	44.9
r.m.s.d. bond lengths (\AA)	0.016
r.m.s.d. bond angles ($^\circ$)	1.47
Ramachandran plot statistics (%):	
- Favoured	98.1
- Allowed	1.9
- Outliers	0.0

Coordinates and structure factors have been deposited with the Worldwide Protein Data Bank (PDB ID: 4AP0). In the Ramachandran plot, 97.8% of residues are in preferred regions, 2.3% are in allowed regions and there are no outliers.

2.2.7.2 Eg5 mutants

Diffraction data were recorded at Diamond Light Source. Data were processed using iMosflm¹⁹⁵ and SCALA from the CCP4 suite of programs¹⁹⁶. The structures of the three Eg5 mutants were solved by molecular replacement (MOLREP) using the native Eg5 structure

(PDB ID: 1II6²⁸) as a search model. The Eg5^{D130V}, Eg5^{A133D} and Eg5^{DM} structures do not have any density for most of the loop L5 region. Loops L2 and L11 are missing in all the apo mutant structures. PDB IDs for the mutants are: 4A1Z (Eg5^{A133D}), 4A28 (Eg5^{D130V}) and 4B7B (Eg5^{DM}). Data collection and refinement statistics for the three crystal structures are shown in Table 2-2 and the quality of the models is summarised in Table 2-3.

Table 2-2: Table representing data collection and refinement statistics of Eg5 mutant and complexes with SB743921.

	Eg5 ^{D130V}	Eg5 ^{A133D}	Eg5 ^{DM}	Eg5 ^{WT} -SB743921	Eg5 ^{A133D} -SB743921
Unit cell dimensions: a, b, c, α , β , γ (Å, deg)	52.0, 78.4, 93.3, 90.0, 93.5, 90.0	52.9, 78.4, 92.7, 90.0, 93.2, 90.0	81.5, 81.5, 114.9, 90.0, 90.0, 120.0	81.4, 81.4, 115.2, 90.0, 90.0, 120.0	81.0, 81.0, 123.6, 90.0, 90.0, 120.0
Space group	$P2_1$	$P2_1$	$P6_5$	$P3_2$	$P6_5$
Molecules per AU	2	2	1	2	1
Resolution range (Å)	30.00 - 2.80	30-2.55	30-2.5	30-2.8	30-2.4
No. of reflections	78496 (14843)	85604 (12271)	110022 (16329)	51872 (6882)	64529 (9362)
No. of unique reflections	18389 (2650)	24512 (3521)	11958 (1744)	9633 (1396)	10595 (1557)
Completeness (%)	99.9 (100)	98.8 (97.9)	99.9 (100)	99.4(99.7)	98.3 (98.9)
Multiplicity	3.3 (3.4)	3.5(3.5)	9.2 (9.2)	6.5(6.0)	7.5(7.0)
R _{sym} (%)	14.4 (49.8)	8.7 (28.6)	9.8 (25.2)	8.9(50.1)	8.9 (35.7)
I/ σ (I)	12.7 (4.6)	10.7 (5.5)	18.7 (7.8)	17.6(2.0)	14.8 (5.6)
Wilson B (Å ²)	48.5	49.6	37.0	83.8	52.8
Refinement statistics					
R _{work} /R _{free} (%)	17.6 / 26.7	18.4 / 26.7	17.9 / 25.0	19.1/24.8	16.1/20.8
Average B factors					
Overall	24.1	46.3	46.8	71.9	23.8
Main chain	22.9	44.5	45.2	72.1	24.3
Side chain	25.4	48.2	48.4	71.6	23.7
No. of Mg ²⁺ ADP/inhibitor/water	2/0/59	2/0/73	1/0/123	2/2/68	1/1/241
r.m.s.d. in bond length (Å) ^b	0.012	0.016	0.009	0.008	0.012
r.m.s.d. in bond angle (deg)	1.456	1.669	1.550	1.439	1.625

Table 2-3: Table representing the different regions of wild-type and mutant Eg5 as seen in the solved structure together with the Ramachandram plot.

		Eg5 ^{D130V}	Eg5 ^{A133D}	Eg5 ^{DM}	Eg5 ^{WT} -SB743921	Eg5 ^{A133D} -SB743921
Ramachandran plot						
No of residues in preferred region [%]		96.2	93.4	96.9	86.3	95.4
No of residues in allowed region [%]		2.7	3.8	2.2	11.1	3.2
Outliers [%]		1.1	2.8	0.9	2.6	1.5
Model						
Chain A	First to last residue [No]	Gly16-Val365	Gly16-Val365	Gly16-Pro363	Gly16-Glu364	Gly16-Glu364
Chain B	First to last residue [No]	Gly16-Val365	Gly16-Val365	--	Gly16-Glu364	--
Missing residues						
Chain A (Range)		Loop L5 (120 – 124) Loop L11 (271 – 283)	Loop L5 (121 – 127) Loop L11 (271 – 280)	Loop L2 (56 – 60) Loop L5 (120 – 124) Loop L11 (271 – 285)	--	--
Chain B (Range)		Loop L2 (56 – 59) Loop L5 (120 – 125) Loop L11 (274 – 288)	Loop L2 (55 – 61) Loop L5 (122 – 127) Loop L11 (274 – 288)	--		

2.2.7.3 Eg5^{WT} and Eg5^{A133D} in complex with SB743921

Diffraction data were collected at Diamond Light Source and processed using iMosflm¹⁹⁵ and SCALA from the CCP4 suite.¹⁹⁶ The structure of the Eg5^{WT}-SB743921 complex was solved by molecular replacement (MOLREP) using 1 molecule of the Eg5-monastrol complex (PDB ID: 1X88¹⁹⁷) as a search model. The structure of the Eg5^{A133D}-SB743921 complex was solved using the complex of wild-type Eg5 as a search model. All structures were initially refined with REFMAC5¹⁹¹ subsequently followed by PHENIX¹⁹². For calculating R_{free} 5% of data were used. Electron-density and difference-density maps, all σ_A -weighted, were inspected and model building carried using Coot¹⁹⁰. The coordinates and the cif dictionary for SB743921 were calculated using the Dundee PRODRG server¹⁹³. Loop L11, which is usually missing in most of the other Eg5-inhibitor complexes, is visible in the Eg5^{WT}-SB743921 and Eg5^{A133D}-SB743921 complex structures. One structure has been deposited as PDB entry 4AS7 (Eg5^{A133D}-SB743921). The Eg5^{WT}-SB743921 is undergoing deposition.

2.2.7.4 Structure of Eg5-BI8 quaternary structure

The structure of the Eg5-ADP-BI8 complex was determined at 1.7 Å resolution. Data collection and refinement statistics are summarised in Table 2-4.

Table 2-4: Data collection and refinement statistics of Eg5 in complex with BI8

Statistics	Eg5-BI8
Unit cell dimensions a, b, c, α , β , γ (Å, °)	107.9, 62.9, 75.1, 90.0, 117.4, 90.0
Space group	C2
Beamline / Detector	I-02 / Q315R
Molecules per asymmetric unit	1
Resolution range (Å)	36.96 – 1.69
No. of unique reflections	49475
Completeness (%)	99.2 (99.2)
Multiplicity	3.9 (3.9)
R_{sym} (%)	8.4 (65.8)
$I/\sigma(I)$	9.3 (2.0)
Wilson B (Å ²) / DPI (Å ²)	23.07 / 0.10
Refinement statistics	
$R_{\text{work}} / R_{\text{free}}$ (%)	19.4 / 23.3
Average B Factors	
Overall	29.8
Main Chain / Side Chain	26.0 / 32.5
No. of ADP / Inhibitor / Water	1 / 2 / 450
³ r.m.s.d. in bond length (Å)	0.011
³ r.m.s.d. in bond angle (deg)	1.414

¹ Values in parentheses pertain to the highest resolution shell

² DPI: Diffraction-component precision index¹⁹⁸

³ r.m.s.d. is the root-mean-square deviation from ideal geometry

2.3 MPP1

2.3.1 Human MPP1

2.3.1.1 Sub-cloning into *E. coli* expression vectors

Codon-optimised DNA coding for the motor domains of human MPP1₁₋₄₄₇ and MPP1₅₇₋₄₉₁ was synthesised by Genscript Inc and then cloned into pET28a vector using *NcoI* and *XhoI* sites. In addition, it was also cloned in pSUMO expression plasmid. The primers for the two different constructs are as follows: MPP1₁₋₄₄₇: Forward Primer: 5'-GCC ATT GCA CAA TAA GTT TGT GTC CCA GAC-3'; Reverse Primer: 5'-GTC TGG GAC ACA AAC TTA TTG TGC AAT GGC-3'; MPP1₅₇₋₄₉₁: Forward Primer: 5'-GAA CAG ATT GGT GGA TGC GGA TCC AAA GAT TAT CTC CAG GTT-3'; Reverse Primer: 5'-CTT GAG AGG AAT TTA AAG TGT CTT AGA CAC AAA CTT TTT GTG-3'. The cloning strategy and the sequences were verified by DNA sequencing.

Cloning of MPP1 constructs were also carried out in other various vectors but due to lack of protein expression capability they are not further pursued.

2.3.1.2 Expression and purification of protein

Plasmids were transformed into *E. coli* BL21 CodonPlus using heat shock at 42°C. Then, 12 L of bacterial culture were grown at 37°C in LB (Luria Broth) added with 100 mg/l ampicillin to an A₆₀₀ of 0.7 and induced overnight with 0.5 mM IPTG at 20°C. Harvested cells were resuspended in buffer A supplemented with 1 mM PMSF, 1 mM Mg-ATP, 1 mM DNaseI and 2.5 mg of lysozyme, and subjected to one cycle of freeze–thaw and sonication. The lysate was centrifuged for 1 hr in a J25 (Beckman) rotor at 30000 g at 4°C.

Clear lysates were loaded on to a 5 ml HisTrap FF column equilibrated in buffer A. The resin was washed with buffer A containing 10 mM imidazole and the proteins eluted on a gradient of buffer B.

For pSUMO vector, fractions containing the protein were pooled and the buffer was exchanged for desalting buffer C. Ulp1 protease, 1 mM Mg^{2+} ATP and 1 mM MgCl_2 were added and reaction mixtures were incubated overnight at 4°C. Uncleaved proteins and protease were removed by running the sample through the HisTrap FF column a second time.

The protein without the fusion tag for pSUMO vector and the protein from first affinity purification for pET28a vector were diluted using buffer I to obtain a final salt concentration of ~30 mM. The diluted sample was then applied to a 5 ml Hi-trap FF Mono S or Q ion exchange column (depending on the pI of the protein) to remove the remaining contaminants.¹⁹⁹ The protein was eluted with a gradient of buffer J. The protein containing fractions were pooled and run through a final step of size exclusion chromatography on a Superdex200 16/60 column equilibrated in gel filtration buffer D.

The protein obtained was pooled and concentrated on an Amicon ultrafiltration device to a final concentration of approx. 5 mg/ml and flash frozen in liquid nitrogen and stored at -80°C after adding 5% glycerol. The proteins have been used freshly purified where possible with occasional use of frozen proteins.

2.3.1.3 *In vitro* screening for inhibitors of the human mitotic kinesin MPP1

2.3.1.3.1 Steady state ATPase measurements and determination of IC_{50} values

Steady state basal and MT-stimulated ATPase rates were measured as previously described for Eg5.¹⁸³ 680 nM MPP1 was used in the basal assay while 50 nM was used in the MT-stimulated activity assay. For evaluating the $K_{m,ATP}$, the concentration of ATP was used within a range from 0 to 2 mM for both basal and MT-stimulated ATPase assays, whereas MTs were used in the range of 0 to 20 μM for $K_{0.5,MTs}$. Kinetics measurements were done at 25°C using a 96-well Sunrise photometer (TECAN, Maennedorf, Switzerland). The data were analysed using Kaleidagraph 4.0. The kinetic parameters k_{cat} , $K_{m,ATP}$, $K_{0.5,MTs}$ were initially calculated and optimised. All calculations were done based on the equation described previously for Eg5 (section 2.2.3.1).

The IC_{50} values for the inhibition of the basal and MT-stimulated ATPase activities of MPP1 were calculated for depsidones and depside analogues at concentrations ranging from 0 to 200 μ M or 0 to 150 μ M based on the solubility of the respective compounds.

2.3.1.3.2 Determination of the type of inhibition of physodic acid for MPP1 in the absence and presence of MTs

The type of inhibition for the depsidones in the absence and presence of MTs was determined based on the steady state ATPase measurements. Physodic acid as the most potent compound was selected for these assays. To characterise the type of inhibition we determined the V_{max} and K_m of ATP in the absence and presence of constant concentration of 1 μ M MTs. For $K_{0.5, MT}$, ATP concentration was fixed at 1 mM.

Inhibitor concentrations of 0, 1, 5 10 and 20 μ M were used to investigate the type of inhibition for both basal and MT-stimulated ATPase activity either with increasing concentration of ATP from 0 to 2 mM or MTs from 0 to 1 μ M.

2.3.1.3.3 Cytophos assay

The Cytophos assay was used as a secondary screening method to measure the inhibition of steady state ATPase activity of MPP1. The assay detects the release of inorganic phosphate and is a modification of the Malachite green method. In the Malachite green assay, the free inorganic phosphate released from the protein in the aqueous solution reacts with the Malachite green producing a green colour and the absorbance is measured at 650 nm. In the Cytophos assay, ATP is added to the solution and kinesin converts it into ADP and inorganic phosphate by its ATPase activity. The amount of inorganic phosphate released from the reaction mixture by kinesin ATPase activity is measured at 650 nm.²⁰⁰

Firstly, a standard plot using control sample (Phosphate standard) and the Cytophos reagent was generated. The control sample was incubated for 5 min followed by 10 min incubation with Cytophos reagent and then measuring the end point absorbance at 650 nm.

For measurement of the inhibition of MPP1 by depsidones and depsides, the Cytophos assay protocol was followed with a final reaction volume of 100 μ l. Protein concentrations of 50, 100, 150, 200 nM were used. Inhibitor concentration was measured

from 0 to 150 μ M for each protein concentration. The ATPase reaction was mixed with freshly prepared ATP at three different concentrations of 100, 200 and 300 μ M and the reaction mixture incubated for 5 min. The compounds were analysed at three different concentrations. Next, the Cytophos reagent was added and the mixture incubated for 10 min. The end point measurement was carried out in a TECAN Sunrise 96-well plate reader at 650 nm. Appropriate blanks were used for each experiment. All experiments were done in triplicate and at 25°C.

2.3.1.4 Crystallisation trials

The initial trials for crystallisation of MPP1₅₄₋₄₉₁ in pET-28a (with a non-cleavable C-terminal his-tag) were set up using different commercial screens from Hampton and Qiagen. 1 μ l of protein (10 mg/ml) and 1 μ l of screen solution were mixed and incubated at 4°C and 19°C and drops checked for crystals for 30 days.

These crystallisation trials did not yield any crystals so two different approaches were tried at this point. The first approach was reductive methylation of the solvent-exposed lysine residues of the protein in solution using a modification of the method of Walter *et al*, 2006 and Rayment *et al*, 1997.^{201,202} The methylation reaction was performed overnight in 50 mM HEPES (pH 7.5), 250 mM NaCl using 1 mg/ml of protein. 20 μ l freshly prepared 1 M dimethylamine-borane complex (ABC) and 40 ml of 1 M formaldehyde were added per ml protein solution and the reactions were gently mixed and incubated at 4°C for 2 hr. A further 20 ml ABC and 40 ml formaldehyde are added and the incubation continued for 2 hr. Finally, 10 ml of ABC was added to the mixture, the reaction incubated overnight at 4°C. Precipitated protein was removed by centrifugation before purification of the soluble methylated protein by size exclusion chromatography with buffer D. Peak fractions were pooled and concentrated to 10 mg/ml and crystal screens set up as before immediately with fresh protein.²⁰¹⁻²⁰³

The second approach is cloning of additional constructs of MPP1 from other various species based on secondary structure predictions and sequence alignment of human MPP1.

2.3.2 MPP1 orthologues in other species

2.3.2.1 Sub-cloning into *E. coli* expression vectors

Protein sequences of MPP1 orthologues were aligned with the motor domain sequence of human Kif5b to define the boundaries of the motor domain, using the ClustalW2 multiple alignment program at the European Bioinformatics Institute (EBI).¹⁹⁹ Codon-optimised cDNAs encoding kinesin motor domains: *M. musculus* MPP1₁₋₄₈₉, *Rattus norvegicus* MPP1₁₋₄₉₀ and *Xenopus laevis* MPP1₁₋₅₁₈ were purchased in vector pUC57 (GenScript). The cDNAs were double restricted with *NcoI* and *XhoI* and cloned into two *E. coli* expression vectors: a modified pProExHT expression plasmid and pSUMO.

The primers for the cloning shorter constructs of MPP1 orthologues are as follows: *Mus musculus* MPP1₅₆₋₄₈₉: Forward Primer: 5'- G GCC AAT TCC CTG GGA TCC AAA AAT TAT CTG C -3'; Reverse Primer: 5' – G GTG GTG GTG CTC GAG TCA TTT TTC TTG AC -3'; *Rattus norvegicus* MPP1₅₄₋₄₉₀: Forward Primer: 5' - CCG GGT GCA AAT TCA CTG GGA TCC AAA AAC TAT CTG C - 3'; Reverse Primer: 5' - GTG GTG GTG GTG GTG CTC GAG TCA TTT TTC TTG GG - 3'; *Xenopus laevis* MPP1₁₋₄₀₉: Forward Primer: 5' – CAG GCG TGT CGT GGA TCC GAA AAA GCG AAT GGC TC - 3'; Reverse Primer: 5' – G GTG GTG CTC GAG TTA TTT TTT CTG CAC GCA CGG - 3' The constructs were verified by DNA sequencing.

Cloning of MPP1 constructs were also carried out in other vectors but, due to poor expression levels, they were not further pursued.

2.3.2.2 Study of MPP1 inhibitor using steady state ATPase assay

Steady state ATPase was measured for MPP1 motor domain from the other species in a similar way as for human MPP1. Kinetics values k_{cat} , $K_{m,ATP}$, $K_{0.5,MTs}$ and IC_{50} was analysed and interpreted as for human MPP1.

2.3.2.3 Crystallisation trials

Crystallisation trials for MPP1 constructs have been carried out under different conditions; 19°C and 4°C, with or without Mg^{2+} ATP, in presence or absence of inhibitor. Protein was used at a concentration of 10 mg/ml. Crystallisation was carried out with the same screens as for human MPP1 and checked regularly for hits up to 30 days.

2.4 Human MKLP-2

2.4.1 Sub-cloning into *E. coli* expression vectors

2.4.1.1 Cloning of MKLP-2₅₆₋₅₀₅, Δ L6 and point mutants of MKLP-2

The cDNA of human MKLP-2₅₆₋₅₀₅ and MKLP-2₅₆₋₅₀₅ Δ loop L6 were purchased in vector pUC57 (GenScript). The cDNAs were double restricted with *Nco*I and *Xho*I and cloned into two *E. coli* pET28a expression vectors. Single MKLP-2 mutants L187A (named MKLP-2^{L187A}), W356A (named MKLP-2^{W356A}) and W359A (MKLP-2^{W359A}) were introduced using the following forward and reverse primers according to the recommendations of the QuickChange kit: MKLP-2^{L187A} (Forward: 5'- G GAT GGA GGG ATT GCC CCC CGG TCC CTG - 3'; Reverse: 5' - CAG GGA CCG GGG GGC AAT CCC TCC CTC CAT CC - 3'), MKLP-2^{W356A} (Forward: 5' - GAT GCT GAG GAG GCC GCG AAG CTC CTA AAA GTG - 3'; Reverse: 5' - CAC TTT TAG GAG CTT CGC GGC CTC CTC AGC ATC - 3'); MKLP-2^{W359A} (Forward: 5'- GAG GAG GCC TGG AAG CTC GCA AAA GTG GGT CG - 3'; Reverse: 5'- CG ACC CAC TTT TGC GAG CTT CCA GGC CTC CTC - 3'). The DNA sequences were verified by sequencing.

2.4.2 Expression and purification of protein of MKLP-2 constructs

The expression plasmids were transformed into *E. coli* BL21(DE3) pLysS. 12 L of bacterial culture were grown for all the MKLP-2 constructs at 37°C in LB medium supplemented with 50 mg/ml kanamycin to an A₆₀₀ of 0.7 and induced overnight with 0.5 mM IPTG at 20°C. Cells were harvested and resuspended in lysis buffer K and then lysed by sonication using 8 sec ON and 8 sec OFF pulses. Lysates were centrifuged at 20,000 rpm for 1 h at 4°C. The supernatant was supplemented with 1 mM Mg²⁺ATP and loaded onto a 5 ml Ni-NTA HisTrap FF column for affinity chromatography. The column was previously equilibrated with buffer L and eluted with a gradient using buffer M. Protein obtained was pooled and diluted with buffer N to reduce the salt concentration for Ion Exchange Chromatography using 5 ml Hi-Trap Mono S column. The column was pre-equilibrated in buffer D and proteins eluted with a gradient in buffer O. The final step of purification involved gel filtration using Superose 16/60 S200 column where the proteins were eluted with buffer P. The protein obtained finally was pooled and concentrated on an Amicon ultrafiltration device to a final concentration of approx. 10 mg/ml and either used fresh or from frozen stock with 5% glycerol for further experiments.

2.4.3 Kinetics and inhibition measurement of MKLP-2 using steady state ATPase assay

Steady state ATPase rates were measured using the same protocol as used for Eg5 and MPP1. The amounts of MKLP-2 proteins used for the experiments were optimised at 1000 nM for basal and 40 nM for MT-stimulated activity assays. The kinetic parameters k_{cat} , $K_{m,ATP}$, and $K_{0.5, MT}$ were also obtained in the similar fashion as for Eg5 and MPP1. To measure $K_{m,ATP}$, ATP concentration was measured from 0 to 2 mM and a fixed concentration of 1 μ M MTs whereas for $K_{0.5,MT}$, MT was measured from 0 to 10 μ M and a fixed concentration of 1 mM ATP.

Inhibition of MKLP-2 wild-type and mutant by paprotrain was measured using an inhibitor concentration ranging from 0 to 150 μ M. All measurements were carried out at least in triplicate.

2.4.4 Crystallisation trials

The initial trials for crystallisation of MKLP-2 wild-type and the mutants with or without the inhibitor paprotrain (1 mM final concentration) were set up using commercial crystallisation screens from Hampton Research (PEG Ion, Natrix, Crystal Screen HT, Index) and Qiagen (JCSG+, PACT). 1 μ l of protein (10 mg/ml) and 1 μ l of screen solution were mixed and incubated at 4°C and 19°C and drops checked for crystals for 30 days.

3 Results

3.1 Analysis of ispinesib as a potent inhibitor of Eg5

While the crystal structure of the Eg5-ispinesib complex has been described in the literature,²⁰⁴ no structure of this complex has been deposited in the Protein Data Bank. There is also a lack of characterisation in the literature of ispinesib binding to Eg5 in the absence of MTs. An integrated investigation of ispinesib binding was therefore carried out using structural, biophysical and biochemical methods to understand the key determinants of ligand binding, to place the structure in the public domain²⁰⁵ and to characterise more fully the binding affinity between ispinesib and Eg5.

3.1.1 Biochemical and biophysical studies of ispinesib binding to Eg5

Ispinesib has been shown to inhibit MT-stimulated Eg5 activity with low nanomolar affinity ($IC_{50} = 2.0 \pm 0.5$ nM and $K_i^{app} \leq 10$ nM)²⁰⁵ compared to monastrol ($IC_{50} = 16$ μ M)²⁰⁶ and STLC ($IC_{50} = 140$ nM and $K_i^{app} \leq 150$ nM).¹¹⁰ It was interesting to observe whether the same holds true under basal conditions in the absence of MTs (Figure 3-1). While the IC_{50} estimate obtained for the MT-stimulated ATPase activity agrees well with the literature data, under basal condition the IC_{50} of ispinesib increases by one order of magnitude to 32.8 ± 0.1 nM (Table 3-1). Due to the higher protein concentration in the basal ATPase assay (80-100 nM compared to 5 nM in MT-simulated assay), it is not uncommon for tight binding inhibitors to appear less potent against the basal compared to the MT-stimulated ATPase activity of kinesins. Repeating the binding experiment to Eg5 by ITC according to the method of Sheth *et al*¹²⁶ (Table 3-2, Figure 3-1) shows that even in the absence of MTs, ispinesib is a tight binding Eg5 ligand ($K_d \leq 10$ nM), in agreement with the data obtained previously¹²⁶.

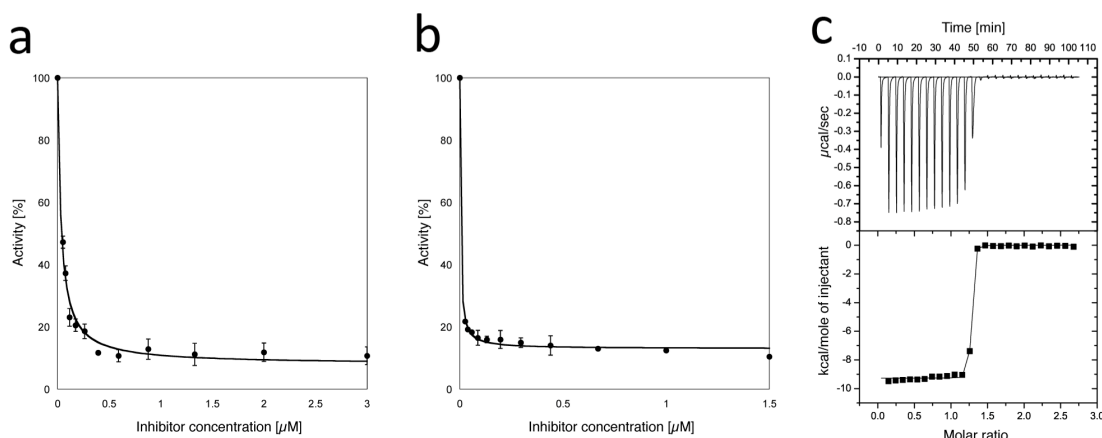


Figure 3-1: Characterisation of Eg5 inhibition by ispinesib.

Inhibition of the a) basal and b) MT-stimulated ATPase activity of Eg5. c) Raw (top) and integrated (bottom) ITC data demonstrating saturable exothermic evolution of heat upon sequential additions of ispinesib to Eg5.

Table 3-1: Inhibition of the Eg5 ATPase activity by ispinesib.

	Basal	MT-stimulated
IC ₅₀ (nM)	38.0 \pm 0.5	3.0 \pm 0.4
Eg5 concentration used (nM)	80 - 100	5

Table 3-2: Thermodynamic data for binding of ispinesib to Eg5-ADP.

Due to the tight binding of ispinesib, the measured apparent K_d can only be treated as an upper limit.

N (stoichiometry)	K_d^{app} (nM)	ΔH (kcal/mol)	$T\Delta S^{app}$ (kcal/mol)
1.270 \pm 0.003	≤ 10	-9.08 \pm 0.04	2.81 \pm 0.23

3.1.2 Structural analysis of Eg5-ispinesib complex

The structure of the Eg5-ispinesib complex was solved at 2.6 Å and refined to an R_{free} of 25.3% with four protein molecules in the asymmetric unit (AU). The four independent complexes in the AU are mostly similar, with pairwise superpositions giving r.m.s.

deviations around 0.6 Å for ≈ 300 C α atoms when chain A, C and D is compared to chain B. Differences did exist between the independent molecules with 15–17 residues at the N-terminus and 2–9 residues at the C-terminal of Eg5_{1–368} being disordered, as are a number of loops. In particular electron density for loops L10 and L11 (Figure 3-2) is absent from all four molecules. The moderate resolution of the data suggested the use of non-crystallographic symmetry (NCS) restraints to increase the observation : parameter ratio but application of 4-fold NCS led to a significant rise in R_{free} so were not used. The rest of the discussion of the Eg5-ispinesib complex is based on chain B unless stated otherwise stated as this chain is structurally more ordered with more electron density visible.

The structure conforms to the canonical structures of the kinesin motor domain fold with an eight-stranded β -sheet sandwiched between three major α -helices on either side (Figure 3-2 a,b). One molecule of Mg²⁺ADP is bound in the nucleotide binding pocket with the magnesium coordinated by the β -phosphate, the hydroxyl side-chain oxygen of Thr112 and three water molecules, resulting in the classic octahedral coordination geometry observed with magnesium. One of the coordination sites is unoccupied and in other high-resolution kinesin structures,¹¹⁴ a water molecule occupies this position. It could be anticipated that with higher resolution data the water molecule would become apparent in the electron density. Ispinesib occupies the inhibitor-binding pocket formed by helix $\alpha 2$, loop L5 and helix $\alpha 3$ (Figure 3-2a).

Comparison with Eg5 structure without a bound inhibitor (PDB id 1II6²⁸) shows that the region around the inhibitor-binding pocket undergoes major conformational changes on ispinesib binding. Additional changes extend towards the other end of the motor domain bringing about larger conformational changes at the switch II cluster (helix $\alpha 4$, loop L12 and helix $\alpha 5$) and the neck linker region¹¹³. In the present structure, all four molecules in the AU (asymmetric unit) are in the final ispinesib-bound state. Helix $\alpha 4$ rotates and moves by around 7 Å in the inhibitor bound state compared to the native structure. The anti-clockwise rotation and shift of helix $\alpha 4$ rearranges the switch II cluster and opens up space enabling the neck linker to dock to the motor domain locking the conformation of the motor domain and slowing the movement of kinesin along the MT track (Figure 3-2 b,c). This shows that ispinesib brings about structural changes in the Eg5 catalytic domain, in agreement with other structures of Eg5 inhibitor complexes where the inhibitor binds to the same allosteric site.¹¹⁹

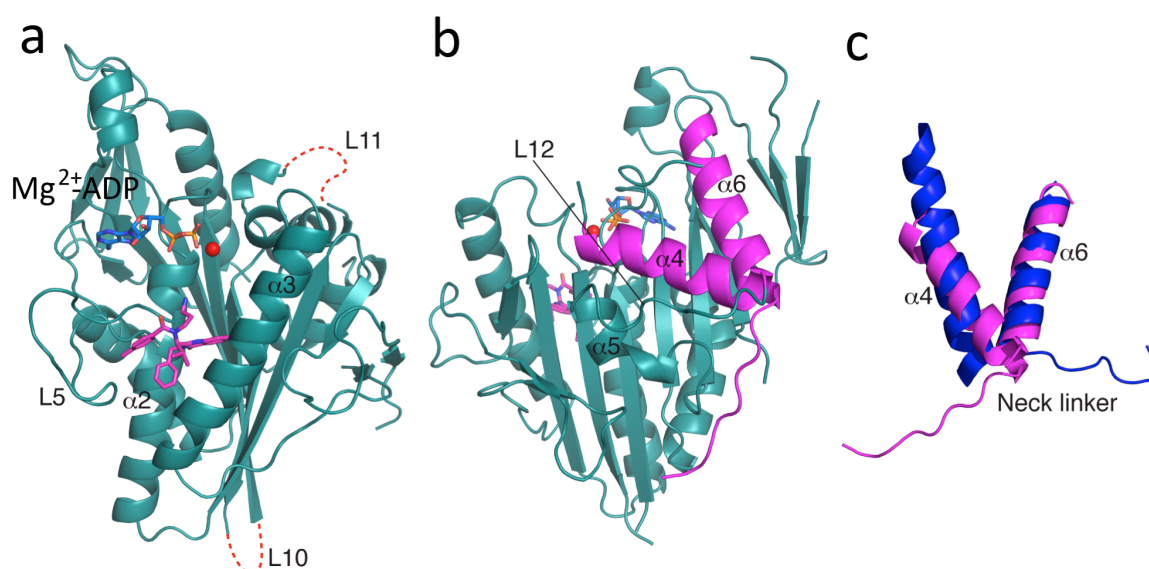


Figure 3-2: Overall structure of the ADP-Eg5-ispinesib ternary complex (chain B).

a) Front view of the Eg5 motor domain in complex with Mg^{2+} (red), ADP (blue) and ispinesib (magenta). Red dotted lines indicate the locations of the disordered loops L10 and L11, selected secondary structure elements and loops are labelled. b) Back view of the Eg5 motor domain with helix $\alpha 4$ of the switch II cluster, the neck linker region as well as the preceding helix $\alpha 6$ highlighted in magenta. c) Detail view of helices $\alpha 4$ and $\alpha 6$ as well as the neck linker region of the Eg5-ispinesib complex (pink) superimposed on the apo-Eg5 structure (blue, from PDB entry 1II6²⁸).

3.1.2.1 Twinning and pseudotranslational symmetry

One bottleneck in solving the Eg5-ispinesib complex structure was the intrinsic problem of twinning and pseudotranslational symmetry with the crystal formation. For this several data sets were collected from Eg5-ADP-ispinesib complex crystals, most of which could not be processed with any commonly used software. The data presented here can be indexed, processed and scaled in primitive orthorhombic, C-centred monoclinic and primitive monoclinic space groups. Structure solution in orthorhombic and C-centred monoclinic space groups by molecular replacement in these space groups is possible, yielding reasonable models initially. However, refinement of all but one of these solutions subsequently fails, either because R-values cannot be decreased or because model completion requires unavoidable clashes or otherwise impossible molecular arrangements. This narrowed the choice of the lattice symmetry to primitive monoclinic. Molecular replacement gave a plausible solution in $P2_1$ with all three permutations of cell axis, indicative of pseudosymmetry and not unexpected given the reasonable scaling statistics of the higher symmetric orthorhombic solution. Two of the three cell choices allow for model improvement through iterative refinement, while the third one is yet again unrefinable. Inspection of the symmetry relationships between protein molecules in

the $P2_1$ -refined models reveals three orthogonal two-fold symmetry axes, two of which could individually function as crystallographic symmetry elements, while the third one has a screw component of ≈ 0.38 , and as such provides only non-crystallographic symmetry. These findings provide an explanation to the lack of refinement for the various orthorhombic models as well as one of the three $P2_1$ axis choices.

In addition, the $P2_1$ model(s) exhibit pure translational (non-crystallographic) symmetry based on the Patterson function revealing a significant off-origin peak (32.31%) of the origin peak that almost, but not quite, mimics a face-centering operation, explaining why scaling and molecular replacement were successful in C2, but again did not yield a reasonable model. In addition to this the Eg5-ispinesib complex crystals suffers from pseudo-merohedral twinning, as suggested by Britton plot²⁰⁷, H-test²⁰⁸ as well as RvR plot²⁰⁹ and supported by a significant drop in R/Rfree of over 7% when switching from untwinned to twin refinement in PHENIX, with the twin law a twofold axis orthogonal to the crystallographic symmetry axis and a twin fraction around 0.4.

Both translational non-crystallographic symmetry and twinning complicate structure solution and even for the valid cell choices similar, refinable, but non-equivalent models were obtained from molecular replacement. The final structure was selected based on refinement statistics, crystallographic packing and precedent for this cell choice and packing in the PDB in entry 2GM1²², the protein component of which was subsequently used as a search model for molecular replacement.

3.1.3 Comparison of ispinisib binding to Eg5 and comparison with other allosteric inhibitors

Ispinesib is buried in the allosteric site and displays numerous interactions with residues of the inhibitor-binding pocket²⁰⁴. At the resolution obtained for our structure (2.6 Å) we did not observe any ordered water molecules in close proximity to the inhibitor. The benzyl moiety of the ligand is buried deeply in the hydrophobic part of the pocket where it stacks with the Pro137 ring and has an edge-to-face interaction with the side-chain of Trp127, as well as hydrophobic interactions with the side chains of Tyr211 and Leu214. In addition the benzyl group also forms an intramolecular edge-to-face stacking interaction with the inhibitor's p-toluyyl moiety, which in turn stacks extensively with the

mostly flat protein backbone of Glu118/Arg119, and also interacts with parts of the side chains of Arg119, Trp127 and Asp130. The isopropyl group of ispinesib is only partly buried between the side chains of Tyr211 and Leu214 as well as the backbone of the latter residue and Glu215. The chlorine substituent of the 7-chloro-3,4-dihydro-4-oxo-3-(phenylmethyl)-2-quinazolinyl sits in another mostly hydrophobic pocket formed by the backbone of Gly217 and the side chains of Leu160, Leu171 and Arg221. In three of the four chains (B/C/D) the primary amine of ispinesib is oriented towards the ADP binding site, and while it is mostly solvent exposed, the amine can interact favourably with the anionic Glu116 side-chain. In chain A on the other hand the aminopropyl moiety is disordered. Taken together, the intrinsic flexibility of the aminopropyl group, together with the observed conformational variability and a mostly solvent exposed position suggests that this functional group is less important for the binding of ispinesib to Eg5 than for other Eg5-targeting compounds which also contain this primary amine. This is further underlined by STLC and related analogues: in this case the primary amine is absolutely essential for Eg5 inhibition²¹⁰ and the analogue with the tertiary amine completely abolishes inhibition whereas the tertiary amine in ispinesib is still capable of inhibiting Eg5 in the low nanomolar range²¹¹. It is remarkable that, aside from the salt bridge between this primary amine and the Glu116 carboxylate, ispinesib makes exclusively hydrophobic interactions with the protein. In this context it is particularly noteworthy that the carbonyl oxygen group of the quinazolin-4-one ring system is buried in a hydrophobic pocket having least possibility for its hydrogen bonding potential. While several potential weak C-H—O hydrogen bonds are likely to at least partially compensate for this; the replacement of this group with a similarly sized hydrophobic group should provide improvements to Eg5 binding, though these modifications would have to be carefully balanced with drug-like properties (Figure 3-3a).

While the unavailability of coordinates/structure factors precludes a detailed analysis, it was thought to be informative to compare our structure to the previously published Eg5-ispinesib complex²⁰⁴. Overall the two models adopt a similar 'final state' conformation, though the previous structure exhibits a number of features that are unusual among the published Eg5 structures and not replicated by our model. Specifically, the helices between $\beta 1$ and $\beta 1a$, as well as parts of the central β -sheet around $\beta 6/\beta 7$ are shifted significantly with respect to the present complex structure. Additionally, loop 11 is ordered in the former structure, while in essentially all other Eg5 complex structures it is

disordered. Zhang *et al.* suggest that these differences from the 'canonical' Eg5 conformation are due to crystal contacts, which is likely given their unique unit cell dimensions and is furthermore compatible with these features being absent from the present structure. Based on the discussion and figures provided by Zhang *et al.*, the conformation and binding mode of ispinesib appears to be virtually identical between the two structures, down to the orientation of the flexible aminopropyl group.

To further investigate the binding mode of ispinesib, we compared the structure of ispinesib-bound Eg5 with the Eg5 complex structures of two other related inhibitors, the pyrrolotriazin-4-one-based 'compound 24' (PDB ID: 2GM1¹²⁰) as well as MK-0731 (PDB ID: 2CJO¹¹⁹) (Figure 3-3).

Aside from the differences in the core ring system, 'compound 24' is virtually identical to ispinesib and it is thus not surprising that the two molecules adopt similar binding modes, with the benzyl, the p-toluyyl and the aminopropyl groups all adopting consistent conformations and making equivalent interactions with the protein. The most significant difference between these two compounds lies in the different attachment of the chlorine substituent to the core ring system, partly necessitated by the change from a quinazolinone (ispinesib) to a pyrrolotriazinone (compound 24). While the chlorine of ispinesib makes its closest contacts with the Leu160 side-chain and the backbone of Gly217, the chlorine of compound 24 points deeper into the binding pocket (the angle between the two C–Cl bonds after superposition is $\approx 104^\circ$) where it interacts predominantly with the side chains of Ile136 and Phe239. Given that the almost perfect alignment of the two core ring systems after superposition of the two complex structures on the protein component supports a lack of excessive strain due to the presence of either chlorine, thus might suggest that either compound could be improved in Eg5 affinity by introducing additional substitutions on the benzo- and pyrrolo-ring, respectively. At the same time, compound 24 is almost two orders of magnitude less potent than Eg5 inhibitor compared to ispinesib¹²⁰, which might mean that it is compound 24 rather than ispinesib that would benefit most from such reciprocal elaboration.

While the 3-phenyl-dihydropyrrole-based MK-0731 at first glance shares few chemical features with ispinesib, a superposition of the two Eg5 complexes reveals the presence of several congruent structural elements. The difluorophenyl ring of MK-0731 takes the place of ispinesib's quinazolinone system, with one fluorine mimicking the chlorine

substituent of ispinesib and the second fluorine superimposing reasonably well with the quinazolinone oxo group, though due to the smaller size of F compared to Cl as well as the steric requirements of the rest of the molecule, MK-0731 inserts less deeply into the binding pocket than ispinesib does. The unsubstituted phenyl ring of MK-0731 binds in the general area occupied by the chemically similar benzyl and p-toluyyl groups of ispinesib. The reduced bulk and the positioning of this phenyl enable the side-chain of Arg119 to close as a lid over this part of MK-0731, enabling favourable stacking interactions not accessible to ispinesib. A feature unique to MK-0731 is the hydroxymethyl attached to the central dihydropyrrole ring. Introduced to increase polarity and thus reduce hERG binding¹¹⁹, this group can be considered as related in purpose to the aminopropyl moiety of ispinesib, but its reduced intrinsic flexibility combined with local steric hindrance makes the hydroxymethyl a potentially better choice that may inspire similar modifications in future ispinesib derivatives, though they will have to be monitored for possible phase II metabolic liabilities. Another feature unique to MK-0731 is its fluoromethylpiperidine 'side-chain'. While it does interact with the protein, this moiety is mostly solvent exposed and as such enables the modulation of physicochemical properties and thus the pharmacokinetics of the inhibitor. Despite the divergent binding features, ispinesib and MK-0731 are remarkably similar in their affinity for Eg5 (the IC_{50} of MK-0731 for MT-stimulated Eg5 is 2 nM¹¹⁹), suggesting again that 'transplanting' features may yield improved Eg5 ligands.

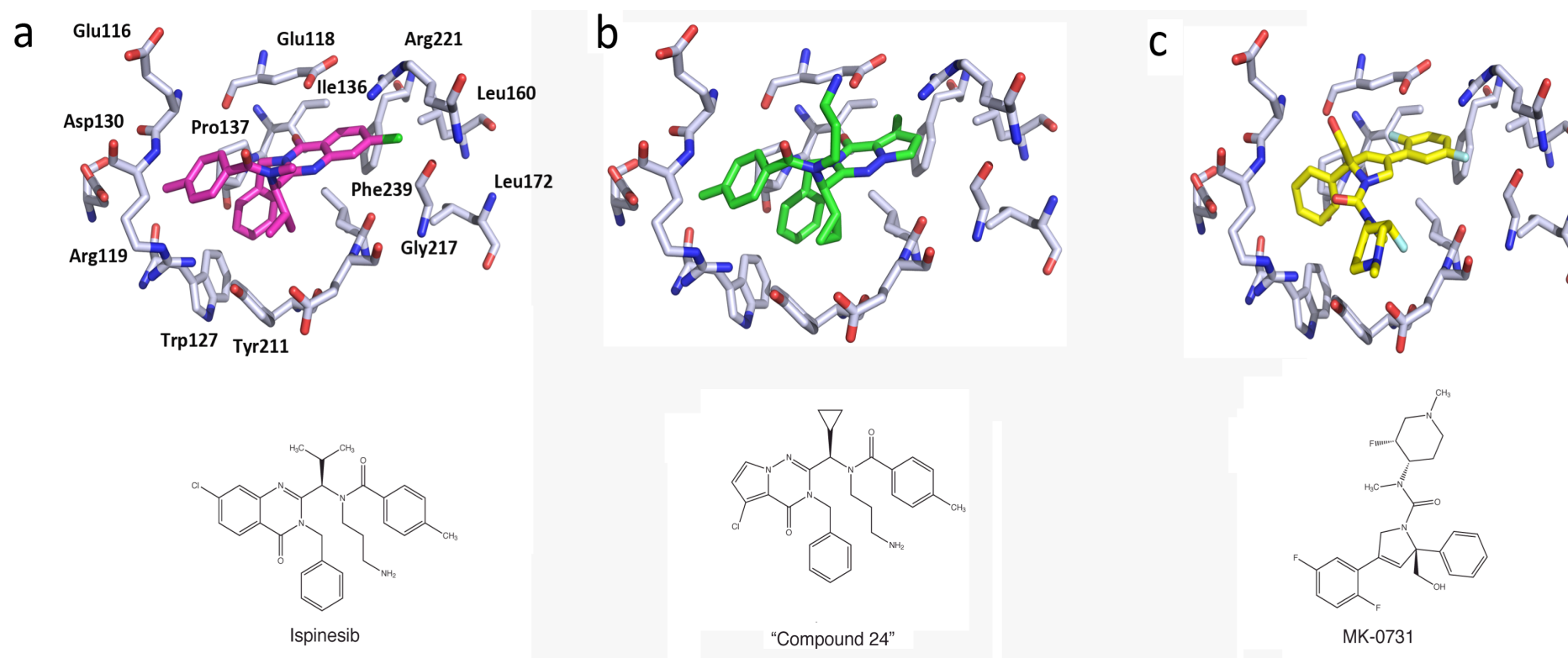


Figure 3-3: Interactions of ispinesib with the Eg5 inhibitor-binding region and comparison with other inhibitors of Eg5.

a) Chemical structure of ispinesib (left); stereo view of ispinesib (purple sticks) bound to the allosteric site of Eg5. Side chains and/or backbone atoms for interacting protein residues are shown as grey sticks and labelled, the protein surface is displayed semi-transparently. Unbiased (i.e. calculated prior to including the ligand in the model) σ A-weighted Fo-Fc electron density for the ligand contoured at 2.5σ is shown in slate. b) Chemical structure (left) and comparison of Eg5 binding mode (right) of "compound 24" (orange). c) Chemical structure (left) and comparison of Eg5 binding mode (right) of MK-0731 (orange).

3.2 Understanding the mechanism of resistance of Eg5 towards small molecule inhibitors

Therapeutic inactivation of any drug target in an actively dividing cell population creates a natural selection burden, which can lead tumour cells to evolve mechanisms of resistance. Cytokinetics demonstrated this process by selecting the ispinesib resistant colorectal tumour cell line HCT116. This resistant cell line was obtained by continuous treatment in the presence of increasing doses of ispinesib¹²⁷. Subsequent sequencing disclosed that resistance was affected by two point mutations in the loop L5 region of the Eg5 catalytic domain, D130V or A133D revealing a possible resistance mechanism for ispinesib. While these two loop L5 mutations confer resistance to ispinesib, the molecular mechanism for resistance is unknown.

To understand this I have used biochemical, biophysical and structural data to explain the development of resistance of Eg5 to potent inhibitor, SB743921. This work was carried out in collaboration with Nahoum Anthony and Simon Mackay (University of Strathclyde) and formed the experimental basis for their molecular dynamics simulations aimed at linking experimentally determined thermodynamic behaviour with structural changes at molecular level.

3.2.1 Kinetic analysis of Eg5

The kinetic parameters for the basal and MT-stimulated ATPase activity in the absence and presence of inhibitors for the two single and the double point mutations Eg5^{D130V}, Eg5^{A133D} and Eg5^{DM} (the A133D, D130V double mutant) were measured and compared with those of wild-type Eg5 (Eg5^{WT}) Figure 3-5a. The k_{cat} values for the MT-stimulated ATPase assays of the mutants show similar rates of ATP turnover to that of the wild-type Eg5 ($5.0 \pm 0.1 \text{ s}^{-1}$) with about 1.9-fold reduction for the double mutant ($2.7 \pm 0.1 \text{ s}^{-1}$). The $K_{0.5,MT}$ and $K_{M,ATP}$ values were also very similar to wild-type Eg5 with a 1.7-fold and a 1.6-fold decrease, respectively (Figure 3-5b and c). Therefore, the kinetic parameters for the MT-stimulated ATPase activity of the wild-type and Eg5 mutants display no significant differences. SB743921 inhibited MT-stimulated ATPase activity with an estimated IC_{50} of $0.14 \pm 0.001 \text{ nM}$ for Eg5^{WT}, which increases by ~4300-fold to $607 \pm 18.5 \text{ nM}$ for Eg5^{D130V} and by ~3500-fold to $484 \pm 26.9 \text{ nM}$ for Eg5^{A133D} (Figure 3-5d and e). For Eg5^{DM} mutant

there was no inhibition by SB743921 observed at a maximum inhibitor concentration of 150 μ M indicating that the mutations work synergistically rather than being additive. The same behaviour was also observed for basal ATPase assays with similar k_{cat} for the wild-type and mutant Eg5 (Figure 3-4b). $K_{\text{m,ATP}}$ increased modestly (by 3-5 fold) for the mutants compared to the wild-type but the effect of this on k_{cat} is small compared with the dramatic effects on inhibition by SB743921. For the single mutants, resistance against ispinesib increased by 10-fold whereas for the Eg5^{DM} it increased by 200-fold. We were similarly able to demonstrate that the single and double mutants fully abolish the inhibition of Eg5 by another antimitotic inhibitor STLC, indicating that these mutations not only confer resistance to SB743921, ispinesib and monastrol¹²⁶, but also to other Eg5 targeting agents.

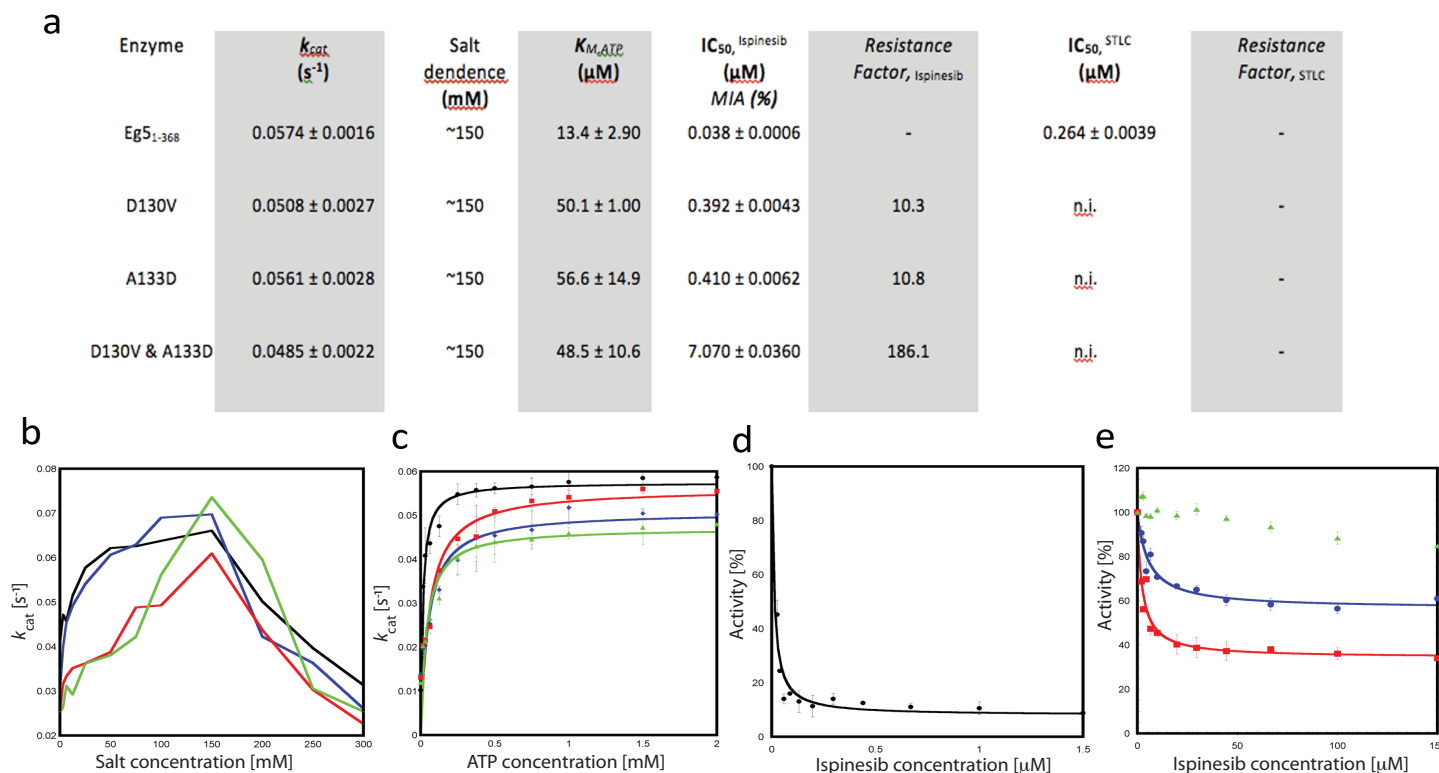


Figure 3-4: Kinetic data for wild-type and mutant Eg5 (Basal ATPase).

a) Kinetic parameters for wild-type and mutant Eg5 and inhibition of their basal ATPase activity by SB743921 and the Eg5 inhibitor STLC. The k_{cat} , $K_{0.5,MTs}$, $K_{M,ATP}$ and estimated IC_{50} values reported represent the mean \pm standard error from three experiments. The resistance factor could not be calculated because we did not observe inhibition of Eg5^{DM}. n.i.: no inhibition; MIA: maximum inhibition attained; Rf: resistance factor. b) k_{cat} and $K_{M,ATP}$ values for Eg5^{WT} (black), Eg5^{A133D} (red), Eg5^{D130V} (blue) and Eg5^{DM} (green). c) k_{cat} and $K_{0.5,MTs}$ values for Eg5^{WT} (black), Eg5^{A133D} (red), Eg5^{D130V} (blue) and Eg5^{DM} (green). d) Inhibition of Eg5^{WT} (black) by SB743921; e) Inhibition of Eg5^{D130V} (red), Eg5^{A133D} (blue) and Eg5^{DM} (green) by SB743921.

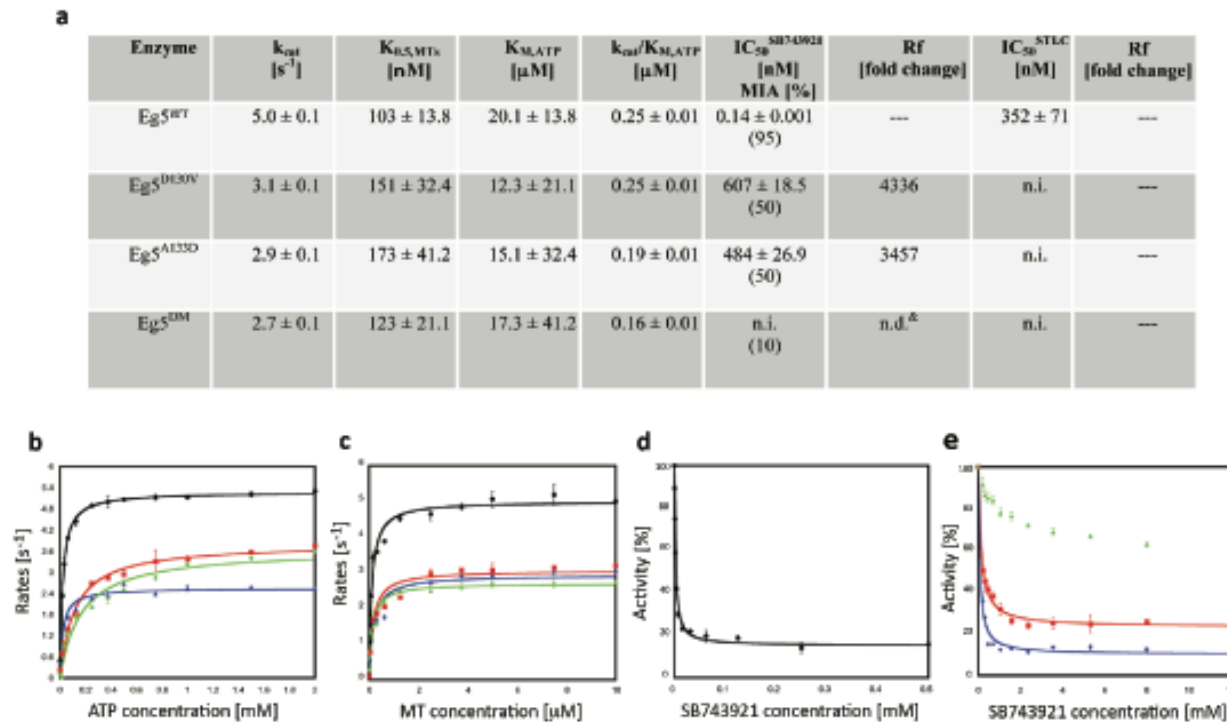


Figure 3-5: Kinetic data for wild-type and mutant Eg5 (MT-stimulated ATPase).

a) Kinetic parameters for wild-type and mutant Eg5 and inhibition of their MT-stimulated ATPase activity by SB743921 and STLC. The k_{cat} , $K_{0.5,MTS}$, $K_{M,ATP}$ and estimated IC_{50} values reported represent the mean ± standard error from three experiments. The resistance factor could not be calculated because we did not observe inhibition of Eg5^{DM}. n.i.: no inhibition; MIA: maximum inhibition attained; Rf: resistance factor. b) k_{cat} and $K_{M,ATP}$ values for Eg5^{WT} (black), Eg5^{A133D} (red), Eg5^{D130V} (blue) and Eg5^{DM} (green). c) k_{cat} and $K_{0.5,MTS}$ values for Eg5^{WT} (black), Eg5^{A133D} (red), Eg5^{D130V} (blue) and Eg5^{DM} (green). d) Inhibition of Eg5^{WT} (black) by SB743921; e) Inhibition of Eg5^{D130V} (red), Eg5^{A133D} (blue) and Eg5^{DM} (green) by SB743921.

3.2.2 Calorimetric analysis of SB743921 binding to Eg5^{WT} and mutants

To assess SB743921 binding to the wild-type and mutants using an independent method and to understand the thermodynamics of the process, we employed ITC. Figure 3-6 (a-d) shows the calorimetric titrations of SB743921 with Eg5^{WT}, Eg5^{D130V}, Eg5^{A133D} and Eg5^{DM}, respectively, whilst Figure 3-6e summarises the measured parameters of SB743921 binding. As expected in all cases the stoichiometry ≈ 1 , indicating binding of one inhibitor molecule per Eg5 catalytic domain. Analysis of the enthalpy change versus molar ratio of SB743921, revealed an apparent K_d for SB743921 of ≤ 10 nM for Eg5^{WT}, which increases considerably to 543 ± 19 nM and 778 ± 7 nM for Eg5^{D130V} and Eg5^{A133D} respectively. The affinity of SB743921 is most negligible in Eg5^{DM}, with a K_d of approximately 30.0 μ M. Consistent with the biochemical data these values show that there is a very large loss of binding affinity in the mutant enzymes.

The most striking feature of the ITC interpretation is the thermodynamics of binding, which is distinctive for the Eg5^{WT} and the mutants' complexes with SB743921. The ranking of binding free energy (ΔG) for each compound replicates the order of the biochemically-determined IC₅₀ values for SB743921, but computing thermodynamic enthalpic and entropic contributions suggests that the forces driving the binding processes are quite different. Mutants binding to SB743921 have enthalpic contributions that are more favourable than the wild-type, particularly for the single point mutations. This provides evidence that, despite favourable interactions with the protein, a high degree of order is imposed by ligand binding in an extreme example of entropy/enthalpy compensation. This results in a lower overall ΔG and weaker binding. This is mirrored in the molecular dynamics simulations studies carried out by our collaborators, Dr. Nahoum Anthony and Prof. Simon Mackay, University of Strathclyde.

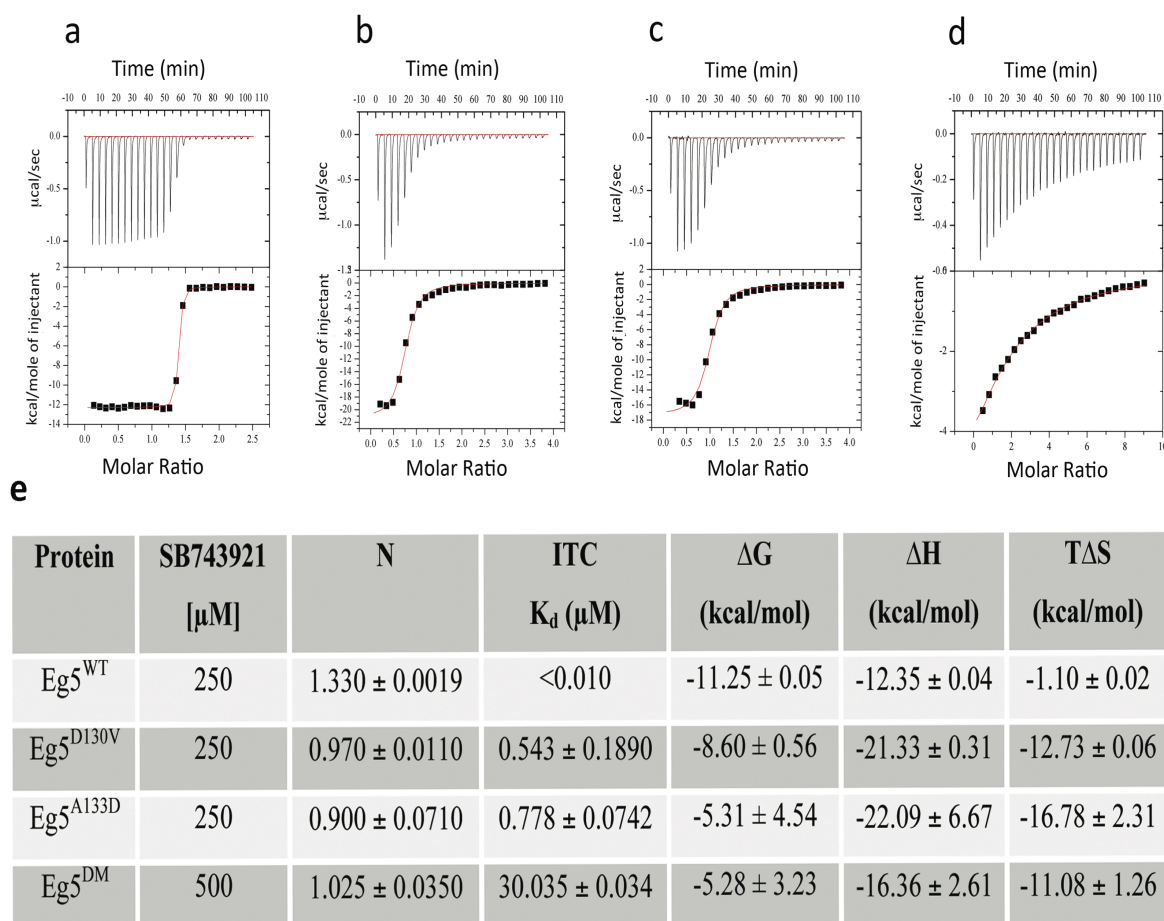


Figure 3-6: ITC analyses of SB743921 binding to wild-type and mutant Eg5.

Raw (upper panels) and normalised ITC data for titrations plotted versus the molar ratio of inhibitor/protein (lower panels) demonstrating saturable exothermic evolution of heat upon sequential additions of SB743921 to a) Eg5^{WT} , b) $\text{Eg5}^{\text{D130V}}$, c) $\text{Eg5}^{\text{A133D}}$ at 250 μM and d) Eg5^{DM} at 500 μM . Data analysis using Origin 5.0 software indicates that the binding data fit well to a single binding site model. e) Thermodynamic parameters extracted from the calorimetric evaluation of wild-type or mutant Eg5 titrated with SB743921. Experiments were performed at least in duplicate at 25°C.

3.2.3 Evaluation of $\text{Eg5}^{\text{D130V}}$, $\text{Eg5}^{\text{A133D}}$ and Eg5^{DM} structures and comparison to Eg5^{WT}

The crystal structures of the mutants were compared with wild-type Eg5 (Eg5^{WT}) (PDB ID: 1II6²⁸), which crystallised with two molecules in the AU. In the binary Eg5^{WT} -ADP complex²⁸, Asp130 and Ala133 are located at the apex of loop L5. The carboxylic acid group of the Asp130 side-chain forms hydrogen bond interactions with the main-chain nitrogen atom of Leu132 (2.55 Å) (Figure 3-7a). Ala133 is the last residue preceding the second half of the interrupted helix $\alpha 2$. In the wild-type structure, the C β -atom of the Ala133 side-chain occupies a small cavity bordered by the side chains of Tyr211 and

Asp130 and the carbonyl main-chain oxygen of Glu129. The hydroxyl or Tyr211 and carboxylate of Glu129 do not appear to hydrogen bond directly to other residues in the protein (Figure 3-7b). In summary, whereas the side-chain of Asp130 seems to play a more structural role by stabilising loop L5, the side-chain of Ala133 does not. All the above analysis is based on molecule A that has better-ordered electron density.

In the Eg5^{D130V}-ADP complex a negatively charged carboxylic acid side-chain is replaced by a hydrophobic isopropyl group (Figure 3-7c). Therefore, the hydrogen bond interactions with Arg119 and Leu132 are no longer present and cannot contribute to the stabilisation of the loop L5 conformation. As a consequence, loop L5 seems to be more flexible, as witnessed by the absence of electron density for part of loop L5 (residues 120 to 124 in molecule A and residues 120 to 125 in molecule B), which could not be completely built. Despite the introduction of this mutation and the loss of hydrogen bonding network associated with the wild-type carboxylate, there are no significant changes to the overall or local structure in the loop L5 region, when compared to Eg5^{WT}.

In the Eg5^{A133D}-ADP complex, replacement of a hydrophobic methyl side-chain with a carboxylate enables a new hydrogen bond to form with the Tyr211 hydroxyl group. Interestingly, the carboxylic acid group of Glu129 sits adjacent to that of Asp133, which implies one of the carboxylates must be in the protonated form to sit so closely (3.10 Å apart) and form a hydrogen bond. These new hydrogen bonds contribute to the stabilisation of the interrupted helix $\alpha 2$ regions at the start and end of loop L5 (Figure 3-7d), although loop L5 itself is disordered and mostly absent (in common with Eg5^{D130V}). Overall, the crystal structure remains essentially unchanged when compared to Eg5^{WT}.

Finally, in the Eg5^{DM}-ADP complex the hydrogen bond between the Asp133 carboxylate and the hydroxyl group of Tyr211 seen in the single mutant is present, although the absence of Glu129 through disorder suggests that the hydrogen bonding with Asp133 is lost. Val130 appears to occupy a similar environment to the single mutant. The conformation of residues 125-129 in Loop L5 is quite different to the wild-type, but this can be attributed to crystal contacts induced through the presence of cadmium in the crystallisation buffer. Overall, there are no significant structural changes in the motor domain of the double mutant compared with Eg5^{WT}.

Without exception, the r.m.s. differences between molecules A and B of the AU of the same crystal form are larger than the differences between molecules of wild-type and mutant Eg5, which suggests structural changes arising from mutation are minimal (Table 3-3). Furthermore, the mutations do not alter the conformation of the switch II cluster (helix $\alpha 4$, loop L12, helix $\alpha 5$), which remains in the so called “obstructive” or “down” position seen in the Eg5^{WT}. Similarly, the neck linker region is undocked and structured in all cases. In addition, there is little structural impact on the overall integrity of the kinesin motor, which explains why they continue to function normally with similar catalytic parameters as determined in the biochemical studies. Having corroborated structure with catalytic function in the unbound wild-type and mutated proteins, we next solved the structures of the Eg5^{WT}-SB743921 and Eg5^{A133D}-SB743921 complexes.

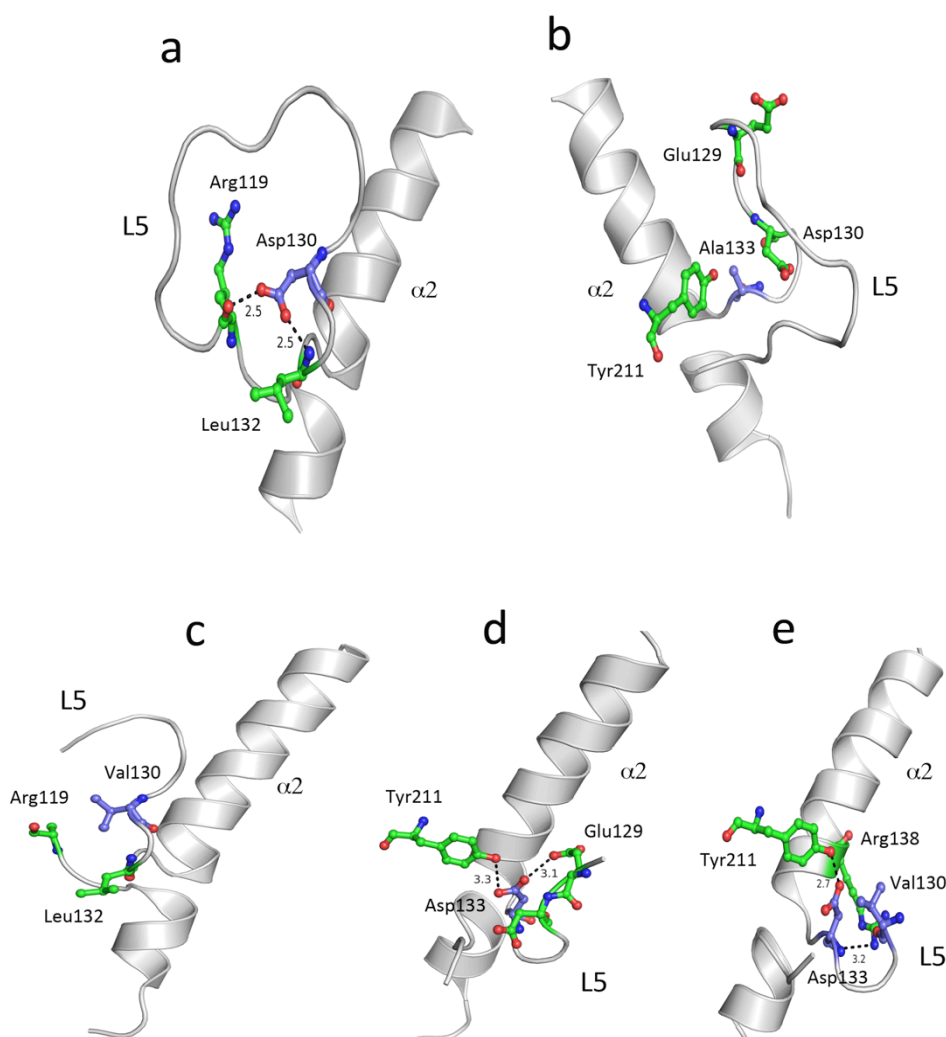


Figure 3-7: Loop L5 region of Eg5^{WT} in comparison with Eg5 mutants.

a) Loop L5 region of Eg5^{WT} showing the interactions between the carboxylate group of Asp130 with Arg119 and Leu132. b) Loop L5 region of Eg5^{WT} showing the local residues close to Ala133, which occupies a small cavity bordered by side chains of Tyr211 and Asp130 and the backbone of Glu129. c) Loop L5 region of Eg5^{D130V} showing that the hydrogen bond interactions are lost when the carboxylate side-chain is changed to an isopropyl group. The loop becomes more flexible and cannot be resolved as a consequence. d) Loop L5 region of Eg5^{A133D} showing the hydrogen bond interactions formed between the new carboxylate and the side chains of Tyr211 and Glu129. Although these new interactions stabilise the base of the loop at its junction with helix $\alpha 2$, the loop itself is disordered. e) Loop L5 region of Eg5^{DM} showing the location of D130V and A133D mutations. As with the single A133D mutant, Asp133 now hydrogen bonds with the side-chain of Tyr211, although the interaction with Glu129 appears to be lost, the latter residue now being disordered. The isopropyl group of Val130 can no longer form hydrogen bonds with residues in the loop, which reproduces the effect seen in the single D130V mutant.

Table 3-3: r.m.s. deviations in Å calculated for wild-type and mutant Eg5 structures.

The deviations were calculated for each molecule of the AU. N.B.: Wild-type and single mutant of Eg5 crystallise in the same space group with 2 molecules in the AU, while Eg5^{DM} contains only one molecule in the AU. Identical pairs (A-A) are coloured in blue (r.m.s.d.: 0.44 Å to 0.60 Å) and different pairs (A-B or B-A) are coloured in red (r.m.s.d.: 0.71 Å to 0.84 Å).

Coordinates	1II6 A	1II6 B	D130V A	D130V B	A133D A	A133D B	DM
1II6 A	X						
1II6 B	0.78	X					
D130V A	0.60	0.81	X				
D130V B	0.84	0.54	0.82	X			
A133D A	0.49	0.75	0.51	0.80	X		
A133D B	0.73	0.44	0.71	0.49	0.71	X	
DM	0.72	0.77	0.80	0.87	0.85	0.78	X

3.2.4 Structural determination and comparison of $Eg5^{WT}$ -SB743921 and Eg^{A133D} -SB743921 complexes

In the $Eg5^{WT}$ -SB743921 complex, the inhibitor binds in an allosteric pocket formed by helix $\alpha 2$ /loop L5/helix $\alpha 3$ (Figure 3-8a). When comparing $Eg5^{WT}$ (PDB ID: 1II6) with the $Eg5^{WT}$ -SB743921 complex, conformational changes were observed to be similar to those described for other $Eg5$ -inhibitor complexes¹¹³. One major difference was the presence of well-defined loop L11 regions visible in both molecules of the AU. Loop 11 is usually highly flexible and not defined in most of the $Eg5$ structures, but is visible in our structures due to crystal contacts with symmetry related molecules (Figure 3-8a). In the $Eg5^{WT}$ -SB743921 complex, the carboxylic acid side-chain of Asp130 forms a hydrogen bond interaction with the main-chain nitrogen of Ser120 in molecule A (2.77 Å) and with backbone nitrogen of Leu132 (3.07 Å) in molecule B stabilising the loop conformation. In the two molecules of the AU, the interactions between residues in the inhibitor-binding pocket and SB743921 are virtually identical, as are the conformations of the two SB743921 molecules (Figure 3-8b). SB743921 is buried in the allosteric site and displays a variety of key interactions with residues in the inhibitor-binding pocket (Figure 3-8c,d). The benzyl moiety (ring A) is buried deeply in the predominantly hydrophobic part of the pocket stacking onto the Pro137 ring. It is also appears to be involved in an edge-to-face interaction with the side-chain of Trp127. Tyr211 is in close proximity and completes the aromatic cluster. The benzyl ring forms an intramolecular edge-to-face interaction with the p-toluyyl ring (ring B) that occupies the part of the pocket formed by Trp127, Tyr211 and Arg119. The side chains of Asp130 and Ala133 are 4.16 Å and 5.18 Å away and unlikely to contribute to the binding of SB743921 through hydrophobic interactions at this distance. The chromen-4-one ring C sits in a pocket bordered by the main-chain carbonyl oxygen atoms of Gly217, Leu160, Leu171 and the side chains of Glu116 and Leu214. The isopropyl group does not sit near any residues. The primary amine of SB743921 and the side-chain oxygen of Glu116 are within hydrogen

bonding distance (3.15 Å). At this resolution we did not observe any water molecules in close proximity to the inhibitor.

Surprisingly, in the Eg5^{A133D}-SB743921 complex the inhibitor adopts the same overall conformation as in the complex with Eg5^{WT} and closely replicates the same contacts with the residues of the inhibitor-binding pocket (Figure 3-8e,f). Like the Eg5^{WT}-SB743921 complex, Eg5^{A133D}-SB743921 has a well-defined loop L11 region. The carboxylic acid side-chain of Asp130 forms hydrogen bond interactions with Leu132 (3.07 Å) stabilising the loop in the mutant structure as in the Eg5^{WT} complex. Interestingly, a salt bridge is formed between Glu128 and Lys207 that is not observed in Eg5^{WT} contributing towards a more compact loop region. The mutation of Ala133 to Asp leads to the carboxylate side-chain moving into the inhibitor pocket, but this is not accompanied by the side-chain of Glu129 as seen in the unbound mutant. Rather, the Glu129 side-chain is now solvent exposed, pointing away from the binding pocket. The geometry of the benzyl moiety (ring A, Figure 3-8c) appears to change with respect to the Pro137 ring and the side-chain of Trp127. Ring B (Figure 3-8c) still occupies the pocket formed by Trp127, Tyr211 and Arg119 but the aromatic rings are further apart. The chromen-4-one ring C interacts with the same pocket bordered by Gly217, Leu160, Leu171 and the side chains of Glu116 and Leu214, although the distances are slightly different compared to the Eg5^{WT}. As in the wild-type complex, the distance between the primary amine of SB743921 and the carboxylate side-chain of Glu116 (2.64 Å) is compatible with hydrogen bond formation. We observed two water molecules interacting with the inhibitor: one with the amide oxygen atom and the other with the primary amine.

One of the unique structural features for Eg5^{DM} and the inhibitor complexes is the presence of cadmium ions. Cadmium is not a physiological cation but was found to be an important ion required for crystallisation in these structures. Cadmium forms strong co-ordinations (4-6) with the side chains of Eg5 residues of the molecules in the AU and symmetry related molecules along with interactions with chloride, cobalt and calcium ions. It also has interactions with water molecules.

Having greater ionic strength than magnesium, cadmium also replaces magnesium in the catalytic site.

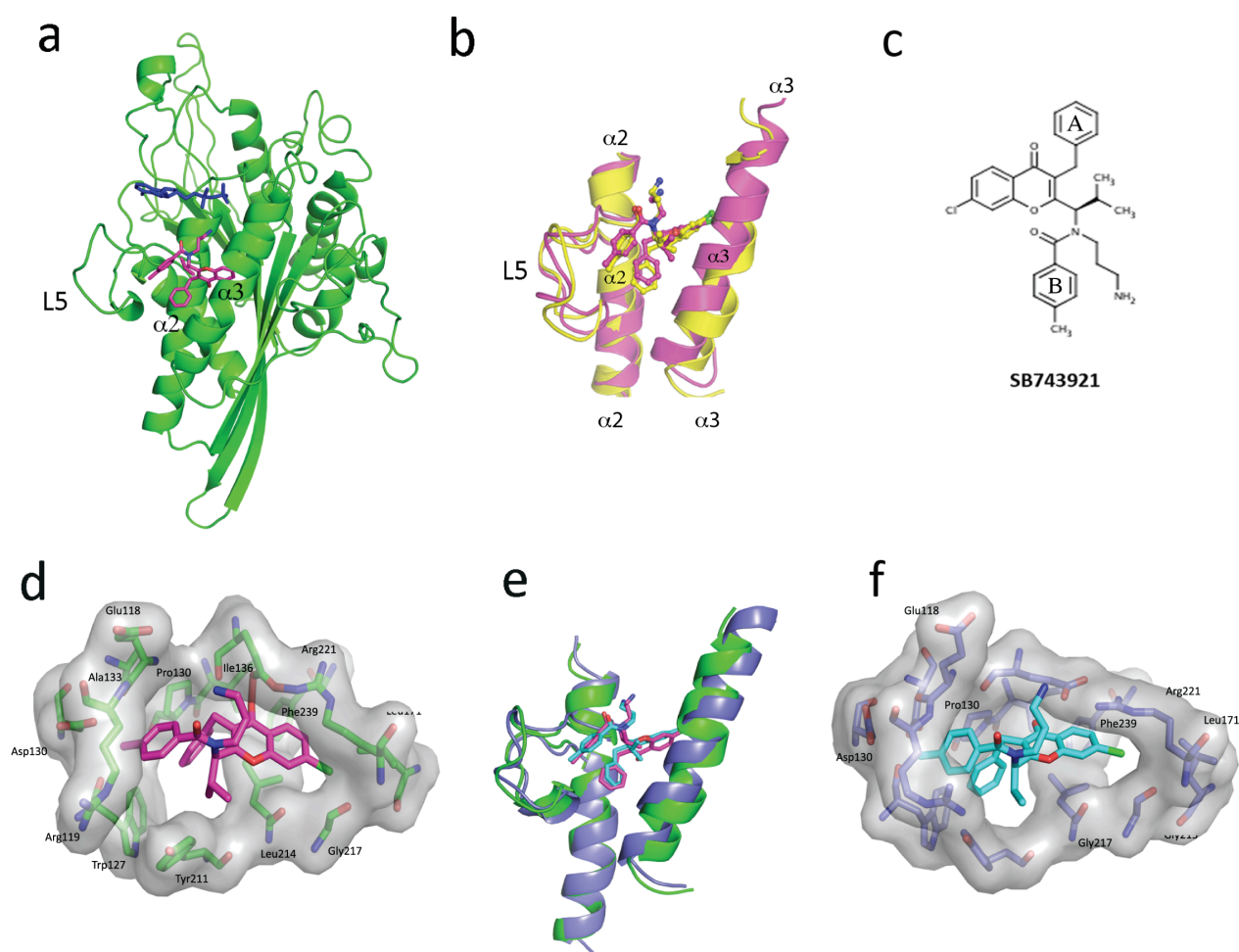


Figure 3-8: Crystal structures of wild-type and mutant Eg5 in complex with SB743921.

a) Overall structure of the Eg5 motor domain showing where SB743921 (magenta sticks) binds with respect to ADP. The inhibitor binds to the loop L5 region that interrupts helix $\alpha 2$ and is bordered by helix $\alpha 3$. b) Magnification of the allosteric binding pocket of Eg5^{WT} in molecules A and B of the AU illustrating that SB743921 has a very similar binding configuration in both complexes. c) Chemical structure of SB743921. d) View of SB743921 bound to the allosteric site of Eg5^{WT}. The inhibitor is represented in magenta, interacting residues are shown in green and the protein surface is displayed semi-transparently. e) Overlay of the allosteric site showing that SB743921 binds to Eg5^{WT} (green and magenta) and Eg5^{A133D} (navy blue and cyan) to form a very similar complex. f) View of SB743921 (cyan) bound to the allosteric site of Eg5^{A133D}. Residues forming the binding pocket are coloured in purple and the protein surface is displayed semi-transparently.

3.3 Studies on a novel allosteric inhibitor-binding pocket of Eg5

As previously mentioned, and without exception, all structurally characterised allosteric inhibitors of Eg5 target an extensively studied allosteric site about 10 Å away from the ATP binding pocket in a region formed by helix $\alpha 2$ /loop L5 and helix $\alpha 3$ ¹¹³. A significant risk of generating multiple inhibitor resistant mutations in this pocket therefore exists. Indeed, as was shown in the previous section, mutants generated by cell culture in the presence of ispinesib were also resistant to the entirely chemically unrelated STLC and monastrol series that also bind at this site. This has led towards studies aimed at identifying a new site to reduce this risk. BI8 (Benzimidazole inhibitor number 8) was among a series of new compounds first identified to bind to Eg5 motor domain in presence of ispinesib and ADP suggesting that they might bind to a completely new allosteric site.¹²⁸ The study below describes the novel inhibitor-binding pocket where BI8 binds and presents the opportunity to develop new set of inhibitors that could be used either alone or in combination with existing Eg5 compounds. Interestingly it was also observed that these inhibitors were effective against ispinesib-resistant Eg5 mutant, making structural characterisation of the ligand-protein interactions particularly valuable.

3.3.1 Kinetic studies of BI8

The benzimidazole compound BI8 (Figure 3-9a) was a potent member of a series of compound identified in 2009²¹², which binds to Eg5 in the presence of ispinesib and ADP. This suggested the existence of a previously undefined allosteric site, which remains experimentally uncharacterised.

Initially, the inhibition of basal and MT-stimulated ATPase activities of Eg5 by BI8 was measured to estimate the IC₅₀. BI8 inhibition was shown to be in the nanomolar range ($\sim 458 \pm 28.3$ nM). In addition, it was observed that MT-stimulated ATPase activity was influenced by salt; with higher the salt concentration lower was the potency of BI8. Figure 3-9 shows the IC₅₀ and salt dependent inhibition.

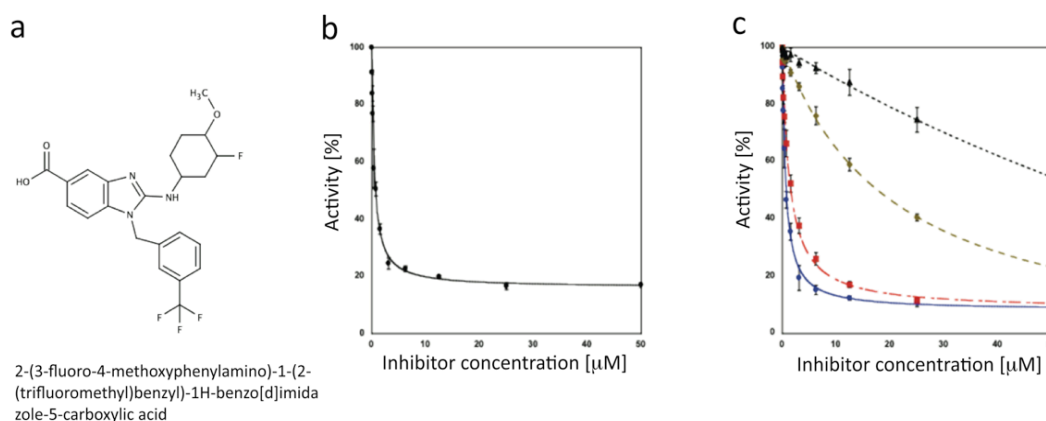


Figure 3-9: Biochemical and phenotype characterisation of the Eg5-BI8 complex.

a) Chemical structure and systematic name of the benzimidazole-based Eg5 inhibitor BI8. b) Concentration-response plots for the inhibition of the basal (left panel; $IC_{50} = 458.8 \pm 28.3$ nM) and c) MT-stimulated Eg5 ATPase activities (right panel) at 150 mM NaCl ($IC_{50} = 590.2 \pm 26.0$ nM; blue circles), 100 mM NaCl (red, $IC_{50} = 1.3026 \pm 0.1127$ μ M), 50 mM (20.993 ± 2.02 nM, olive) and without addition of salt (partial inhibition; black).

3.3.2 The crystal structure of Eg5-BI8 and comparison with the structure of Eg5-ispinesib

The crystal structure of Eg5-BI8 complex unexpectedly showed, two molecules of BI8 bound to Eg5. First molecule bound in a novel pocket and the second in a pocket partially overlapping the known ispinesib site. Electron density for the compound at both sites is well defined.

3.3.2.1 The novel Eg5 inhibitor-binding pocket for BI8 binding

The crystal structure shows that BI8 binds to a novel inhibitor-binding pocket formed by helix $\alpha 4$ of the switch II cluster, helix $\alpha 6$ preceding the neck linker region and $\beta 3$ (Figure 3-10a). The electron density map for the inhibitor is very well defined (Figure 3-10b). The electron density map for the inhibitor is very well defined with the entire molecule apparent (Figure 3-10b). The neck linker region is undocked but ordered representing the intermediate inhibitor bound state. The structural change observed is helices $\alpha 4$ and $\alpha 6$ move outwards by about 2 Å to accommodate the inhibitor (Figure 3-10c). The characteristic feature of the interaction between the inhibitor and novel binding pocket is that of an extensive

network of aromatic residues (Figure 3-10d). Tyr352 side-chain forms a face-to-face interaction with the imidazole ring and an edge-to-edge interaction with the benzyl ring of BI8, the trifluoromethyl-benzyl ring has an edge-to-edge aromatic interaction with Tyr104. Analysis of the structure using the Glide module from the Schrodinger modelling software suite identified these aromatic residues as having particularly favourable interactions with the ligand. Among other interactions, the 3-fluoro-4-methoxyphenyl group establishes a CH- π -interaction with the Leu292 side-chain ($\alpha 4$). The carboxylic acid group is solvent exposed and displays hydrogen bond interactions with structural water molecules. H-bond interactions with side chains of Arg297 and Thr300 are mediated by one of the water molecule. The solvent exposed nitrogen atom of the imidazole ring makes an interaction with one structural water molecule. The amino group of the methoxyphenyl moiety forms a hydrogen bond interaction with the hydroxyl group of Tyr104 ($\beta 3$). The 3-fluoro substituent of the methoxyphenyl group demonstrates polar interactions with the side-chain of Ile288 and the main-chain oxygen of Asn289 (both $\alpha 4$). The last observed H-bond interaction is between the methoxy group and the main-chain carbonyl oxygen of Glu270 and Asn289.

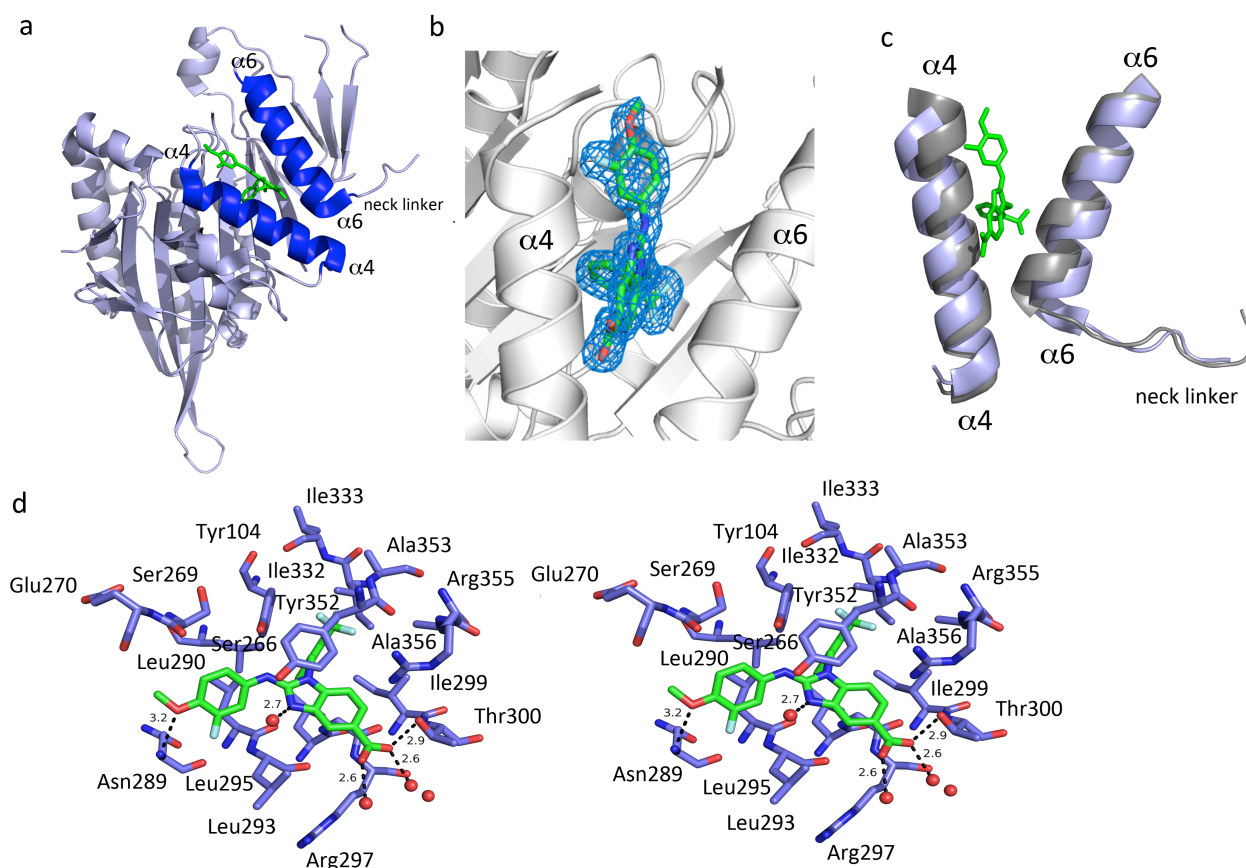


Figure 3-10: Characterisation of the novel inhibitor-binding pocket in Eg5.

a) Back view of Eg5 showing the novel allosteric binding pocket occupied by BI8 (coloured in green), formed by helix $\alpha4$ of the switch II cluster and helix $\alpha6$, preceding the neck linker. b) Electron density omit map (coloured in blue) contoured at 3σ for BI8 bound in the novel pocket. c) Conformational changes induced upon binding of BI8 in the helix $\alpha4/\alpha6$ pocket (blue), compared to native Eg5 (gray). d) Magnification of the inhibitor-binding pocket. BI8 is shown in green and residues forming the inhibitor-binding pocket are coloured in purple. Water molecules are shown as red spheres and hydrogen bond interactions are shown as dotted lines.

3.3.2.2 Analysis of the second inhibitor-binding site for BI8 and comparison with phase II clinical candidate ispinesib binding

The second pocket is formed by helices $\alpha2$ and $\alpha3$ and loops L7 and L9 (Figure 3-11a) and partially overlaps the binding site of well-characterised Eg5 inhibitors such as ispinesib (Figure 3-11b) and monastrol. Electron density for this site appeared only towards the end of the refinement and parts of the molecule, such as the methoxy group, are disordered (Figure 3-11c) suggesting either greater flexibility or lower occupancy for BI8. Although loop L5 does not seem to be directly involved in inhibitor binding it displays a new conformation that differs

from the ones described for the native Eg5 structure or the conformation described for other Eg5-inhibitor bound complexes (Figure 3-11d). Trp127, which is solvent exposed in the native Eg5 structure, moves by 7.2 Å ($C\alpha-C\alpha$) and now interacts with Asp130 (loop L5) and Glu215 ($\alpha 3$). The upper part of helix $\alpha 3$ is rotated by approximately 14° around an axis close to the apex of the helix to accommodate the inhibitor leading to a shift of about 7 Å at the top of helix $\alpha 3$ (Figure 3-11d). These radical changes on BI8 binding have not been observed previously with any other Eg5 structure and are most likely due to inhibitor binding. In contrast to the novel site, BI8 binding at this site does not demonstrate the network of aromatic interactions and this would be expected to reduce the binding energy by comparison. There are some hydrophobic interactions, notably with the side chains of Leu160 and Leu172 and also a stacking interaction between Arg221 and the methoxybenzene group of BI8. Hydrogen bonding interactions are also present with the anilinic nitrogen forming a water-mediated hydrogen bond to Ser237. The 5- carboxylic acid group of the benzimidazole moiety is solvent exposed and displays several hydrogen bonds with nearby water molecules but these water molecules do not appear to mediate interaction with the protein.

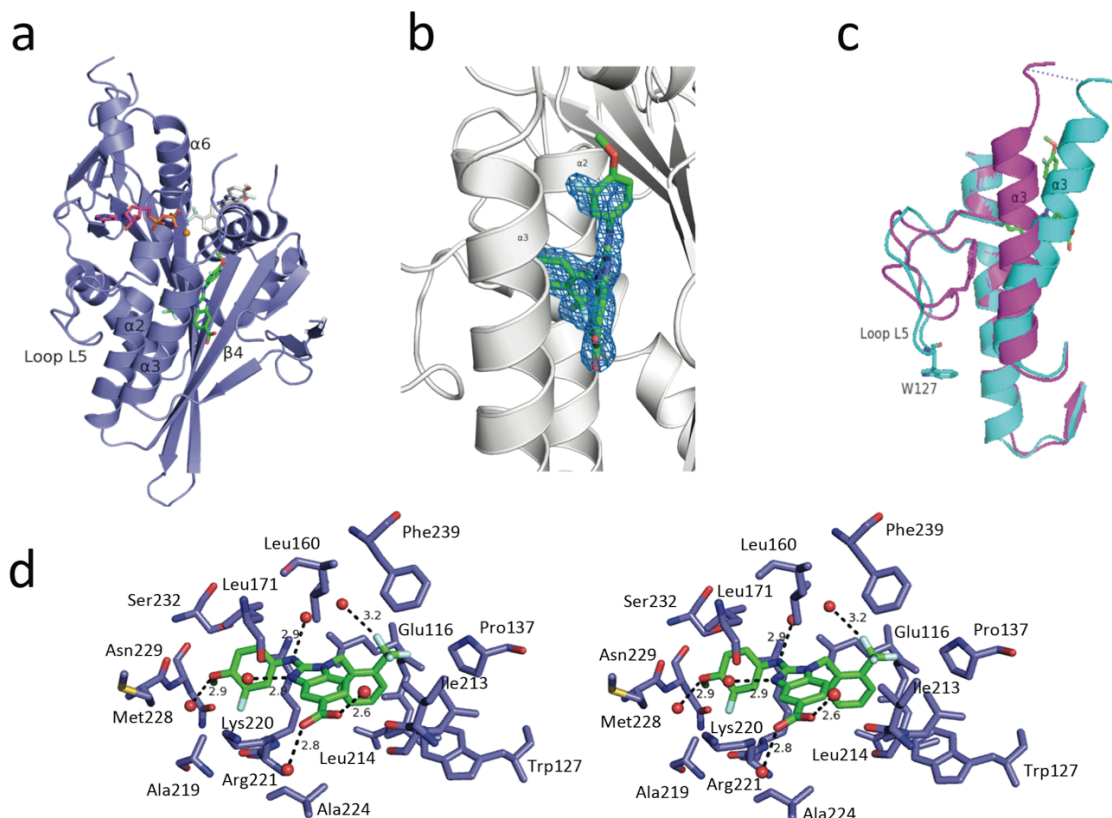


Figure 3-11: Characterisation of the second allosteric binding pocket.

a) Front view of Eg5 in complex with Mg^{2+} ADP (pink) and BI8 (green) bound in the allosteric inhibitor-binding pocket formed by helices $\alpha 2$ and $\alpha 3$ and loops L7 as well as L9. BI8 bound in the novel site is coloured in grey. b) $F_o - F_c$ omit map of BI8 bound in the inhibitor-binding pocket, contoured at 3σ (coloured in blue). The methoxy group has no density in the omit map indicating that its position is flexible. c) Binding of BI8 to the allosteric pocket leads to significant proximal structural changes in loop L5 and helix $\alpha 3$. d) Stereoplot of the magnification of the inhibitor-binding pocket showing residues involved in BI8 binding.

In the intermediate state structure, local changes at the inhibitor-binding pocket have not been transmitted along the structure to the switch II cluster and neck linker, which is trapped in the same position as in the native structure undocked and perpendicular to helix $\alpha 6$). The switch II cluster (helix $\alpha 4$ /loop L12/helix $\alpha 5$) is thought to be pivotal for force generation by translating small structural changes in the nucleotide binding pocket into larger conformational changes in the neck linker region, which is in the so called “down” or “obstructive” position. This causes the neck linker region not to dock to the motor domain that minimises its ATP hydrolysis capacity and in turn its motion.

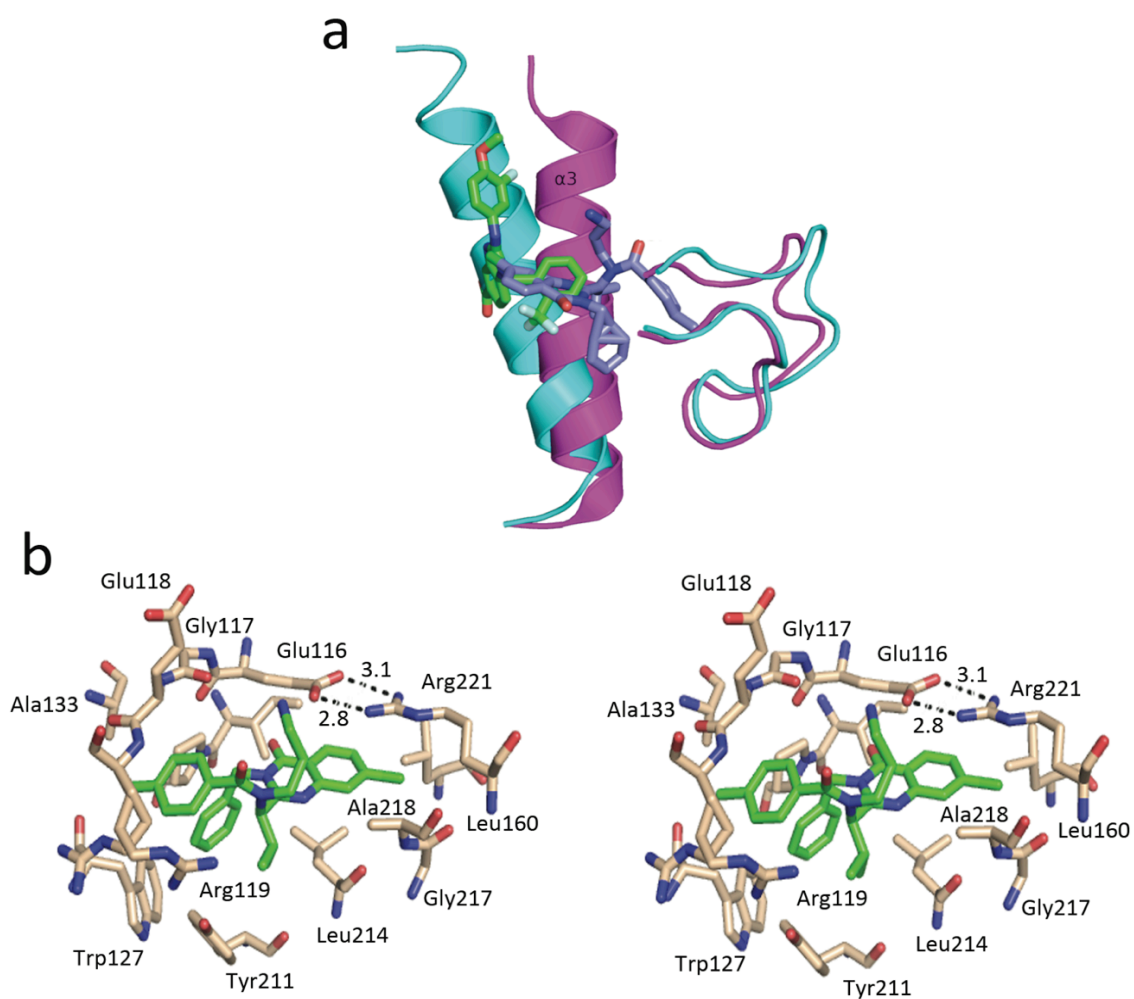


Figure 3-12: Comparison of Eg5-BI8 and Eg5-ispinesib complexes.

a) Overlay of Eg5-BI8 and Eg5-ispinesib complexes in the inhibitor-binding regions. There is a significant overlap of BI8 (blue colour) with ispinesib (shaded in green). b) Important hydrogen bonds (represented by black broken lines) within 4 Å between ispinesib (green) and Eg5 residues, and structural water molecules (represented by red spheres) are shown. Blue broken lines represents the salt bridge between Glu116 and Arg221, which stabilise the quinazoline ring of the inhibitor.

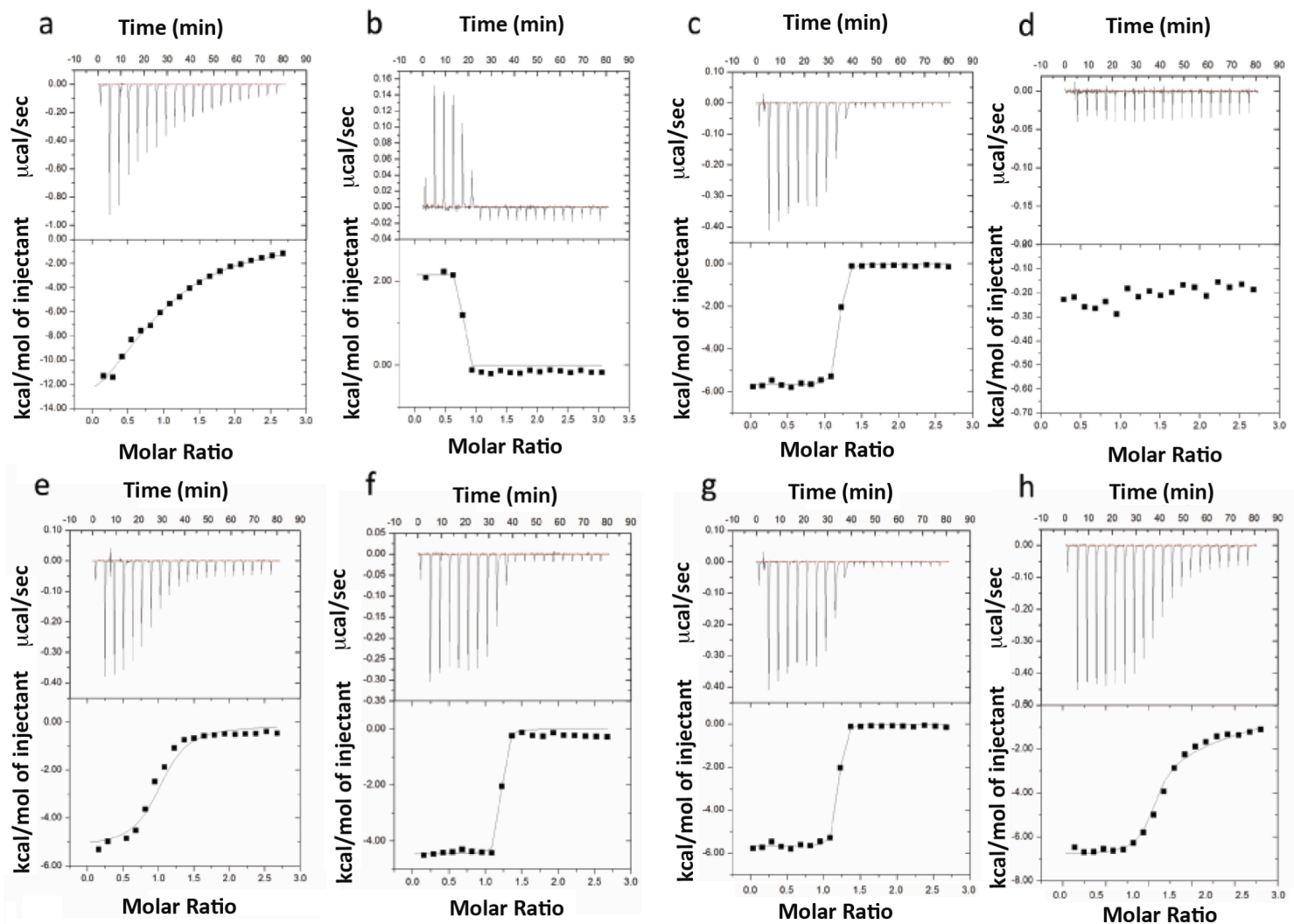
3.3.3 *Isothermal titration calorimetry*

In order to dissect the contribution made to the measured biochemical inhibition by each of the inhibitor-binding pockets, we investigated the interaction between Eg5 and BI8 using ITC competition assays. By blockading the ispinesib site using saturating concentrations of ispinesib and then titrating in BI8, the binding of BI8 to the novel pocket can be isolated and characterised thermodynamically.

Firstly, the “ispinesib blockade” method was validated by demonstrating that ispinesib could block the binding of the relatively weak inhibitor, monastrol that also binds at the ispinesib site. Ispinesib was injected into a solution of Eg5 and potent binding observed with a K_d value of $> 0.01 \mu\text{M}$ and a heat of binding of $-5.82 \pm 0.19 \text{ kcal/mol}$. Monastrol was then titrated into the ispinesib-bound Eg5 and no binding was observed, consistent with the ispinesib pocket being fully occupied and preventing the less potent monastrol binding. The reverse experiment was then carried out with monastrol being injected first. Although the K_d ($14.3 \pm 0.65 \mu\text{M}$) was higher, the heat of binding ($-15.88 \pm 0.369 \text{ kcal/mol}$) was also significantly larger than that of ispinesib. Ispinesib was then titrated into monastrol-bound Eg5 and an isotherm was observed, indicating that ispinesib was displacing monastrol. The heat of binding to the monastrol complex was endothermic ($\Delta H = 2.2 \text{ kcal/mol}$), as would be expected given the individual heats of binding (Figure 3-13). All the inhibitors bind with a ligand protein stoichiometry of 1:1.

With the blockade method validated, BI8 was injected followed by ispinesib. In contrast to the previous experiment, ITC data measured by titrating in BI8 indicate a ratio of BI8 to Eg5 of 2:1 with the data being best modelled with the sequential binding of two molecules of BI8 to Eg5 (Figure 3-13e). This two-site binding is in agreement with our novel crystal structure. The data indicate the existence of one strong ($K_d = 0.65 \pm 0.002 \mu\text{M}$) and one weaker ($K_d = 27.518 \pm 3.936 \mu\text{M}$) inhibitor-binding pocket. Subsequent injection of ispinesib to the saturated preformed Eg5-BI8 complex showed that ispinesib could bind to Eg5 with a ratio of 1:1, indicating that it can replace BI8 from one binding site only, probably the overlapping site (helix $\alpha 2$ /loop L5/helix $\alpha 3$) (Figure 3-13f).

The reverse experiment in which ispinesib was injected before BI8 showed that BI8 (Figure 3-13g) could still bind to the preformed Eg5-ispinesib complex with a binding stoichiometry of 1:1 (Figure 3-13h). The data indicate that the second allosteric binding pocket (helix $\alpha 2$ /loop L5/helix $\alpha 3$) is occupied by ispinesib, BI8 with its significantly higher K_d value cannot replace ispinesib but only can bind to the novel pocket that is still unoccupied. Since the K_d for this site corresponds moderately well to the higher affinity interactions from the titration of BI8 alone, we hypothesise that the potent binding event responsible for the observed biochemical inhibition is at the novel pocket. The stoichiometry of binding (N), K_d values, entropic and enthalpic values are represented in Figure 3-13i.



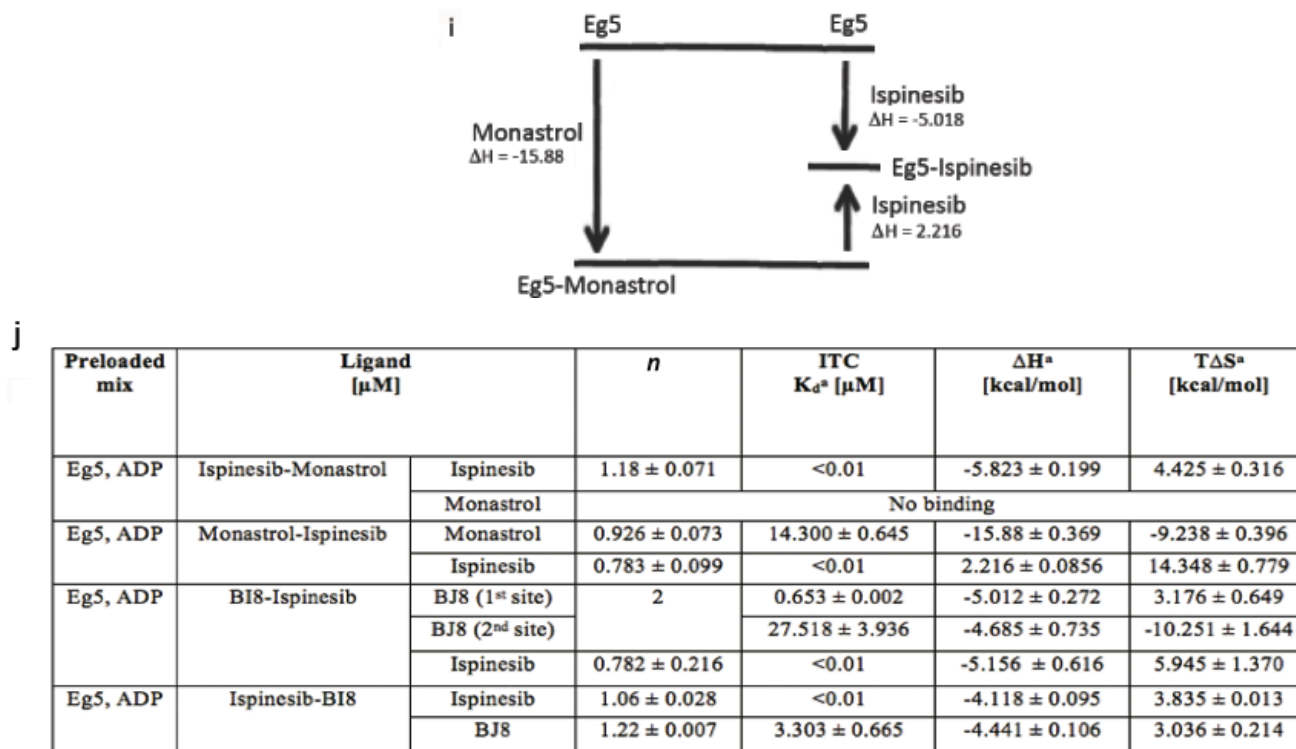


Figure 3-13: ITC analyses of ligand binding to Eg5.

Raw isothermal titration calorimetric data (upper panels) and normalised ITC data for titrations plotted versus the molar ratio of titrant/protein (lower panels) demonstrating saturable exothermic and endothermic evolution of heat upon sequential additions of a) monastrol (500 μM) and b) ispinesib (500 μM) to Eg5-monastrol complex. The reverse experiment was performed by sequential additions of c) ispinesib (500 μM) and d) monastrol (500 μM) to Eg5-ispinesib complex. Additions of e) BI8 (500 μM) followed by f) ispinesib (500 μM) to Eg5-BI8 complex. The reverse experiment with sequential additions of g) ispinesib (500 μM) and h) BI8 (500 μM) to Eg5-ispinesib complex. i) Thermodynamic cycle for ligand (ispinesib/monastrol) binding to Eg5, showing the relationship between the enthalpic changes of binding on monastrol, ispinesib and ispinesib competitively replacing monastrol from the allosteric binding site. j) Summary of ITC data for BI8 in combination with two other Eg5-specific inhibitors, ispinesib and monastrol. Data analysis indicates that the binding data fit well to a two binding site model for BI8 and a single binding site model for ispinesib.

3.3.4 SPR analysis of BI8 binding to Eg5

While the ITC data suggests that physiologically relevant binding of BI8 is at the novel site, it is not conclusive and further confirmation was required. Two site binding of BI8 was further investigated using SPR to determine the binding affinity for the novel site and if possible to dissect the two sites. This technique further provided evidence as an orthogonal method for the results already obtained from the ITC data.

3.3.4.1 Study of two site binding of BI8 to Eg5

SPR experiments were performed by an initial BI8 injection (Figure 3-14a) that allowed the measurement of steady state affinity for the two sites binding using the best-fit model that gave a K_d values of 470 nM and ~34 μ M, respectively (Figure 3-14g) comparable to the affinities estimated from ITC measurements (Figure 3-14j). A similar “ispinesib blockade” strategy to that used in the ITC experiments was then used to distinguish the binding affinity at each site. Ispinesib injection at a saturating concentration of 10 μ M (Figure 3-14c-black) after the BI8 injection competitively removes any remaining BI8 and from the mutual binding site or blocks BI8 binding to this site in the subsequent BI8 titration (helix α 2/loop L5/helix α 3). Following ispinesib injection a second BI8 injection (Figure 3-14b) allowed BI8 to bind to the new α 4/ α 6 site identified by the crystal structure. Fitting the second BI8 injection data with one site steady state affinity model demonstrates a K_d of 640 ± 9.2 nM (Figure 3-14g). To confirm that ispinesib is still bound to Eg5 during the latter BI8 injection a second single saturating ispinesib injection was performed (Figure 3-14c-red) which showed no response towards Eg5 binding proving that ispinesib was bound to Eg5 for the duration of the injections. To demonstrate the validity of the “ispinesib blockade” method in the SPR system, a similar control set-up was used for monastrol and ispinesib (Figure 3-14d-f). Monastrol binding to Eg5 was first measured (Figure 3-14d) with a K_d of 1.28 μ M (Figure 3-14j). A second ispinesib injection at 10 μ M (Figure 3-14c-black) competitively removed monastrol due to its significantly higher affinity and blocks monastrol binding during subsequent titration of monastrol. A final ispinesib

injection (Figure 3-14f-red) showed that ispinesib of the first injection remained bound to Eg5 throughout the entire run of the experiment. In summary both ITC and SPR experiments confirm the two site binding of BI8 as well as that BI8 binds to the novel $\alpha 4/\alpha 6$ site with nanomolar affinity.

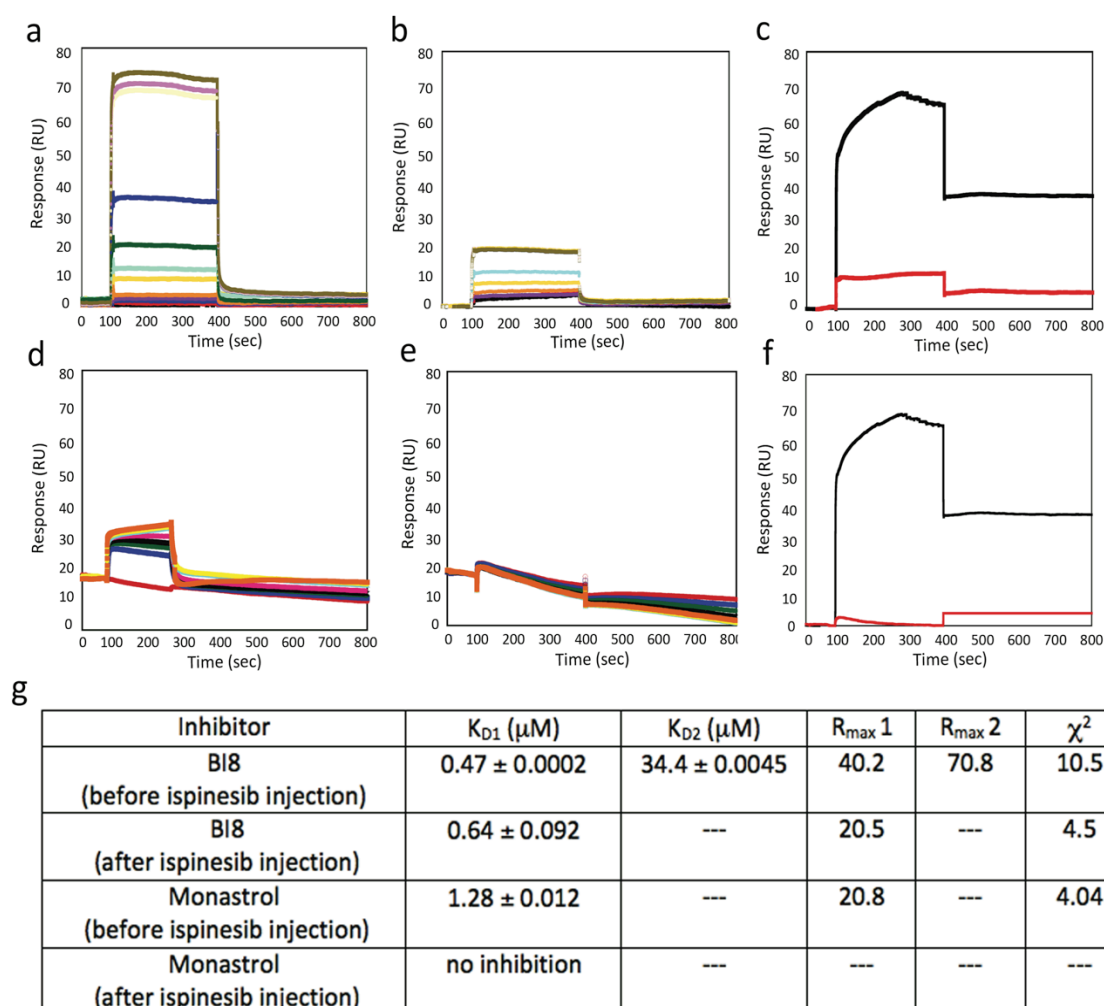


Figure 3-14: Binding studies of BI8, ispinesib and monastrol to double histidine tagged Eg5 immobilised on NTA surface.

a) SPR binding curves for various concentrations of BI8 injection from 0 to 528 μM monitored on a surface with 2000 RU of double histidine tagged Eg5. b) SPR binding curves for various concentrations of second BI8 injection from 0 to 528 μM monitored on a surface with 2000 RU of double histidine tagged Eg5 after injection of saturating concentration of ispinesib indicating BI8 binding to a novel second site. c) Ispinesib injection at 10 μM before (black) and after (red) second BI8 injection. The first ispinesib injection competitively removes BI8 from the mutual site which allows BI8 to bind only to the second novel site whereas the second ispinesib injection with low or no response confirmed that ispinesib remains bound to Eg5 through second BI8 injection. d) SPR binding curves for various concentrations of monastrol injection from 0 to 40 μM monitored on a surface with 2000 RU of double histidine tagged Eg5. e) SPR binding curves for various concentrations of second monastrol injection from 0 to 40 μM monitored on a

surface with 2000 RU of double histidine tagged Eg5 after injection of saturating concentration of ispinesib indicating monastrol cannot bind as monastrol has lower affinity than ispinesib for the same binding site. f) Ispinesib injection at 10 μ M before (black) and after (red) second BI8 injection. The first ispinesib injection competitively removes monastrol from the allosteric inhibitor-binding site thus monastrol shows no response upon second injection and second ispinesib injection with low or no response confirmed that ispinesib remains bound to Eg5 throughout second monastrol injection. The data were globally fitted using a steady state affinity model for g) 2(BI8):1(Eg5). All measurement for SPR binding were reference corrected and model for steady state binding suggested good fit with χ^2 around ≥ 10 .

3.4 MPP1

3.4.1 Human MPP1

3.4.1.1 Physodic acid discovered as an inhibitor of human mitotic kinesin MPP1

3.4.1.1.1 MPP1 expression and purification

Human MPP1 is a protein with 1781 residues. It contains a N-terminal motor domain (aa 56 to 486) with the characteristic loop L6 insertion (aa 186 to 262), a particularly long discontinuous coiled coil region (aa 568 to 1516) and a C-terminal globular domain (aa 1517 to 1780) (Figure 3-15a). Two MPP1 constructs were cloned, one coding for residues 1 to 477, which include the small N-terminal domain of unknown function (residues 1 to 56) preceding the motor domain. The second construct contained residues 57-491 that encode a protein covering the MPP1 motor domain (named MPP1₅₇₋₄₉₁) and part of the neck linker (Figure 3-15a and b). They were transformed into an *E. coli* expression vector for expression and purification and the proteins were used for further experiments. Mass spectrometry fingerprint analyses with sequence coverage of 56 % and 77 % confirmed that the two purified proteins were human MPP1. Gel filtration analysis revealed that MPP1₁₋₄₇₇ (51 kDa) and MPP1₅₇₋₄₉₁ (43 kDa) were both monomeric in solution (Figure 3-15b and c).

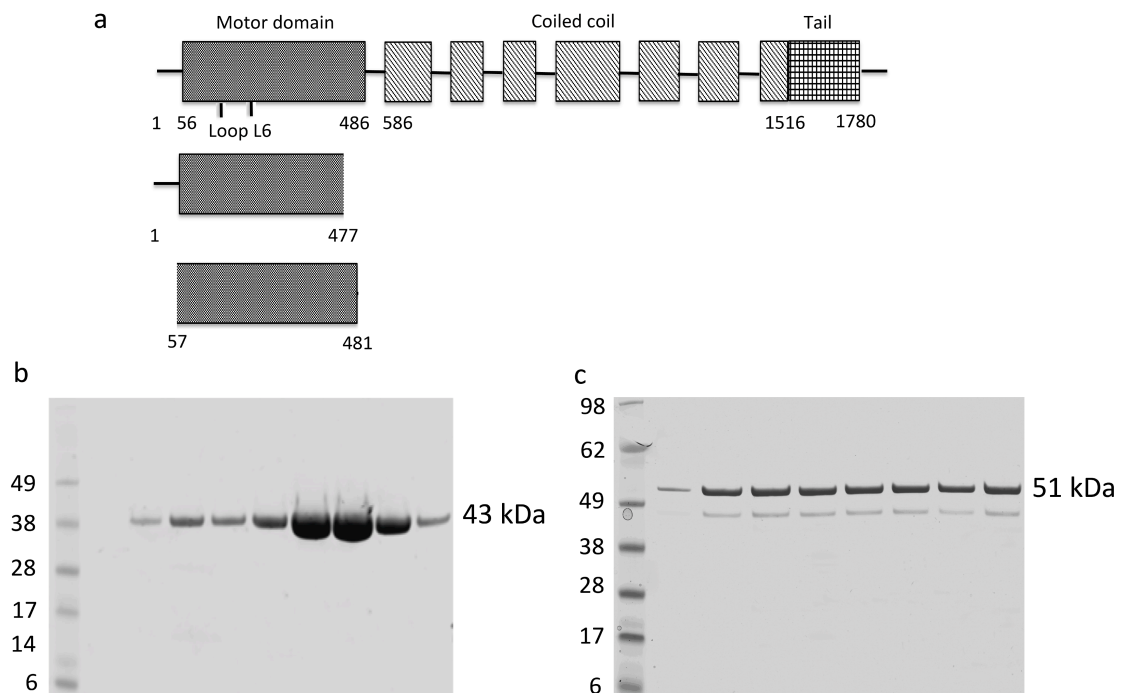


Figure 3-15: Bar diagram of full length MPP1 and two expressed MPP1 motor domains.

a) Bar diagram of human MPP1. MPP1 has a small N-terminal domain of unknown function (aa 1-56) preceding the motor domain (aa 57-486). The motor domain contains an unusually long insertion in the loop L6 region, which is unique for kinesin-6 family members, and nucleotide binding as well as MT interacting regions. The motor domain is followed by a stalk domain predicted to form a discontinuous coiled coil (aa 586-1515). The globular C-terminal domain (aa 1516-1780) contains a phosphorylation site (Thr1604) and the Pin1 interacting region. Two MPP1 constructs were used in this study: MPP1₁₋₄₇₇ covers the small N-terminal region and the motor domain, whereas MPP1₅₇₋₄₉₁ codes for the motor only. SDS-PAGE of motor protein constructs after gel filtration - b) MPP1₁₋₄₇₇ c) MPP1₅₇₋₄₉₁. Mass spectrometry confirmed both the proteins and the low percentage of degraded product that was obtained after purification of MPP1₁₋₄₇₇.

3.4.1.1.2 Steady state ATPase measurements and determination of IC_{50} values

To optimise the experimental conditions for inhibitor screening and further inhibition assays we first investigated the basic kinetic parameters of MPP1₁₋₄₇₇ and MPP1₅₇₋₄₉₁ (Table 3-4 and Figure 3-16). The salt-dependence of the basal ATPase activity by measuring the k_{cat} in the presence of increasing NaCl concentrations was determined. The activity of MPP1 was seen to decrease with increasing salt concentration indicating that the basal MPP1 ATPase activity for both proteins is best measured in the absence of salt (Figure 3-16a). The basal ATPase activity in the presence of increasing ATP concentrations, in the absence of salt, was then

determined to analyse the kinetic parameters of the MPP1 constructs. The maximum k_{cat} is $0.016 \pm 0.001 \text{ s}^{-1}$ with an $K_{\text{M,ATP}}$ of $685 \pm 16 \text{ }\mu\text{M}$ for MPP1₁₋₄₇₇ and a k_{cat} of $0.010 \pm 0.001 \text{ s}^{-1}$ with a $K_{\text{M,ATP}}$ of $128 \pm 2.1 \text{ }\mu\text{M}$ for MPP1₅₇₋₄₉₁. Subsequently, the MT-stimulated ATPase measurements led k_{cat} values of $3.1 \pm 0.2 \text{ s}^{-1}$ and $4.1 \pm 0.1 \text{ s}^{-1}$ for MPP1₁₋₄₇₇ and MPP1₅₇₋₄₉₁, respectively, corresponding to 193-fold and 410-fold stimulations compared to the basal ATPase activities. $K_{\text{M,ATP}}$ values of $44 \pm 4 \text{ }\mu\text{M}$ and $82 \pm 2 \text{ }\mu\text{M}$ (Figure 3-16c) and $K_{0.5,\text{MT}}$ values of $102 \pm 3 \text{ nM}$ and $112 \pm 1 \text{ nM}$ were determined for MPP1₁₋₄₇₇ and MPP1₅₇₋₄₉₁, respectively (Figure 3-16d).

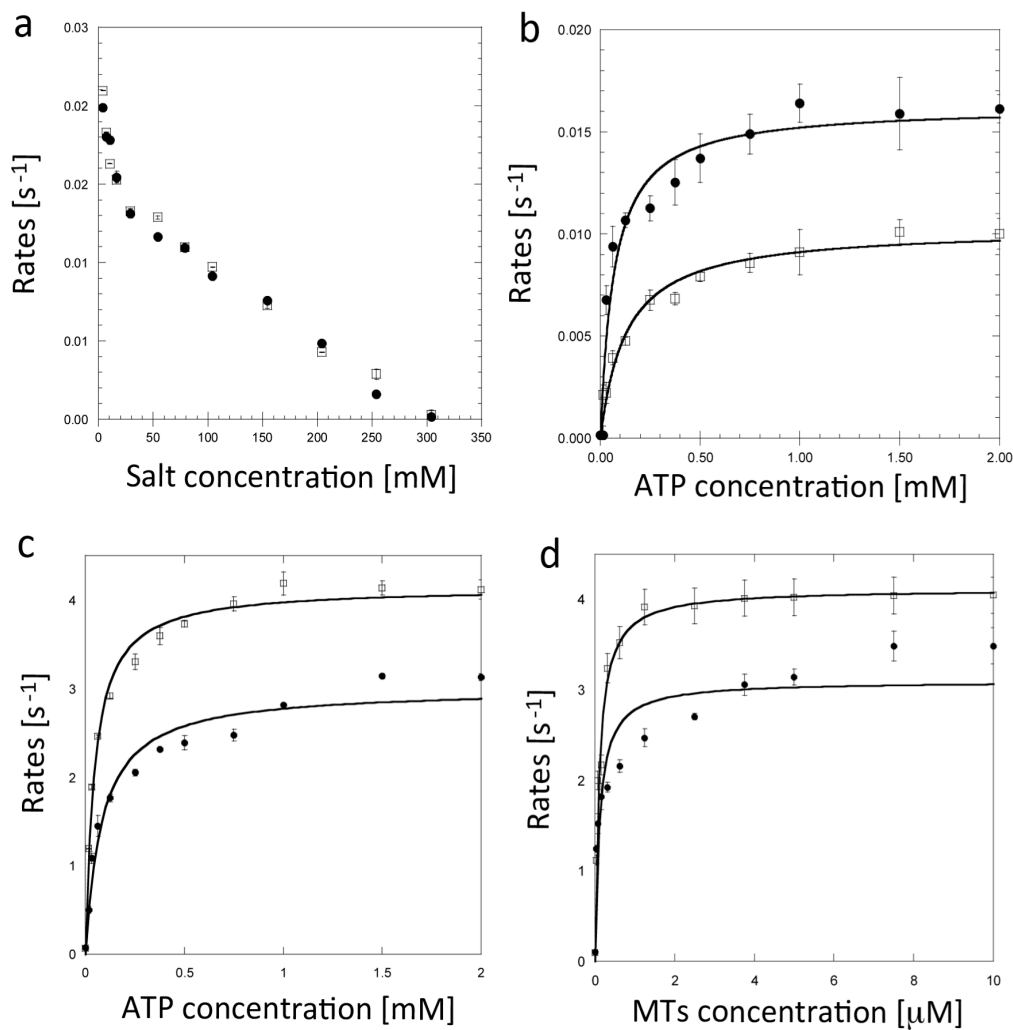


Figure 3-16: Characterisation of the basal and MT-stimulated ATPase activity of MPP1.

a) Effect of the NaCl concentration on the basal ATPase activity of MPP1₁₋₄₇₇ (●) and MPP1₅₇₋₄₉₁ (○) at saturating ATP concentration of 2 mM. b) The basal ATPase activity for MPP1₁₋₄₇₇ (●) and MPP1₅₇₋₄₉₁ (○) in the presence of increasing ATP concentration, measured in the absence of salt, NaCl. c) Determination of the MT-stimulated ATPase

activity of MPP1₁₋₄₇₇ (●) and MPP1₅₇₋₄₉₁ (○) d) MT-stimulated ATPase activity of MPP1₁₋₄₇₇ (●) and MPP1₅₇₋₄₉₁ (○) at increasing MT concentrations.

Table 3-4: Basal and MT-stimulated steady state ATPase activity of MPP1 proteins

Enzyme	Mass spec finger print coverage [%]	Gel filtration MW [kDa]	Basal ATPase activity		MT-stimulated ATPase activity		
			k_{cat} [s ⁻¹]	$K_{\text{M,ATP}}$ [μM]	k_{cat} [s ⁻¹]	$K_{\text{M,ATP}}$ [μM]	$K_{0.5,\text{MT}}$ [nM]
MPP1 ₁₋₄₇₇	56	51	0.016 ± 0.001	68.5 ± 16.2	3.1 ± 0.2	44 ± 4.1	102 ± 3.2
MPP1 ₅₇₋₄₉₁	77	43	0.0103 ± 0.001	128 ± 2.1	4.1 ± 0.1	82 ± 2.3	112 ± 1.0

3.4.2 Identification of compound inhibiting MPP1

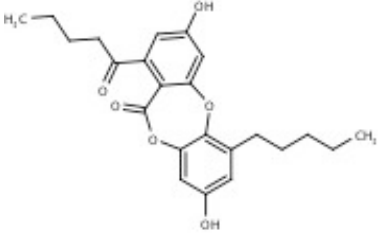
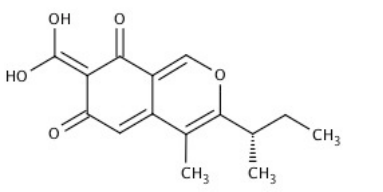
Screening for MPP1 inhibitors was performed by measuring the inhibition of the basal ATPase activity in the absence of salt and in the presence of 1 mM ATP using the protein construct MPP1₅₇₋₄₉₁. Several small molecule libraries from the National Cancer Institute (NCI), USA were screened including the mechanistic, the structural diversity and the natural product sets and full details are described in the materials and methods section. 61 hits were obtained in the single point primary screen from a total of 2520 compounds. A repetition of the primary screening was performed to confirm the initial hits and 15 compounds were found to still inhibit MPP1. A schematic representation is given in Figure 3-17.

3.4.2.1.1 Cytophos assay

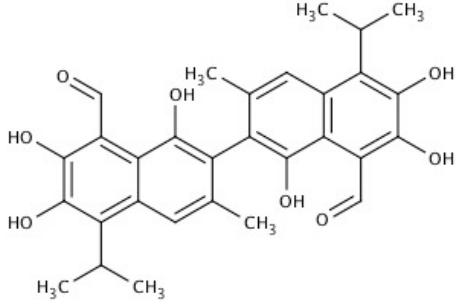
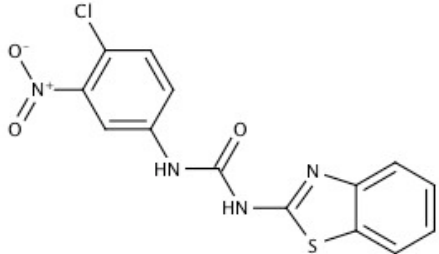
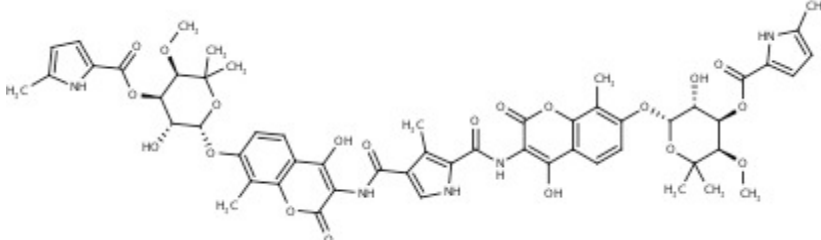
To further confirm the 15 primary hits as inhibitors of MPP1 a secondary screen, the Cytophos assay,²¹³ was used. The Cytophos assay relies on the formation of a Malachite green/phosphate complex instead of a coupled redox reaction. This provides a useful partially orthogonal assay system and eliminates false positives due to lactate dehydrogenase and pyruvate kinase inhibition. Table 3-5 shows the inhibition profiling of the 15 compounds. Compounds that showed 50% or more inhibition were selected for the subsequent analysis. 13 compounds inhibited MPP1 while the remaining two had no effect on MPP1 activity. Several of these compounds have issues with drug-like properties but some represent reasonable starting points. Interestingly, when these compounds were measured to see their effect on Eg5 and MKLP-2 activity, 10 were found to also inhibit either Eg5 or MKLP-2. Thus, 3 compounds were finally found to specifically inhibit MPP1. Among them Norlobaric acid was selected for further SAR study due to it being the most potent compound, having reasonable drug-like properties (logP, molecular weight, solubility, net charge) and commercial availability of analogues. Table 3-5 provides the details of the secondary screening of compounds targeting MPP1. It also provides specificity measurements identifying three compounds, which only inhibit MPP1 activity.

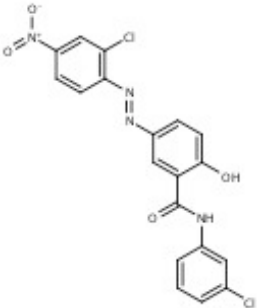
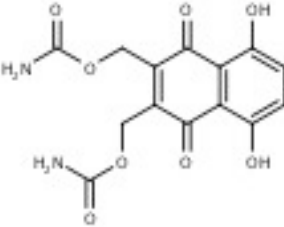
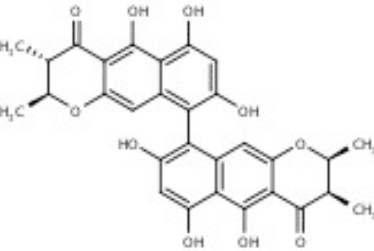
Table 3-5: Inhibition profiling of 13 compounds against MPP1 activity using Cytophos assay.

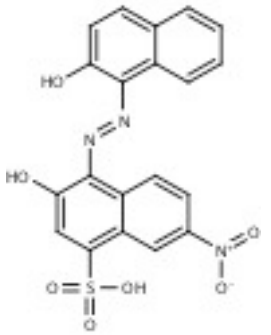
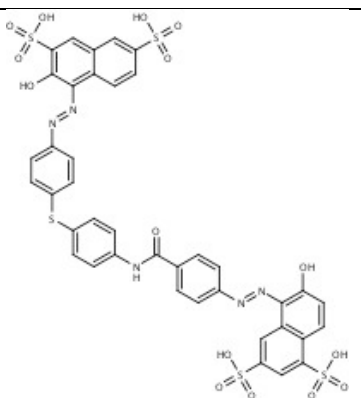
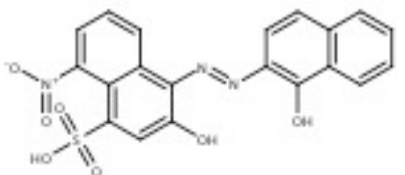
15 compounds obtained from primary screening were tested by Cytophos assay as a secondary screening method. 13 out of 15 were identified to inhibit MPP1 and two (green) did not inhibit MPP1. These compounds were also measured for inhibition of Eg5 and MKLP-2 ATPase activities. 10 compounds were found to inhibit Eg5 and/or MKLP-2 whereas 3 compounds were specific to MPP1. Norlobaric acid (NSC 31867) with the highest potency was selected for further SAR and specificity studies. The other consideration for selecting Norlobaric acid was the availability of analogues for further biochemical studies. n.i. no inhibition; n.d. not determined.

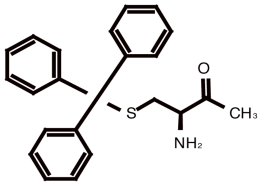
NSC number	Structure	Inhibition of MPP1 ₅₄₋₄₉₁ [%]	Inhibition of Eg5 ₁₋₃₆₈ [%]	Inhibition of MKLP-2 ₅₆₋₅₀₅ [%]
31867		90.2 ± 4.3	25.8 ± 3.4	19.17 ± 1.2
114344		80.3 ± 0.2	31.1 ± 1.1	23.8 ± 0.3

353527		86.9 ± 2.3	30.5 ± 2.1	15.5 ± 0.3
633209		77.9 ± 0.2	29.7 ± 3.1	24.9 ± 0.1
534		93.6 ± 1.1	64.8 ± 0.1	60.6 ± 0.9
18298		70.3 ± 0.9	68.3 ± 0.1	68.5 ± 1.9

56817		22.1 ± 0.9	n.d.	n.d.
329249		75.1 ± 2.3	77.8 ± 0.6	89.9 ± 0.1
107412		82.1 ± 1.5	59.9 ± 1.0	66.9 ± 0.9

135618		27.6 ± 1.2	n.d.	n.d.
224124		65.1 ± 1.1	31.3 ± 0.1	66.9 ± 1.6
345647		80.5 ± 0.6	36.6 ± 2.5	82.3 ± 0.2

73413		72.8 ± 0.8	34.9 ± 0.1	72.0 ± 0.2
76027		72.4 ± 0.5	96.4 ± 0.3	78.3 ± 1.9
85561		74.9 ± 1.2	35.2 ± 0.3	72.8 ± 0.4

STLC (positive control)		2.6 ± 0.01	90.3 ± 1.0	11.7 ± 0.1
No inhibitor	---	n.i.	n.i.	n.i.

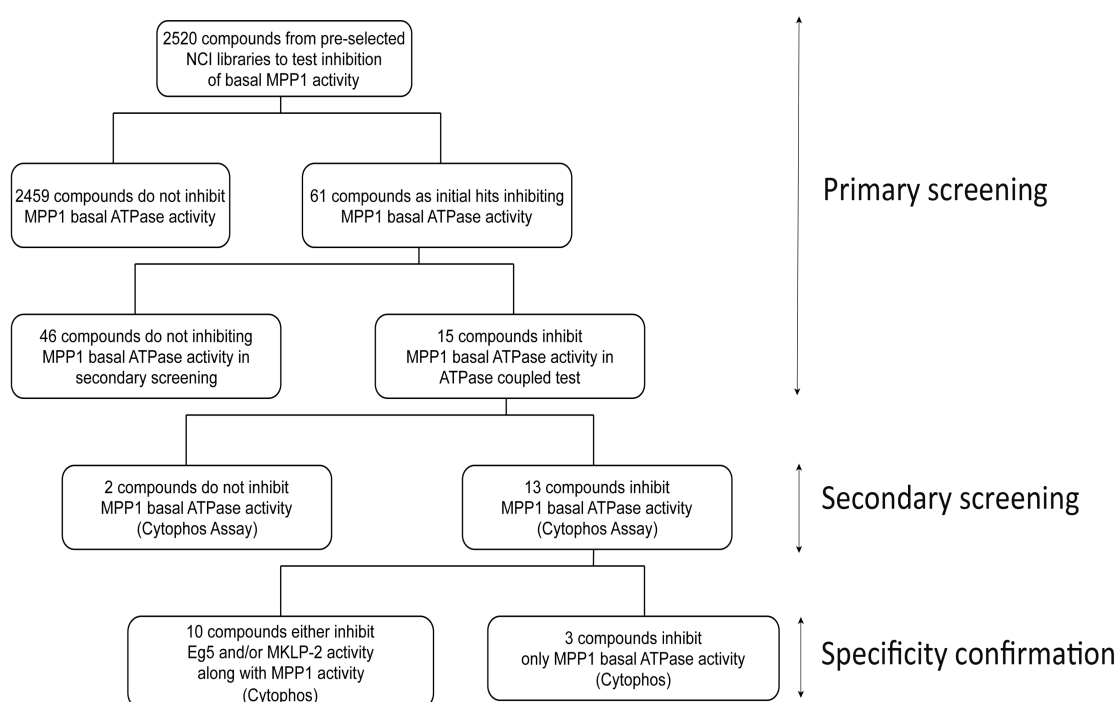


Figure 3-17: Schematic representation of inhibitor screening against MPP1 activity.

The figure gives a representation of the inhibitor screening of MPP1 performed on 2520 compounds from the NCI. The primary screening with ATPase activity assay and the secondary screening (Cytophos assay) identified 13 hits of MPP1 that were further narrowed down to three hits after determining the specificity against Eg5 and MKLP-2. Consequently, Norlobaric acid with the maximum inhibition against MPP1 was selected for further SAR studies.

3.4.3 Initial SAR study of inhibitor analogues of Norlobaric acid

Selection of Norlobaric acid led to the identification of a series of 11 structurally related depsidones and depsides through similarity and substructure searching of commercial and non-commercial databases. Depsides get their name due to the presence of polyphenyls composed of two or more monocyclic aromatic units linked by an ester bond. Similarly depsidones have a similar structure with the presence of a cyclic ester. Both depsides and depsidones are naturally occurring compounds obtained from lichens. Examples for depsides and depsidones are shown in Figure 3-18. These compounds were either obtained commercially or from the NCI. Some of the compounds have also been synthesised by Dr. Sophie Tomasi and her group, CNRS, France.

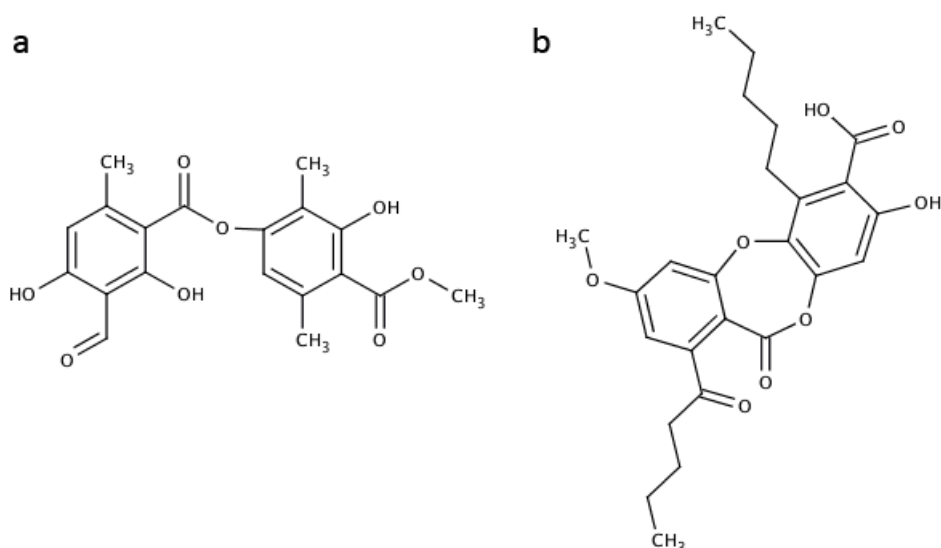


Figure 3-18: Structure of depsides and depsidones.

a) The structure of the depside Atranorin shows the monocyclic aromatic units linked by an ester bond. b) The structure of the depsidone Lobaric acid shows a similar structure to that of depsides but with the presence of an additional seven ring cyclic ester.

SAR study of 11 analogues was performed with the determination of their IC_{50} values for the inhibition of the basal and MT-stimulated ATPase activity (Table 3-6).

Among the 11 compounds, Physodic acid (1) was the most active, inhibiting the basal and MT-stimulated ATPase activities with IC_{50} values of $4.6 \pm 0.8 \mu M$ and $10.7 \pm 1.7 \mu M$, respectively. The depsides Atranorin (7) and DiffRACTaic acid (8) did not inhibit MPP1 ATPase activity.

Analysis of the structure of these compounds and their relation to the inhibition of MPP1 activity revealed that the most active MPP1 inhibitors such as Norlobaric acid (1), Physodic acid (2) and Lobaric acid (9) contain 2 alkyl substituents. Physodic acid shares a high structural similarity to the initial inhibitor of MPP1, Norlobaric acid. The differences are the rearrangement of a keto group on one of the two alkyl chains and addition of a carboxyl group to one of the aromatic rings. The depsidones Variolaric acid (10), Salazinic acid (4), Stictic acid (5) and Norstictic acid (6), which contain an additional five-membered ring system but lack the alkyl chains are either weak inhibitors of MPP1 or are inactive which may

be due to the loss of the alkyl chain. The depsides used in this study also showed no effect on the activity of MPP1 suggesting the important role of the alkyl chains in inhibiting MPP1 (Figure 3-19).

To test the specificity of Physodic acid for MPP1, the inhibition for 13 available kinesins was investigated. Table 3-7 represents the specificity measurements of Physodic acid against the 13 human kinesins.

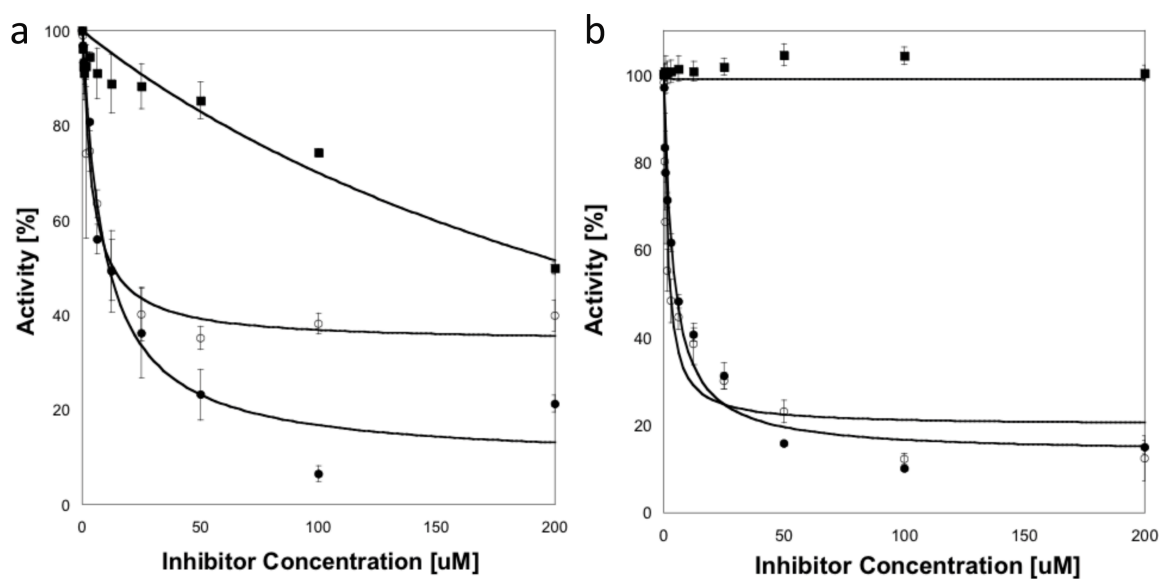
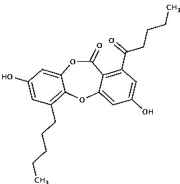
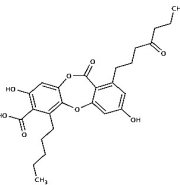
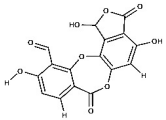
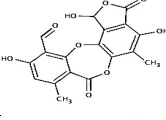
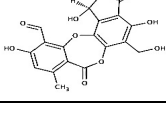


Figure 3-19: Inhibition of MPP-1₅₄₋₄₉₁ ATPase activity by depsidones.

a) Inhibition of basal ATPase activity of MPP-1 by Norlobaric acid (NSC31867, ○), Physodic acid (NSC5916, ●) and Parellic/Psoromic acid (NSC92186, ■). b) Inhibition of MT-stimulated ATPase activity of MPP-1 by Norlobaric acid (NSC31867, ○), Physodic acid (NSC5916, ●) and Parellic acid (NSC92186, ■).

Table 3-6: SAR study of depsidones and depsides from lichen as potential inhibitors of human MPP1.

The inhibition of the basal and MT-stimulated MPP1 ATPase activities for two protein constructs, MPP1₅₇₋₄₉₁ and MPP1₁₋₄₇₇ are shown. MIA: Maximum inhibition attained; n.i. no inhibition.

Cmpd (NSC number)	Structure	Inhibition of basal ATPase activity MPP1 ₅₇₋₄₉₁ [μ M]	Inhibition of MT-stimulated ATPase activity MPP1 ₅₇₋₄₉₁ [μ M]	Inhibition of basal ATPase activity MPP1 ₁₋₄₇₇ [μ M]	Inhibition of MT-stimulated ATPase activity MPP1 ₁₋₄₇₇ [μ M]
1 NSC31867 Norlobaric acid		18.7 \pm 2.6	24.4 \pm 3.5	10.8 \pm 1.7	7.6 \pm 0.7
2 NSC5916 Physodic acid		5.4 \pm 0.5	5.8 \pm 0.9	10.4 \pm 1.7	4.6 \pm 0.8
5 NSC87511 Stictic acid		n.i.	52.1 \pm 19.3	n.i.	90.6 \pm 18.8
6 Norstictic acid		n.i.	32.8 \pm 7.8	50.6 \pm 5.4	45.2 \pm 4.9
4 NSC87509 Salazinic acid		24.8 \pm 4.0	49.8 \pm 11.2	31.4 \pm 3.8	74.1 \pm 15.8

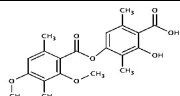
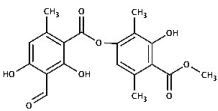
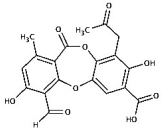
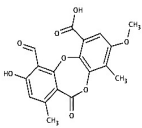
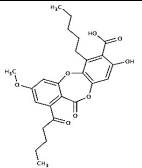
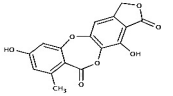
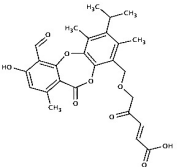
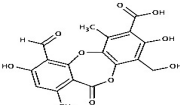
8 NSC5901 Diffraitaic acid		n.i.	n.i.	n.i.	n.i.
7 Atranorin		n.i.	n.i.	n.i.	n.i.
13 STOCK1N-66068		n.i.	16.6 ± 2.8	n.i.	23.1 ± 1.8
3 NSC92186 Psoromic acid		63.6 ± 6.6	29.2 ± 8.8	77.3 ± 12.6	21.9 ± 3.4
9 Lobaric acid		23.7 ± 3.1	16.0 ± 3.4	13.0 ± 1.9	28.0 ± 8.1
10 Variolaric acid		n.i.	n.i.	n.i.	n.i.
11 Fumarprotocetraric acid		5.4 ± 2.3	17.8 ± 2.2	4.6 ± 1.0	19.7 ± 3.6
12 Protocetraric acid		n.i.	58.8 ± 11.4	13.9 ± 2.8	36.7 ± 9.2

Table 3-7: Specificity of Physodic acid tested on the inhibition of the basal and MT-stimulated ATPase activities of a variety of human kinesins involved in mitosis or intracellular transport.

Kinesin	Family	Inhibition of basal ATPase activity [%]	Inhibition of MT-stimulated ATPase activity [%]
MPP1 ₅₇₋₄₉₁	kinesin-6	90	90
Kif15	kinesin-12	n.i.	n.i.
Eg5	kinesin-5	n.i.	n.i.
MKLP-1	kinesin-6	20	40
MKLP-2	kinesin-6	n.i.	n.i.
Kif7	kinesin-4	20	n.i.
Kif27	kinesin-4	20	n.i.
CENP-E	kinesin-7	50	60
Kif5A	kinesin-1	n.i.	n.i.
Kif5C	kinesin-1	20	n.i.
Kif3b	kinesin-2	20	40
Kif9	kinesin-9	40	50
Kif4	kinesin-4	40	40
Kif24	kinesin-13	10	5

3.4.3.1.1 Determination of the type of inhibition of physodic acid for MPP1 in the absence and presence of MTs

The screen identified physodic acid as the most potent inhibitor of MPP1. The assay was then used to determine the type of inhibition. In the absence of MTs, physodic acid is an uncompetitive inhibitor of MPP1 with respect to ATP (Figure 3-20a). Similarly, in the presence of MTs, physodic acid is also an uncompetitive inhibitor of MPP1 with respect to ATP (Figure 3-20b). In all experiments the highest concentration of ATP was fixed well above the $K_{m,ATP}$ for MPP1. In

addition MPP1 demonstrates mixed inhibition with respect to MTs (Figure 3-20c).

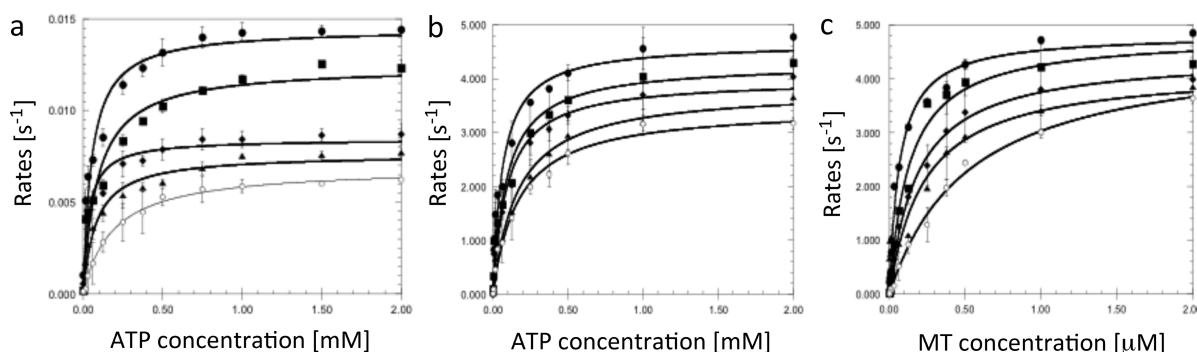


Figure 3-20: Type of inhibition of MPP-1₅₄₋₄₉₁ ATPase activity measured with Physodic acid.

a) The type of inhibition determined in the absence of MTs at increasing ATP concentrations. Physodic acid is uncompetitive with respect to ATP as shown by (●) 0; (■) 1 μM ; (◆) 5 μM ; (▲) 10 μM ; (◇) 20 μM of inhibitor concentration at increasing concentrations of ATP up to 2 mM. b) The type of inhibition determined in the presence of MTs at increasing ATP concentrations. Physodic acid is uncompetitive with respect to ATP in the MT-stimulated ATPase assay as shown by (●) 0; (■) 1 μM ; (◆) 5 μM ; (▲) 10 μM ; (◇) 20 μM of inhibitor concentration at increasing concentrations of ATP up to 2 mM. c). Physodic acid demonstrates mixed inhibition for MPP1 with respect to MTs as shown by (●) 0; (■) 1 μM ; (◆) 5 μM ; (▲) 10 μM ; (◇) 20 μM of inhibitor concentration at increasing concentrations of MTs up to 20 μM .

The molecules described here do not have ideal drug-like properties. They contain undesirable substructures such as aldehyde groups, which are known to be reactive, or esters that are prone to hydrolysis. However, the selectivity exhibited suggests a genuine inhibitory effect and further characterisation will be necessary to demonstrate this.

3.4.3.2 Crystallisation trials

The crystal structure of the MPP1 motor domain would provide insights into the structure and conformation of the loop L6 region that differentiates kinesin-6 members from all other kinesins. The initial trials for crystallisation of MPP1₅₄₋₄₉₁ in pET-28a (with a non-cleavable C-terminal his-tag) did not yield any crystals.

Crystallisation trials of different constructs of purified MPP1 motor domains were unsuccessful so a second approach using methylation of the solvent-exposed lysine residues was adopted. Reductive methylation²⁰¹ has been shown to be an effective rescue strategy for proteins recalcitrant to crystallisation with a moderate but significant success rate in generating useful crystals. This approach generally decreases the solubility of the protein and it is thought that this is due to the increase in hydrophobicity resulting from the methyl groups. However this approach also failed to yield crystals of MPP1. Consequently, orthologues of MPP1 were investigated as further avenues towards a crystal structure.

3.4.4 MPP1 orthologues from *M. musculus*, *R. norvegicus* and *X. laevis*

3.4.4.1 Protein expression of different MPP1 motor domain orthologues

MPP1 from *R. norvegicus*, *M. musculus* and *X. laevis* share 85%, 80% and 60% sequence similarity in the motor domain, respectively, with human MPP1 (Figure 3-21). Each of these orthologues was expressed in *E. coli* as described in the materials and methods. Protein preparations after the final gel filtration chromatography were obtained at almost 75-90% purity. A representative SDS-PAGE for MPP1 from each species is shown in Figure 3-22.

```

Hs      MESNFNQEGVPRPSYVFSADPIARPSIN-FDGIKLDLSHEFSLVAPN----TEANSFES 55
Mm      MESHLNPDGVPPRPSYVFSADPIARPLEIN-FDGVKLDLSHEFSLVASN----PAANSLGS 55
Rn      MESHLNQGVPPRPSYVFSADPIARPSIN-FDGVKLDLSHEFSLVAAN----PGANSLES 55
Xl      MKPAEVKYPPPRPSYLGVAITYPERDEPQPIDDLRTNLADKFLSLGGSESESTQKDSLGS 60
      *: .      *****: * . . . * : : : : : * : : : * : . . . : : *

Hs      KDYLQVCLRIRPFTQSEKE-LESEGCVHILDSQTVVLKEPQ-CILGRLSEKSSGQMAQKF 113
Mm      KNYLQVCLRIRPFTQSEKE-HEAEGCVQVLDSQSVLLKDPQ-SILGHLSEKSSGQVAQKF 113
Rn      KNYLQVCLRIRPFTQSEKG-HEAEGCVQVLDSQTVLLKDPQ-SILGHLSEKSSGQMAQKF 113
Xl      QDHMQVYLRVRPFTAGTEQKEAQDCISIPDSSSVLVKPPHNSQACRLSEKANGSVAQKF 120
      : : : : * * : : : * * . .      * : : : : * * : . .      : : : : * : : : : *

Hs      SFSKVFGPATTQKEFFQGCIMQPVKDLLKGQSRLIFTYGLTNSGKTYTFQGTEENIGILP 173
Mm      SFSKVFGPETSQKEFFLGCIMQPVKDLLEGHSRLIFTYGLTNSGKTYTFQGTEENIGILP 173
Rn      SFSRVFGPETSQKEFFQGCIMQPVKDLLKGHSRLIFTYGLTNSGKTYTFQGTEENIGILP 173
Xl      TFTHVFGPDTQAQFFDGTIKQHVIDFIKGQNRLIFTYGVTNAGKTFTFQGTKDNEGILP 180
      : : : : * * : * : * * * * * : : : : : . : : : : * : : : : * : : : : * * * *

Hs      RTLNVLFDSLQERLYTKMNLKPHRSREYLRLSSEQEKEEIASKSALLRQIKEVTVHN--- 230
Mm      RTLNVLFDSLQERLYTKMSFKPHRCREYLKLSSDQEKEESANKNTLLRQIKEVTIHN--- 230
Rn      RTLNVLFDSLQERLYTKMSFKPHRCREYLQLSSDQEKEESANKNTLLRQIKEVTIHN--- 230
Xl      RSDMDLFNSIQGRVYNKMDVKPHRCKDYVRLTKEQVKAEVALKNSVLRQIKEVDCSIRSN 240
      * : : : : * : * : * . : : : . : : : : * * * * * : : : : : * : : : : *

Hs      -----DSDDTLYG-SLTNSLNIS-EFEESIKDYEQANLNMANSIKFSVWVSFFEIYNEY 282
Mm      -----DSYDVLG-HLTNSLTIP-EFEESVNSCDQSSLNVDN-IKYSVWVSFFEIYNES 281
Rn      -----DSYDILCG-RLTNSLTIP-EFEETMNCEQSSLNVDN-IKYSVWVSFFEIYNES 281
Xl      NSRNCQDTTDFINDEGLTNSSSILSDMDDHLRHSEESKLALDGSAKFSVWVSFEIYNEC 300
      * : * : .      ***** * : : : : . . : : : * : .      * : : : : * : : : : *

Hs      IYDLFVPVS-SKFQKRKMLRLSQDVKGYSFIKDLQWIQVSDSKEAYRLKLGIKHQSVAF 341
Mm      IYDLFVPVS-SKFQKRKMLRLSQDIKGYSFIKDLQWVQVSDSKEAYRLKLGVKHQSVAF 340
Rn      IYDLFVPVS-SKLQKRKMLRLSQDVKGYSFIKDLQWIQVSDSKEAYRLKLGVKHQSVAF 340
Xl      IYDLLDPISGDKFYKRKTLRLALDLKGYSFVKDLQWIEVSDSTEACKILALGKKFQSIAY 360
      ***** : * * . : * * * : * : : : : : : : : : : : : : : * : * * * . : : : : *

Hs      TKLNNASSRSHSIFTVKILQIEDSEMSRVIRVSELSLCDLAGSERTMKTQNEGERLRETG 401
Mm      TKLNNASSRSHSIFTIRILQIEDSEIPRVTRVSELSLCDLAGSERSMKTQNEGERLREAG 400
Rn      TKLNNASSRSHSIFTIRILQIEDSEIPRVTRVSELSLCDLAGSERSMKTQSEGERLREAG 400
Xl      TKLNNSSSRSHSIFTVRLKIEDSDIPRVLKVSELALCDLAGSERCTKTQNEGERLKESG 420
      * * * . : : : : : : : : : : : : : : : * : : : : : : : : : * * . : : : : * : : : : *

Hs      NINTSLLTLGKCINVLKNSEKSKFQHVPFRESKLTHYFQSFFNGKGKICMIVNISQCYL 461
Mm      NINTSLLTLGKCINVLKNSEKSKVQ-HVPFRESKLTHYFQSFFTGKGKICMIINISQSCS 459
Rn      NINTSLLTLGKCISVLKNSDKSKIQHVPFRESKLTHYFQSFFTGKGKICMIINISQCCS 460
Xl      NINTSLLILGKCINALKTSQQSKAQHVPFRESKLTHYFQSFFSGKGKVCMIVNICQSAS 480
      * * * * * * : * * . : * * : * * : * * * : * * : * * : * * : * * : * * .

```

```

Hs      AYDETLNVLKFSAIAQKVCVPDTLNSSQEKLFGPVKSSQDVSLDSN-SNSKILN-VKRAT 519
Mm      AYDETLNVLKFSTTAQRVYVPDTLSSSQEKSFASNKSLQDVSLDSN-LDNKILN-VKRKT 517
Rn      AYDETLNVLKFSTVAQKVYVPDTLSSSQEKSFGSTKSLQDVSLGSN-LDNKILN-VKRKT 518
Xl      SYDETLNVLKFSAVAQKVLILESCQNSEAVPCVQKKSAREVSFIINNADSKHWNSRKRAT 540
          :*****:  **:  :  :  :  :  :  :  :  :  :  :  :  :  :  :  :  :  :  :  :  :  :  :

```

Figure 3-21: Sequence alignment of MPP1 motor domains from different species.

Human MPP1 shares 85% similarity with *M. musculus* MPP1, 80% with *R. norvegicus* MPP1 and 60% with *X. laevis* MPP1.

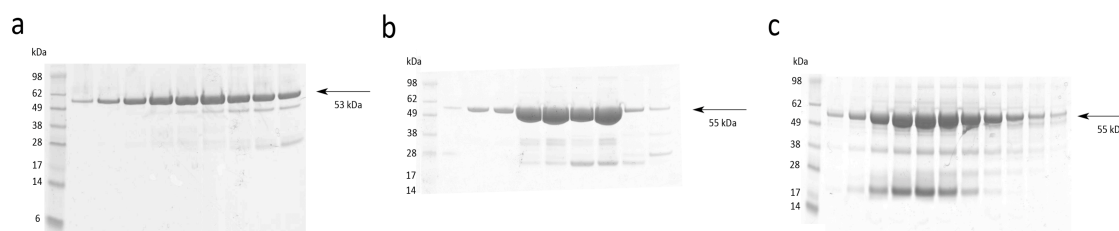


Figure 3-22: Protein expression of MPP1 orthologues.

Figure shows purified proteins of MPP1 orthologue from a) *M. musculus*, b) *R. norvegicus* and c) *X. laevis*.

3.4.4.2 Study of Physodic acid using steady state ATPase assay

The kinetic parameters in the form of k_{cat} for the activity of the proteins, $K_{m,ATP}$ for the affinity towards ATP and $K_{0.5,MTs}$ for their affinity for MTs in all three orthologues of human MPP1 shows similarity to that of human MPP1 as shown in Figure 3-23(a-d) and Table 3-8.

Physodic acid was then tested against the three MPP1 orthologues to test whether it is effective against the orthologues human MPP1. Under MT-stimulated conditions MPP1 of *M. musculus* is inhibited by physodic acid with an IC_{50} value of $10.8 \pm 0.73 \mu M$ whereas MPP1 of *R. norvegicus* is inhibited with an IC_{50} of $13.6 \pm 1.20 \mu M$ and MPP1 of *X. laevis* MPP1 with an IC_{50} of $12.2 \pm 1.91 \mu M$ (Figure 3-23e-f).

This indicates that physodic acid not only inhibits human MPP1 but also MPP1 from other species sharing a moderate to high degree of sequence similarity with human MPP1 with similar potency. This will have practical benefits as purified human MPP1 is unstable and these alternative enzymes provide a surrogate system.

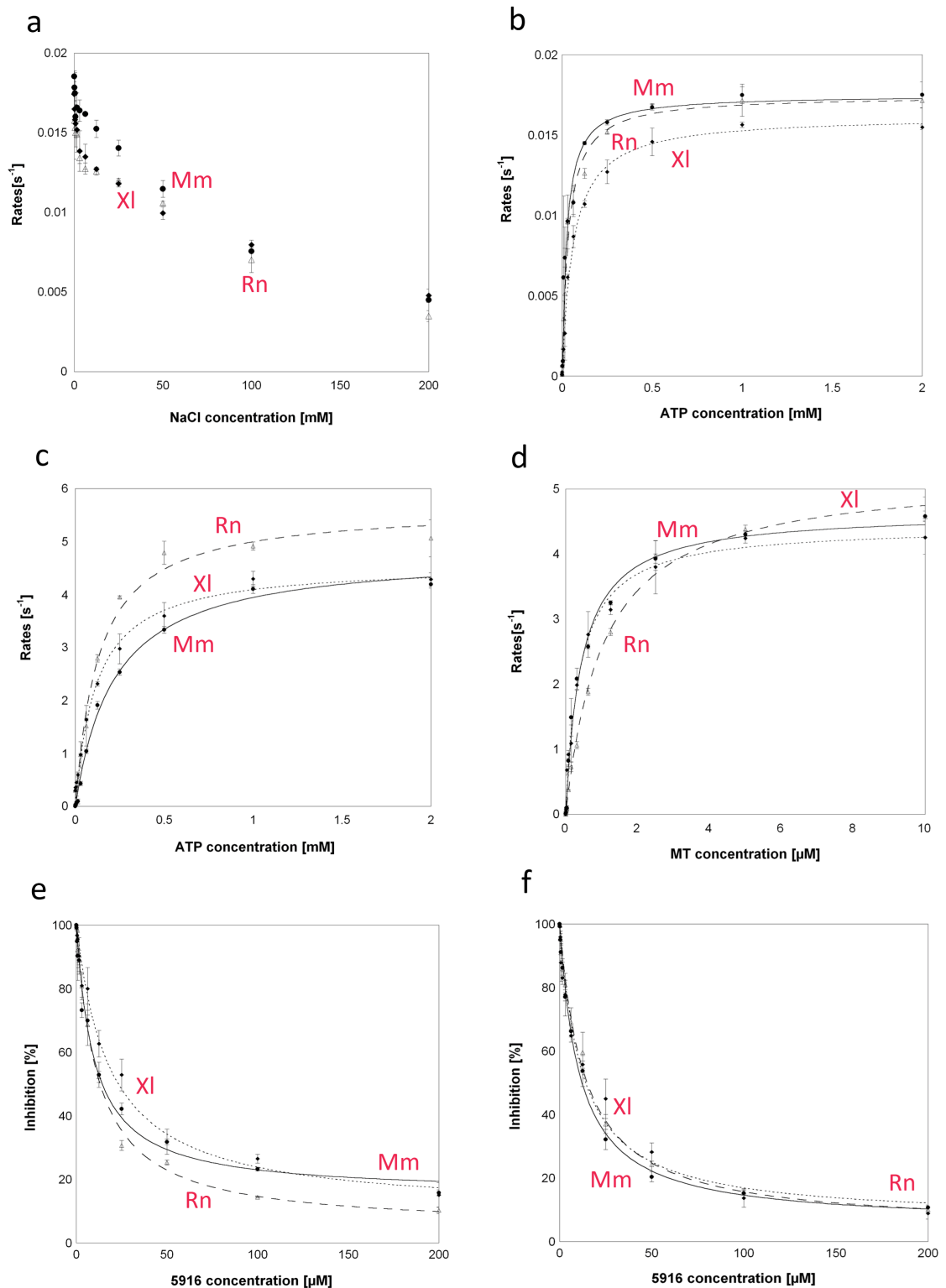


Figure 3-23: Characterisation and inhibition of the basal and MT-stimulated ATPase activity of MPP1 orthologues from three different species.

a) Effect of the NaCl concentration on the basal ATPase activity of *M. musculus* (●), *R. norvegicus* (Δ) and *X. laevis* (◆) MPP1 at saturating ATP concentration of 1 mM. b) The basal ATPase activity for *M. musculus* (●), *R. norvegicus* (Δ) and *X. laevis* (◆) in the presence of increasing ATP concentration, measured at a concentration of 0 mM NaCl. c) Determination of the MT-stimulated ATPase activity of *M. musculus* (●), *R.*

norvegicus (Δ) and *X. laevis* (\blacklozenge) MPP1 d) MT-stimulated ATPase activity of *M. musculus* (\bullet), *R. norvegicus* (Δ) and *X. laevis* (\blacklozenge) MPP1 at increasing MT concentrations. e) Inhibition of the basal ATPase activity of *M. musculus* (\bullet), *R. norvegicus* (Δ) and *X. laevis* (\blacklozenge) MPP1 by Physodic acid. f) Inhibition of the MT-stimulated ATPase activity of *M. musculus* (\bullet), *R. norvegicus* (Δ) and *X. laevis* (\blacklozenge) MPP1 by Physodic acid (5916). Mm – *M. musculus*, Rn – *R. norvegicus*, Xl- *X. laevis*.

Table 3-8: Kinetic parameters for MPP1 from three different species and inhibition of their basal and MT-stimulated ATPase activity by Physodic acid.

The kinetic parameters: k_{cat} , $K_{0.5, \text{MTs}}$, $K_{\text{m,ATP}}$ and estimated IC_{50} for Physodic acid for the MPP1 orthologues. The kinetic parameters are similar to that of the human MPP1. Also, Physodic acid is potent against these three species as seen for human MPP1. All values reported represent the mean \pm standard error from three experiments.

Species	Basal ATPase assay			MT-stimulated ATPase assay			
	k_{cat} [s ⁻¹]	$K_{\text{m,ATP}}$ [μM]	Inhibition of basal ATPase activity of MPP1 [μM]	k_{cat} [s ⁻¹]	$K_{\text{m,ATP}}$ [μM]	$K_{0.5, \text{MT}}$ [nM]	Inhibition of MT-stimulated ATPase activity of MPP1 [μM]
<i>M. musculus</i>	0.0174 \pm 0.0005	25.4 \pm 3.0	9.89 \pm 1.07	4.809 \pm 0.142	40.1 \pm 1.1	434 \pm 4.6	10.8 \pm 0.73
<i>R. norvegicus</i>	0.0174 \pm 0.0003	33.8 \pm 3.1	11.9 \pm 0.78	5.654 \pm 0.210	30.1 \pm 0.4	800 \pm 1.3	13.6 \pm 1.20
<i>X. laevis</i>	0.0162 \pm 0.004	59.3 \pm 4.1	18.8 \pm 2.18	4.570 \pm 0.149	61.1 \pm 1.2	395 \pm 3.9	12.2 \pm 1.91

3.4.4.3 Crystallisation trials

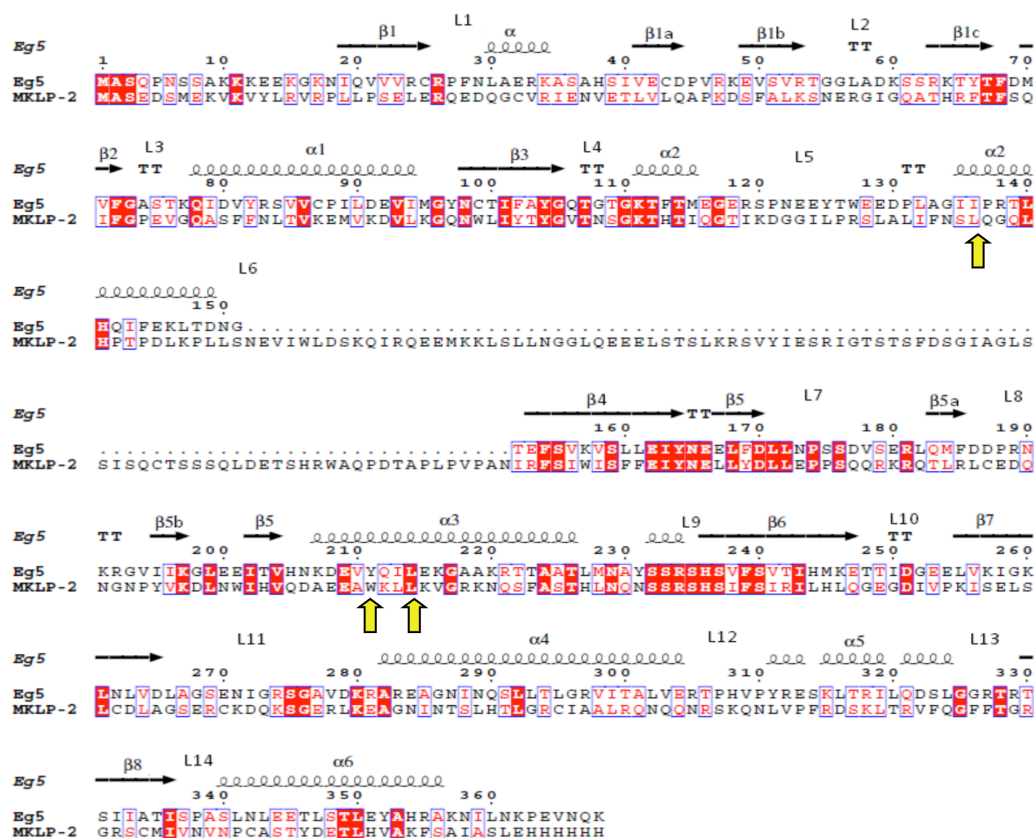
With crystallisation trials of human MPP1 unsuccessful, crystallisation trials of MPP1 from other species were also carried out using a range of commercial screens as described in Materials and Methods. The trials were unsuccessful.

3.5 Human MKLP-2

3.5.1 *Expression and purification of protein*

MKLP-2 shares sequence homology with the motor domain of other kinesins. Ample structural information is available for Eg5 thus it is used as a subject sequence for sequence alignment and secondary structure predictions of MKLP-2. This indicates similar secondary structural elements in the MKLP-2 and Eg5 motor domains²⁸ (Figure 3-24a). It also shows the very long loop L6 insertion in MKLP-2 and few residues (marked in yellow arrow), with a unique insertion in the conserved motor domain that is observed only for kinesin-6 members. The protein expressions after the final gel filtration chromatography were obtained at almost 90% purity. A representative SDS-PAGE for MKLP-2 motor domain is shown Figure 3-24b.

a



b

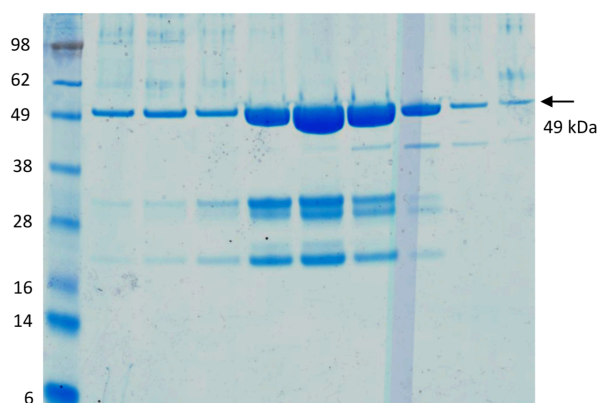


Figure 3-24: Sequence alignment and SDS-PAGE of purified MKLP-2 motor domain.

a) Sequence alignment of MKLP-2 and Eg5 motor domains predicting the secondary structure elements based on sequence similarity. It shows the loop L6 insertion of MKLP-2 that might form the putative inhibitor-binding site and a few residues around loop L6 that might contribute to inhibitor-binding. The yellow arrow represents the single mutations of MKLP-2 motor domain used in the study based on residues in Eg5 motor domain that play an important role in ligand binding. b) Protein obtained after final purification of MKLP-2₅₆₋₅₀₅. The protein was confirmed by mass spectroscopic analysis. The lower molecular weight bands were confirmed to be either degraded MKLP-2 (18 kDa) or contaminant DNA Cap Binding protein (28 kDa)

3.5.2 Characterisation of putative inhibitor-binding site

Paprotrain¹⁶⁶ has been identified as the first inhibitor of MKLP-2. To narrow down the putative inhibitor-binding site, a deletion mutant of MKLP-2 motor domain was created without the long loop L6 region (MKLP-2₅₆₋₅₀₅ΔL6). Also, three further mutants were generated; each containing a single alanine mutation (L187A, W356A and W359A). These residues were selected based on Eg5 structures where these residues were shown to undergo significant conformational changes on inhibitor binding as shown in various X-ray crystal structures of Eg5-inhibitor complexes.²¹⁴

Initial kinetic characterisation and salt-dependence kinetic assays were carried out in an analogous manner to MPP1. MKLP-2 also showed the highest activity in the absence of NaCl in ATPase assays (Figure 3-25a). The kinetic parameters for the basal and MT-stimulated ATPase activity in the absence and presence of inhibitors for the mutations MKLP-2^{L187A}, MKLP-2^{W356A}, MKLP-2^{W359A} were determined and compared to those of wild-type MKLP-2 (MKLP-2^{WT}). The k_{cat} values for the basal and MT-stimulated ATPase assays of the mutants show similar rates of ATP hydrolysis to that of the wild-type MKLP-2 (Figure 3-25a). The basal and MT-stimulated $K_{\text{M,ATP}}$ values were also very similar to wild-type MKLP-2 with a maximum of 0.6-fold decrease. Also, $K_{0.5,\text{MT}}$ are also very similar for the wild-type and mutant MKLP-2 (Figure 3-25b-d). Therefore, the kinetic parameters for the basal and MT-stimulated ATPase activity of the wild-type and MKLP-2 mutants display no significant differences (Table 3-9). Wild-type and mutant MKLP-2 were then assayed in the presence of paprotrain in both basal and MT-stimulated ATPase assays. MKLP-2^{WT} is inhibited with an IC_{50} of 2.5 ± 0.4 and 0.98 ± 0.18 μM respectively for basal and MT-stimulated ATPase assay (Figure 3-25e-f). For MKLP-2^{L187A} and MKLP-2^{W356A} the decrease in affinity for paprotrain is insignificant suggesting that these residues have no role to play in inhibitor binding. However, the IC_{50} for MKLP-2^{W359A} increases by ~20 fold for the inhibition of MT-stimulated ATPase activity of MKLP-2. For the MKLP-2₅₆₋₅₀₅ΔL6 mutant there was no inhibition by paprotrain observed indicating that loop L6 plays a vital role in inhibitor binding.

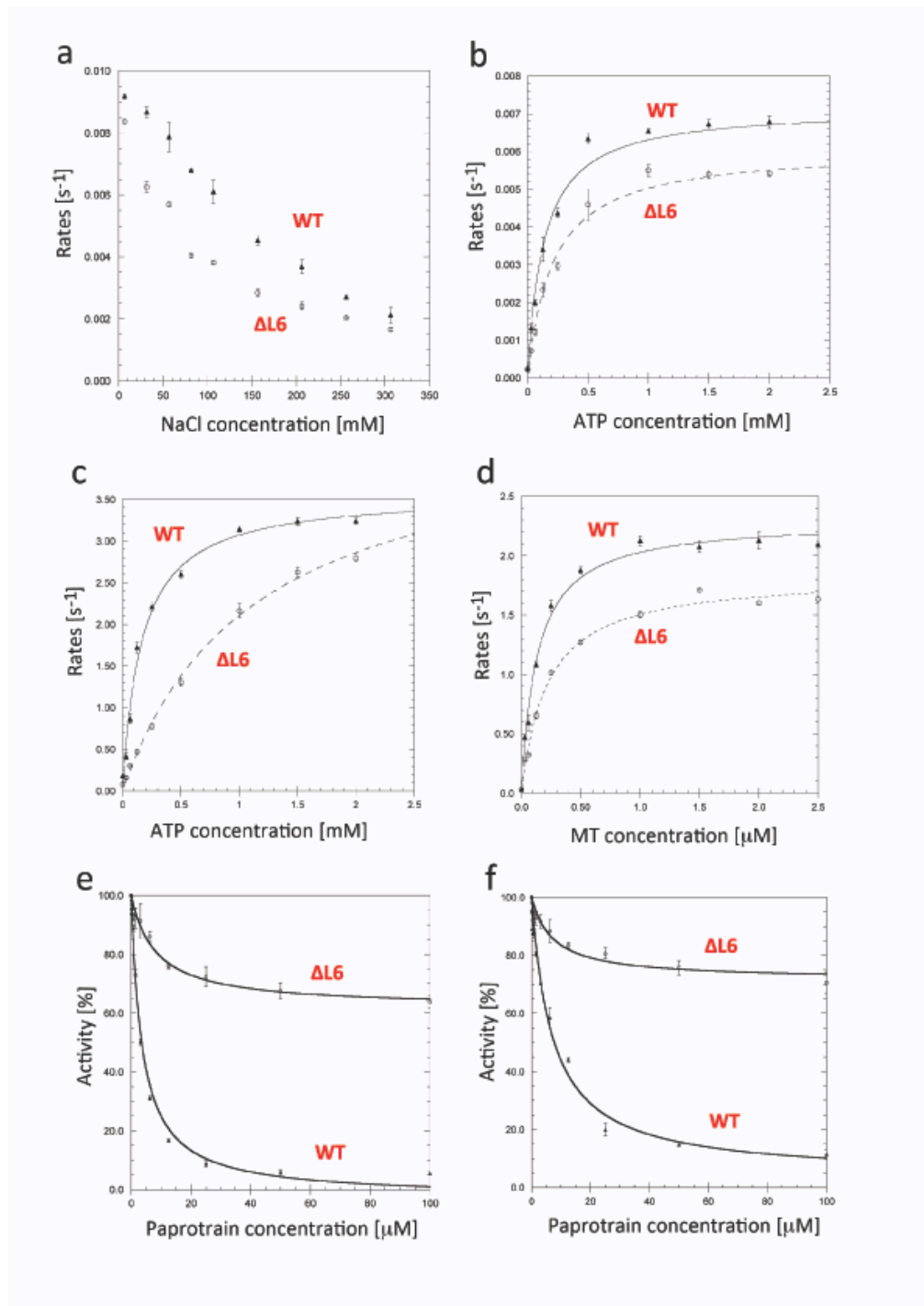


Figure 3-25: Characterisation of the basal and MT-stimulated ATPase activity of MKLP-2.

a) Effect of the NaCl concentration on the basal ATPase activity of MKLP-2₅₆₋₅₀₅ (●) and MKLP-2₅₆₋₅₀₅ $\Delta L6$ (○) at saturating ATP concentration of 1 mM. b) The basal ATPase activity for MKLP-2₅₆₋₅₀₅ (●) and MKLP-2₅₆₋₅₀₅ $\Delta L6$ (○) in the presence of increasing ATP concentration, measured at a concentration of 0 mM NaCl. c) Determination of the MT-stimulated ATPase activity of MKLP-2₅₆₋₅₀₅ (●) and MKLP-2₅₆₋₅₀₅ $\Delta L6$ (○) d) MT-stimulated ATPase activity of MKLP-2₅₆₋₅₀₅ (●) and MKLP-2₅₆₋₅₀₅ $\Delta L6$ (○) at increasing MT concentrations. e) Inhibition of basal ATPase activity of MKLP-2 wild-type (●) and loop L6-deletion mutant (○) by paprotrain. f) Inhibition of MT-stimulated ATPase activity of MKLP-2 wild-type (●) and loop L6-deletion mutant (○) by paprotrain. MKLP-2₅₆₋₅₀₅ wild type is represented as WT and MKLP-2₅₆₋₅₀₅ $\Delta L6$ is represented as $\Delta L6$.

Table 3-9: Summary of kinetic parameters for wild-type and mutants of MKLP-2.

Enzyme	Basal			MT-stimulated			
	k_{cat} [s ⁻¹]	$K_{M,ATP}$ [μM]	$IC_{50}^{Paprotain}$ [μM] MIA* [%]	k_{cat} [s ⁻¹]	$K_{M,ATP}$ [μM]	$K_{0.5,MT}$ [nM]	$IC_{50}^{Paprotain}$ [μM] MIA [%]
MKLP-2 ^{WT}	0.045 ± 0.0001	82 ± 1.9	1.5 ± 0.4 (85)	5.89 ± 0.27	74.7 ± 1.2	130 ± 0.05	0.98 ± 0.2 (95)
MKLP-2 ^{L6}	0.044 ± 0.0002	18 ± 0.005	n.i. (40)	5.0 ± 0.15	210 ± 20	61.4 ± 0.06	n.i. (30)
MKLP-2 ^{L187A}	0.043 ± 0.004	60 ± 0.2	1.07 ± 0.16 (80)	7.59 ± 0.05	232 ± 6.2	54.3 ± 0.8	3.6 ± 0.6 (70)
MKLP-2 ^{W356A}	0.044 ± 0.003	39.9 ± 1.0	1.13 ± 0.19 (60)	6.47 ± 0.25	161 ± 2.1	42.1 ± 0.1	1.3 ± 0.2 (60)
MKLP-2 ^{W359A}	0.030 ± 0.003	27.1 ± 0.1	7.11 ± 1.1 (70)	5.43 ± 0.15	147 ± 1.4	95.4 ± 1.6	18.6 ± 2.8 (60)

*MIA: Maximum inhibition attained

3.5.3 SAR study of MKLP-2 inhibitors using steady state ATPase assays

An initial SAR study to investigate the importance of different substituents of paprotrain was carried out using both basal and MT-stimulated MKLP-2 ATPase assays. The chemical structure of paprotrain¹⁶⁶ and other compounds from this study are shown in Table 3-10.

The analogues were initially synthesised for the measurement of inhibition of MKLP-2 and an SAR study was carried out in collaboration with Drs. Christophe Labrière and Catherine Guillou. The inhibition of the basal and MT-stimulated ATPase activity of 135 inhibitor analogues are summarised in Table 3-10. All description of compounds are based on this table. Further analysis of the compounds based on the *in vitro* inhibition is still ongoing.

To rationalise the SAR study, the structure of paprotrain was delineated into five regions: (A) the pyridine ring, (B) the indole ring, (C) the double bond bridge, (D) the nitrile function and (E) the substituent of the double bond as shown in Figure 3-26.

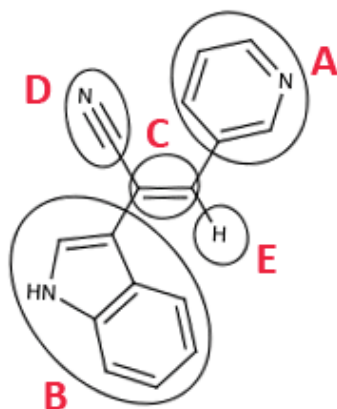


Figure 3-26: Structure of paprotrain with the different regions of modification for SAR study.

Paprotrain analogues were synthesised after delineating the paprotrain structure into five different regions A-E. The SAR analysis is based on each individual region or in combination of different regions.

Firstly substitution of the pyridine ring (region A) with phenyl rings and/or introduction of a functional group in the same *meta* position as the nitrogen atom of the pyridine ring results in a total loss of inhibition (**332-1**). Introduction of large constituents in the *para* position as SMe (**44-3**) are unfavourable for the inhibition of basal and MT-stimulated ATPase activities of MKLP-2.

Changes in the indole ring (region B) such as introduction of a methoxy group in the 6 or 4 positions (**260-1** and **398-1**) or introduction of a nitrogen atom in the 7-position of the indole (**505-1**) decreases the inhibitory potency. When the 7-position (**399-1**) is substituted by a methoxy group total loss of inhibition occurred. Substitution in the 5-position with an ethoxy group (**387-1**) leads to the compound being more potent than paprotrain. Large substituents like phenyl (**621-1**) or thiophene (**622-1**) present in 2-position resulted in loss of inhibition as well. Alkylation (**418-2**) or acylation (**419-2**) of the indole leads to inactive compounds.

Modulations of the central linker (region C) were undertaken. Shorter (one atom, **296-1**) or longer (three atoms, i.e. **170-2** or four atoms i.e. **412-2**) linker between the indole and the pyridine rings lead to inactive molecules. The vinylogous derivative **524-1** is inactive showing that the nitrile position of the nitrile function is also sensitive.

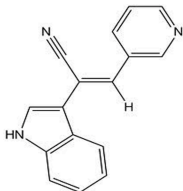
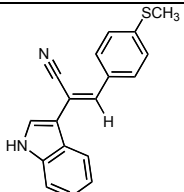
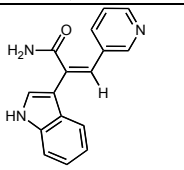
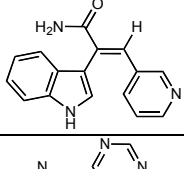
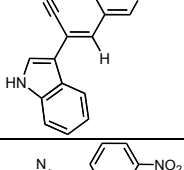
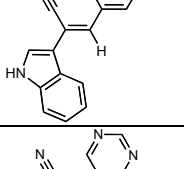
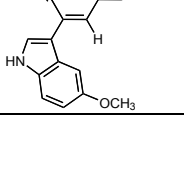
Substitution of the nitrile function (region D) mostly rendered the compounds either inactive (**133-1**) or the potency decreased considerably (**93-1** and **115-1**).

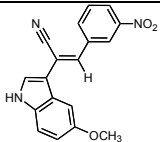
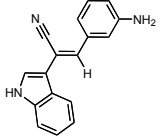
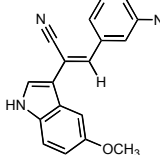
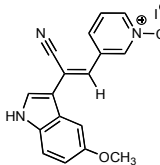
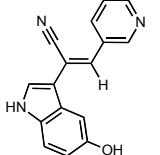
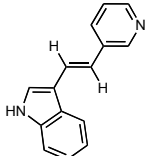
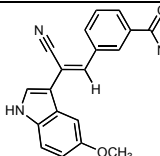
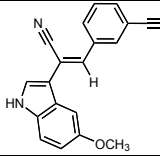
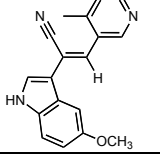
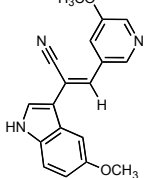
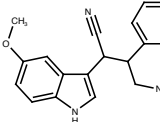
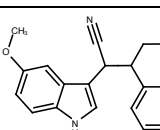
Modifications of the double bond bridge (region C) and removing the substituent of the double bond (region E) (**163-1**) leads to higher potency than paprotrain.

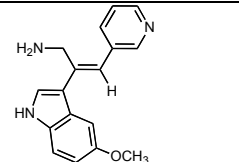
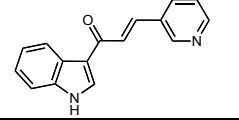
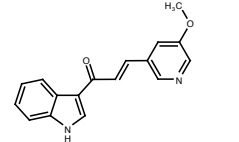
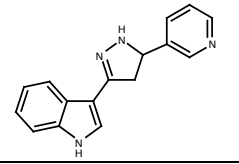
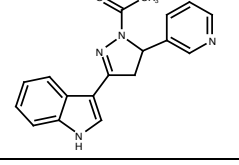
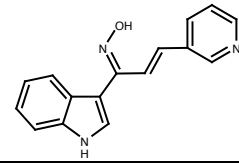
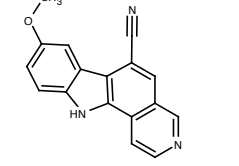
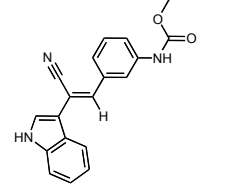
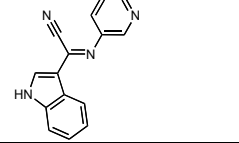
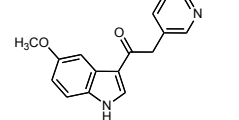
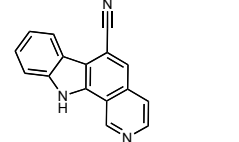
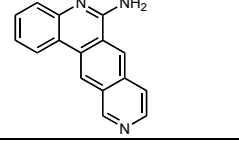
Overall two compounds, **163-1** and **387-1** were found in this SAR study to have 2-fold more potency than paprotrain. Further cell-based analyses of the active compounds as well as specificity measurements are still underway.

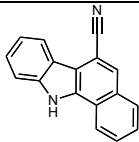
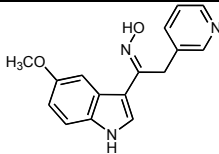
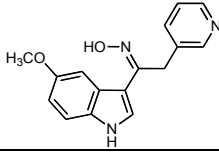
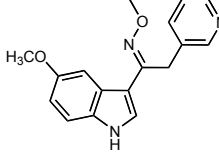
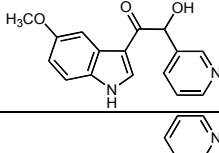
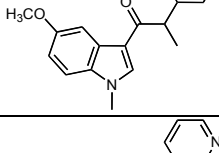
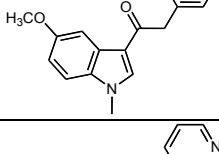
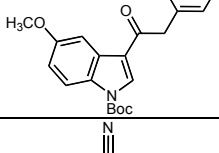
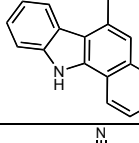
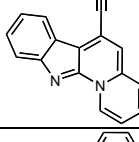
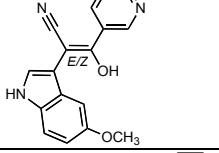
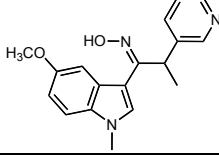
Table 3-10: Inhibition of basal and MT-stimulated ATPase activities by paprotrain analogues.

The table represents the IC₅₀ values for the inhibition of the basal and MT -stimulated ATPase activities of around 135 paprotrain analogues. n.i. : no inhibition

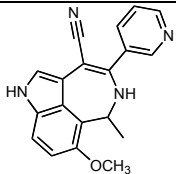
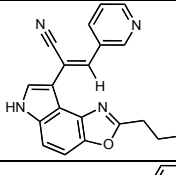
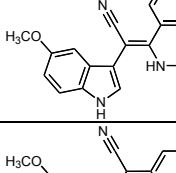
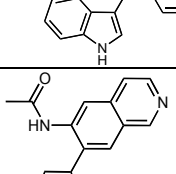
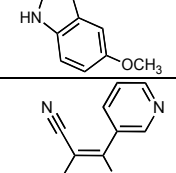
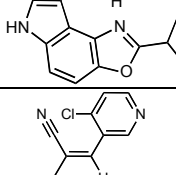
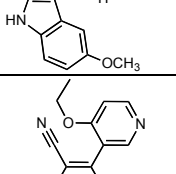
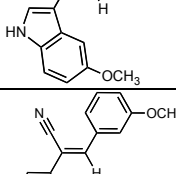
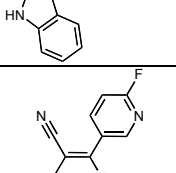
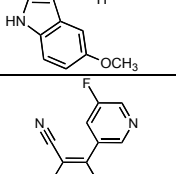
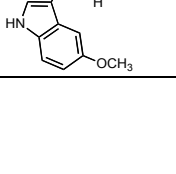
Compound Number	Structure	Inhibition of basal ATPase activity IC ₅₀ (μM)	Inhibition of MT-stimulated ATPase activity IC ₅₀ (μM)
Paprotrain		1.35 ± 0.2	0.83 ± 0.1
44-3		n.i.	n.i.
93-1		n.i.	82.9 ± 54.5
93-2		n.i.	n.i.
97-2		10.6 ± 4.8	6.4 ± 0.5
98-3		n.i.	0.6 ± 0.2
100-2		4.1 ± 1.2	3.2 ± 0.5

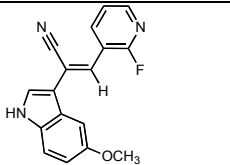
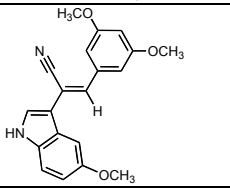
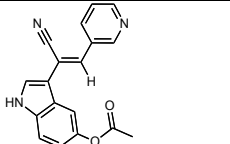
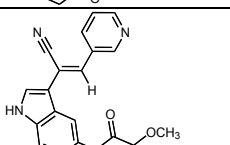
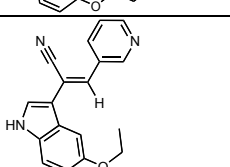
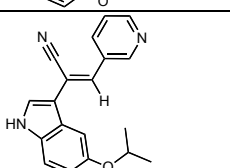
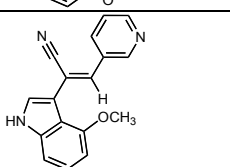
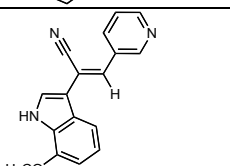
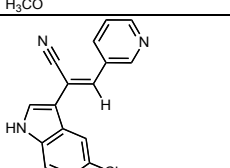
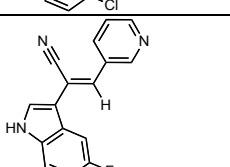
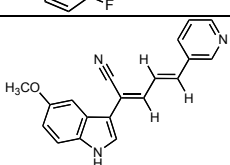
101-2		n.i.	0.5 ± 0.1
104-1		n.i.	n.i.
105-1		n.i.	50.3 ± 20.5
108-1		14.8 ± 1.2	5.4 ± 2.2
112-1		2.6 ± 0.1	0.8 ± 0.1
115-2		5.91 ± 1.1	4.91 ± 2.1
120-3		12.5 ± 5.8	17.4 ± 4.4
121-1		1.9 ± 0.3	0.3 ± 0.1
128-2		4.1 ± 1.6	1.1 ± 0.1
129-1		11.9 ± 2.1	5.3 ± 2.2
130-2		n.i.	n.i.
130-4		n.i.	n.i.

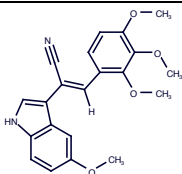
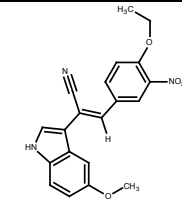
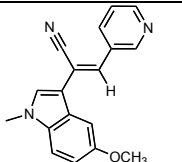
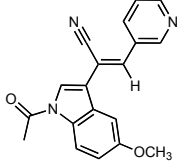
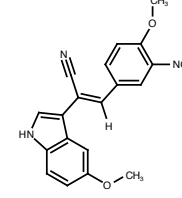
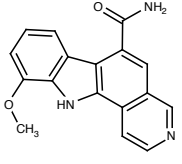
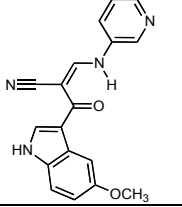
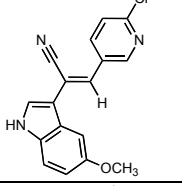
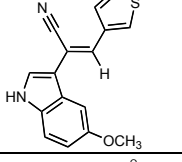
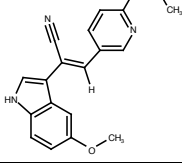
133-1		n.i.	n.i.
134-1		n.i.	n.i.
138-2		n.i.	n.i.
147-1		n.i.	n.i.
150-1		n.i.	n.i.
151-1		n.i.	n.i.
154-1		n.i.	n.i.
160-1		n.i.	n.i.
163-1		1.5 ± 0.2	0.6 ± 0.1
173-1		n.i.	n.i.
174-1		n.i.	n.i.
174-2		n.i.	n.i.

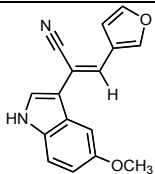
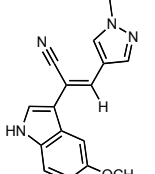
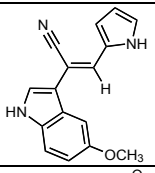
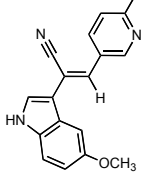
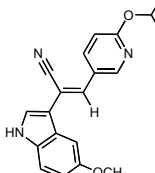
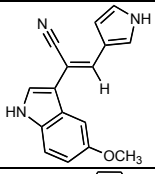
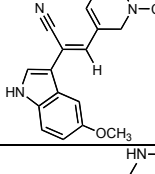
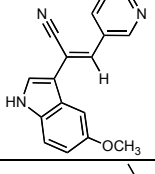
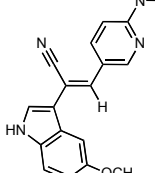
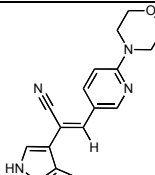
176-1		n.i.	n.i.
182-1		n.i.	n.i.
182-2		n.i.	n.i.
191-2		n.i.	n.i.
195-2		n.i.	n.i.
206-1		n.i.	n.i.
206-2		n.i.	n.i.
207-1		n.i.	n.i.
209-1		n.i.	n.i.
209-2		n.i.	n.i.
210-2		n.i.	n.i.
215-3		n.i.	n.i.

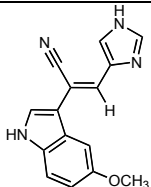
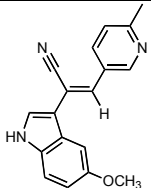
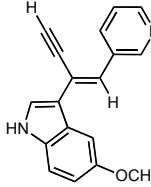
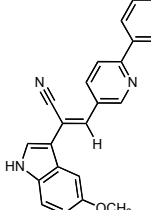
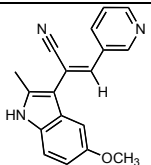
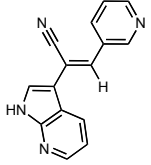
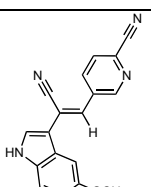
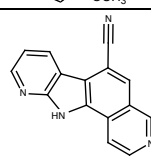
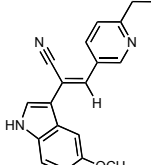
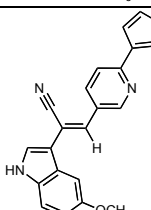
216-1		n.i.	n.i.
217-1		n.i.	n.i.
226-1		n.i.	n.i.
228-2		n.i.	n.i.
229-1		n.i.	n.i.
239-1		n.i.	n.i.
239-2		n.i.	n.i.
252-2		n.i.	n.i.
260-1		5.6 ± 0.9	5.4 ± 0.7
261-2		n.i.	n.i.
262-1		n.i.	n.i.
277-1		n.i.	n.i.

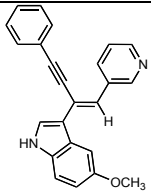
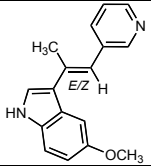
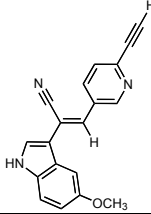
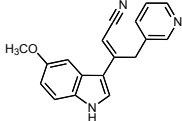
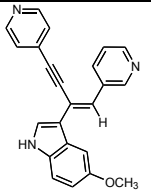
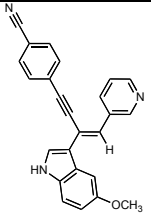
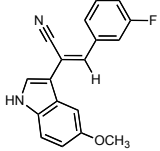
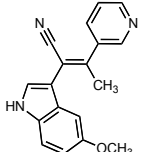
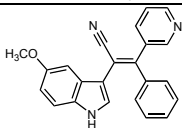
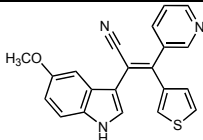
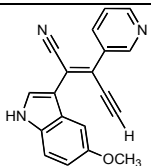
287-2		n.i.	n.i.
291-1		n.i.	1.1 ± 0.2
294-1		n.i.	n.i.
296-1		n.i.	n.i.
310-1		n.i.	n.i.
312-1		n.i.	n.i.
320-1		5.0 ± 2.1	0.5 ± 0.1
320-2		n.i.	n.i.
332-1		n.i.	n.i.
343-3		2.7 ± 0.5	2.3 ± 0.2
344-1		n.i.	n.i.

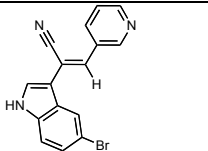
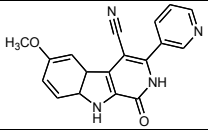
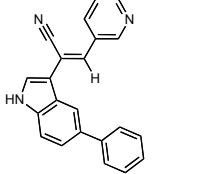
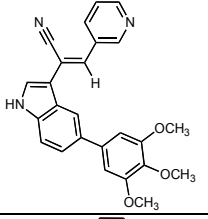
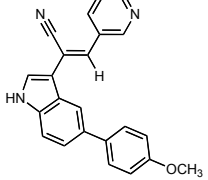
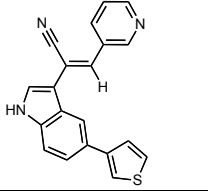
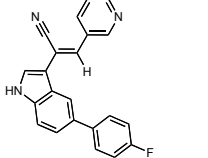
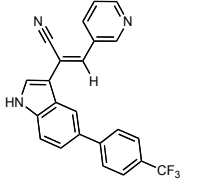
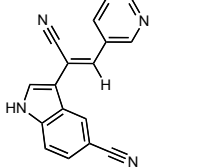
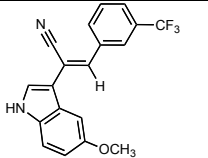
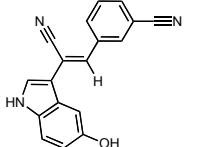
351-3		1.8 ± 0.7	3.4 ± 2.3
365-2		3.3 ± 0.9	6.8 ± 0.8
375-1		2.8 ± 0.3	3.6 ± 0.4
377-3		3.0 ± 2.2	3.9 ± 0.9
387-1		1.1 ± 0.5	0.9 ± 0.1
389-1		1.5 ± 1.5	1.6 ± 0.3
398-1		4.2 ± 1.5	3.3 ± 0.3
399-1		n.i.	n.i.
400-2		0.5 ± 0.6	2.8 ± 0.4
401-1		1.0 ± 0.4	2.6 ± 0.4
412-1		n.i.	n.i.

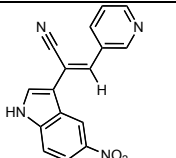
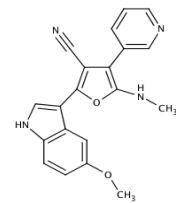
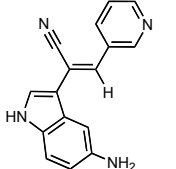
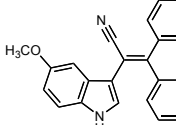
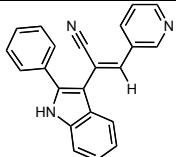
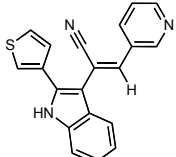
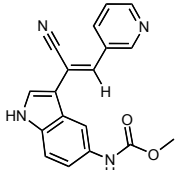
416-1		n.i.	n.i.
417-2		n.i.	n.i.
418-2		n.i.	n.i.
419-1		n.i.	n.i.
429-1		n.i.	n.i.
430-1		n.i.	n.i.
436-3		n.i.	n.i.
457-1		9.4 ± 2.6	12.9 ± 2.1
464-1		n.i.	7.4 ± 2.6
466-1		n.i.	n.i.

467-1		n.i.	n.i.
469-1		n.i.	4.3 ± 1.4
472-1		n.i.	n.i.
473-1		9.9 ± 4.7	10.9 ± 2.5
474-1		n.i.	n.i.
475-2		n.i.	n.i.
481-2		n.i.	n.i.
482-1		n.i.	n.i.
484-1		n.i.	n.i.
485-2		n.i.	n.i.

486-2		n.i.	n.i.
494-1		3.6 ± 0.4	6.1 ± 1.0
496-2		6.1 ± 1.2	3.2 ± 0.4
501-1		n.i.	n.i.
504-2		n.i.	n.i.
505-1		11.0 ± 4	10.2 ± 1.2
506-1		4.5 ± 1.7	8.2 ± 2.3
507-2		n.i.	n.i.
508-1		n.i.	n.i.
512-1		n.i.	n.i.

513-1		n.i.	n.i.
514-1		4.7 ± 1.3	1.9 ± 0.3
515-1		n.i.	n.i.
524-1		n.i.	n.i.
540-1		n.i.	n.i.
541-1		n.i.	n.i.
550-3		n.i.	n.i.
562-2		3.9 ± 1.1	3.1 ± 1.2
565-1		n.i.	n.i.
566-1		n.i.	n.i.
567-2		n.i.	n.i.

574-1		13.3 ± 2.7	3.1 ± 1.2
577-1		n.i.	n.i.
585-2		n.i.	n.i.
587-1		6.8 ± 1.5	10.2 ± 2.1
588-1		n.i.	n.i.
589-1		n.i.	n.i.
591-1		11.4 ± 4.2	16.6 ± 8.6
592-2		n.i.	1.6 ± 0.5
593-1		n.i.	n.i.
596-1		n.i.	n.i.
601-1		1.4 ± 0.3	0.8 ± 0.2

607-1		n.i.	n.i.
609-1		n.i.	n.i.
619-1		1.4 ± 0.3	0.8 ± 0.2
620-1		n.i.	n.i.
621-1		n.i.	n.i.
622-1		n.i.	n.i.
624-1		3.7 ± 1.4	0.4 ± 0.3

3.5.4 Crystallisation trials

Crystallisation trials of the purified human MKLP-2 motor domain constructs (MKLP-2₁₋₅₉₁, MKLP-2₅₆₋₅₀₅, MKLP-2₅₄₋₄₉₆, MKLP-2₅₆₋₅₀₅) have been unsuccessful.

4 Discussion and future perspectives

4.1 Understanding the mechanism of Eg5 targeting drugs and future directions

4.1.1 A better understanding of ispinesib binding and affinity towards the Eg5 motor domain

Eg5 shows significant potential as a drug target for cancer chemotherapy, and correspondingly has attracted widespread attention with numerous inhibitors in various phases of drug development.^{8,119,122} All Eg5 inhibitors developed to date target the globular motor domain, where they bind to one of three distinct sites: ATP competitive inhibitors bind either in or close to the ATP binding site (P-loop)^{131,215}, whereas allosteric inhibitors either bind to the loop L5 region or at the interface between helix $\alpha 4$ and $\alpha 6$.¹³¹ The allosteric pocket of Eg5 is an attractive target, not only because it can provide specificity to inhibitors over closely related kinesins, which generally possess a much shorter loop L5 region that cannot furnish a comparable binding pocket, but also have an edge over other inhibitor binding in competition to ATP/ADP due to the highly conserved nucleotide site. Previous work has shown that ispinesib is a promising allosteric Eg5 inhibitor that is already in multiple phase II clinical trials and the work presented in this thesis towards understanding its interaction will inform the design of novel compounds in this site. It is therefore surprising that so far no structural data in the form of PDB co-ordinates for the Eg5-ispinesib complex had been available. The structure presented in this thesis of the ternary Eg5-ADP-ispinesib complex seeks to remedy this. The interaction of ispinesib with Eg5 is dominated by hydrophobic interactions and there are essentially no hydrophilic interactions. Analysis of the binding mode, as well as a comparison with other allosteric Eg5 inhibitors, suggests a number of ways in which ispinesib could be modified while either retaining or even improving its affinity for Eg5, an argument further supported by the development of the second generation ispinesib based analogue SB-743921⁸ and the amount of additional data on the development of ispinesib-related compounds in the patent literature²¹⁶. Interactions of the quinazolinone ring system in ispinesib with residues of Eg5 form a crucial part in the high potency of the inhibitor. The aromatic rings of Trp127, Tyr211 and Phe239 around the inhibitor-binding pocket of Eg5 interact strongly with this ring system of ispinesib leading to tight binding of the inhibitor. Recent development of SB743921 explores substitution of atoms in the aromatic portion

of ispinesib increasing bonding energies in and around the ring system. In addition, the chlorine substituent of ispinesib does not harness all interactions with Phe239 and Leu216 suggesting that affinity can be further improved by additional substitutions on the benzo-ring. Modification of the solvent-exposed amino-alkyl group may not enable better interactions but instead provide better physiochemical properties, which might help in better modulating the pharmacokinetic properties of the drug candidate. This information should prove invaluable for future iterations of this inhibitor scaffold, be it to improve potency, to alter pharmacokinetics or to counter the ever-present threat of resistance¹²⁷.

4.1.2 The underlying mechanism of resistance of Eg5 towards small molecule inhibitors

The major challenge in cancer chemotherapy is the emergence of resistance. Tumour cells may take different routes to avoid inhibition of a primary target, which include a wide variety of mechanisms such as up-regulating alternative pathways, increasing expression of drug efflux pumps or expressing drug-resistant variants of the targeted protein for example through point mutations in, or close to, the inhibitor-binding pocket. These processes are evolutionary adaptations to the natural selection pressure exerted by intervention with a chemotherapeutic agent. Most of the information on the mechanisms that lead to the development of resistance is gained from experiments conducted in tumour cell lines and only sparse information is available for resistance mechanisms in tumours since this requires tumour biopsies after relapse. In some cases the identification of the underlying mechanism that leads to resistance during cancer treatment may lead to the development of second generation treatments, as observed for example for the treatment of CML²¹⁷.

When tumour cells lines were exposed to prolonged treatment with ispinesib; it led to the development of resistance demonstrating mutations in the loop L5 region of Eg5. The integrated combination of methods presented in this thesis, including kinetic assays, calorimetry, X-ray crystallography together with molecular simulations (Dr. Nahoum Anthony and Prof. Simon Mackay) were performed to understand the mechanism of resistance against the second generation clinical candidate SB743921 at the molecular level. The kinetic parameters in the form of k_{cat} , $K_{m,ATP}$ and $K_{0.5,MTS}$ for the catalytic basal and MT-stimulated ATPase activity are essentially unchanged for the wild-type and

mutated forms of Eg5. The single mutations Eg5^{A133D} and Eg5^{D130V} generate considerable resistance factors of 3,500 - 4,300 in the presence of SB743921. Subsequent calorimetric analyses confirm that the binding affinity of SB743921 for the mutated Eg5 proteins is markedly reduced, which accounts for their continued turnover of the ATP hydrolysis cycle and the consequent motor function in the presence of the inhibitor. Again, from an evolutionary perspective this is to be expected – natural selection has resulted in a mutant protein with lower affinity for the inhibitor while retaining function in response to the selective pressure of chemotherapeutic intervention, Sheth and colleagues^{126,128} showed that inhibition by another Eg5 inhibitor, monastrol, could also be greatly reduced by these two mutations. Inhibitory effects of STLC are also observed to diminish in the mutant enzymes. In fact, the mutations not only diminish but also fully abolish the inhibitory effects of STLC. It is therefore striking that these mutations not only confer resistance to ispinesib and to its structurally related analogue SB743921, but also to other Eg5-targeting agents with distinct chemical scaffolds such as monastrol and STLC. It is likely that other ispinesib-related agents in clinical development would also be inactivated by these mutations.

The most intriguing question that arises is how the reduced affinity has emerged. The thermodynamics of the binding free energy as revealed by the calorimetric studies indicate that the mutated proteins actually have an improved enthalpic interaction with SB743921. In other words, when a complex between a mutated protein and inhibitor is formed, the net non-bonded interactions are more favourable compared with Eg5^{WT}. Mutations invoking resistance against small molecule inhibitors have predominantly been explained through reduced interactions involving steric or electrostatic repulsion somewhere in the binding site²¹⁸. Calorimetric, crystallographic and molecular simulation studies suggest that this is not necessarily the case, and that there are other factors in which have significant implications for drug design against resistant forms of proteins that may evolve during clinical exposure. The crystal structures of Eg5^{WT} and Eg5^{A133D} in complex with SB743921 showed that the mutation does not produce any obvious repulsive interactions compared with the wild-type, and indeed, that the two complexes are very similar in this region. Additional simulation studies with Eg5^{A133D} confirm that in terms of enthalpy, SB743921 makes more favourable interactions with the binding site identify that specific residues make quantifiably better interactions in the mutated form, which overall can explain the improved enthalpy shown experimentally. Significantly, the

mutated residue itself does not impact on the non-bonded interactions. Instead, the thermodynamic behaviour of the protein due to the mutation creates disorder in other regions of the protein following the second law of thermodynamics and this plays a major role in the development of resistance.

Crystallographic and MD studies confirm the enthalpic gain through mutation but its overall relation to the reduced affinity for the chemotherapeutic agent and its ability to allow normal catalytic function is intriguing. The role of water is thought to be fundamental to this process, as all biological processes are carried out in this solvent. In this case, with respect to ligand, SB743921 – this compound is the same in all studies, so the hydrophobic effect of promoting ligand binding through its expulsion from water cavities is constant. Thermodynamically, it is the differences between the complexes that are the key in this process. Crystallographic studies show that structurally the mutants in the absence of SB743921 are practically identical, enabling them to function normally as the wild-type proteins. Thus the reactants are virtually identical but the products are different and therefore changes in entropy are associated with the complex structure itself. To gain further insight into such changes in disorder and the linkage to the movement of the mutated complex along with its propensity to rigidify during binding for the mutants compared with the wild-type MD simulations were carried out. Reduced flexibility in the protein-ligand complex is associated with increased order and structural restraint, which is unfavourable in entropy terms. The A133D mutation can cause a chain of local rearrangement of hydrogen bonding and salt bridging (Figure 4-1) that transmits structural changes throughout the whole complex and causes reduced flexibility in specific regions. New hydrogen bonds between residues in different sub-domains (Figure 4-2) appear to check movement and rigidify the overall complex. The enthalpic gain through tighter association with the binding site is therefore lost through the transmitted ordering of the complex.

These analyses refine the previously held notions that resistance is a result of a protein having reduced affinity for a ligand through less favourable interactions with the binding site. Essentially, it can be illustrated from our experimental results that mutations can induce resistance by using the randomness of nature in its evolutionary selection process that has found a way to confound the ordered attempts of rational drug design. The resistance mechanism can be thought of as an extreme example of “entropy/enthalpy compensation”²¹⁹ where a beneficial enthalpic component is balanced, and in this case

outweighed, by an opposing entropic effect. The phenomenon typically occurs when ligands are designed to optimise interactions with a receptor but here, natural selection has resulted in a similar result.

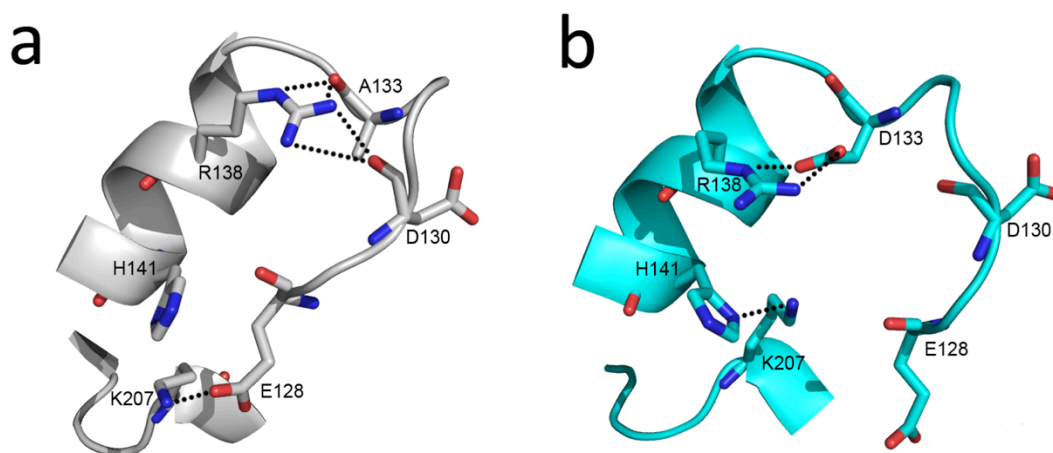


Figure 4-1: Structural changes that occur around the A133D mutation due to thermodynamic fluctuation on inhibitor-binding.

a) Interactions seen in the minimised average structure of the SB743921-Eg5^{WT} complex (gray) taken from the production phase of the equilibrated structure (hydrogen bonds are displayed as dotted lines). Arg138 guanidine forms hydrogen bonds with the backbone carbonyl oxygens of Ala133 and Asp130. Additionally, under these simulated conditions, a salt bridge is formed between Glu128 and Lys207. b) Interactions seen in the minimised average structure of the SB743921-Eg5^{A133D} complex (cyan) taken from the production phase of the equilibrated structure. Instead of the Arg138 guanidine hydrogen bonding with the backbone carbonyl oxygens of Ala133 and Asp130 seen in the simulated wild-type complex, the Arg side-chain moves by 4.1 Å and instead makes a salt bridge with the new Asp133 carboxylate. As a result of this shift, the side-chain of Glu128 is moved away from Asp133 by 3.3 Å and the salt bridge between Glu128 and Lys207 is broken. There are a number of consequences of this rearrangement. Firstly, in the mutant form Lys207 is able to move 5.4 Å to form a hydrogen bond with the His141 side-chain, thus moving helix $\alpha 3$ (207-225) closer to the inhibitor-binding pocket. As a result, Arg221 and Glu116 are closer and form a stronger salt bridge, which reduces the flexibility of residues 205-209 in the mutant.

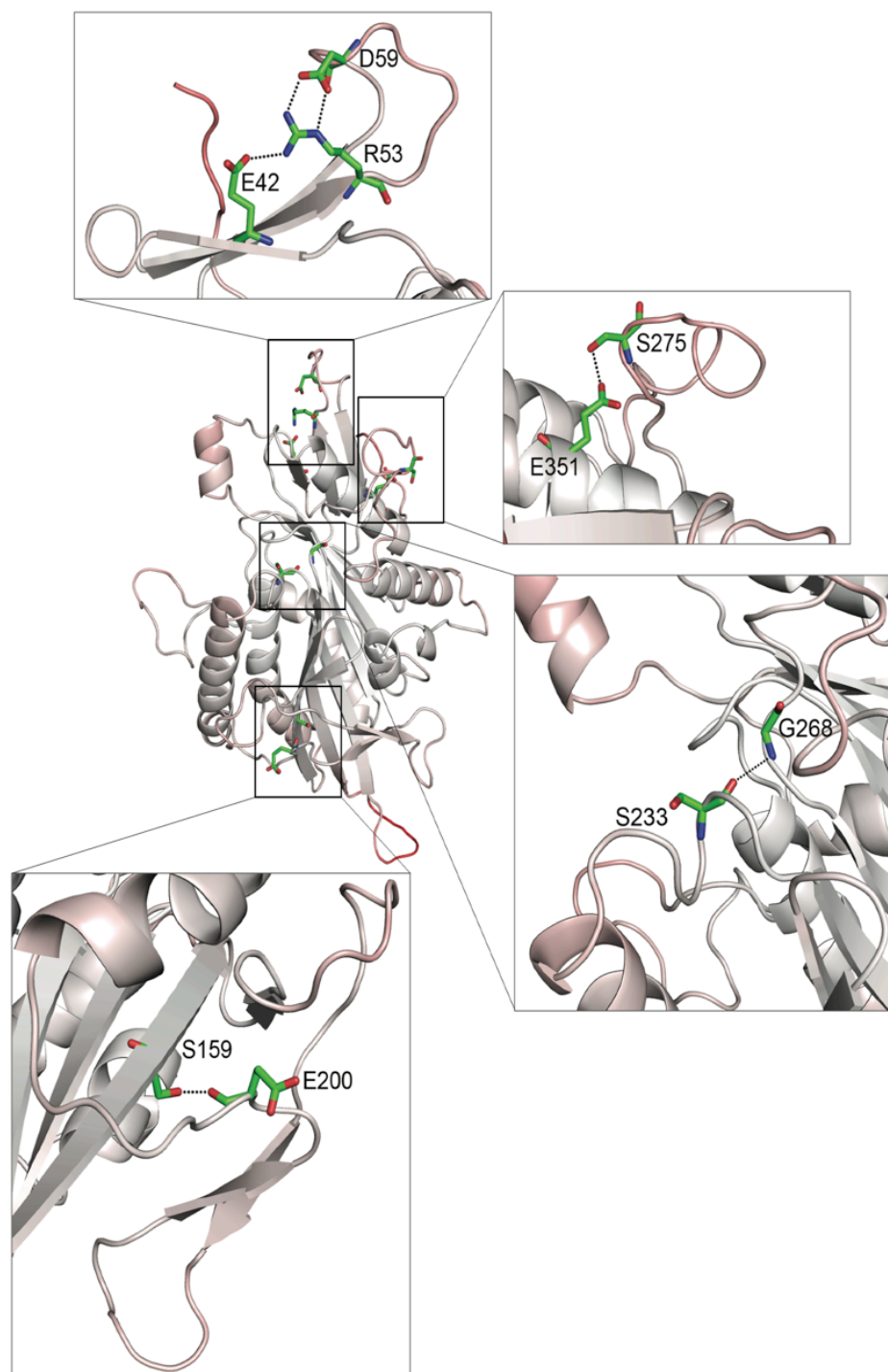


Figure 4-2: The far-reaching effects of the A133D mutation propagated throughout the SB743921- Eg5^{A133D} complex during MD simulations that predicts the rigidification of the structure when compared with the Eg5^{WT} complex.

The red colour and its depth in the protein are associated with higher fluctuation. Residues that form new interactions are highlighted. The backbone carbonyl oxygen of Glu200 is able to make a hydrogen bond with the side-chain hydroxyl of Ser159, reducing fluctuation of residues 198-202. Two salt bridges form with the side-chain of Arg53, one with the Glu42 carboxylate on one side and with Asp59 on the other, both of which rigidify loop L2 (aa 55-62) in the mutant. A hydrogen bond is also apparent in the mutant between the backbone carbonyl of Ser233 and the backbone NH of Gly268, which anchors helix α_3 (aa 222-235) in place, whilst another hydrogen bond between the side-chain carboxylate of Glu351 in helix α_6 (aa 344-355) and the side-chain hydroxyl of Ser275 anchors loop L11 (aa 273-282) in place.

4.1.3 Dissection of the novel allosteric site of Eg5 and its significance in drug discovery of Eg5 targeting drugs

Development of resistance against ispinesib in the loop L5 allosteric site of Eg5 posed a challenge to devise new methods of targeting Eg5. One potential method is to target a new allosteric site with inhibitors, which is unaffected by mutations in the loop L5 region. Previous studies based on the BI8 series of inhibitors have suggested the presence of a new site located around the helix $\alpha 6$ – neck linker region^{128,131} but experimental identification of this site has been elusive. We solved the crystal structure of the Eg5 motor domain in complex with one such inhibitor BI8 suggested to bind to the new allosteric site. The crystal structure of the Eg5-ADP-BI8 complex reveals a novel inhibitor-binding site, between helix $\alpha 4$ and $\alpha 6$ of the Eg5 motor domain, remote from the extensively studied ispinesib allosteric site. Unexpectedly, inhibitor-binding was also observed close to the ispinesib site but using three orthogonal biophysical and biochemical techniques, we have shown that high affinity binding is the result of binding to the novel site.

The binding mode of the allosteric inhibitor BI8 to the pocket formed by helix $\alpha 2$ /loop L5/helix $\alpha 3$ and the sequence of structural changes leading to the final inhibitor bound state have been revealed in considerable detail using steady state and pre-steady state kinetics as well as biophysical and structural methods.^{108,114} The crystal structure of the Eg5-ADP-BI8 complex provides the structural basis for understanding the mechanism of action of compounds such as BI8 that target the novel inhibitor-binding pocket near helices $\alpha 4/\alpha 6$. An obvious mechanism is evident from the analysis of the inhibitor-binding pocket where, by binding between helix $\alpha 4$ of the switch II cluster and helix $\alpha 6$ preceding the neck linker, BI8 might lock the conformation of Eg5. Consequently, Eg5 may be unable to undergo the conformational changes required by the catalytic cycle. Small changes in the nucleotide-binding pocket induced by ATP hydrolysis are thought to lead to amplified structural changes in the switch II cluster and neck linker region which provoke the molecular motion responsible for shifting the two anti-parallel MTs apart to form the bipolar spindle. As observed for loop L5-targeting drugs, the neck linker conformation is in an ordered state that is either in an intermediate ‘undocked’ or final ‘docked’ state slowing down the ATP release leading to slower motor movement across MTs. In the BI8 complex the neck linker is an ordered ‘undocked’ state, which might follow similar mechanism of inhibition of Eg5 ATPase activity. BI8 bound between helices $\alpha 4$ and $\alpha 6$

(Figure 4-3) might hamper the movement of both the switch II cluster and the $\alpha 6$ -neck linker regions. This would not only reduce the ATP turnover by Eg5 but also hinder its motility along MTs, which are pivotal for proper function. Thus, it can be said that though BI8 does not exactly mimic the mechanism as for loop L5 targeting inhibitors but shares major resemblance with the mechanism of inhibition of these drug candidates.

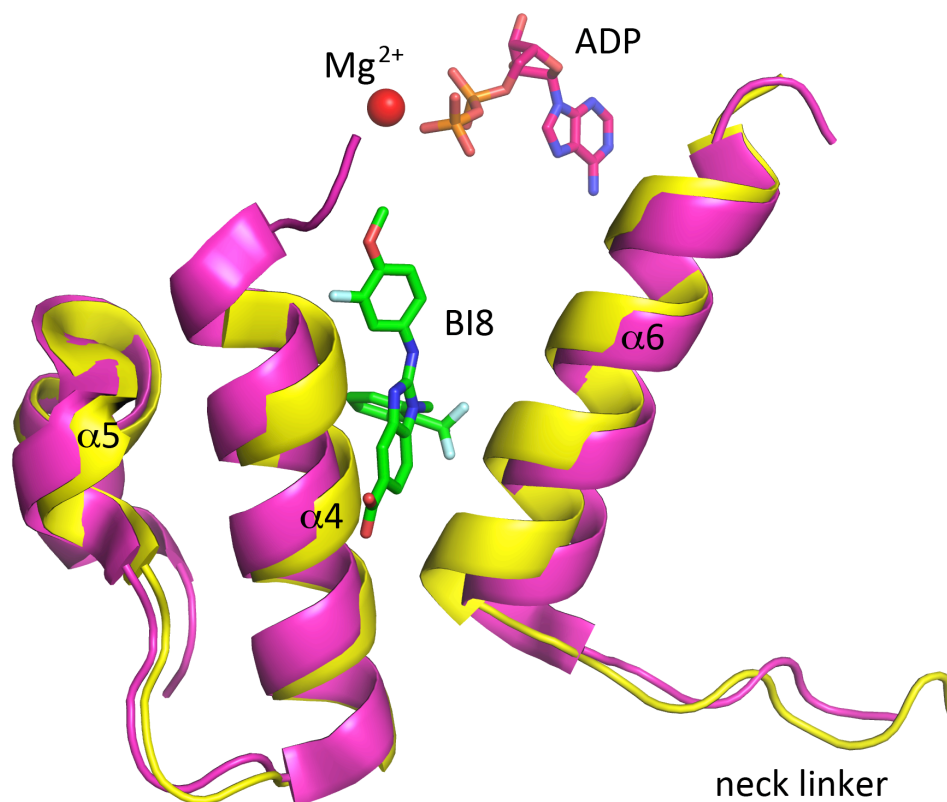


Figure 4-3: BI8 binding and mechanism of inhibition.

BI8 (green) is docked at the interface of helices $\alpha 4$ and $\alpha 6$ about 13 Å away from the nucleotide-binding site demonstrated with the structure of ADP (orange-red). During the ATP hydrolysis cycle of Eg5 large conformational changes in switch II cluster cause movements around the $\alpha 6$ -neck linker region causing Eg5 to move along MTs²²⁰ which might be blocked due to loss of flexibility of these region on BI8 binding.

This discovery of a new inhibitor-binding site in Eg5, coupled with the identification of the benzimidazole series of inhibitors, creates the opportunity for both structure-based and ligand based approaches to develop novel inhibitor series in Eg5. The significant conformational changes on ligand binding generate a well-defined “druggable” pocket and the crystal structure now enables the application of structure-based design and screening approaches. Significantly, the development of these inhibitors at this site into cancer therapeutics has the potential for delaying the onset of resistance to drugs targeting the ispinesib site. This could be particularly relevant since mutants highly resistant to ispinesib treatment have been observed in cell culture and combination

therapy is a well-established approach to slowing the onset of resistance.¹²⁸ With the existing benzimidazole inhibitors already demonstrating inhibition in the nanomolar range *in vitro*, there is an exciting possibility that these drugs can provide a new avenue towards cancer chemotherapy along with the validated MTs targeting drugs and Eg5 loop L5-targeting drugs.

4.1.4 Future perspectives of drugs targeting Eg5

Based on the mechanistic characterisation of Eg5 targeting drugs using kinetic, biophysical and studies, several new approaches can be used for the future development of Eg5 inhibitors. The structure of ispinesib provides a basis to understand the underlying mechanism of highly potent drugs in this series. New structurally similar compounds can thus be synthesised and used for further increasing the potency, efficacy and drug-like properties. The X-ray structure of the complex also makes it possible to comprehend the individual interactions of different residues in the inhibitor-binding pocket of Eg5 with ispinesib. Thus, a combined approach of structure-based and ligand based drug design will take ispinesib and ispinesib like compounds a step further where not just the potency but also the drug-like properties of the compound can be improved.

Identifying a role of thermodynamics of inhibitor-binding reveals a unique mechanism of resistance. Development of resistance is an inherent property, which is inevitable for most if not all drugs. Previously identified resistance mechanisms for cancer chemotherapeutic drugs at various stages of drug development are mostly caused by steric hindrance developed against the inhibitor.²²¹⁻²²⁴ The involvement of 'enthalpy/entropy compensation' in the development of resistance is novel for cancer targeting drugs. Hence, the development of new ispinesib-related compounds has to be approached in a way which does not only aims at increasing the efficacy of the drug candidates but also goes through a thorough investigation of the thermodynamic property of binding.

The alternative approach to address resistance is to find inhibitors that target a different allosteric site. The crystal structure of the Eg5-ADP-BI8 complex shows that the novel benzimidazole compound BI8 can bind to a new site between helices $\alpha 4$ and $\alpha 6$ and also to the region around the other well studied inhibitor site comprising of loop L5 and helices $\alpha 2$ and $\alpha 3$. This crystal structure is the first experimental demonstration of this site and opens up new areas towards Eg5 drug discovery. BI8 has been shown to bind to

the novel site with a higher affinity than the site near loop L5 thus development of BI8 analogues with higher potency will be the future directions. With existing inhibitors already showing IC_{50} s in the nanomolar range, the detailed characterisation of the interactions generated by the structure provides a strong foundation for these future efforts.

4.2 Development of MPP1 as a new drug target

MPP1, with its apparently exclusive role in cytokinesis, is a possible new target for cancer chemotherapy. Up-regulation of MPP1 in bladder cancer provides evidence for it being a potential therapeutic target.¹⁴⁵ The inhibitor of MPP1 reported in this thesis provides the initial step towards MPP1 drug development.

4.2.1 Analysing the inhibitor of MPP1

Many of the so far identified secondary metabolites in lichens are unique. Lichen metabolites have been shown to possess interesting biological properties including antioxidant, antimicrobial, antiherbivore and insecticidal activities.²²⁵ Several lichens have also demonstrated weak cytotoxic activity²²⁶ and for a few isolated lichen metabolites growth inhibition and apoptotic cell death has been reported.²²⁷ One interesting class of lichen compounds is represented by the depsidones containing the dibenzodioxepinone scaffold (Figure 4-4). To date however the identity of the protein targets for any of the active compounds has not been clear. Identification of MPP1 as one possible target for depsidones provides an interesting prospect towards cancer chemotherapy.

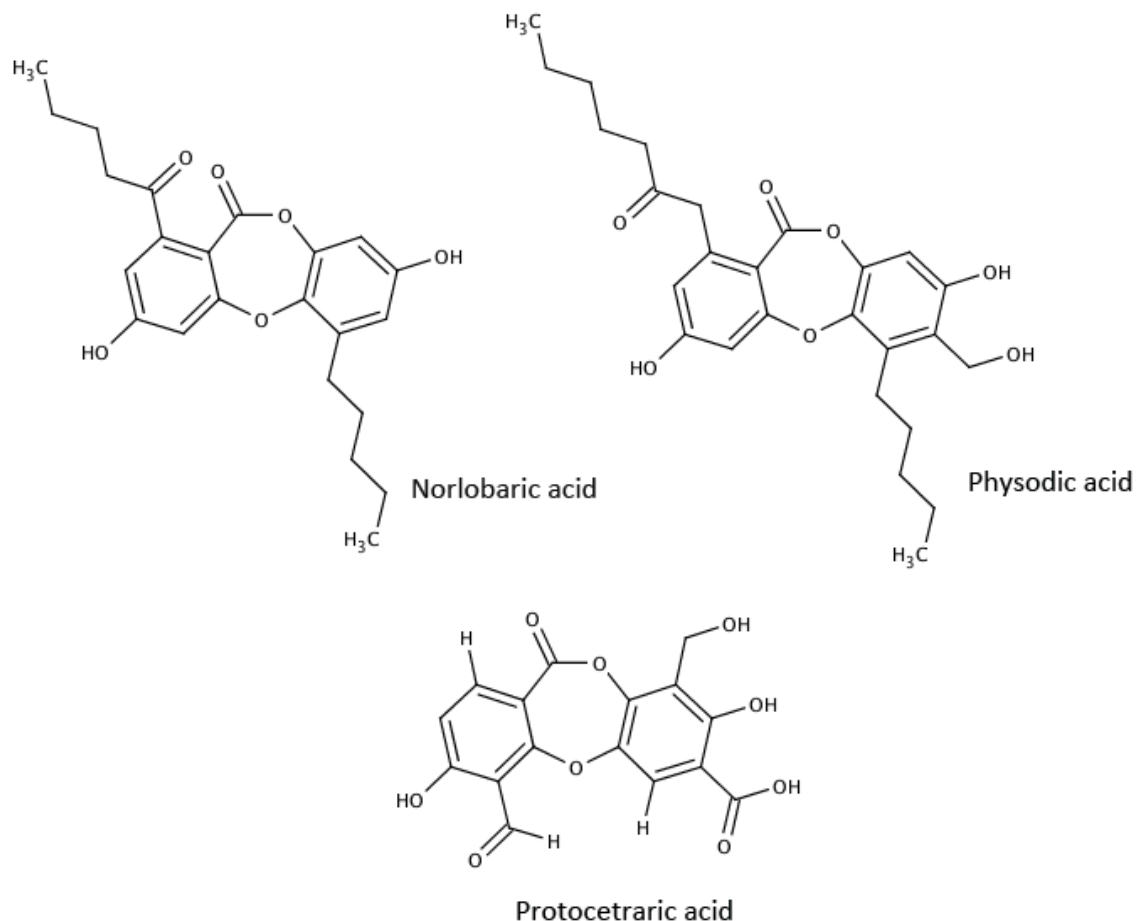


Figure 4-4: Chemical structures of compounds tested for MPP1 inhibition.

The initial tested inhibitor of MPP1; Norlobaric acid is with a dibenzodioxepinone scaffold. Thereafter, Physodic acid was found to be the most potent compound while testing for few analogues from commercial and non-commercial sources. On the other hand Protocetraric acid showed no inhibition of MPP1 ATPase activity. This shows initial evidence of the importance of the alkyl chains in the inhibitors.

The MPP1 inhibitors presented in this thesis open up new areas of drug discovery in this field. A more ligand based approach to getting more potent compounds targeting MPP1 and improving its drug quality will be the things to be studied and analysed hereafter. The identification also provides a tool compound to further probe the cellular function of MPP1.

4.2.2 Orthologues of human MPP1 for drug discovery

Human MPP1 proved difficult to express and purify but the biochemical studies presented here have shown that the human MPP1 inhibitors are also effective against MPP1 from *M. musculus* and *R. norvegicus* whose MPP1 motor domains share around 80 % sequence similarity with the human protein. These proteins can therefore provide a useful surrogate for human MPP1. An important step in drug discovery is to obtain a complex X-ray crystal structure of the protein and the ligand. MPP1 from other species offers a surrogate system that will in future provide opportunities in the direction of improving the potency and stability of MPP1 targeting inhibitors.

4.3 Advances and progress in drug discovery of MKLP-2

4.3.1 Identification of unique structural elements in MKLP-2 involved in inhibitor-binding

The unique feature of kinesin-6 family members is the large approximately ~96 amino acids domain-like insertion in the loop L6 region with unknown function. Other kinesins have only a few residues (about 6 amino acids) at this location. In the absence of any structural information on the MKLP-2 - paprotrain¹⁶⁶ complex, the study on MKLP-2 deletion and substitution mutants in and around loop L6 provides key initial information towards understanding the ligand binding determinants of MKLP-2. The inhibition study has provided a tool, which points to loop L6 being the most essential structural element in MKLP-2 that interacts with paprotrain. MKLP-2 with and without the loop L6 have completely contrasting IC₅₀ values with the inhibitor paprotrain. Whereas the wild-type protein gives an IC₅₀ of around 1 μ M, the inhibitor does not inhibit the mutant MKLP-2 without loop L6. In contrast, three single mutants of MKLP-2 in the helices and strands around loop L6 show limited decrease in potency of paprotrain. This data suggests that residues around the loop may also play some role in inhibitor-binding but further studies are necessary to understand their role. A full alanine scanning mutagenesis study would be a more rigorous approach in that respect. An alternative approach is to obtain the crystal structure of MKLP-2 motor domain that would provide information about the structural elements of the domain especially the loop L6. The crystallisation trials presented in this thesis were not fruitful. Further pursuing the trials based on new cloning techniques and using a wider variety of crystallisation approaches may overcome the

difficulties in crystallisation of the MKLP-2 motor domain. Also, using alternative macromolecular structural approaches like NMR or SAXS might provide evidence about the structural organisation of the motor domain and the loop L6 region.

4.3.2 Progress of paprotrain based drug design of MKLP-2 inhibitors

The previously described inhibitor paprotrain was the first MKLP-2 inhibitor that induces apoptosis in a range of tumour cell lines (HCT 116, BXPC-3, CFPAC-1, NCI-H1299, ASPC-1, K562)¹⁶⁶. In an effort to improve the efficiency of paprotrain a series of paprotrain analogues were synthesised by Christophe Labiere from Dr. Catherine Guillou's laboratory at the CNRS in Gif-sur-Yvette, France. On the basis of the *in vitro* SAR study presented in this thesis it can be concluded that the replacement of the pyridine ring by different substituted phenyl rings or modification of the central double bond (length, reduction or substitution degree) lead to inactive or less active compounds which can be related to no inhibition in the SAR study. However, substitution of the indole ring enhanced the potency of the compounds. Taken together, the reported results show analogues of paprotrain are promising lead compounds for the inhibition of human MKLP-2. To support this there are compounds like **121-1** and **387-1**, which show 2-fold higher potency, compared to paprotrain. Further analysis towards improvement of these compounds can be done using the information obtained from these studies.

Overall the SAR study of around 135 compounds only improves the potency by two fold. This suggests the need of a structure based drug design to better understand the interaction between MKLP-2 motor domain and the inhibitor. Future directions would be towards obtaining the structure of MKLP-2 motor domain and find the inhibitor binding site.

4.4 Conclusion

The central theme of the work in this thesis is the structural and mechanistic characterisation of inhibitor-binding to Eg5. The structure of the Eg5-ispinesib complex provides insights into the interactions of a potent tight binding inhibitor that could drive future drug development targeting Eg5. Studies on Eg5 mutants and the new inhibitor BI8 have both explained the little-understood mechanism by which resistance to ispinesib is generated in mutant Eg5 and also identified experimentally for the first time a novel inhibitor-binding site. This work might provide a basis for overcoming or slowing resistance to drugs targeting Eg5.

In addition, significant progress has been made in the expression, purification and biochemical characterisation of two kinesin-6 members; MPP1 and MKLP-2. Identification of the first inhibitor of MPP1 and progress in developing improved inhibitors for MKLP-2 provides new avenues to develop these proteins as possible targets for therapeutic intervention. The work on MPP1 and MKLP-2 presented in this thesis lays the foundations for structural biology and drug design efforts similar to those which have proved very fruitful in Eg5.

5 Bibliography

1. Engelhardt, W.A. & Liubimova, M.N. [Myosin and adenosine triphosphatase (Nature, 144, 688, Oct. 14, 1939)]. *Molekuliarnaia biologiya* **28**, 1229-30 (1994).
2. Gibbons, I.R. Studies on the Protein Components of Cilia from Tetrahymena Pyriformis. *Proceedings of the National Academy of Sciences of the United States of America* **50**, 1002-10 (1963).
3. Brady, S.T. A novel brain ATPase with properties expected for the fast axonal transport motor. *Nature* **317**, 73-5 (1985).
4. Vale, R.D., Reese, T.S. & Sheetz, M.P. Identification of a novel force-generating protein, kinesin, involved in microtubule-based motility. *Cell* **42**, 39-50 (1985).
5. Kamath, K., Oroudjev, E. & Jordan, M.A. Determination of microtubule dynamic instability in living cells. *Methods in cell biology* **97**, 1-14 (2010).
6. Rath, O. & Kozielski, F. Kinesins and cancer. *Nature reviews. Cancer* **12**, 527-39 (2012).
7. Kantarjian, H.M. et al. Phase I/II multicenter study to assess the safety, tolerability, pharmacokinetics and pharmacodynamics of AZD4877 in patients with refractory acute myeloid leukemia. *Investigational new drugs* **30**, 1107-15 (2012).
8. Holen, K.D. et al. A first in human study of SB-743921, a kinesin spindle protein inhibitor, to determine pharmacokinetics, biologic effects and establish a recommended phase II dose. *Cancer chemotherapy and pharmacology* **67**, 447-54 (2011).
9. Beer, T.M. et al. Southwest Oncology Group phase II study of ispinesib in androgen-independent prostate cancer previously treated with taxanes. *Clinical genitourinary cancer* **6**, 103-9 (2008).
10. Lee, C.W. et al. A phase II study of ispinesib (SB-715992) in patients with metastatic or recurrent malignant melanoma: a National Cancer Institute of Canada Clinical Trials Group trial. *Investigational new drugs* **26**, 249-55 (2008).
11. Kolomeisky, A.B. & Fisher, M.E. Molecular motors: a theorist's perspective. *Annual review of physical chemistry* **58**, 675-95 (2007).
12. Vale, R.D. & Fletterick, R.J. The design plan of kinesin motors. *Annual review of cell and developmental biology* **13**, 745-77 (1997).
13. Lasek, R.J. & Brady, S.T. Attachment of transported vesicles to microtubules in axoplasm is facilitated by AMP-PNP. *Nature* **316**, 645-7 (1985).
14. Scholey, J.M., Porter, M.E., Grissom, P.M. & McIntosh, J.R. Identification of kinesin in sea urchin eggs, and evidence for its localization in the mitotic spindle. *Nature* **318**, 483-6 (1985).
15. Good, J.A., Skoufias, D.A. & Kozielski, F. Elucidating the functionality of kinesins: an overview of small molecule inhibitors. *Seminars in cell & developmental biology* **22**, 935-45 (2011).
16. Hirokawa, N., Noda, Y., Tanaka, Y. & Niwa, S. Kinesin superfamily motor proteins and intracellular transport. *Nature reviews. Molecular cell biology* **10**, 682-96 (2009).
17. Miki, H., Setou, M., Kaneshiro, K. & Hirokawa, N. All kinesin superfamily protein, KIF, genes in mouse and human. *Proceedings of the National Academy of Sciences of the United States of America* **98**, 7004-11 (2001).
18. Dagenbach, E.M. & Endow, S.A. A new kinesin tree. *Journal of cell science* **117**, 3-7 (2004).
19. Yang, J.T., Laymon, R.A. & Goldstein, L.S. A three-domain structure of kinesin heavy chain revealed by DNA sequence and microtubule binding analyses. *Cell* **56**, 879-89 (1989).
20. Woehlke, G. & Schliwa, M. Walking on two heads: the many talents of kinesin. *Nature reviews. Molecular cell biology* **1**, 50-8 (2000).
21. Gruneberg, U. et al. KIF14 and citron kinase act together to promote efficient cytokinesis. *The Journal of cell biology* **172**, 363-72 (2006).
22. Carleton, M. et al. RNA interference-mediated silencing of mitotic kinesin KIF14 disrupts cell cycle progression and induces cytokinesis failure. *Molecular and cellular biology* **26**, 3853-63 (2006).

23. Hunter, A.W. et al. The kinesin-related protein MCAK is a microtubule depolymerase that forms an ATP-hydrolyzing complex at microtubule ends. *Molecular cell* **11**, 445-57 (2003).
24. Kull, F.J., Sablin, E.P., Lau, R., Fletterick, R.J. & Vale, R.D. Crystal structure of the kinesin motor domain reveals a structural similarity to myosin. *Nature* **380**, 550-5 (1996).
25. Liu, H.L., Pemble Iv, C.W. & Endow, S.A. Neck-motor interactions trigger rotation of the kinesin stalk. *Scientific reports* **2**, 236 (2012).
26. Ogawa, T., Nitta, R., Okada, Y. & Hirokawa, N. A common mechanism for microtubule destabilizers-M type kinesins stabilize curling of the protofilament using the class-specific neck and loops. *Cell* **116**, 591-602 (2004).
27. Parke, C.L., Wojcik, E.J., Kim, S. & Worthylake, D.K. ATP hydrolysis in Eg5 kinesin involves a catalytic two-water mechanism. *The Journal of biological chemistry* **285**, 5859-67 (2010).
28. Turner, J. et al. Crystal structure of the mitotic spindle kinesin Eg5 reveals a novel conformation of the neck-linker. *The Journal of biological chemistry* **276**, 25496-502 (2001).
29. Sablin, E.P., Kull, F.J., Cooke, R., Vale, R.D. & Fletterick, R.J. Crystal structure of the motor domain of the kinesin-related motor ncd. *Nature* **380**, 555-9 (1996).
30. Smith, C.A. & Rayment, I. X-ray structure of the magnesium(II).ADP.vanadate complex of the Dictyostelium discoideum myosin motor domain to 1.9 Å resolution. *Biochemistry* **35**, 5404-17 (1996).
31. Fisher, A.J. et al. X-ray structures of the myosin motor domain of Dictyostelium discoideum complexed with MgADP.BeFx and MgADP.AIF₄. *Biochemistry* **34**, 8960-72 (1995).
32. Kull, F.J., Vale, R.D. & Fletterick, R.J. The case for a common ancestor: kinesin and myosin motor proteins and G proteins. *Journal of muscle research and cell motility* **19**, 877-86 (1998).
33. Nitta, R., Kikkawa, M., Okada, Y. & Hirokawa, N. KIF1A alternately uses two loops to bind microtubules. *Science* **305**, 678-83 (2004).
34. Woehlke, G. et al. Microtubule interaction site of the kinesin motor. *Cell* **90**, 207-16 (1997).
35. Hirose, K., Lowe, J., Alonso, M., Cross, R.A. & Amos, L.A. Congruent docking of dimeric kinesin and ncd into three-dimensional electron cryomicroscopy maps of microtubule-motor ADP complexes. *Molecular biology of the cell* **10**, 2063-74 (1999).
36. Kaan, H.Y., Hackney, D.D. & Kozielski, F. The structure of the kinesin-1 motor-tail complex reveals the mechanism of autoinhibition. *Science* **333**, 883-5 (2011).
37. Sindelar, C.V. et al. Two conformations in the human kinesin power stroke defined by X-ray crystallography and EPR spectroscopy. *Nature structural biology* **9**, 844-8 (2002).
38. Zhu, C. et al. Functional analysis of human microtubule-based motor proteins, the kinesins and dyneins, in mitosis/cytokinesis using RNA interference. *Molecular biology of the cell* **16**, 3187-99 (2005).
39. Sablin, E.P. & Fletterick, R.J. Nucleotide switches in molecular motors: structural analysis of kinesins and myosins. *Current opinion in structural biology* **11**, 716-24 (2001).
40. de Cuevas, M., Tao, T. & Goldstein, L.S. Evidence that the stalk of Drosophila kinesin heavy chain is an alpha-helical coiled coil. *The Journal of cell biology* **116**, 957-65 (1992).
41. Hackney, D.D., Levitt, J.D. & Suhan, J. Kinesin undergoes a 9 S to 6 S conformational transition. *The Journal of biological chemistry* **267**, 8696-701 (1992).
42. Brown, C.L. et al. Kinesin-2 is a motor for late endosomes and lysosomes. *Traffic* **6**, 1114-24 (2005).
43. Verhey, K.J. & Hammond, J.W. Traffic control: regulation of kinesin motors. *Nature reviews. Molecular cell biology* **10**, 765-77 (2009).
44. Grummt, M. et al. Importance of a flexible hinge near the motor domain in kinesin-driven motility. *The EMBO journal* **17**, 5536-42 (1998).
45. Hackney, D.D. & Stock, M.F. Kinesin's IAK tail domain inhibits initial microtubule-stimulated ADP release. *Nature cell biology* **2**, 257-60 (2000).
46. Wendt, T. et al. A structural analysis of the interaction between ncd tail and tubulin protofilaments. *Journal of molecular biology* **333**, 541-52 (2003).

47. Karabay, A. & Walker, R.A. The Ncd tail domain promotes microtubule assembly and stability. *Biochemical and biophysical research communications* **258**, 39-43 (1999).
48. Howard, J., Hudspeth, A.J. & Vale, R.D. Movement of microtubules by single kinesin molecules. *Nature* **342**, 154-8 (1989).
49. Hackney, D.D. Highly processive microtubule-stimulated ATP hydrolysis by dimeric kinesin head domains. *Nature* **377**, 448-50 (1995).
50. Kanai, Y., Dohmae, N. & Hirokawa, N. Kinesin transports RNA: isolation and characterization of an RNA-transporting granule. *Neuron* **43**, 513-25 (2004).
51. Hirokawa, N. Organelle transport along microtubules - the role of KIFs. *Trends in cell biology* **6**, 135-41 (1996).
52. Cole, D.G. Intraflagellar transport: keeping the motors coordinated. *Current biology : CB* **15**, R798-801 (2005).
53. Hao, L., Acar, S., Evans, J., Ou, G. & Scholey, J.M. Analysis of intraflagellar transport in *C. elegans* sensory cilia. *Methods in cell biology* **93**, 235-66 (2009).
54. Hirokawa, N. & Noda, Y. Intracellular transport and kinesin superfamily proteins, KIFs: structure, function, and dynamics. *Physiological reviews* **88**, 1089-118 (2008).
55. Hirokawa, N., Noda, Y. & Okada, Y. Kinesin and dynein superfamily proteins in organelle transport and cell division. *Current opinion in cell biology* **10**, 60-73 (1998).
56. Blangy, A. et al. Phosphorylation by p34cdc2 regulates spindle association of human Eg5, a kinesin-related motor essential for bipolar spindle formation in vivo. *Cell* **83**, 1159-69 (1995).
57. Le Guellec, R., Paris, J., Couturier, A., Roghi, C. & Philippe, M. Cloning by differential screening of a *Xenopus* cDNA that encodes a kinesin-related protein. *Molecular and cellular biology* **11**, 3395-8 (1991).
58. Barton, N.R., Pereira, A.J. & Goldstein, L.S. Motor activity and mitotic spindle localization of the *Drosophila* kinesin-like protein KLP61F. *Molecular biology of the cell* **6**, 1563-74 (1995).
59. Hildebrandt, E.R. & Hoyt, M.A. Mitotic motors in *Saccharomyces cerevisiae*. *Biochimica et biophysica acta* **1496**, 99-116 (2000).
60. Schaar, B.T., Chan, G.K., Maddox, P., Salmon, E.D. & Yen, T.J. CENP-E function at kinetochores is essential for chromosome alignment. *The Journal of cell biology* **139**, 1373-82 (1997).
61. Wordeman, L., Wagenbach, M. & von Dassow, G. MCAK facilitates chromosome movement by promoting kinetochore microtubule turnover. *The Journal of cell biology* **179**, 869-79 (2007).
62. Stumpff, J., von Dassow, G., Wagenbach, M., Asbury, C. & Wordeman, L. The kinesin-8 motor Kif18A suppresses kinetochore movements to control mitotic chromosome alignment. *Developmental cell* **14**, 252-62 (2008).
63. Wordeman, L. & Mitchison, T.J. Identification and partial characterization of mitotic centromere-associated kinesin, a kinesin-related protein that associates with centromeres during mitosis. *The Journal of cell biology* **128**, 95-104 (1995).
64. Stout, J.R. et al. Kif18B interacts with EB1 and controls astral microtubule length during mitosis. *Molecular biology of the cell* **22**, 3070-80 (2011).
65. Li, J., Wang, J., Jiao, H., Liao, J. & Xu, X. Cytokinesis and cancer: Polo loves ROCK'n' Rho(A). *Journal of genetics and genomics = Yi chuan xue bao* **37**, 159-72 (2010).
66. Fontijn, R.D. et al. The human kinesin-like protein RB6K is under tight cell cycle control and is essential for cytokinesis. *Molecular and cellular biology* **21**, 2944-55 (2001).
67. Abaza, A. et al. M phase phosphoprotein 1 is a human plus-end-directed kinesin-related protein required for cytokinesis. *The Journal of biological chemistry* **278**, 27844-52 (2003).
68. Xu, X., He, C., Zhang, Z. & Chen, Y. MKLP1 requires specific domains for its dendritic targeting. *Journal of cell science* **119**, 452-8 (2006).
69. Oguchi, Y., Uchimura, S., Ohki, T., Mikhailenko, S.V. & Ishiwata, S. The bidirectional depolymerizer MCAK generates force by disassembling both microtubule ends. *Nature cell biology* **13**, 846-52 (2011).

70. Ems-McClung, S.C. & Walczak, C.E. Kinesin-13s in mitosis: Key players in the spatial and temporal organization of spindle microtubules. *Seminars in cell & developmental biology* **21**, 276-82 (2010).
71. Huang, Y. et al. Defects in chromosome congression and mitotic progression in KIF18A-deficient cells are partly mediated through impaired functions of CENP-E. *Cell cycle* **8**, 2643-9 (2009).
72. Lee, Y.M. et al. Cell cycle-regulated expression and subcellular localization of a kinesin-8 member human KIF18B. *Gene* **466**, 16-25 (2010).
73. Kurasawa, Y., Earnshaw, W.C., Mochizuki, Y., Dohmae, N. & Todokoro, K. Essential roles of KIF4 and its binding partner PRC1 in organized central spindle midzone formation. *The EMBO journal* **23**, 3237-48 (2004).
74. Morris, N.R. Mitotic mutants of *Aspergillus nidulans*. *Genetical research* **26**, 237-54 (1975).
75. Kapitein, L.C. et al. The bipolar mitotic kinesin Eg5 moves on both microtubules that it crosslinks. *Nature* **435**, 114-8 (2005).
76. Liu, M. et al. Parkin regulates Eg5 expression by Hsp70 ubiquitination-dependent inactivation of c-Jun NH2-terminal kinase. *The Journal of biological chemistry* **283**, 35783-8 (2008).
77. Hirokawa, N., Nitta, R. & Okada, Y. The mechanisms of kinesin motor motility: lessons from the monomeric motor KIF1A. *Nature reviews. Molecular cell biology* **10**, 877-84 (2009).
78. Kashina, A.S. et al. A bipolar kinesin. *Nature* **379**, 270-2 (1996).
79. Zhao, Y.C., Kull, F.J. & Cochran, J.C. Modulation of the kinesin ATPase cycle by neck linker docking and microtubule binding. *The Journal of biological chemistry* **285**, 25213-20 (2010).
80. Kikkawa, M. et al. Switch-based mechanism of kinesin motors. *Nature* **411**, 439-45 (2001).
81. Cochran, J.C. & Gilbert, S.P. ATPase mechanism of Eg5 in the absence of microtubules: insight into microtubule activation and allosteric inhibition by monastrol. *Biochemistry* **44**, 16633-48 (2005).
82. Harrington, T.D. et al. Analysis of the interaction of the Eg5 Loop5 with the nucleotide site. *Journal of theoretical biology* **289**, 107-15 (2011).
83. Waitzman, J.S. et al. The loop 5 element structurally and kinetically coordinates dimers of the human kinesin-5, Eg5. *Biophysical journal* **101**, 2760-9 (2011).
84. Verhey, K.J., Kaul, N. & Soppina, V. Kinesin assembly and movement in cells. *Annual review of biophysics* **40**, 267-88 (2011).
85. McDonnell, A.V., Jiang, T., Keating, A.E. & Berger, B. Paircoil2: improved prediction of coiled coils from sequence. *Bioinformatics* **22**, 356-8 (2006).
86. Sawin, K.E., LeGuellec, K., Philippe, M. & Mitchison, T.J. Mitotic spindle organization by a plus-end-directed microtubule motor. *Nature* **359**, 540-3 (1992).
87. Cole, D.G., Saxton, W.M., Sheehan, K.B. & Scholey, J.M. A "slow" homotetrameric kinesin-related motor protein purified from *Drosophila* embryos. *The Journal of biological chemistry* **269**, 22913-6 (1994).
88. Ferenz, N.P., Gable, A. & Wadsworth, P. Mitotic functions of kinesin-5. *Seminars in cell & developmental biology* **21**, 255-9 (2010).
89. Sarli, V. & Giannis, A. Targeting the kinesin spindle protein: basic principles and clinical implications. *Clinical cancer research : an official journal of the American Association for Cancer Research* **14**, 7583-7 (2008).
90. Stout, J.R., Rizk, R.S., Kline, S.L. & Walczak, C.E. Deciphering protein function during mitosis in PtK cells using RNAi. *BMC cell biology* **7**, 26 (2006).
91. Blangy, A., Arnaud, L. & Nigg, E.A. Phosphorylation by p34cdc2 protein kinase regulates binding of the kinesin-related motor HsEg5 to the dynactin subunit p150. *The Journal of biological chemistry* **272**, 19418-24 (1997).
92. Kapoor, T.M. & Mitchison, T.J. Eg5 is static in bipolar spindles relative to tubulin: evidence for a static spindle matrix. *The Journal of cell biology* **154**, 1125-33 (2001).

93. Weinger, J.S., Qiu, M., Yang, G. & Kapoor, T.M. A nonmotor microtubule binding site in kinesin-5 is required for filament crosslinking and sliding. *Current biology : CB* **21**, 154-60 (2011).
94. Ma, N. et al. Poleward transport of TPX2 in the mammalian mitotic spindle requires dynein, Eg5, and microtubule flux. *Molecular biology of the cell* **21**, 979-88 (2010).
95. Lin, S. et al. Inhibition of Kinesin-5, a microtubule-based motor protein, as a strategy for enhancing regeneration of adult axons. *Traffic* **12**, 269-86 (2011).
96. Falnikar, A., Tole, S. & Baas, P.W. Kinesin-5, a mitotic microtubule-associated motor protein, modulates neuronal migration. *Molecular biology of the cell* **22**, 1561-74 (2011).
97. Ferhat, L. et al. Expression of the mitotic motor protein Eg5 in postmitotic neurons: implications for neuronal development. *The Journal of neuroscience : the official journal of the Society for Neuroscience* **18**, 7822-35 (1998).
98. Saijo, T. et al. Eg5 expression is closely correlated with the response of advanced non-small cell lung cancer to antimitotic agents combined with platinum chemotherapy. *Lung cancer* **54**, 217-25 (2006).
99. Xing, N.D. et al. A potent chemotherapeutic strategy in prostate cancer: S-(methoxytrityl)-L-cysteine, a novel Eg5 inhibitor. *Asian journal of andrology* **13**, 236-41 (2011).
100. Liu, M. et al. Ectopic expression of the microtubule-dependent motor protein Eg5 promotes pancreatic tumorigenesis. *The Journal of pathology* **221**, 221-8 (2010).
101. Castillo, A., Morse, H.C., 3rd, Godfrey, V.L., Naeem, R. & Justice, M.J. Overexpression of Eg5 causes genomic instability and tumor formation in mice. *Cancer research* **67**, 10138-47 (2007).
102. Hansen, G.M. & Justice, M.J. Activation of Hex and mEg5 by retroviral insertion may contribute to mouse B-cell leukemia. *Oncogene* **18**, 6531-9 (1999).
103. Nowicki, M.O. et al. Chronic myelogenous leukemia molecular signature. *Oncogene* **22**, 3952-63 (2003).
104. Kaiser, A. et al. All-trans-retinoic acid-mediated growth inhibition involves inhibition of human kinesin-related protein HsEg5. *The Journal of biological chemistry* **274**, 18925-31 (1999).
105. Kline-Smith, S.L. & Walczak, C.E. The microtubule-destabilizing kinesin XKCM1 regulates microtubule dynamic instability in cells. *Molecular biology of the cell* **13**, 2718-31 (2002).
106. Ding, S. et al. Overexpression of Eg5 predicts unfavorable prognosis in non-muscle invasive bladder urothelial carcinoma. *International journal of urology : official journal of the Japanese Urological Association* **18**, 432-8 (2011).
107. Mayer, T.U. et al. Small molecule inhibitor of mitotic spindle bipolarity identified in a phenotype-based screen. *Science* **286**, 971-4 (1999).
108. Cochran, J.C., Gatial, J.E., 3rd, Kapoor, T.M. & Gilbert, S.P. Monastrol inhibition of the mitotic kinesin Eg5. *The Journal of biological chemistry* **280**, 12658-67 (2005).
109. DeBonis, S. et al. In vitro screening for inhibitors of the human mitotic kinesin Eg5 with antimitotic and antitumor activities. *Molecular cancer therapeutics* **3**, 1079-90 (2004).
110. Skoufias, D.A. et al. S-trityl-L-cysteine is a reversible, tight binding inhibitor of the human kinesin Eg5 that specifically blocks mitotic progression. *The Journal of biological chemistry* **281**, 17559-69 (2006).
111. Kozielski, F. et al. Proteome analysis of apoptosis signaling by S-trityl-L-cysteine, a potent reversible inhibitor of human mitotic kinesin Eg5. *Proteomics* **8**, 289-300 (2008).
112. Leizerman, I., Avunie-Masala, R., Elkabets, M., Fich, A. & Gheber, L. Differential effects of monastrol in two human cell lines. *Cellular and molecular life sciences : CMLS* **61**, 2060-70 (2004).
113. Yan, Y. et al. Inhibition of a mitotic motor protein: where, how, and conformational consequences. *Journal of molecular biology* **335**, 547-54 (2004).
114. Kaan, H.Y., Ulaganathan, V., Hackney, D.D. & Kozielski, F. An allosteric transition trapped in an intermediate state of a new kinesin-inhibitor complex. *The Biochemical journal* **425**, 55-60 (2010).
115. Maliga, Z. et al. A pathway of structural changes produced by monastrol binding to Eg5. *The Journal of biological chemistry* **281**, 7977-82 (2006).

116. Wallace, A.C., Laskowski, R.A. & Thornton, J.M. LIGPLOT: a program to generate schematic diagrams of protein-ligand interactions. *Protein engineering* **8**, 127-34 (1995).
117. Lad, L. et al. Mechanism of inhibition of human KSP by ispinesib. *Biochemistry* **47**, 3576-85 (2008).
118. Jiang, C. et al. Design, synthesis and evaluation of tetrahydroisoquinolines as new kinesin spindle protein inhibitors. *Chemical & pharmaceutical bulletin* **57**, 567-71 (2009).
119. Cox, C.D. et al. Kinesin spindle protein (KSP) inhibitors. 9. Discovery of (2S)-4-(2,5-difluorophenyl)-n-[(3R,4S)-3-fluoro-1-methylpiperidin-4-yl]-2-(hydroxymethyl)-N-methyl-2-phenyl-2,5-dihydro-1H-pyrrole-1-carboxamide (MK-0731) for the treatment of taxane-refractory cancer. *Journal of medicinal chemistry* **51**, 4239-52 (2008).
120. Kim, K.S. et al. Synthesis and SAR of pyrrolotriazine-4-one based Eg5 inhibitors. *Bioorganic & medicinal chemistry letters* **16**, 3937-42 (2006).
121. Carol, H. et al. Initial testing (stage 1) of the kinesin spindle protein inhibitor ispinesib by the pediatric preclinical testing program. *Pediatric blood & cancer* **53**, 1255-63 (2009).
122. Blagden, S.P. et al. A phase I trial of ispinesib, a kinesin spindle protein inhibitor, with docetaxel in patients with advanced solid tumours. *British journal of cancer* **98**, 894-9 (2008).
123. Esaki, T. et al. Phase I Study to Assess the Safety, Tolerability and Pharmacokinetics of AZD4877 in Japanese Patients with Solid Tumors. *Archives of drug information* **4**, 23-31 (2011).
124. Infante, J.R. et al. A Phase I study to assess the safety, tolerability, and pharmacokinetics of AZD4877, an intravenous Eg5 inhibitor in patients with advanced solid tumors. *Cancer chemotherapy and pharmacology* **69**, 165-72 (2012).
125. Gerecitano, J.F. et al. A Phase I trial of the kinesin spindle protein (Eg5) inhibitor AZD4877 in patients with solid and lymphoid malignancies. *Investigational new drugs* (2012).
126. Sheth, P.R. et al. Thermodynamics of nucleotide and inhibitor binding to wild-type and ispinesib-resistant forms of human kinesin spindle protein. *Biochemistry* **48**, 11045-55 (2009).
127. Jackson, J.R., Auger, K. R., Gilmartin, A., Wai, E. K., Luo, L., Concha, N., Parrish, C. A., Sutton, D., Diamond, M. A., Giardiniere, M., Zhang, S.-Y., Huang, P. S., Wood, K. W., Belmont, L., Lee, Y., Bergnes, G., Anderson, R., Brejc, K., Sakowicz, R. . A resistance mechanism for the KSP inhibitor ispinesib implicates point mutations in the compound binding site. in *Proceedings of the AAC-NCI-EORTC Molecular Targets and Cancer Therapeutics Meeting, AACR* (Philadelphia, PA, 2005).
128. Sheth, P.R. et al. Novel benzimidazole inhibitors bind to a unique site in the kinesin spindle protein motor domain. *Biochemistry* **49**, 8350-8 (2010).
129. Rickert, K.W. et al. Discovery and biochemical characterization of selective ATP competitive inhibitors of the human mitotic kinesin KSP. *Archives of biochemistry and biophysics* **469**, 220-31 (2008).
130. Groen, A.C. et al. A novel small-molecule inhibitor reveals a possible role of kinesin-5 in anastral spindle-pole assembly. *Journal of cell science* **121**, 2293-300 (2008).
131. Luo, L. et al. ATP-competitive inhibitors of the mitotic kinesin KSP that function via an allosteric mechanism. *Nature chemical biology* **3**, 722-6 (2007).
132. Hill, E., Clarke, M. & Barr, F.A. The Rab6-binding kinesin, Rab6-KIFL, is required for cytokinesis. *The EMBO journal* **19**, 5711-9 (2000).
133. Hardin, J., King, R., Thomas-Virnig, C. & Raich, W.B. Zygotic loss of ZEN-4/MKLP1 results in disruption of epidermal morphogenesis in the *C. elegans* embryo. *Developmental dynamics : an official publication of the American Association of Anatomists* **237**, 830-6 (2008).
134. Dereeper, A., Audic, S., Claverie, J.M. & Blanc, G. BLAST-EXPLORER helps you building datasets for phylogenetic analysis. *BMC evolutionary biology* **10**, 8 (2010).
135. Dereeper, A. et al. Phylogeny.fr: robust phylogenetic analysis for the non-specialist. *Nucleic acids research* **36**, W465-9 (2008).
136. Westendorf, J.M., Rao, P.N. & Gerace, L. Cloning of cDNAs for M-phase phosphoproteins recognized by the MPM2 monoclonal antibody and determination of the phosphorylated

- epitope. *Proceedings of the National Academy of Sciences of the United States of America* **91**, 714-8 (1994).
137. Matsumoto-Taniura, N., Pirollet, F., Monroe, R., Gerace, L. & Westendorf, J.M. Identification of novel M phase phosphoproteins by expression cloning. *Molecular biology of the cell* **7**, 1455-69 (1996).
 138. Kelley, L.A. & Sternberg, M.J. Protein structure prediction on the Web: a case study using the Phyre server. *Nature protocols* **4**, 363-71 (2009).
 139. Cole, C., Barber, J.D. & Barton, G.J. The Jpred 3 secondary structure prediction server. *Nucleic acids research* **36**, W197-201 (2008).
 140. Arnold, K., Bordoli, L., Kopp, J. & Schwede, T. The SWISS-MODEL workspace: a web-based environment for protein structure homology modelling. *Bioinformatics* **22**, 195-201 (2006).
 141. Kamimoto, T., Zama, T., Aoki, R., Muro, Y. & Hagiwara, M. Identification of a novel kinesin-related protein, KRMP1, as a target for mitotic peptidyl-prolyl isomerase Pin1. *The Journal of biological chemistry* **276**, 37520-8 (2001).
 142. Jensen, L.J. et al. STRING 8--a global view on proteins and their functional interactions in 630 organisms. *Nucleic acids research* **37**, D412-6 (2009).
 143. Liu, F. et al. A genomewide screen for late-onset Alzheimer disease in a genetically isolated Dutch population. *American journal of human genetics* **81**, 17-31 (2007).
 144. De Toledo, M., Coulon, V., Schmidt, S., Fort, P. & Blangy, A. The gene for a new brain specific RhoA exchange factor maps to the highly unstable chromosomal region 1p36.2-1p36.3. *Oncogene* **20**, 7307-17 (2001).
 145. Kanehira, M. et al. Oncogenic role of MPHOSPH1, a cancer-testis antigen specific to human bladder cancer. *Cancer research* **67**, 3276-85 (2007).
 146. Sternberg, C.N. The treatment of advanced bladder cancer. *Annals of oncology : official journal of the European Society for Medical Oncology / ESMO* **6**, 113-26 (1995).
 147. Zochodne, D.W., Auer, R. & Fritzler, M.J. Longstanding ataxic demyelinating polyneuropathy with a novel autoantibody. *Neurology* **60**, 127-9 (2003).
 148. Gruneberg, U., Neef, R., Honda, R., Nigg, E.A. & Barr, F.A. Relocation of Aurora B from centromeres to the central spindle at the metaphase to anaphase transition requires MKlp2. *The Journal of cell biology* **166**, 167-72 (2004).
 149. Neef, R. et al. Choice of Plk1 docking partners during mitosis and cytokinesis is controlled by the activation state of Cdk1. *Nature cell biology* **9**, 436-44 (2007).
 150. Mishima, M., Pavicic, V., Gruneberg, U., Nigg, E.A. & Glotzer, M. Cell cycle regulation of central spindle assembly. *Nature* **430**, 908-13 (2004).
 151. Jang, J.K., Rahman, T., Kober, V.S., Cesario, J. & McKim, K.S. Misregulation of the kinesin-like protein Subito induces meiotic spindle formation in the absence of chromosomes and centrosomes. *Genetics* **177**, 267-80 (2007).
 152. Buchan, D.W. et al. Protein annotation and modelling servers at University College London. *Nucleic acids research* **38**, W563-8 (2010).
 153. Bornberg-Bauer, E., Rivals, E. & Vingron, M. Computational approaches to identify leucine zippers. *Nucleic acids research* **26**, 2740-6 (1998).
 154. Gough, J., Karplus, K., Hughey, R. & Chothia, C. Assignment of homology to genome sequences using a library of hidden Markov models that represent all proteins of known structure. *Journal of molecular biology* **313**, 903-19 (2001).
 155. Echard, A. et al. Interaction of a Golgi-associated kinesin-like protein with Rab6. *Science* **279**, 580-5 (1998).
 156. Neef, R., Klein, U.R., Kopajtich, R. & Barr, F.A. Cooperation between mitotic kinesins controls the late stages of cytokinesis. *Current biology : CB* **16**, 301-7 (2006).
 157. Hummer, S. & Mayer, T.U. Cdk1 negatively regulates midzone localization of the mitotic kinesin Mklp2 and the chromosomal passenger complex. *Current biology : CB* **19**, 607-12 (2009).
 158. Hornick, J.E., Karanjeet, K., Collins, E.S. & Hinchcliffe, E.H. Kinesins to the core: The role of microtubule-based motor proteins in building the mitotic spindle midzone. *Seminars in cell & developmental biology* **21**, 290-9 (2010).

159. Walczak, C.E. & Shaw, S.L. A MAP for bundling microtubules. *Cell* **142**, 364-7 (2010).
160. Reichert, N. et al. Lin9, a subunit of the mammalian DREAM complex, is essential for embryonic development, for survival of adult mice, and for tumor suppression. *Molecular and cellular biology* **30**, 2896-908 (2010).
161. Matsuoka, A. et al. Lenalidomide induces cell death in an MDS-derived cell line with deletion of chromosome 5q by inhibition of cytokinesis. *Leukemia : official journal of the Leukemia Society of America, Leukemia Research Fund, U.K* **24**, 748-55 (2010).
162. Zhu, C. & Jiang, W. Cell cycle-dependent translocation of PRC1 on the spindle by Kif4 is essential for midzone formation and cytokinesis. *Proceedings of the National Academy of Sciences of the United States of America* **102**, 343-8 (2005).
163. Adams, R.R., Maiato, H., Earnshaw, W.C. & Carmena, M. Essential roles of Drosophila inner centromere protein (INCENP) and aurora B in histone H3 phosphorylation, metaphase chromosome alignment, kinetochore disjunction, and chromosome segregation. *The Journal of cell biology* **153**, 865-80 (2001).
164. Kallio, M.J., McClelland, M.L., Stukenberg, P.T. & Gorbsky, G.J. Inhibition of aurora B kinase blocks chromosome segregation, overrides the spindle checkpoint, and perturbs microtubule dynamics in mitosis. *Current biology : CB* **12**, 900-5 (2002).
165. Lee, S.H., McCormick, F. & Saya, H. Mad2 inhibits the mitotic kinesin MKlp2. *The Journal of cell biology* **191**, 1069-77 (2010).
166. Tcherniuk, S. et al. Relocation of Aurora B and survivin from centromeres to the central spindle impaired by a kinesin-specific MKLP-2 inhibitor. *Angewandte Chemie* **49**, 8228-31 (2010).
167. Li, Y., Gorbea, C., Mahaffey, D., Rechsteiner, M. & Benezra, R. MAD2 associates with the cyclosome/anaphase-promoting complex and inhibits its activity. *Proceedings of the National Academy of Sciences of the United States of America* **94**, 12431-6 (1997).
168. Wilmeth, L.J., Shrestha, S., Montano, G., Rashe, J. & Shuster, C.B. Mutual dependence of Mob1 and the chromosomal passenger complex for localization during mitosis. *Molecular biology of the cell* **21**, 380-92 (2010).
169. Hegyaljay, R., Paal, A., Langmar, Z., Sobel, G. & Banhidy, F. [Women's knowledge about cervical cancer]. *Orvosi hetilap* **151**, 302-5 (2010).
170. Yu, T., Peng, Y.C. & Androphy, E.J. Mitotic kinesin-like protein 2 binds and colocalizes with papillomavirus E2 during mitosis. *Journal of virology* **81**, 1736-45 (2007).
171. DiMagno, E.P., Reber, H.A. & Tempero, M.A. AGA technical review on the epidemiology, diagnosis, and treatment of pancreatic ductal adenocarcinoma. American Gastroenterological Association. *Gastroenterology* **117**, 1464-84 (1999).
172. Taniuchi, K. et al. Down-regulation of RAB6KIFL/KIF20A, a kinesin involved with membrane trafficking of discs large homologue 5, can attenuate growth of pancreatic cancer cell. *Cancer research* **65**, 105-12 (2005).
173. Imai, K. et al. Identification of HLA-A2-restricted CTL epitopes of a novel tumour-associated antigen, KIF20A, overexpressed in pancreatic cancer. *British journal of cancer* **104**, 300-7 (2011).
174. Yan, G.R. et al. Genistein-induced mitotic arrest of gastric cancer cells by downregulating KIF20A, a proteomics study. *Proteomics* **12**, 2391-9 (2012).
175. Lu, Y. et al. Cross-species comparison of orthologous gene expression in human bladder cancer and carcinogen-induced rodent models. *American journal of translational research* **3**, 8-27 (2010).
176. Claerhout, S. et al. Gene expression signature analysis identifies vorinostat as a candidate therapy for gastric cancer. *PloS one* **6**, e24662 (2011).
177. Gasnereau, I. et al. KIF20A mRNA and its product MKlp2 are increased during hepatocyte proliferation and hepatocarcinogenesis. *The American journal of pathology* **180**, 131-40 (2012).
178. Jordan, M.A. & Wilson, L. Microtubules as a target for anticancer drugs. *Nature reviews. Cancer* **4**, 253-65 (2004).
179. Wilson, L. & Jordan, M.A. New microtubule/tubulin-targeted anticancer drugs and novel chemotherapeutic strategies. *Journal of chemotherapy* **16 Suppl 4**, 83-5 (2004).

180. Katsetos, C.D. & Draber, P. Tubulins as Therapeutic Targets in Cancer: from Bench to Bedside. *Current pharmaceutical design* (2012).
181. Alahmad, A. et al. Desmoplakin and KIF20B as target antigens in patients with paroxysmal nocturnal haemoglobinuria. *British journal of haematology* **151**, 273-80 (2010).
182. Nigg, E.A.M., T.U.; Huemmer, S.; Barr, F.; Nbormann, J.; 2-Phenylquinoxalines as inhibitors of MPP1 for treatment of proliferative diseases. in *World patent WO 2006-EP459. 2006 Aug 3*. (Europe).
183. Hackney, D.D. & Jiang, W. Assays for kinesin microtubule-stimulated ATPase activity. *Methods in molecular biology* **164**, 65-71 (2001).
184. Freyer, M.W. & Lewis, E.A. Isothermal titration calorimetry: experimental design, data analysis, and probing macromolecule/ligand binding and kinetic interactions. *Methods in cell biology* **84**, 79-113 (2008).
185. Dong, W.J., Wang, C.K., Gordon, A.M., Rosenfeld, S.S. & Cheung, H.C. A kinetic model for the binding of Ca²⁺ to the regulatory site of troponin from cardiac muscle. *The Journal of biological chemistry* **272**, 19229-35 (1997).
186. O'Shannessy, D.J. & Winzor, D.J. Interpretation of deviations from pseudo-first-order kinetic behavior in the characterization of ligand binding by biosensor technology. *Analytical biochemistry* **236**, 275-83 (1996).
187. Kabsch, W. Xds. *Acta crystallographica. Section D, Biological crystallography* **66**, 125-32 (2010).
188. Cowtan, K., Emsley, P. & Wilson, K.S. From crystal to structure with CCP4. *Acta crystallographica. Section D, Biological crystallography* **67**, 233-4 (2011).
189. Kantardjieff, K.A. & Rupp, B. Matthews coefficient probabilities: Improved estimates for unit cell contents of proteins, DNA, and protein-nucleic acid complex crystals. *Protein science : a publication of the Protein Society* **12**, 1865-71 (2003).
190. Emsley, P. & Cowtan, K. Coot: model-building tools for molecular graphics. *Acta crystallographica. Section D, Biological crystallography* **60**, 2126-32 (2004).
191. Murshudov, G.N., Vagin, A.A. & Dodson, E.J. Refinement of macromolecular structures by the maximum-likelihood method. *Acta crystallographica. Section D, Biological crystallography* **53**, 240-55 (1997).
192. Adams, P.D. et al. PHENIX: building new software for automated crystallographic structure determination. *Acta crystallographica. Section D, Biological crystallography* **58**, 1948-54 (2002).
193. Schuttelkopf, A.W. & van Aalten, D.M. PRODRG: a tool for high-throughput crystallography of protein-ligand complexes. *Acta crystallographica. Section D, Biological crystallography* **60**, 1355-63 (2004).
194. Chen, V.B. et al. MolProbity: all-atom structure validation for macromolecular crystallography. *Acta crystallographica. Section D, Biological crystallography* **66**, 12-21 (2010).
195. Battye, T.G., Kontogiannis, L., Johnson, O., Powell, H.R. & Leslie, A.G. iMOSFLM: a new graphical interface for diffraction-image processing with MOSFLM. *Acta crystallographica. Section D, Biological crystallography* **67**, 271-81 (2011).
196. The CCP4 suite: programs for protein crystallography. *Acta Crystallogr D Biol Crystallogr* **50**, 760-3 (1994).
197. Yan, Y. et al. Inhibition of a mitotic motor protein: where, how, and conformational consequences. *J Mol Biol* **335**, 547-54 (2004).
198. Blow, D.M. Rearrangement of Cruickshank's formulae for the diffraction-component precision index. *Acta crystallographica. Section D, Biological crystallography* **58**, 792-7 (2002).
199. Wilkins, M.R. et al. Protein identification and analysis tools in the ExPASy server. *Methods in molecular biology* **112**, 531-52 (1999).
200. Kodama, T., Fukui, K. & Kometani, K. The initial phosphate burst in ATP hydrolysis by myosin and subfragment-1 as studied by a modified malachite green method for determination of inorganic phosphate. *Journal of biochemistry* **99**, 1465-72 (1986).

201. Walter, T.S. et al. Lysine methylation as a routine rescue strategy for protein crystallization. *Structure* **14**, 1617-22 (2006).
202. Rayment, I. Reductive alkylation of lysine residues to alter crystallization properties of proteins. *Methods in enzymology* **276**, 171-9 (1997).
203. Rayment, I. et al. Three-dimensional structure of myosin subfragment-1: a molecular motor. *Science* **261**, 50-8 (1993).
204. Zhang, B., Liu, J.F., Xu, Y. & Ng, S.C. Crystal structure of HsEg5 in complex with clinical candidate CK0238273 provides insight into inhibitory mechanism, potency, and specificity. *Biochemical and biophysical research communications* **372**, 565-70 (2008).
205. Talapatra, S.K.K., F.; Schuettelkopf, A.; The structure of the ternary Eg5-ADP-ispinesib complex. *Acta crystallographica. Section D, Biological crystallography* (2012).
206. DeBonis, S. et al. Interaction of the mitotic inhibitor monastrol with human kinesin Eg5. *Biochemistry* **42**, 338-49 (2003).
207. Britton, D. Estimation of twinning parameter for twins with exactly superimposed reciprocal lattices. *Acta Crystallogr A* **28**, 296-297 (1972).
208. Yeates, T.O. Detecting and overcoming crystal twinning. *Methods in enzymology* **276**, 344-58 (1997).
209. Lebedev, A.A., Vagin, A.A. & Murshudov, G.N. Intensity statistics in twinned crystals with examples from the PDB. *Acta crystallographica. Section D, Biological crystallography* **62**, 83-95 (2006).
210. Debonis, S. et al. Structure-activity relationship of S-trityl-L-cysteine analogues as inhibitors of the human mitotic kinesin Eg5. *Journal of medicinal chemistry* **51**, 1115-25 (2008).
211. Sakowicz, R. et al. Antitumor activity of a kinesin inhibitor. *Cancer research* **64**, 3276-80 (2004).
212. Lahue, B.R., Ma, Y., Shipps, G.W., Jr., Seghezzi, W. & Herbst, R. Substituted benzimidazoles: A novel chemotype for small molecule hKSP inhibitors. *Bioorganic & medicinal chemistry letters* **19**, 3405-9 (2009).
213. Funk, C.J., Davis, A.S., Hopkins, J.A. & Middleton, K.M. Development of high-throughput screens for discovery of kinesin adenosine triphosphatase modulators. *Analytical biochemistry* **329**, 68-76 (2004).
214. Brier, S., Lemaire, D., DeBonis, S., Forest, E. & Kozielski, F. Molecular dissection of the inhibitor binding pocket of mitotic kinesin Eg5 reveals mutants that confer resistance to antimitotic agents. *Journal of molecular biology* **360**, 360-76 (2006).
215. Parrish, C.A. et al. Novel ATP-competitive kinesin spindle protein inhibitors. *Journal of medicinal chemistry* **50**, 4939-52 (2007).
216. Matsuno, K., Sawada, J. & Asai, A. Therapeutic potential of mitotic kinesin inhibitors in cancer. *Expert Opinion on Therapeutic Patents* **18**, 253-274 (2008).
217. Hochhaus, A. Chronic myelogenous leukemia (CML): resistance to tyrosine kinase inhibitors. *Annals of oncology : official journal of the European Society for Medical Oncology / ESMO* **17 Suppl 10**, x274-9 (2006).
218. Krishnamurty, R. & Maly, D.J. Biochemical mechanisms of resistance to small-molecule protein kinase inhibitors. *ACS chemical biology* **5**, 121-38 (2010).
219. Graziano, G. Comment on "Entropy/enthalpy compensation: hydrophobic effect, micelles and protein complexes" by E. Fiescaro, C. Compari and A. Braibanti, *Phys. Chem. Chem. Phys.*, 2004, 6, 4156. *Physical chemistry chemical physics : PCCP* **7**, 1322-3; discussion 1324-5 (2005).
220. Valentine, M.T., Fordyce, P.M. & Block, S.M. Eg5 steps it up! *Cell division* **1**, 31 (2006).
221. Orr, G.A., Verdier-Pinard, P., McDaid, H. & Horwitz, S.B. Mechanisms of Taxol resistance related to microtubules. *Oncogene* **22**, 7280-95 (2003).
222. Clark, J., Cools, J. & Gilliland, D.G. EGFR inhibition in non-small cell lung cancer: resistance, once again, rears its ugly head. *PLoS medicine* **2**, e75 (2005).
223. Kobayashi, S. et al. EGFR mutation and resistance of non-small-cell lung cancer to gefitinib. *The New England journal of medicine* **352**, 786-92 (2005).

224. Torkamani, A. & Schork, N.J. Prediction of cancer driver mutations in protein kinases. *Cancer research* **68**, 1675-82 (2008).
225. Molnar, K. & Farkas, E. Current results on biological activities of lichen secondary metabolites: a review. *Zeitschrift fur Naturforschung. C, Journal of biosciences* **65**, 157-73 (2010).
226. Bezivin, C., Tomasi, S., Lohezic-Le Devehat, F. & Boustie, J. Cytotoxic activity of some lichen extracts on murine and human cancer cell lines. *Phytomedicine : international journal of phytotherapy and phytopharmacology* **10**, 499-503 (2003).
227. Russo, A., Piovano, M., Lombardo, L., Garbarino, J. & Cardile, V. Lichen metabolites prevent UV light and nitric oxide-mediated plasmid DNA damage and induce apoptosis in human melanoma cells. *Life sciences* **83**, 468-74 (2008).